

Mollow triplet emission properties and dephasing effects in semiconductor quantum dots

Von der Fakultät Mathematik und Physik
der Universität Stuttgart
zur Erlangung der Würde eines
Doktors der Naturwissenschaften (Dr. rer. nat.)
genehmigte Abhandlung

Vorgelegt von

Stefanie Weiler

aus Leonberg

Hauptberichter:	Prof. Dr. P. Michler
Mitberichter:	Prof. Dr. T. Pfau
Tag der Einreichung:	26.09.2013
Tag der mündlichen Prüfung:	25.11.2013

Institut für Halbleiteroptik und Funktionelle Grenzflächen
Universität Stuttgart
2013

Contents

1	Introduction	1
2	Theoretical Background	9
2.1	Properties of low-dimensional semiconductor structures	9
2.1.1	Single particle energy states	11
2.1.2	Excitons	12
2.1.3	Exciton fine-structure splitting	13
2.2	Representation of different light states and photon correlation	15
2.2.1	Quantization of the electromagnetic field	16
2.2.2	Thermal Light	18
2.2.3	Fock States	20
2.2.4	Coherent States	21
2.2.5	Photon correlation	22
2.3	Two-level system photon interaction	25
2.3.1	Basic quantum mechanical concepts	25
2.3.2	Interaction Hamiltonian	26
2.3.3	Optical Bloch equations	28
2.3.4	Resonance fluorescence	29
2.4	Cavity quantum electrodynamics	37
2.4.1	Jaynes-Cummings model, <i>strong</i> and <i>weak coupling regime</i>	38
3	Experimental Techniques	43
3.1	Low temperature micro-photoluminescence setup	43
3.2	<i>Hanbury Brown & Twiss</i> -interferometer for photon statistics measurements	46

3.3	Time-correlated single photon counting for radiative decay time measurements	48
3.4	<i>Michelson</i> interferometer for coherence time measurements	49
3.5	Scanning <i>Fabry-Pérot</i> interferometer for high-resolution μ -PL	51
4	Emission properties of resonantly excited QDs	53
4.1	Resonance fluorescence on QDs	54
4.2	Resonance fluorescence: A quantum mechanical description	55
4.3	Planar sample structure	58
4.4	Resonant spectroscopy of single QDs	58
4.5	Power- and detuning-dependence of resonance fluorescence	61
4.6	Excitation-induced dephasing	64
4.7	Polaron master equation for a resonant excited TLS with phonon interaction	66
4.8	Detuning-dependent Mollow triplet: Regimes of sideband broadening and narrowing	71
4.9	Mollow quintuplets	77
5	Indistinguishable photons from the Mollow sidebands	83
5.1	Mollow triplet photon statistics	87
5.2	Experimental techniques	89
5.2.1	<i>Hong-Ou-Mandel</i> -setup for two-photon interference measurements	90
5.2.2	Double <i>Michelson</i> interferometer filtering technique	91
5.3	Experimental results	97
5.3.1	Mollow triplet sideband coherence	98
5.3.2	Auto-correlations	100
5.3.3	Indistinguishability of the Mollow triplet sideband emission	102
5.3.4	Decay timescale of the emission	109
6	Phonon-assisted incoherent excitation	113
6.1	Dephasing in semiconductor QDs	113
6.1.1	Radiative dephasing	114
6.1.2	Pure dephasing	117
6.2	Experimental results	124
6.2.1	Theory	127
6.2.2	Experiment versus Theory	131

6.2.3	Emission coherence	133
6.3	Discussion	136
7	Non-resonant quantum dot-cavity coupling	139
7.1	Theoretical descriptions of NRC	140
7.1.1	NRC for large emitter-mode detunings	140
7.1.2	NRC for small emitter-mode detunings	141
7.2	Micropillar sample structure	143
7.3	NRC under quasi-resonant QD excitation	145
7.3.1	Temperature-dependent μ -PL	146
7.3.2	Correlation measurements	148
7.3.3	Decay time and coherence time measurements	150
7.4	NRC under resonant QD excitation	154
8	Conclusion and Outlook	157
9	Zusammenfassung	165
A	Material parameters	175
	Bibliography	176
	Publications	195
	Lebenslauf	199
	Danksagungen	201

Chapter 1

Introduction

The various forms of quantum information processing make use of the quantum mechanical properties of light [1].

One application is quantum computing. Its basis is formed by two readily distinguishable states, e.g. horizontal and vertical photon polarization or different spin orientation (up, down) of electrons or nucleons, to represent binary 0 and 1. The striking difference to classical computers, where the bits represent either 0 or 1, is the fact that each qubit can be in a coherent superposition state of $|0\rangle$ and $|1\rangle$. Therefore a collection of N qubits is described by 2^N wave function amplitudes. Due to this fundamental difference, a quantum computer can be efficient for example in the factorization of large numbers known as the *Shor's algorithm*, where the required mathematical operations are reduced from exponential to polynomial class and can therefore be performed within much shorter timescales. One reason why Shor's algorithm created intense interest is that the RSA encryption method used in classical cryptography is based on the difficulty of factorizing large integer numbers.

One way to avoid the risk that a large quantum computer might decode the classically encrypted data within a reasonable period of time is to employ quantum-based cryptography for secure quantum key distribution. In 1984 Bennett and Brassard proposed their famous quantum key distribution protocol named BB84 [2]. In such protocols the sender is traditionally named Alice and the receiver called Bob. The security lies in the fact of the non-cloning theorem of photons. This allows to recognize an eavesdropper that intercepts the photons from Alice and

tries to send a copy of each photon to Bob. When single-photons are employed for the key distribution protocol, an eavesdropping attempt can be recognized by evaluating the quantum bit error rate. Several groups of researchers have performed proof-to-principle experiments which clearly demonstrate the feasibility of quantum key distribution. To name but a few out of the many, this has been shown for single-photon sources, namely electrically driven quantum dots (QDs) [3], and also very recently for free-space long distance key distribution from an airplane to the ground [4] or a hot-air balloon [5]. The latter two experiments were carried out with strongly attenuated lasers.

A fundamental feature of coherent laser emission is the *Poissonian* photon-number distribution, which entails the major drawback that even for a strongly attenuated source the generation of zero or two photons in addition to the desired single-photon emission is likely. When Alice and Bob exchange more than one photon at a time, a possible eavesdropper can remain unnoticed, leading to an insecure quantum key distribution. To eliminate this risk, single-photon sources, such as atoms, ions, molecules, solid state defect centers and quantum dots need to be employed which possess the ability to deterministically emit one photon at a time. QDs have been proven to be single-photon emitters even at room temperatures [6, 7] with the distinct advantage of wide-range tailorability concerning the confinement potential and therefore the emission wavelength. In addition, these solid-state based single-photon emitters can be used for integrated optical architecture, which is highly advantageous due to the demand for miniaturization. The principle idea of integrated circuits is to guide light in waveguides. Logic operations are based on beam splitter elements, e.g. forming a CNOT or Hadamard gate, realized by two waveguides which are brought sufficiently close together so that the evanescent fields overlap. The correct functionality of integrated circuits relies on the utilization of indistinguishable photons for these on chip approaches [8].

One possibility for quantum bit transfer is via free-space, for which wavelengths of about 770 nm are beneficial, because the Earth's atmosphere has a high transmission window there and thus naturally provides a low-loss communication channel, which is only weakly dispersive and non-birefringent. In contrast for applications based on long-distance fibers, the telecommunication wavelength of 1.3 μm and 1.55 μm have the advantage of weak signal damping. One drawback

when using telecommunication wavelength is that standard silicon-based detectors cannot be used for photon detection. These detectors are limited to wavelengths below $\sim 1 \mu\text{m}$ due to the band gap energy of the material. Another possible approach to enhance the transmission distance is to employ a quantum repeater [9]. In contrast to classical channels, where repeater stations simply amplify the signal, this is not possible for quantum information because of the non-cloning theorem. Quantum repeaters are based on the principle idea of teleportation [10], i.e. entanglement swapping. The most widely used method to create entangled photon pairs is by the nonlinear optical process of parametric down conversion. One disadvantage of this process is the *Poissonian* distribution of the created photon pairs. The generation of entangled purely single-photon pairs is therefore desirable. One way to create such a Bell state is via the biexciton-exciton cascade in a QD, in the specific case of exciton fine-structure splitting below the linewidth of the emission. Quantum state tomography on the biexciton-exciton cascade has revealed Bell state emission with a high fidelity [11, 12]. The photon extraction efficiency can even be enhanced by utilizing the Purcell effect of a photonic molecule (double micropillar cavity) when either emission channel is resonant with a cavity mode [13]. The entanglement of the created state is limited by the coherence of the emitted entangled photons. Non-resonant pumping schemes usually suffer a lower emission coherence compared to resonant excitation. This is due to phonon-induced carrier relaxation from higher energetic states; in addition, the relaxation process induces a timing jitter. A resonant two-photon excitation scheme has therefore been proven successfully to reveal a better degree of fidelity in quantum state tomography compared to the non-resonant excitation scheme [14].

Due to the fact that QDs are solid state systems embedded in a host matrix they interact with solid state environment, leading to dephasing in the system. This can be due to several reasons, e.g. due to phonons or carriers, which are trapped in the vicinity of the QD. Some dephasing processes can be avoided, e.g. a resonant excitation scheme circumvents phonon-assisted carrier relaxation processes from higher QD-shells, via direct creation of electron-hole pairs into the QD s-shell. The resonance fluorescence offers the possibility to create close to *Fourier transform-limited* highly indistinguishable photons. A detailed knowledge about the emission properties of the resonance fluorescence of a QD under special consideration of the interaction with the solid state is there-

fore indispensable. From a general point of view, it is necessary to understand the different dephasing processes and the resulting emission properties of excitons in QDs to judge the applicability and also the limitations of the photons emitted by dephasing-affected radiative recombination of electron-hole pairs.

In view of the demands of possible application in quantum information processing, the studies presented in this thesis focus on the following aspects:

- Profound investigations of the Mollow triplet emission properties of the resonance fluorescence emission of a QD under excitation above emitter saturation.
- The verification of indistinguishable photons from the Mollow triplet sidebands.
- Detailed studies of the longitudinal acoustic phonon-exciton interaction leading to phonon-assisted QD excitation.
- The verification of the emission properties of a non-resonantly coupled emitter mode system.

In the following **outline** the content of the chapters of this thesis is sketched out.

In **chapter 2** a fundamental description of low-dimensional semiconductor structures is introduced. Special focus is put on the zero-dimensional quantum dot structure, which reveals atom-like discrete energy eigenstates for the confined carriers. The formation of Coulomb-correlated electron-hole pairs, termed *excitons*, is addressed in particular. In explicit consideration of spin exchange interaction, the exciton ground state can be fine-structure split, dependent on the shape of the QD potential. In addition, the description and characteristics of three different photon fields are introduced, more precisely thermal (chaotic) and coherent light, which can both be described classically, whereas the third class of photon number (Fock) states reveals a non-classical behavior. The photon statistics in terms of second-order auto-correlation on the different light fields is discussed in detail, revealing photon bunching, time-uncorrelated photon emission (*Poissonian* statistics) and antibunching, respectively. For a comprehensive introduction to the emission of a resonantly excited two level-system (TLS), termed resonance

fluorescence (RF), the optical Bloch equations are derived from the system Hamiltonian of a TLS excited by a monochromatic resonant laser field. Particular attention is paid to the characteristic features of the RF emission above and below emitter saturation, with special focus on the distinct features of second-order photon-correlations, emission spectra and first-order correlations. The final part of the chapter introduces the concept of cavity quantum electrodynamics for a TLS embedded in a microcavity. Whereas systems in the strong coupling regime can coherently exchange energy between the cavity mode and the TLS, weak coupling is manifested in a crossing of the emitter and cavity resonance under systematic relative detuning of both emission energies. In addition, weak coupling offers the distinct advantage of controlling the emitter dynamics via the *Purcell effect*.

The basic experimental techniques which are applied for the optical investigations in this thesis are presented in **chapter 3**. Low-temperature micro-photoluminescence is introduced as the basic building block for all further techniques applied to characterize the emission of a quantum dot. For second-order photon-correlation measurements a *Hanbury Brown* and *Twiss*-setup is commonly employed. The investigation of the decay time of electron-hole pairs inside a QD are performed via the technique of time-correlated single-photon counting (TCSPC). Besides the decay time and temporal photon correlation, another important quantity that characterizes the photon emission is the coherence time measured via Michelson interferometric Fourier spectroscopy. Furthermore, a *Fabry-Pérot* based high-resolution micro-photoluminescence spectroscopy technique is used experimentally, indispensable for resolving the characteristic Mollow triplet, the hallmark of RF, which is studied extensively in this thesis.

In **chapter 4** a quantum-mechanical description of RF in terms of *dressed states* is introduced. The basic properties of an experimentally derived power-dependent Mollow triplet series under strictly resonant excitation together with a detuning-dependent Mollow triplet series taken under constant excitation power are compared to theoretical expectations. This comparison shows that the TLS-based theory can reproduce the main features of RF, moreover it reveals first indications that a full description of the system needs the consideration of the interaction of the exciton with the solid-state surrounding medium. One effect of the solid state interaction is excitation-induced dephasing of

RF manifested in Mollow sideband broadening with increasing excitation power. A theoretical model that includes linear coupling between excitons and longitudinal acoustic (LA) phonons via deformation potential coupling developed by *Prof. Stephen Hughes* and co-workers is the polaron master equation approach. In this thesis the basic concepts together with the physical meaning of important parameters are introduced. For a detuning-dependent Mollow triplet series the model predicts Mollow triplet sideband narrowing or broadening dependent on the ratio of pure dephasing rate to decay rate of the system. The regime of sideband broadening has been accessed experimentally and the experimental results are compared to the theoretical predictions. Good agreement is found on the basis of independently derived modelling parameters. The final part of the chapter presents the Mollow quintuplet emission of resonantly excited excitons. Due to the exciton fine-structure splitting, the excitation laser can theoretically excite an exciton in one or the other fine structure component, leading to two individual Mollow triplets in the spectral domain, and therefore a combined integrated five-peak Mollow quintuplet emission spectrum. The experimental proof of Mollow quintuplet observation in accordance with theoretical predictions is the aim of the corresponding investigations.

The goal of the study presented in **chapter 5** is the verification of indistinguishable photons from the Mollow triplet sidebands. The experimental proof of photon indistinguishability is based on a beam splitter interference experiment, which is named after *Hong, Ou* and *Mandel*, who performed the pioneering work on two-photon indistinguishability verification in 1987. The corresponding *Hong-Ou-Mandel* setup is described as well. For the indistinguishability measurements a crucial requirement is background-free single-photon emission, therefore the theoretically expected photon statistics of the three individual Mollow lines are discussed. In addition, a double Michelson interferometric filtering technique needs to be employed to tackle the experimental challenge of the individual and background-free spectral selection of one Mollow triplet component. The technique is based on selective destructive interference of two Mollow triplet components while the third one interferes constructively. Preliminary to the two-photon interference measurements the emission properties in terms of Mollow triplet sideband coherence and auto-correlation on the individual lines are presented. The two-photon interference measurements on the red as well

as the blue Mollow sideband for different Rabi splittings reveal highly indistinguishable photons with a post-selected interference contrast up to 97% under continuous wave excitation. The values derived from the independent pre-characterization reveal excellent agreement with the data; the only discrepancy between experimentally measured and extracted values is found for the decay time, possible reasons for which are discussed in detail at the end of the chapter.

In **chapter 6** a comprehensive study of the effect of phonon-assisted incoherent excitation (PAIE) is presented. An overview of different dephasing mechanisms in QDs is presented. A standard model capable to describe the linear exciton-phonon interaction is the independent boson model. The coupling mechanism for In(Ga)As/GaAs QDs to acoustic phonons is due to deformation potential coupling; besides this, there is piezoelectric coupling to acoustic and polar coupling to optical phonons. Spectral diffusion effects due to the influence of carriers outside the QD can also affect the spectral emission properties. The joint experiment-theory study on PAIE, the effect of QD s-shell excitation by a detuned off-resonant laser via phonon mediation, is investigated. The QD emission intensity extracted from laser scans over the QD s-shell resonance exhibits the so-called QD intensity plot. These plots reveal a sharp zero phonon line at the QD s-shell resonance surrounded by acoustic phonon replica at the lower and higher energy detuning side. The intensity plots are reproduced theoretically by the polaron master equation approach. First, the influence of different parameters is analyzed theoretically under systematic variation. In a second step, the theoretical predictions are compared to experimental results, which reveal excellent agreement. A high emission coherence is beneficial to possible applications. Therefore, the coherence time of the QD under resonant excitation is compared to the coherence under PAIE, the latter is found to be ten times lower compared to the resonant emission coherence and independent of the specific emitter-laser detuning.

The study in **chapter 7** focuses on the investigation of the emission properties of a non-resonantly coupled (NRC) system of a QD coupled to two modes of the surrounding microcavity. The micropillar sample structure together with the corresponding mode emission spectra is introduced along with the two non-resonantly coupled modes under investigation, namely the fundamental mode FM and a higher order mode M2 situated spectrally close to the QD. A detailed bibliogra-

phy overview on NRC, which describes the effect of QD excitation but photon emission via a detuned cavity mode channel, is presented at the beginning of the chapter. The comprehensive experimental study begins with a temperature-dependent micro-photoluminescence series under quasi-resonant QD excitation. The distinct crossing between QD and M2 reveals a typical key feature for a system in the weak emitter-mode coupling regime. Via auto- and cross-correlation measurements the feeding of both non-resonantly coupled modes by the QD under investigation can be proven unambiguously. The QD emission decay time decreases towards emitter-mode (M2) resonance due to the *Purcell* effect. The spectrally close mode M2 reveals a similar decay time trend, whereas the far detuned FM emission dynamics is unaffected by the specific (but large) detuning from the QD. The emission coherence of both modes is found to be low and independent of the specific emitter-mode detuning. This can be attributed to the influence of dephasing due to non-resonant coupling and the distinct spectral properties of the two individual modes. In contrast, the QD emission shows a more than 15-times higher coherence for low temperatures and large emitter-mode detunings. The effect of NRC is also observable under strictly resonant QD excitation. With increasing excitation strength, first the spectrally close M2 mode starts to couple non-resonantly and at higher powers non-resonant coupling of the far detuned FM can be traced as well.

Chapter 2

Theoretical Background

2.1 Properties of low-dimensional semiconductor structures

In the last few decades low-dimensional semiconductor structures have been an intense field of research. Particular attention has been paid to the zero-dimensional semiconductor quantum dot (QD) structures, artificially created to confine the wave function of trapped charge carriers in all three dimensions. Whenever the carrier confinement reduces the mobility of a particle to a size lower than its *de Broglie* wavelength λ^{dB} , quantization effects become important.

With the introduction of the effective mass $m_{e,h}^*$ for electrons and holes and k_B as the *Boltzmann* constant the *de Broglie* wavelength reads

$$\lambda_{e,h}^{dB} = \frac{2\pi\hbar}{\sqrt{3m_{e,h}^*k_B T}} \quad , \quad (2.1)$$

typically values are in the order of a few tens of nanometers for electrons and holes. An important characteristic for three-dimensional carrier confinement is the delta-like density of energy states. Due to these discrete energy eigenstates in the QD that resemble the electronic shells in atoms they are also referred to as *artificial atoms*.

In this thesis the investigations are performed on In(Ga)As/GaAs semiconductor quantum dots. The three-dimensional carrier confinement is achieved by the epitaxial growth of self-assembled QDs composed

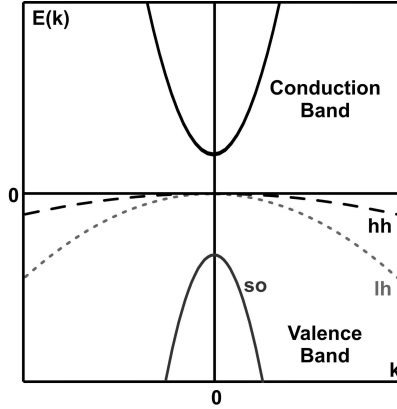


Figure 2.1: Schematic of the band structure of a direct zinc blende type semiconductor. The conduction band, and the three valence bands are plotted. The latter can be distinguished by the angular momentum of the charge carrier due to spin-orbit coupling, they are denoted as heavy holes (hh), light holes (lh) and spin split-off holes (so), respectively.

of a low-bandgap material ($E_{InAs}^{Gap} = 0.42 \text{ eV}$) embedded in a higher-bandgap material ($E_{GaAs}^{Gap} = 1.52 \text{ eV}$) [15]. For zinc-blende type direct semiconductors like GaAs and InAs, the band structure in dependence on the momentum \mathbf{k} is shown in Fig. 2.1. Spin-orbit coupling leads to a splitting of the valence band into three subbands: heavy holes (hh), light holes (lh) and spin split-off holes (so).

It is worth to mention that there are also other types of QD structures that ensure the three-dimensional confinement of carriers. For example in natural QDs [16] the excitons are localized by potential fluctuations due to composition and strain effects in the wetting layer. Colloidal QDs (also called nanocrystals) or core-shell QDs are fabricated by chemical techniques. Their applicability is limited in terms of long term stability, due to the fact, that they suffer from optical bleaching [17]. In electrostatic quantum dots the electron confinement potential is created by external voltages, applied to electrodes [18]. In contrast to the above described QDs only electrons are confined within the dot and the temperatures for investigations have to be very low $T < 1 \text{ K}$ [19].

2.1.1 Single particle energy states

Self-assembled QDs have typically a lateral size between 20–50 nm and a height of 2–5 nm and can be lens-, disc- or needle-like depending on the individual growth technique as well as the growth conditions. The small height leads to a strong confinement along the growth z-direction. According to the adiabatic approximation it is possible to decouple the in-plane (xy) and perpendicular (z) motion. In the latter case only the confined ground state needs to be considered, since the small vertical size is manifested in a large energetic splitting. In the xy-plane an ideal QD confinement with perfect in-plane rotational symmetry in terms of a harmonic confinement potential is assumed for the following discussion [20]. Therefore the problem reduces to a solution of the two-dimensional harmonic oscillator:

$$\hat{H} = \frac{\hat{p}_x^2}{2m^*} + \frac{\hat{p}_y^2}{2m^*} + \frac{m^*\omega_x^2 x^2}{2} + \frac{m^*\omega_y^2 y^2}{2} . \quad (2.2)$$

Assuming perfect rotational symmetry with $\omega_x = \omega_y = \omega$, the energetic eigenvalues of the system are

$$E = (n_x + n_y + 1)\hbar\omega \quad \text{with } n_{x,y} = 0, 1, 2, \dots . \quad (2.3)$$

For the denomination of the energetic states it is instructive to introduce the quantum numbers $s = n_x + n_y$ ($s = 0, 1, 2, \dots$) and $l = n_x - n_y$, where the latter is found to correspond to the angular momentum for the harmonic oscillator problem in polar coordinates [21]. The energetic shells are denoted in analogy to atoms as s-, p-, d-shell, a schematic depiction is found in Fig. 2.2. The eigenstates are equidistant in energy, and each shell is $2(s+1)$ -fold degenerate, where the two accounts for the two possible spin configurations. For the hole states only the hh need to be taken into account, due to the presence of strain in the material resulting from the lattice mismatch between the QD and barrier material. This results in a splitting between hh and lh by more than 100 meV for InAs/GaAs material systems [20], much larger than the energetic separation between the different shells inside the QD.

Depending on the dot diameter the number of confined higher energetic shells is limited. For very small dots d- or p-shells might not always exist.

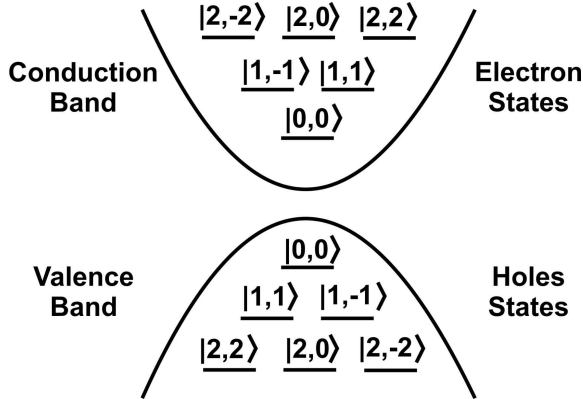


Figure 2.2: Eigenvalue spectrum of a QD modelled via a two-dimensional harmonic oscillator with rotational symmetry. The eigenstates are labeled with shell index s and angular quantum momentum l as $|s, l\rangle$.

2.1.2 Excitons

Lifting an electron from the valence band to the conduction band with a hole remaining in the latter one leads to the formation of an exciton, which is a joint quasi-particle bound via Coulomb interaction. The resulting energy is slightly smaller than that of the single particles due to the Coulomb interaction, this energetic difference is referred to as *exciton binding energy*.

When considering only the ground shell of the QD, there are different possible exciton configurations. If the QD s -shell is occupied by a single electron and hole respectively, the configuration is simply called an exciton. In contrast to this neutral configuration an additional second electron in the conduction band or hole in the valence band can lead to a negatively or positively charged trion. Due to the Pauli principle a biexciton with two electrons and holes in the ground state can be formed, here the Coulomb interaction energy differs compared to an exciton. The energy difference between twice the energy of non-interacting excitons and the full biexcitonic complex of four interacting particles is usually termed *biexciton binding energy*.

In terms of the single particle states introduced above the wavefunction for excitons can be expressed as [20]:

$$|\Psi\rangle = \sum_i^{s,s'} A_i^{s,s'} |s, +l\rangle_e |s', -l\rangle_h \quad . \quad (2.4)$$

Here the first (second) state vector describes the electron (hole).

For optical active transitions the electron-hole pair creation, i.e. the lift of an electron from the valence to the conduction band accompanied by photon absorption leads to certain selection rules due to angular momentum conservation. In zinc blende-type semiconductors the transition of an electron from the p-like valence to the s-like conduction band is accompanied by a change in the angular momentum by $\Delta m_j = \pm 1$. This change in angular momentum is accounted for by the momentum of the emitted or absorbed photon (spin 1 particle). Therefore the harmonic oscillator part of the wave function has to conserve the angular momentum $\Delta l = 0$ (vertical transitions in Fig. 2.2). Additionally only transitions between the same shell are optically active $s = s'$. Worth to note, that symmetry breaking in the QD structure can lift the strictness of the selection rule for optical transitions [20].

2.1.3 Exciton fine-structure splitting

For the derivation of the energetic eigenstates in a QD the spin has so far only be considered in terms of the Pauli principle where two carriers with opposite spin can occupy one electronic level. The following discussion of the fine-structure is restricted to the exchange interaction coupling the spins of the electrons and holes. Worth to note that there are other possible contributions such as Zeeman interaction in an external magnetic field or the Overhauser shift due to spin coupling with the lattice nuclei [22].

The general form of the spin Hamiltonian for the electron-hole exchange interaction of an exciton formed by a hole with spin J_h and by an electron with spin S_e is given by [20]

$$H_{exchange} = - \sum_{i=x,y,z} (a_i J_{h,i} \cdot S_{e,i} + b_i J_{h,i}^3 \cdot S_{e,i}) \quad . \quad (2.5)$$

In contrast to trion and biexciton configurations where electron and/or hole spins are paired antisymmetrically and thus leading to a vanishing exchange interaction, $H_{exchange} \neq 0$ for the exciton. The single particle states that need to be considered are the heavy hole $J_h = 3/2$, $J_{h,z} = \pm 3/2$ and electron $S_e = 1/2$, $S_{e,z} = \pm 1/2$ states. From these four

different states are formed characterized by their angular momentum projections $M = S_{e,z} + J_{e,z}$, which are degenerate without the exchange interaction. The $|M| = 2$ state cannot couple to the light field and is therefore referred to as dark state. This is due to the fact that the angular momentum needs is not conserved for a possible process of optical exciton decay leading to $|\Delta M| = 2$ and photon emission $|\Delta S| = 1 \neq 2$. For the same reason the $|M| = 1$ state is optically active (bright state). With the states $|+1\rangle, |-1\rangle, |+2\rangle, |-2\rangle$ as a basis the exchange Hamiltonian can be written as [23]

$$H_{exchange} = \frac{1}{2} \begin{pmatrix} +\delta_0 & +\delta_1 & 0 & 0 \\ +\delta_1 & +\delta_0 & 0 & 0 \\ 0 & 0 & -\delta_0 & +\delta_2 \\ 0 & 0 & +\delta_2 & -\delta_0 \end{pmatrix} \quad (2.6)$$

The exchange interaction splits the bright and dark exciton states by $\delta_0 = 1.5(a_z + 2.25b_z)$. The new eigenstates of the dark exciton are a superposition of $|\pm 2\rangle$, split by $\delta_2 = 0.75(b_x + b_y)$. Depending on the dot symmetry the bright states are either degenerate or for a broken rotational symmetry ($b_x \neq b_y$) split by $\delta_1 = 0.75(b_x - b_y)$ (for a visualization see Fig. 2.3).

For the radiative cascade from biexciton to the empty ground state $|XX\rangle \rightarrow |X\rangle \rightarrow |0\rangle$ two scenarios are possible, which are depicted in Fig. 2.4: (a) For a QD with rotational symmetry the exciton states $|\pm 1\rangle$ are degenerate and both decay paths become indistinguishable. This is especially interesting for the generation of polarization-entangled photon pairs [12]. In general QDs have been observed to be anisotropic, leading to an asymmetric potential, and therefore a non-vanishing fine-structure splitting. In this case the new eigenstates of the exciton are a linear combination of $|\pm 1\rangle$, $|X\rangle = 1/\sqrt{2}(|+1\rangle \pm |-1\rangle)$, therefore the transitions are linearly polarized.

The above summarized findings, e.g. the energy eigenstates of QDs, the Coulomb reduced electron-hole pair energy of an exciton and the exchange interaction can be categorized by distinct energies for GaAs based self-assembled QDs [20]:

Energy	Order of magnitude
Kinetic energy	$\sim (50 - 100)$ meV
Excitonic binding energy	$\sim (25 - 50)$ meV
Fine-structure effects	~ 1 meV

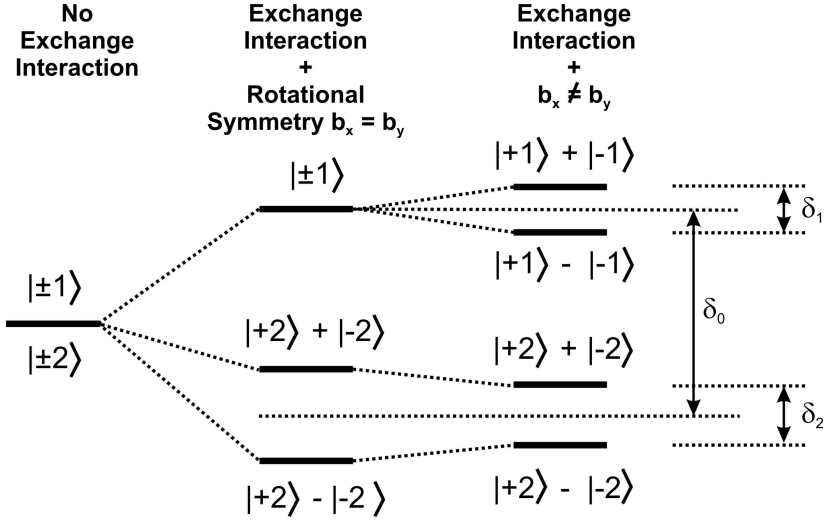


Figure 2.3: Energy levels of the exciton. In the case of no exchange interaction, the four possible states are degenerate, whereas the exchange interaction splits the exciton configuration into bright $|\pm 1\rangle$ and dark superposition states of $|\pm 2\rangle$. An introduction of asymmetry in the QD potential results in an additional splitting of the bright states, which are then a superposition of the initial states [24].

2.2 Representation of different light states and photon correlation

One fundamental experimental tool employed for the investigations presented in this thesis is auto- and cross-correlations. In this section the quantization of the electromagnetic field, the quantum mechanical description of the harmonic oscillator and the three different types of photon fields are introduced, which are essential for the understanding of the phonon correlations. The characteristic features of the second-order correlation function of thermal and coherent light as well as the Fock states are then presented at the end of the section.

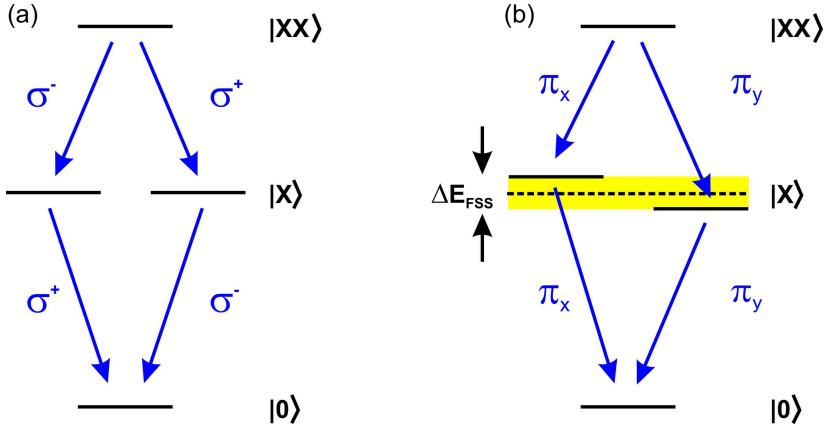


Figure 2.4: (a) Biexciton-exciton decay channels for the ideal case of zero fine-structure splitting $\Delta E_{FSS} = 0$ and (b) $\Delta E_{FSS} \neq 0$. For the two different cases, the emitted photons are either circularly or linearly polarized.

2.2.1 Quantization of the electromagnetic field

The classical theory of electromagnetic radiation is based on the *Maxwell equations*. For the conversion from a classical to a quantum mechanical description the field vectors must be employed as operators instead of algebraic quantities. To make an appropriate transition for the quantization of the electromagnetic field, the equations of the classical theory are first put into a suggestive form. The central step will then be the replacement of the classical harmonic oscillator by the corresponding quantum mechanical formulation [25].

The *Maxwell equations* can alternatively be expressed in terms of scalar and vector potentials Φ and \mathbf{A} . Under Coulomb gauge ($\nabla \cdot \mathbf{A} = 0$) and the consideration of electromagnetic waves in free space, i.e. charge and current-free ($\rho = 0$, $\mathbf{J} = 0$), the condition for the vector potential reads

$$\nabla^2 \mathbf{A} - \frac{1}{c^2} \frac{\partial^2 \mathbf{A}}{\partial t^2} = 0 \quad . \quad (2.7)$$

This wave equation under consideration of periodic boundary conditions is satisfied by the following approach for the vector potential \mathbf{A} ,

$$\mathbf{A}(\mathbf{r}, t) = \sum_{\mathbf{k}} \left(\mathbf{A}_{\mathbf{k}} \exp(-i\omega_{\mathbf{k}}t + i\mathbf{k}\mathbf{r}) + \mathbf{A}_{\mathbf{k}} \exp(i\omega_{\mathbf{k}}t - i\mathbf{k}\mathbf{r}) \right) \quad (2.8)$$

It then follows logically to calculate the radiative energy as [25]

$$E = \sum_{\mathbf{k}} \epsilon_0 V \omega_{\mathbf{k}}^2 (A_{\mathbf{k}} A_{\mathbf{k}}^* + A_{\mathbf{k}}^* A_{\mathbf{k}}) \quad (2.9)$$

From this classical expression the transition to the field quantization is carried out via comparison with the quantum mechanical harmonic oscillator, which is introduced in the following.

The quantum mechanical harmonic oscillator

For one dimension the Hamiltonian reads

$$H = \frac{\hat{p}^2}{2m} + \frac{1}{2} m \omega^2 \hat{q}^2 \quad (2.10)$$

where the position and momentum operator \hat{q} and \hat{p} comply with the commutation relation

$$[\hat{q}, \hat{p}] = i\hbar \quad (2.11)$$

It is convenient to replace \hat{q} and \hat{p} by the so-called destruction and creation operators

$$\hat{a} = (2m\hbar\omega)^{-1/2} (m\omega\hat{q} + i\hat{p}) \quad (2.12)$$

$$\hat{a}^+ = (2m\hbar\omega)^{-1/2} (m\omega\hat{q} - i\hat{p}) \quad (2.13)$$

Under consideration of the commutation relation $[\hat{a}, \hat{a}^+] = 1$, the Hamiltonian and its effect on the energy eigenstate $|n\rangle$ with eigenvalue E_n can be re-written as

$$H|n\rangle = \frac{1}{2} \hbar\omega (\hat{a}\hat{a}^+ + \hat{a}^+\hat{a})|n\rangle = \hbar\omega \left(\hat{a}^+\hat{a} + \frac{1}{2} \right) |n\rangle = E_n |n\rangle \quad (2.14)$$

and the effect of \hat{a} and \hat{a}^+ on $|n\rangle$ as annihilation and creation operator

$$\hat{a}|n\rangle = \sqrt{n}|n-1\rangle \quad (2.15)$$

$$\hat{a}^+|n\rangle = \sqrt{n+1}|n+1\rangle \quad (2.16)$$

can be verified.

The electromagnetic field can then be quantized by the association of a quantum mechanical harmonic oscillator with each field mode. A comparison between the classical radiative field energy of Eq. 2.9 and the energy of the quantum mechanical oscillator of Eq. 2.14 suggests the conversion from vector potential amplitudes to quantum mechanical mode operators

$$\mathbf{A}_{\mathbf{k}} \rightarrow \sqrt{\frac{\hbar}{2\epsilon_0 V \omega_{\mathbf{k}}}} \hat{a}_{\mathbf{k}} \quad (2.17)$$

$$\mathbf{A}_{\mathbf{k}}^* \rightarrow \sqrt{\frac{\hbar}{2\epsilon_0 V \omega_{\mathbf{k}}}} \hat{a}_{\mathbf{k}}^+ \quad (2.18)$$

The vector potential converts into a sum of positive and negative frequency parts. Knowing $\hat{\mathbf{A}}$, the electric and magnetic field operators can be calculated according to $\hat{\mathbf{E}} = -\partial\hat{\mathbf{A}}/\partial t - \nabla\phi$. Thus, also $\hat{\mathbf{E}}$ separates into a positive and negative frequency part

$$\hat{\mathbf{E}}(\mathbf{r}, t) = \hat{\mathbf{E}}^+(\mathbf{r}, t) + \hat{\mathbf{E}}^-(\mathbf{r}, t) \quad , \quad (2.19)$$

with

$$\hat{E}^{(+)}(\mathbf{r}, t) \propto \hat{a} \exp\left(-i(\mathbf{k} \cdot \mathbf{r} - \omega t)\right) \quad (2.20)$$

$$\hat{E}^{(-)}(\mathbf{r}, t) \propto \hat{a}^+ \exp\left(i(\mathbf{k} \cdot \mathbf{r} - \omega t)\right) \quad . \quad (2.21)$$

The quantum mechanical expression of the electric field will be important for the representation of the second-order correlation function in chapter 2.2.5.

2.2.2 Thermal Light

Here we consider the equilibrium situation between emission and absorption of a radiation field with an emitter ensemble representing the

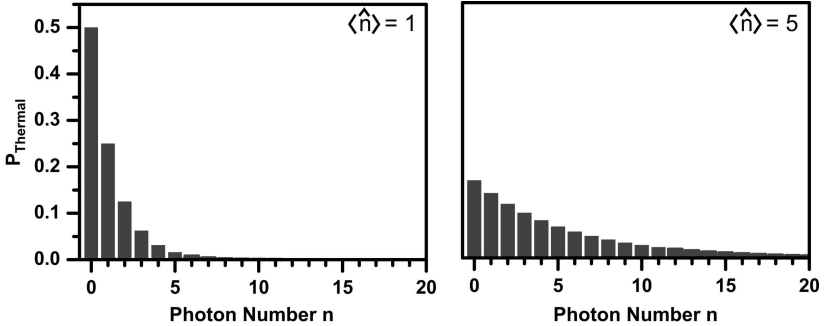


Figure 2.5: Photon probability distribution for a thermal light field with average photon number $\langle \hat{n} \rangle = 1$ (left) and $\langle \hat{n} \rangle = 5$ (right).

walls of a cavity at temperature T , known as the *black body emitter model*. Insight the cavity harmonic oscillator modes are formed. The probability of thermal excitation of n photons in a specific mode with energy $\hbar\omega$ is then given by

$$P(n) = \frac{\exp(-E_n/k_B T)}{\sum_n \exp(-E_n/k_B T)} \quad , \quad (2.22)$$

with $E_n = \hbar\omega(n + 1/2)$. Therefore the mean photon number excited in the field mode at temperature T is calculated to be [24, 25]

$$\langle \hat{n} \rangle = \sum_n n P(n) = \frac{1}{\exp(\hbar\omega/k_B T) - 1} \quad , \quad (2.23)$$

which represents the *Bose-Einstein statistics* of the mean thermal photon in a single mode. The probability of finding n photons in the field can be expressed as by use of $\langle \hat{n} \rangle$ as

$$P_{\text{Thermal}} = \frac{\langle \hat{n} \rangle^n}{(\langle \hat{n} \rangle + 1)^{n+1}} \quad . \quad (2.24)$$

Figure 2.5 shows the photon distribution of Eq. 2.24 for two different average photon numbers. As can be seen an empty mode (zero photons) has the highest probability, for higher photon numbers this probability decreases monotonically. A typical thermal light source reveals $\langle \hat{n} \rangle \gg 1$, thus the photons are most probable to form clusters of varying photon

number. This phenomenon is called photon bunching. The fluctuations of a thermal light source are found to exceed the average number of photons in the field

$$(\Delta n)^2 = \langle \hat{n}^2 \rangle - \langle \hat{n} \rangle^2 = \langle \hat{n} \rangle + \langle \hat{n} \rangle^2 \quad . \quad (2.25)$$

Due to these large fluctuations in the photon number, a thermal light source is often termed chaotic source.

2.2.3 Fock States

In contrast to thermal or coherent light states there is no classical analog to Fock states $|n\rangle$ [25], they can only be described quantum mechanically. Due to the fact that Fock states are eigenstates of the photon number operator $\hat{n} = \hat{a}^\dagger \hat{a}$

$$\hat{n}|n\rangle = \hat{a}^\dagger \hat{a}|n\rangle = n|n\rangle \quad , \quad (2.26)$$

their expectation value for the photon number equals the eigenvalue for the state itself

$$\langle \hat{n} \rangle = \langle n | \hat{a}^\dagger \hat{a} | n \rangle = n \quad . \quad (2.27)$$

Due to the definition of the Fock states the photon number uncertainty vanishes completely

$$(\Delta \hat{n})^2 = \langle \hat{n}^2 \rangle - \langle \hat{n} \rangle^2 = 0 \quad . \quad (2.28)$$

As a consequence of *Heisenberg's uncertainty law* between photon number and phase, the fully specified photon number of Fock states leads to a completely undefined phase ($\Delta\phi \rightarrow \infty$).

From a statistical point of view, such a photon field exhibits sub-Poissonian statistics, the probability of detecting i photons in the Fock state $|n\rangle$ is found to be

$$P_{Fock} = \begin{cases} 0, & \text{if } i \neq n \\ 1, & \text{if } i = n \end{cases} \quad . \quad (2.29)$$

For an average photon number of $\langle \hat{n} \rangle = 1$ and 5 this characteristic photon distribution of Eq. 2.29 is illustrated in Fig. 2.6.

Concerning the investigations in this thesis especially the Fock state $|1\rangle$ is of significance because it represents the corresponding light state created by an ideal single-photon emitter, e.g. a quantum dot.

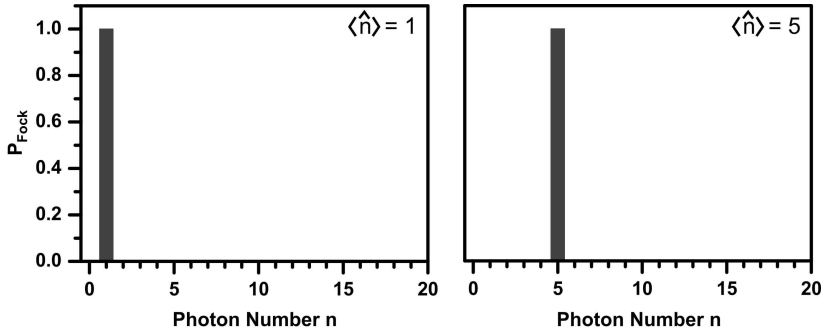


Figure 2.6: Photon probability distribution for Fock states with average photon number $\langle \hat{n} \rangle = 1$ (left) and $\langle \hat{n} \rangle = 5$ (right).

2.2.4 Coherent States

Coherent states are characterized by a minimum uncertainty product, the electric field variations of coherent states approach that of a classical wave with stable amplitude and fixed phase for strong excitation conditions; therefore they closely resemble the emission of a single-mode laser operated well above threshold [25].

The coherent states $|\alpha\rangle$, also denoted as Glauber states can be expressed as a linear superposition of photon number states $|n\rangle$

$$|\alpha\rangle = e^{-\frac{1}{2}|\alpha|^2} \sum_n \frac{\alpha^n}{\sqrt{n!}} |n\rangle \quad . \quad (2.30)$$

These states are right eigenstates of the destruction operator $\hat{a}|\alpha\rangle = \alpha|\alpha\rangle$. Knowing the expectation values

$$\langle \hat{n} \rangle = |\alpha|^2 \quad \text{and} \quad (2.31)$$

$$\langle \hat{n}^2 \rangle = |\alpha|^4 + |\alpha|^2 \quad , \quad (2.32)$$

the photon-number variance for coherent states is

$$(\Delta n)^2 = \langle \hat{n}^2 \rangle - \langle \hat{n} \rangle^2 = |\alpha|^2 = \langle \hat{n} \rangle \quad . \quad (2.33)$$

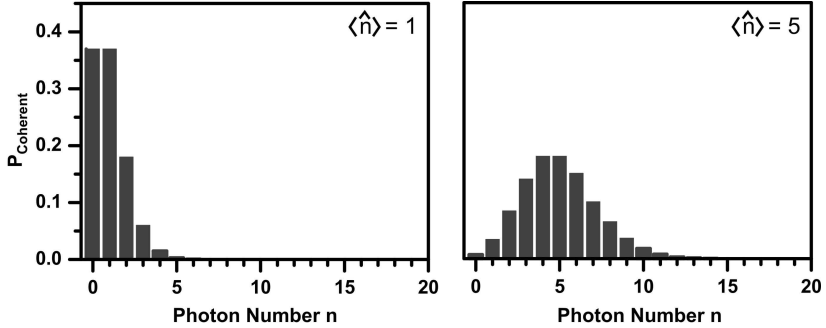


Figure 2.7: Photon probability distribution for a coherent light field with average photon number $\langle \hat{n} \rangle = 1$ (left) and $\langle \hat{n} \rangle = 5$ (right).

The fractional uncertainty in the number of photons

$$\frac{\Delta n}{\langle \hat{n} \rangle} = \frac{1}{|\alpha|} = \frac{1}{\sqrt{\langle \hat{n} \rangle}} \quad (2.34)$$

decreases with increasing value of the coherent state amplitude $|\alpha|$ and the fluctuations are found to approach zero with growing photon number.

The probability of finding n photons in the coherent light field is obtained by use of Eq. 2.30 and found to be

$$P_{\text{Coherent}} = |\langle n | \alpha \rangle|^2 = e^{-|\alpha|^2} \frac{|\alpha|^{2n}}{n!} = e^{-\langle \hat{n} \rangle} \frac{\langle \hat{n} \rangle^n}{n!} . \quad (2.35)$$

For an average photon number of $\langle \hat{n} \rangle = 1$ and 5 this characteristic Poissonian distribution of Eq. 2.35 is illustrated in Fig. 2.7.

2.2.5 Photon correlation

In order to distinguish between photon fields with different statistical properties it is instructive to measure the intensity correlation with a *Hanbury Brown* and *Twiss*-type setup (presented in chapter 3.2). The classical description of the normalized intensity auto-correlation can be expressed as

$$g^{(2)}(\tau) = \frac{\langle \bar{I}(t)\bar{I}(t+\tau) \rangle}{\langle \bar{I}(t) \rangle^2} = \frac{\langle E^*(t)E^*(t+\tau)E(t+\tau)E(t) \rangle}{\langle E^*(t)E(t) \rangle^2} \quad , \quad (2.36)$$

with the cycle-averaged intensity \bar{I} of the mode. It reveals insight into correlation effects of subsequent mode intensity measurements at times t and $t + \tau$. This intensity correlation is also called second-order correlation function, due to the fact that the intensity is proportional to the square of the electric field, thus the correlation is of second order in $E(t)$.

As a next step a more general quantum mechanical expression of the second-order correlation function is derived. This is essential for the derivation of second-order correlation of Fock states, which cannot be described classically. In the framework of second quantization the electric field of a single-mode plane-wave is given by a positive and negative frequency part of the field operator (see Eqs. 2.19, 2.20, 2.21).

With this representation the quantum mechanical expression of the normalized second-order correlation function becomes

$$g^{(2)}(\tau) = \frac{\langle \hat{E}^{(-)}(t)\hat{E}^{(-)}(t+\tau)\hat{E}^{(+)}(t+\tau)\hat{E}^{(+)}(t) \rangle}{\langle \hat{E}^{(-)}(t)\hat{E}^{(+)}(t) \rangle^2} \quad . \quad (2.37)$$

It is worth noting that for fields with time-independent photon statistics, the correlation function is only dependent on the time difference τ between two subsequently photon detection events. For sufficient long time delays $\tau \rightarrow \infty$ the photons become statistically independent, therefore revealing $g^{(2)}(\tau \rightarrow \infty) \rightarrow 1$. For the data analysis this long time delay correlation value can be employed as a reference for the *Poissonian* normalization of the statistics measurement. In contrast, the crucial value to differentiate between different light states is the simultaneous photon correlation $g^{(2)}(\tau = 0)$. For a single mode at $\tau = 0$ the second-order auto-correlation can be expressed as

$$g^{(2)}(\tau = 0) = \frac{\langle \hat{a}^+\hat{a}^+\hat{a}\hat{a} \rangle}{\langle \hat{a}^+\hat{a} \rangle^2} \quad (2.38)$$

$$= 1 + \frac{(\Delta n)^2 - \langle \hat{n} \rangle}{\langle \hat{n} \rangle^2} \quad . \quad (2.39)$$

In the following, the difference in the second-order auto-correlation with respect to the different light states is to be discussed. Figure 2.8 shows

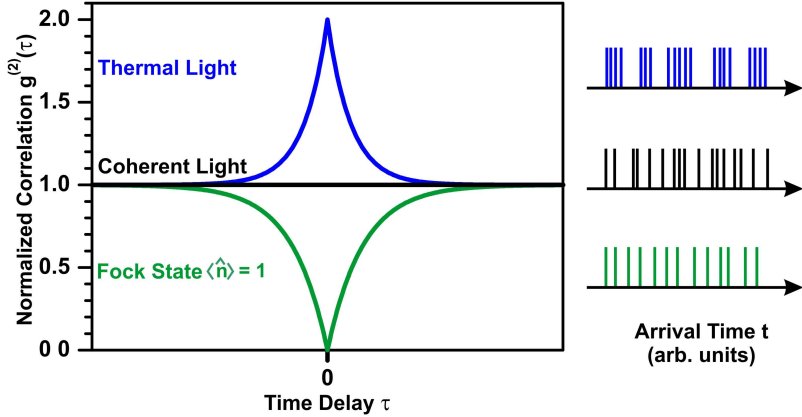


Figure 2.8: Left: Normalized correlation function $g^{(2)}(\tau)$ for thermal and coherent light as well as the single-photon Fock state. Right: Illustration of temporal photon correlation for the three different states. For thermal light the photons tend to arrive in bunches, whereas coherent light reveals temporally uncorrelated photons. The characteristic antibunching of the single-photon Fock state is reflected in a distinct arrival time difference between subsequent single photons.

the normalized second-order correlation function versus time delay τ of thermal and coherent light as well as the single-photon Fock state. As mentioned above all light states reveal $g^{(2)}(\tau \rightarrow \infty) \rightarrow 1$.

Thermal light:

According to Eq. 2.25 the fluctuation for a thermal light field is given by $(\Delta n)^2 = \langle \hat{n} \rangle + \langle \hat{n} \rangle^2$. Therefore the normalized second-order correlation function for zero photon delay is $g^{(2)}(\tau = 0) = 2$. This enhanced correlation-value compared to the normalized Poissonian level $g^{(2)}(\tau \rightarrow \infty) \rightarrow 1$ reflects the increased probability of simultaneous photon detection and the characteristic of photons to arrive in bunches for a thermal light source.

Coherent light (Glauber states):

The fluctuations of coherent light are equal to the mean photon number

in the field $(\Delta n)^2 = \langle \hat{n} \rangle$ (Eq. 2.33), therefore $g^{(2)}(\tau) = 1$ for $\tau = 0$ and all delays $\tau \neq 0$. Hence the time-delay between subsequent photon detections for the coherent light field is completely random and the normalized second-order correlation function is a flat line. This characteristic signature implies Poissonian statistics of the photon field.

Fock states:

Fock states have a defined number of photons therefore the fluctuation vanishes ($(\Delta n)^2 = 0$) and Eq. 2.39 reads

$$g_{Fock}^{(2)}(\tau = 0) = 1 - \frac{1}{n} \quad \text{for } n \geq 1 \quad . \quad (2.40)$$

The normalized second-order correlation function can attain values of $0 \leq g^{(2)}(\tau) < 1$. For the single-photon Fock state $|1\rangle$ the auto-correlation reveals $g^{(2)}(\tau = 0) = 0$. The completely vanishing correlation indicates that the probability of simultaneous detection of two photons is zero. This distinct time-delay between subsequent photon detection events leading to a suppressed simultaneous second-order auto-correlation value is referred to as antibunching. The second-order correlation measurements provide a valuable tool to identify single-photon emission, e.g. from a quantum dot. For the two-photon Fock state $g^{(2)}(\tau = 0) = 0.5$, this value represents the upper bound for the proof of a true single-photon emitter via second-order auto-correlation.

2.3 Two-level system photon interaction

2.3.1 Basic quantum mechanical concepts

In the following, a two-level system (TLS) with the ground state denoted as $|g\rangle$ and the excited state $|e\rangle$ is considered. The time-dependent normalized wave function can be expressed as a superposition of ground and excited state

$$|\Psi(t)\rangle = c_g(t)|g\rangle + c_e(t)|e\rangle \quad \text{with } |c_g(t)|^2 + |c_e(t)|^2 = 1 \quad . \quad (2.41)$$

For the theoretical concepts introduced in the following chapters it is instructive to establish the density matrix formalism. All quantum mechanical information that characterizes $|\Psi(t)\rangle$ can also be extracted from the density operator defined as:

$$\hat{\rho}(t) = |\Psi(t)\rangle\langle\Psi(t)| \quad . \quad (2.42)$$

For the TLS the density operator becomes:

$$\hat{\rho}(t) = \rho_{gg}(t)|g\rangle\langle g| + \rho_{ge}(t)|g\rangle\langle e| + \rho_{eg}(t)|e\rangle\langle g| + \rho_{ee}(t)|e\rangle\langle e| \quad , \quad (2.43)$$

with the matrix elements defined as

$$\begin{aligned} \rho_{gg}(t) &= c_g(t) \cdot c_g(t)^* & \rho_{ee}(t) &= c_e(t) \cdot c_e(t)^* \\ \rho_{eg}(t) &= c_e(t) \cdot c_g(t)^* & \rho_{ge}(t) &= c_g(t) \cdot c_e(t)^* \quad . \end{aligned}$$

The diagonal matrix elements represent the *population*, whereas the off-diagonal elements are the *coherence* of the system.

The system dynamics, i.e. the time-dependence of the density operator in the Schrödinger picture, is described by the following differential equation

$$\frac{d}{dt}\hat{\rho}(t) = \frac{1}{i\hbar} [\hat{H}(t), \hat{\rho}(t)] \quad . \quad (2.44)$$

2.3.2 Interaction Hamiltonian

If the Hamiltonian \hat{H}_A for an unperturbed TLS, with $\hbar\omega_0$ being the energetic separation between ground and excited state, is applied to the two eigenstates, they reveal $\hat{H}_A|g\rangle = 0$ and $\hat{H}_A|e\rangle = \hbar\omega_0|e\rangle$, respectively. In the next step the interaction of the TLS with a monochromatic laser field is considered. Assuming only dipole interaction between the dipole moment of the TLS $\hat{\mathbf{d}}$ and the electric laser field $\hat{\mathbf{E}}$ the Hamiltonian can be written as [26]:

$$\hat{H} = \hat{H}_A - \hat{\mathbf{d}} \cdot \hat{\mathbf{E}} \quad . \quad (2.45)$$

Before expanding the Hamiltonian in the basis $|g\rangle$ and $|e\rangle$, the lowering (raising) operators of the TLS are introduced as $\hat{\sigma} = |g\rangle\langle e|$ ($\hat{\sigma}^+ = |e\rangle\langle g|$), which yield the following relations:

$$\langle\hat{\sigma}\rangle = \rho_{eg} \quad , \quad \langle\hat{\sigma}^+\rangle = \rho_{ge} \quad , \quad \langle\hat{\sigma}^+\hat{\sigma}\rangle = \rho_{ee} \quad (2.46)$$

Since the dipole operator has odd parity ($\hat{\mathbf{d}} = -e\hat{\mathbf{r}}$) the interaction part of the Hamiltonian only has contributions from off-diagonal elements. The operator can therefore be expressed as

$$\hat{\mathbf{d}} = \mathbf{d}_{eg}(\hat{\sigma} + \hat{\sigma}^+) \quad \text{with} \quad \mathbf{d}_{eg} = \langle g | \hat{d} | e \rangle \quad . \quad (2.47)$$

By use of Eq. 2.47 and under consideration of the formulation of the electric field

$$\hat{\mathbf{E}} = \frac{\hat{\mathbf{E}}_0}{2}(e^{i\omega_L t} + e^{-i\omega_L t}) \quad , \quad (2.48)$$

the Hamiltonian reads

$$\hat{H} = \hbar\omega_0\hat{\sigma}^+\hat{\sigma} - \frac{\hbar\Omega}{2}(\hat{\sigma}e^{i\omega_L t} + \hat{\sigma}^+e^{-i\omega_L t} + \hat{\sigma}e^{-i\omega_L t} + \hat{\sigma}^+e^{i\omega_L t}) \quad (2.49)$$

with the Rabi frequency

$$\Omega = (1/\hbar)(\mathbf{d}_{eg} \cdot \mathbf{E}) \quad , \quad (2.50)$$

which quantifies the interaction strength between the electric field and the dipole.

The Hamiltonian can be simplified by transformation into a coordinate system rotating with the laser frequency ω_L . Via the substitution $\tilde{\sigma} = e^{-i\omega_L t}\hat{\sigma}$

$$\tilde{H} = \hbar\Delta\tilde{\sigma}^+\tilde{\sigma} - \frac{\hbar\Omega}{2}(\tilde{\sigma} + \tilde{\sigma}^+ + \tilde{\sigma}e^{-i2\omega_L t} + \tilde{\sigma}^+e^{i2\omega_L t}) \quad . \quad (2.51)$$

In the rotating frame the energy of the laser is the constant reference energy, therefore the detuning between the laser and the TLS resonance energy is introduced as $\Delta \equiv \omega_L - \omega_0$. The last two summands of the Hamiltonian oscillate with twice the laser frequency. The negligence of these varying terms is called rotating wave approximation (RWA) [27, 28]. The validity of this approximation is justified by the fact that for optical frequencies this oscillation is much faster in the order of femtoseconds than the response time of the detectors. The resulting time-independent Hamiltonian reads:

$$\tilde{H}_{RWA} = \hbar\Delta\tilde{\sigma}^+\tilde{\sigma} - \frac{\hbar\Omega}{2}(\tilde{\sigma} + \tilde{\sigma}^+) \quad . \quad (2.52)$$

2.3.3 Optical Bloch equations

For a damped TLS it can be shown that the interactions with a reservoir can be included by the Lindblad formalism [29,30]. The time evolution of the density matrix has the following form:

$$\frac{d}{dt}\hat{\rho}(t) = \frac{1}{i\hbar}[\hat{H}(t), \hat{\rho}(t)] + \mathcal{L}(\hat{\rho}) \quad \text{with} \quad (2.53)$$

$$\mathcal{L}(\hat{\rho}) = \sum_k (\hat{L}_k \hat{\rho} \hat{L}_k^\dagger - 1/2 \hat{L}_k^\dagger \hat{L}_k \hat{\rho} - 1/2 \hat{\rho} \hat{L}_k^\dagger \hat{L}_k) \quad (2.54)$$

with $\hat{L} = \sqrt{\Gamma_{ij}}|i\rangle\langle j|$ describing the dissipation from state $|i\rangle$ to $|j\rangle$ with the rate Γ_{ij} .

For the TLS two mechanisms of dissipation are possible. It can radiatively decay via spontaneous emission from state $|e\rangle$ to $|g\rangle$, the corresponding rate is $\Gamma_{eg} = \Gamma_1$. Pure dephasing of the system does not change the population, here the corresponding rate is $\Gamma_{ee} = \Gamma_{pure}$. When including these two dissipation processes in Eq. 2.53, the equations of motion in the rotating laser frame and RWA become [31]:

$$\dot{\rho}_{ge} = -\frac{i\Omega}{2}(\rho_{ee} - \rho_{gg}) - (i\Delta + \frac{1}{2}\Gamma_1 + \Gamma_{pure})\rho_{ge} \quad , \quad (2.55)$$

$$\dot{\rho}_{gg} = \frac{i\Omega}{2}(\rho_{ge} - \rho_{eg}) + \Gamma_1\rho_{ee} \quad , \quad (2.56)$$

$$\dot{\rho}_{ee} = -\frac{i\Omega}{2}(\rho_{ge} - \rho_{eg}) - \Gamma_1\rho_{ee} \quad . \quad (2.57)$$

These equations are called **optical Bloch equations**. The damping of the population is given by the radiative decay rate $\Gamma_1 = 1/T_1$. The time evolution of the coherence is damped by $\Gamma_1/2 + \Gamma_{pure}$, defined as

$$\Gamma_2 = \frac{1}{T_2} = \frac{1}{2}\Gamma_1 + \Gamma_{pure} = \frac{1}{2T_1} + \frac{1}{T_{pure}} \quad . \quad (2.58)$$

T_2 is the total dephasing time of the system and T_{pure} describes the characteristic pure dephasing that leaves the population of the TLS unchanged, but disturbs its phase. For the case of negligible pure dephasing, the system is *Fourier transform-limited* and the maximally achievable coherence time of $T_2 = 2T_1$ is reached. Pure dephasing in semiconductor quantum dots can be caused by interaction with lattice phonons, charge carrier scattering is also a possible mechanism.

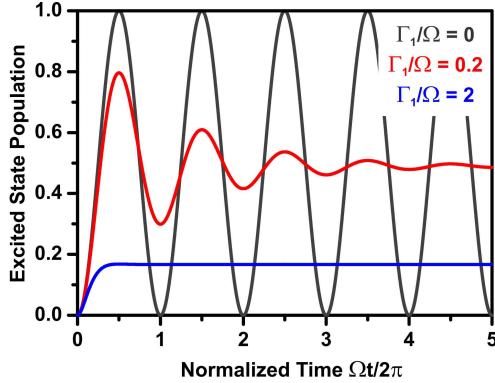


Figure 2.9: Excited state population of the TLS as a function of time normalized with respect to the Rabi oscillation period. No damping $\Gamma_1/\Omega = 0$ results in undamped Rabi oscillations of the system. At increasing relative decay Γ_1/Ω first the oscillations are damped and for higher values the system reaches its steady-state excited state population without oscillating. Pure dephasing has been neglected in the discussion $\Gamma_{pure} = 0$. Plot according to Ref. [33].

A detailed discussion about possible dephasing mechanisms in QDs is presented in chapter 6.

2.3.4 Resonance fluorescence

The optical Bloch equations are a set of coupled differential equations that can be solved under the consideration of boundary conditions. The solution for the density matrix elements reveals insight into the population ρ_{ee}, ρ_{gg} and the coherence ρ_{eg}, ρ_{ge} of the driven TLS. In the following, the various aspects of the resonance fluorescence signal under continuous wave resonant emitter state preparation will be discussed. A detailed mathematical derivation of the presented results can be found in [25, 28, 31–34].

Figure 2.9 illustrates the excited state population ρ_{ee} of the TLS versus time for different damping conditions. For $\Gamma_1/\Omega = 0$ the ρ_{ee} oscillates undamped. Nevertheless this case cannot be observed in the experiment, due to vacuum fluctuations leading to a finite lifetime of the

excited state of the TLS, hence $\Gamma_1 \neq 0$ and therefore the oscillations are damped. Depending on the ratio Γ_1/Ω , the population undergoes several damped oscillations (red trace) or asymptotically reaches its steady-state value without oscillating (blue trace). From the dependence on Γ_1/Ω of the excited state population, it is obvious that one can distinguish two different regimes of resonant emitter state preparation. In the regime below saturation (low excitation power) the internal dynamics of the system are faster than the driving Rabi frequency $\Omega^2 \ll (T_1 T_2)^{-1}$, therefore the TLS does not undergo Rabi oscillations. In the regime above saturation (high excitation power) $\Omega^2 \gg (T_1 T_2)^{-1}$, the driving Rabi frequency is faster than the internal dynamics. Here the system can coherently exchange energy with the external field resulting in several damped Rabi oscillations before reaching its steady-state value. These distinct differences in ρ_{ee} above and below saturation lead to completely different features of a resonantly driven TLS in terms of first- and second-order correlation and the resulting spectral properties as will be discussed in the following.

As visible in Fig. 2.9, the system reaches a certain steady-state population for $t \rightarrow \infty$, this value can be expressed as [33]

$$\rho_{ee}(t \rightarrow \infty) = \rho_{ee}^{ss} = \frac{1}{2} \frac{\Omega^2 T_1 / T_2}{(\Delta^2 + T_2^{-2} + \Omega^2 T_1 / T_2)} \quad , \quad (2.59)$$

From the steady-state population valuable information about the system can be obtained, since ρ_{ee}^{ss} equals the averaged fluorescence intensity, which is found to increase with Ω^2 for low excitation conditions. The population saturates at $1/2$ under strong excitation $\Omega^2 \gg (T_1 T_2)^{-1}$ of the TLS. In addition, the effect of power-broadening becomes evident when considering the FWHM of the emission

$$FWHM = \frac{2}{T_2} \sqrt{1 + T_1 T_2 \Omega^2} \quad . \quad (2.60)$$

Only for low excitation $\Omega^2 \ll (T_1 T_2)^{-1}$ it is possible to derive the coherence of the emitter from the linewidth, which yields $FWHM = 2/T_2$. Obviously the broadening of the emission line with increasing excitation power is an intrinsic feature of any TLS, not accompanied by a reduction in the coherence time T_2 of the system.

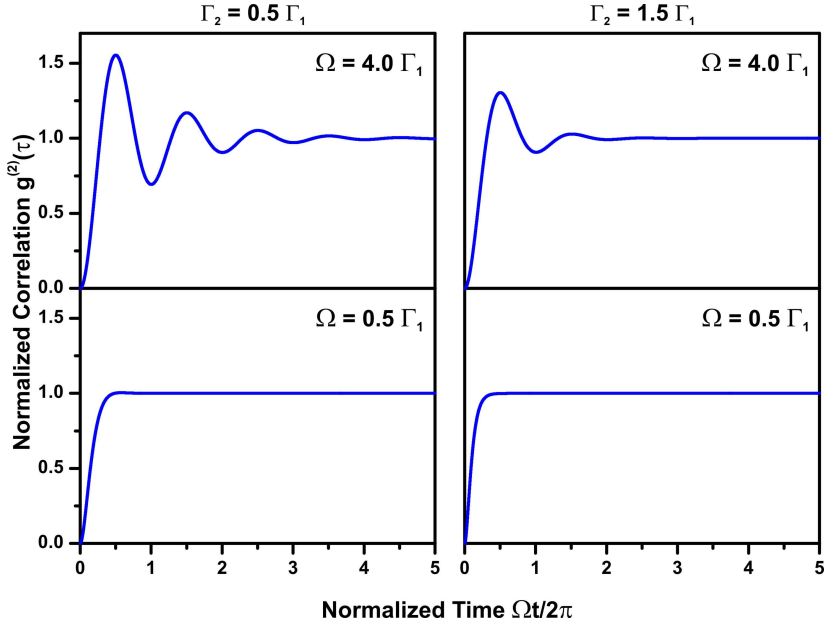


Figure 2.10: Normalized second-order photon correlation function versus normalized time, plotted for different excitation conditions of $\Omega = 0.5\Gamma_1$ below and $\Omega = 4\Gamma_1$ above saturation. The left panel depicts the case for a Fourier-transform limited system, whereas the right panel shows the situation of a system with significant contribution of additional dephasing $\Gamma_{\text{pure}} = \Gamma_1$.

Second-order correlation

The oscillation of the excited state population has distinct influence on the second-order correlation. In order to calculate $g^{(2)}(\tau)$ for the resonantly-driven TLS, the quantum mechanical description of a dipolar emitter is introduced [34]:

$$\hat{\mathbf{E}}^{(+)}(\mathbf{r}, t) = \frac{\omega_0^2}{4\pi\epsilon_0 c^2} \frac{d_{ge}}{|\mathbf{r}|} \hat{\sigma} \quad . \quad (2.61)$$

Inserting this expression for the electric field into Eq. 2.37 leads to the following form of the normalized second-order correlation function [28]:

$$g^{(2)}(\tau) = \frac{\langle \hat{\sigma}^+(t)\hat{\sigma}^+(t+\tau)\hat{\sigma}(t+\tau)\hat{\sigma}(t) \rangle}{\langle \hat{\sigma}^+(t)\hat{\sigma}(t) \rangle^2} . \quad (2.62)$$

The antibunching behavior $g^{(2)}(0) = 0$ of the resonantly-excited TLS becomes obvious, since $\hat{\sigma}^2|\Psi\rangle = 0$. The full solution for all τ can be obtained by employment of the quantum-regression theorem, which leads to [33]:

$$g^{(2)}(\tau) = 1 - e^{-\frac{\Gamma_1+\Gamma_2}{2}\cdot\tau} \cdot \left(\cos(B\tau) + \frac{\Gamma_1 + \Gamma_2}{2B} \sin(B\tau) \right) , \quad (2.63)$$

with the damped Rabi frequency given as

$$B = \sqrt{\Omega^2 - (\Gamma_1 - \Gamma_2)^2/4} . \quad (2.64)$$

Figure 2.10 depicts $g^{(2)}(\tau)$ above $\Omega = 4\Gamma_1$ and below $\Omega = 0.5\Gamma_1$ saturation of the TLS for the *Fourier-transform limited* case of $\Gamma_2 = 0.5\Gamma_1$ (left panel) and with significant contribution of pure dephasing $\Gamma_2 = 1.5\Gamma_1$ (right panel). The oscillations of the excited-state population above saturation are manifested in oscillations of the $g^{(2)}(\tau)$. It should be mentioned that for the experimental conditions in this thesis, which include Rabi frequencies exceeding $40 \mu\text{eV}$, the resulting oscillation period is shorter than ~ 100 ps. Therefore they cannot be resolved with the HBT-setup providing a instrumental response of ≥ 450 ps.

First-order correlation

The normalized first-order correlation function is defined as:

$$g^{(1)}(\tau) = \frac{\langle \hat{E}^{(-)}(t)\hat{E}^{(+)}(t+\tau) \rangle}{\langle \hat{E}^{(-)}(t)\hat{E}^{(+)}(t) \rangle} . \quad (2.65)$$

With Eq. 2.61 the function reads:

$$g^{(1)}(\tau) = \frac{\langle \hat{\sigma}^+(t)\hat{\sigma}(t+\tau) \rangle}{\langle \hat{\sigma}^+(t)\hat{\sigma}(t) \rangle} = g_{coh}^{(1)}(\tau) + g_{incoh}^{(1)}(\tau) . \quad (2.66)$$

$g^{(1)}(\tau)$ can be decomposed in a coherent τ -independent part and incoherent τ -dependent part. The incoherent part results from true excitation and decay of the TLS. Due to radiative decay even in the absence of further pure dephasing, the coherence cannot exceed the maximum

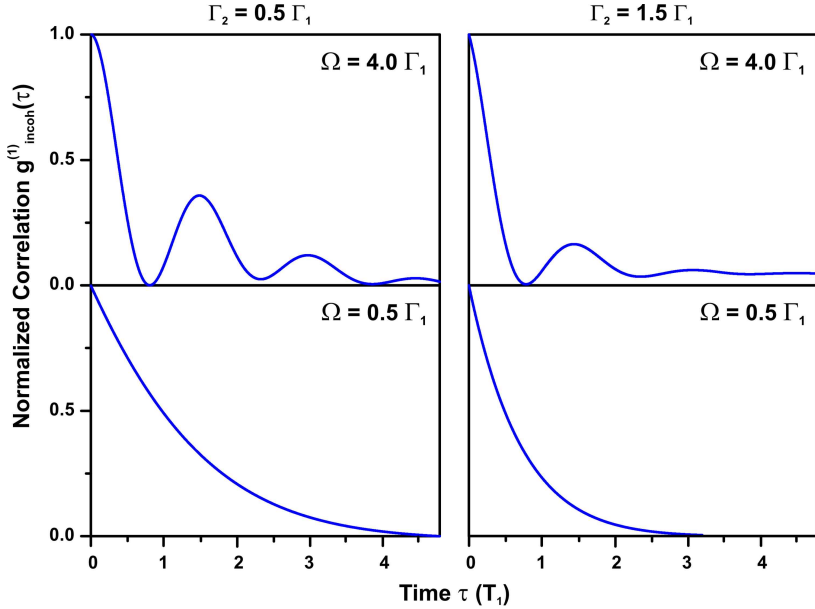


Figure 2.11: Normalized $g_{incoh}^{(1)}(\tau)$ for different excitation conditions of $\Omega = 0.5\Gamma_1$ below and $\Omega = 4\Gamma_1$ above saturation. The left panel depicts the case for a *Fourier-transform limited* system, whereas the right panel shows the situation of a system with significant contribution of additional dephasing. For the calculations a typical value for the radiative decay rate of $\Gamma_1 = 1.25$ GHz ($T_2 = 800$ ps) has been assumed.

value at the *Fourier-transform limit* where $T_2 = 2T_1$. In contrast, the τ -independent coherent part results from photon absorption and emission becoming one coherent scattering event, so that the coherence is found to be infinitely long.

The coherent part of the first-order correlation function is calculated to be

$$g_{coh}^{(1)}(\tau) = \frac{\Omega^2 \Gamma_1^2}{4(\Omega^2 + \Gamma_1 \Gamma_2)^2} \quad , \quad (2.67)$$

and therefore independent of the delay time τ , whereas the incoherent part is a function of τ and reads [33]:

$$g_{incoh}^{(1)}(\tau) = \frac{\Omega^2}{2(\Omega^2 + \Gamma_1\Gamma_2)} \left[\frac{1}{2} e^{-\Gamma_2\tau} + e^{-(1/2(\Gamma_1+\Gamma_2)\tau)} \left(\frac{1}{2} \frac{\Omega^2 + \Gamma_1\Gamma_2 - \Gamma_1^2}{\Omega^2 + \Gamma_1\Gamma_2} \cos(B\tau) - \frac{1}{4B} \frac{\Omega^2(\Gamma_2 - 3\Gamma_1) + \Gamma_1(\Gamma_2 - \Gamma_1)^2}{\Omega^2 + \Gamma_1\Gamma_2} \sin(B\tau) \right) \right] . \quad (2.68)$$

Figure 2.11 depicts $g_{incoh}^{(1)}(\tau)$ for different excitation conditions above and below saturation of the TLS, for the *Fourier-transform limited* case $\Omega = 0.5\Gamma_1$ (left panel) and with additional pure dephasing (right panel). Below saturation the first-order correlation function reveals an exponential decay, whereas above saturation Rabi oscillation can be observed in the time-domain, which is stronger damped in the presence of pure dephasing.

Spectral function

The emission spectrum of a TLS can be calculated from the first-order coherence function as a *Fourier transform* via the *Wiener-Khintchine theorem*

$$S(\omega) = \int_0^\infty g^{(1)}(\tau) \cdot e^{i(\omega_L - \omega_s) \cdot \tau} d\tau \quad , \quad (2.69)$$

The coherent part of $g^{(1)}(\tau)$ is a delta peak at the TLS resonance. The incoherent part calculated according to Eq. 2.69 is illustrated in Fig. 2.12. Below saturation of the TLS ($\Omega = 0.5\Gamma_1$), the spectrum reveals a single Lorentzian line. For strong excitation conditions $\Omega = 4\Gamma_1$, the single line develops into a triplet structure, the so-called Mollow triplet. The two Mollow sidebands are separated by the Rabi frequency from the central peak. This is also reflected in the oscillation period of the first-order correlation function in the time domain, which corresponds to the Rabi frequency of the system.

Within the limitation of very intense fields $\Omega \gg \Gamma_1, |\Delta|$ and negligible pure dephasing $\Gamma_{pure} = 0$ the resonance fluorescence spectrum reads (For a detailed derivation and more general expression see [35].)

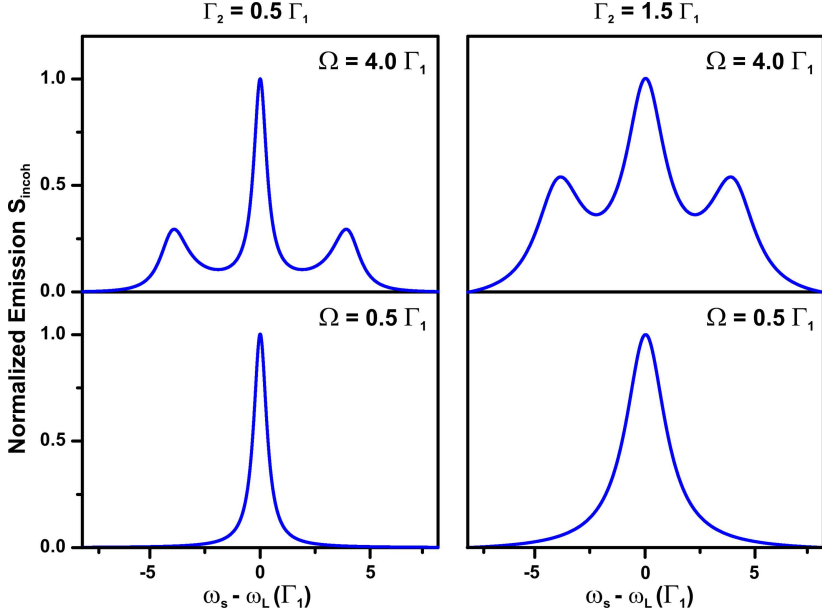


Figure 2.12: Normalized spectrum of the incoherent part of the resonance fluorescence emission. As expected the additional dephasing (right panel) broadens the spectral width of the individual peaks.

$$\begin{aligned}
 S(\omega_s) = & 2\pi \left(\frac{\Delta^2 + \left(\frac{\Gamma_1}{2}\right)^2}{\Omega^2} \delta(\omega_s - \omega_L) \right) + \frac{\frac{1}{2} \left(\frac{\Gamma_1}{2}\right)}{(\omega_s - \omega_L)^2 + \left(\frac{\Gamma_1}{2}\right)^2} \\
 & + \frac{\frac{1}{4} \left(\frac{3}{4}\Gamma_1\right)}{(\omega_s - \omega_L - \Omega)^2 + \left(\frac{3}{4}\Gamma_1\right)^2} + \frac{\frac{1}{4} \left(\frac{3}{4}\Gamma_1\right)}{(\omega_s - \omega_L + \Omega)^2 + \left(\frac{3}{4}\Gamma_1\right)^2} .
 \end{aligned} \tag{2.70}$$

The first summand is the coherent part of the spectrum, whereas the other three represent the incoherent Mollow triplet emission. The relative height of the red sideband : central peak : blue sideband is 1 : 3 : 1, the relative area 1 : 2 : 1 and the width in angular frequencies is found to be Γ_1 for the central Mollow line and $3/2 \cdot \Gamma_1$ for the sidebands, respectively.

Coherent and incoherent scattering part

From the calculations of the first-order correlation and the corresponding spectral function it is obvious that the resonance fluorescence signal has an incoherent and a coherent contribution. The incoherent part of the emission reveals the characteristic Mollow triplet in the spectral domain, linked to a finite coherence of the emission. The coherent part has an infinitely long coherence time, reflected in a delta-peak spectral component at resonance of the TLS. In the following, the relative magnitude of these two contributions in dependence on the excitation conditions in terms of a saturation parameter S will be discussed. For strictly resonant excitation conditions $\Delta = 0$ the saturation parameter is defined as

$$S = \frac{\Omega^2}{\Gamma_2 \Gamma_1} \quad . \quad (2.71)$$

The total emitted radiation power can be expressed via a sum of coherent and incoherent contribution as [28, 32]

$$P_{tot} = P_{coh} + P_{incoh} = \hbar\omega_0 \frac{\Gamma_1^2}{4\Gamma_2} \frac{S}{(1+S)^2} + \hbar\omega_0 \frac{\Gamma_1 S (\Gamma_2 + \Gamma_2 S - \Gamma_1/2)}{2\Gamma_2 (1+S)^2} \quad (2.72)$$

Figure 2.13 illustrates the coherent P_{coh} and incoherent contribution P_{incoh} to the total emitted radiation power P_{tot} as a function of saturation parameter $S \propto \Omega^2$. For increasing Rabi frequency the coherent contribution reaches a maximum value at $S \sim 1$ and decreases for $S \gg 1$, whereas the incoherent contribution increases for increasing S . For large values of S the steady state excited state population reaches $1/2$ and therefore P_{tot} reaches its asymptotic limit of $0.5\Gamma_1$. For the *Fourier transform-limited* case displayed in Fig. 2.13(a), the coherent contribution exceeds the incoherent contribution for $S < 1$. Under the conditions of additional pure dephasing depicted in Fig. 2.13(b) even for low saturation parameters P_{coh} does not dominate the emission, thus increasing pure dephasing in the system hampers the investigation of the coherent emission part of resonance fluorescence.

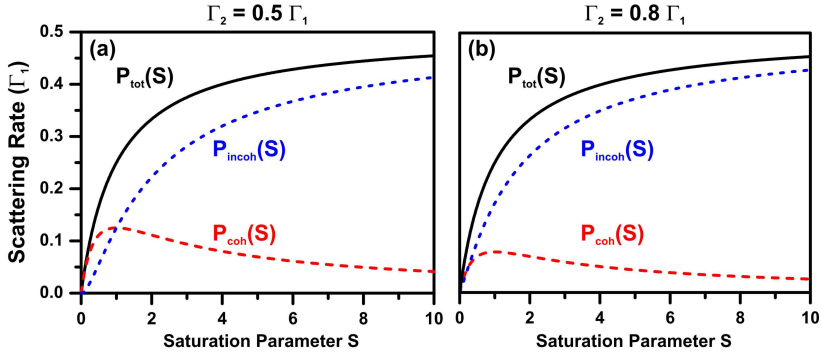


Figure 2.13: Magnitude of the coherent P_{coh} and incoherent P_{incoh} emission part of resonance fluorescence to the total emitted radiation P_{tot} versus saturation parameter $S \propto \Omega^2$. (a) At the Fourier transform-limit P_{coh} overbalances the emission for $S \ll 1$, at larger S the incoherent parts overtakes the coherent part and dominates the emission. (b) For $\Gamma_{pure} \neq 0$ the overall trend is the same, except for small values of S , here P_{coh} is lower if compared to the Fourier transform-limited case.

2.4 Cavity quantum electrodynamics

Cavity quantum electrodynamics (cQED) describes the interaction of a TLS such as a semiconductor QD with the confined photons of a cavity. The confinement changes the photon density of states and can therefore modify the emission properties of the TLS, in particular the emission dynamics of the system. Experimentally, there are different approaches to engineer the photon density of states in the vicinity of QDs via embedding them into optical microcavities such as micropillars, microdiscs or photonic crystals [36]. For the ideal case of a lossless cavity and the emitter initialized in the excited state, a photon can be emitted by a spontaneous electron-hole recombination process. This photon is stored inside the cavity, where it can be reabsorbed by the quantum emitter after a characteristic timescale. Inside such an ideal cavity the spontaneous emission process becomes reversible and the periodic emission and absorption is manifested in Rabi oscillations.

For the interaction between the TLS and the surrounding mode two different regimes can be distinguished when considering a realistic system with distinct dissipation processes, in which the photons leave

the cavity after a characteristic timescale. If the photonic loss rate is smaller than the coupling rate the system operates in the *strong coupling regime*. Here the emitter and the cavity mode coherently exchange energy leading to Rabi oscillations that are damped due to the dissipative processes. In the *weak coupling regime* irreversible decay dominates over coherent exchange. The spontaneous emission rate can be enhanced or inhibited by the *Purcell effect*, compared with its vacuum level, by tuning the emitter in and out of resonance with the cavity mode. Usually the emitter-cavity coupling is described by the *Jaynes-Cummings model* [37, 38].

2.4.1 Jaynes-Cummings model, *strong and weak coupling regime*

The *Jaynes-Cummings* Hamiltonian in rotating wave approximation for an ideal system, in which the decoherence of the emitter and the photon field can be neglected, reads

$$\hat{H}_{JC} = \hat{H}_{TLS} + \hat{H}_{cavity} + \hat{H}_{interaction} \quad (2.73)$$

$$= \hbar\omega_0\hat{\sigma}^+\hat{\sigma} + \hbar\omega_{cav}\hat{a}^+\hat{a} + \hbar g(\hat{\sigma}^+\hat{a} + \hat{\sigma}\hat{a}^+) \quad , \quad (2.74)$$

g denotes the coupling strength between the TLS and the cavity, which is defined as the scalar product of the transition matrix element of the QD dipole moment \mathbf{d} with the local electric field value at the dot position inside the cavity \mathbf{E} ($g = |\langle \mathbf{d} \cdot \mathbf{E} \rangle|$). For the case of the exciton at the electric field maximum of the cavity mode, the coupling constant can be expressed in terms of the oscillator strength $f = 2m\omega_0 d^2 / (e^2 \hbar)$ [39] as

$$g = \sqrt{\frac{\hbar^2}{4\epsilon_r\epsilon_0} \frac{e^2 f}{mV_M}} \quad . \quad (2.75)$$

Here ϵ_0 and ϵ_r are the vacuum and relative medium permittivity, m , the free electron mass and V_M denotes the volume in space occupied by the specific mode of the cavity, distinctly different to the geometric volume of the cavity itself.

The spectrum of the *Jaynes-Cummings* Hamiltonian consists of the ground state $|g, 0\rangle$ and a ladder of doublet states $|e, n\rangle$, $|g, n + 1\rangle$ with $n = 0, 1, \dots$. At emitter-cavity resonance the coupled states split into so-called dressed states, energetically separated by $2g\sqrt{n + 1}$. The

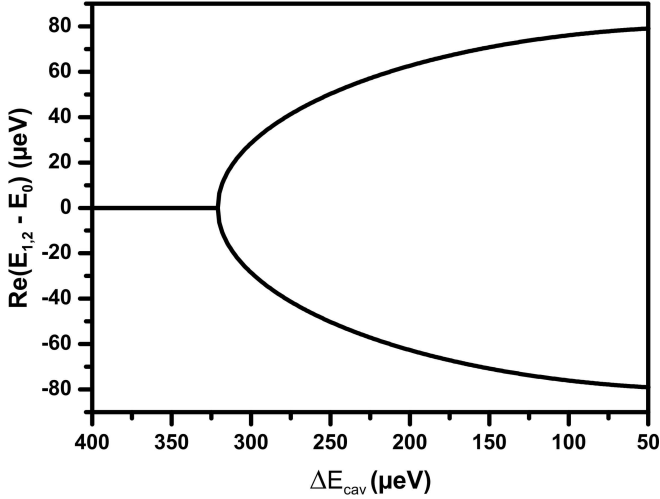


Figure 2.14: Real part of $E_{1,2} - E_0$ for a typical coupling strength of $g = 80 \mu\text{eV}$ [40]. The splitting of the eigenenergies occurs at the threshold condition for strong coupling.

splitting depends on the number of photons in the mode n , in which the splitting for the $n = 0$ -state is referred to as vacuum Rabi splitting.

For a non-ideal cavity, decoherence processes such as photon leakage out of the cavity, where the emission is coupled to a continuum of quasi-modes need to be considered. As described in chapter 2.3.3, dissipation losses can be accounted for via the Lindblad formalism. A detailed calculation of the optical Bloch equations for the *Jaynes-Cummings* system and the resulting solution of the time-dependent population can be found in Ref. [33].

Strong coupling regime

If the decoherence processes are slow enough, the system is in the *strong coupling* regime, in which the Rabi oscillations are damped due to the dissipation. The energies of the two eigenmodes at resonance can then be expressed as [39]

$$E_{1,2} = E_0 - i(\Delta E_{cav} - \Delta E_X)/4 \pm \sqrt{g^2 - (\Delta E_{cav} - \Delta E_X)^2/16} \quad , \quad (2.76)$$

in which E_0 denotes the energy of the uncoupled exciton (labeled X) and cavity mode (labeled cav), while ΔE_{cav} and ΔE_X are their FWHM respectively.

The vacuum Rabi splitting is found to be

$$\Delta E = 2\sqrt{g^2 - (\Delta E_{cav} - \Delta E_X)^2/16} \quad . \quad (2.77)$$

As long as the square root in Eq. 2.76 remains real, the states are split and the system is in the *strong coupling* regime. Therefore the condition for *strong coupling* is

$$g^2 - (\Delta E_{cav} - \Delta E_X)/16 > 0 \quad . \quad (2.78)$$

Figure 2.14 illustrates the crossover between *weak coupling*, in which the exciton and cavity states are degenerate at resonance to *strong coupling* in dependence on the cavity linewidth ΔE_{cav} .

Weak coupling regime

Here the spontaneous emission process is irreversible and no Rabi oscillations occur. Nevertheless, the spectral density in the vicinity of the QD is modified inside the cavity and influences the spontaneous emission process of the TLS. Depending on the vacuum field and the orientation of the emitter dipole with respect to the polarization of the cavity mode, the emission rate can be enhanced or inhibited compared to a QD without surrounding cavity. This change in the emission rate was initially proposed by *Purcell* in 1946 [41]. The ratio between the free-space and cavity-modified emission rate is therefore called *Purcell factor* F_P and can be expressed as [42]

$$F_P = \frac{\tau_{free}}{\tau_{cav}} = \frac{3Q(\lambda_{cav}/n)^3}{4\pi^2 V_M} \frac{\lambda_{cav}^2}{\lambda_{cav}^2 + 4Q(\lambda_X - \lambda_{cav})^2} \frac{|\mathbf{E}(\mathbf{r})|^2}{|\mathbf{E}_{max}|^2} \quad , \quad (2.79)$$

in which \mathbf{E}_{max} and $\mathbf{E}(\mathbf{r})$ denote the value of the electric field at the emitter position and the antinode of the field respectively. For a QD located at the electric field maximum and energetic emitter mode resonance, the Purcell factor reads

$$\frac{\tau_{free}}{\tau_{cav}} = \frac{3Q(\lambda_{cav}/n)^3}{4\pi^2 V_M} . \quad (2.80)$$

Therefore it is obvious that the quality factor Q of the cavity determines to what degree the spontaneous emission rate can be influenced by emitter-mode tuning.

Chapter 3

Experimental Techniques

In the following sections the basic experimental methods and the corresponding setups in terms of low temperature micro-photoluminescence (chapter 3.1), photon statistic measurements (chapter 3.2), radiative decay time (chapter 3.3) and coherence time measurements (3.4) together with high-resolution micro-photoluminescence (chapter 3.5) will be introduced. These are standard techniques that are commonly employed for the determination of the QD emission properties.

3.1 Low temperature micro-photoluminescence setup

A schematic depiction of the micro-photoluminescence (μ -PL) setup employed for the measurements presented in the following chapters is shown in Fig. 3.1(a). The sample under investigation is mounted on a coldfinger and held in a helium flow cryostat (*Cryo Vac Conti*) indirectly cooling the sample at a high vacuum pressure of $p < 10 \text{ mbar}^{-6}$. Low temperatures down to 4 K (liquid helium) are required to minimize the interaction of QD charge carriers with phonons and additionally to prevent their thermal escape out of the QD. With the aid of an external heating device it is possible to controllably vary the sample temperature between 4 – 300 K ($\Delta T = \pm 0.5 \text{ K}$).

The setup contains two different excitation lasers both pumped with a 10 W continuous wave (cw) frequency doubled Nd:YVO₄ solid state

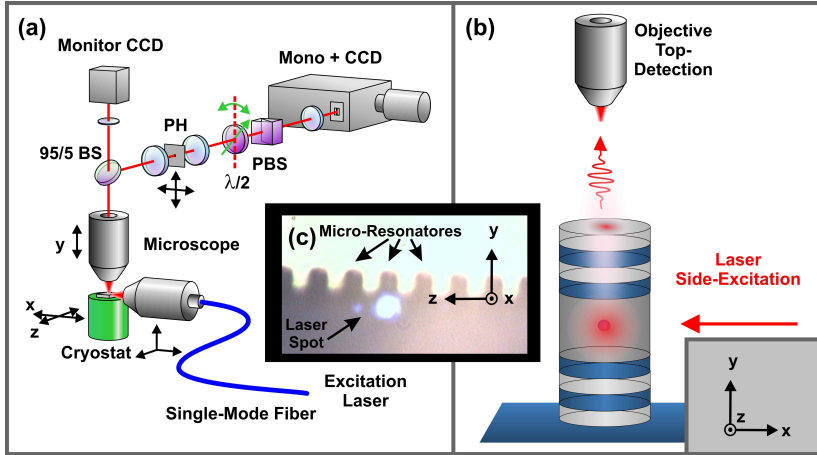


Figure 3.1: (a) Depiction of the micro-photoluminescence (μ -PL) setup [24]. For an effective laser stray-light suppression under resonant excitation conditions three different methods are employed: An orthogonal geometry between excitation and emission detection, spatial filtering with a pinhole (PH) and additionally polarization suppression via a combination of $\lambda/2$ retarder plate and a polarizing beam splitter (PBS). (b) Illustration of the orthogonal excitation-detection geometry of a QD in a micropillar cavity. (c) Webcam image of a micropillar sample from the side. The excitation laser beam and the micro-resonators are clearly visible, thus making it easy to address and investigate individual pillars.

laser (*Coherent Verdi V10*) operating at 532 nm.

For ps-pulsed excitation a Ti:Sapphire laser (*Coherent Mira 900*) with a variable output wavelength ranging between $\lambda = 700 - 1000$ nm, an average output power of 1.3 W and a repetition rate of 76.2 MHz is provided. The shape of the ps-pulses can be monitored with an autocorrelator (*APD Pulse Check*) and is found to be ~ 2 ps (temporal FWHM).

The second laser available in the setup is a frequency stabilized Ti:Sapphire cw ring laser (*Coherent 899 Ring*). Due to its special mirror optics the accessible wavelengths range from 875 – 925 nm with a maximum output power of ~ 700 mW. Having two etalons inside, it possesses a narrowband linewidth of nominally ~ 500 kHz, thus offering the opportunity to selectively excite single quantum emitters within

their homogeneous linewidth of electronic resonances.

The laser output wavelength can be measured with a wavemeter (*Coherent Wave Master*, accuracy of ~ 1.5 GHz). The desired laser beam power can be adjusted by attenuation with neutral density glass filters, a Fresnel reflection attenuator (*Newport High Energy Variable Attenuator*) and a combination of $\lambda/2$ retarder plate and polarizing beam splitter. For power measurements a sensitive power meter (*Newport Optical Power Meter 1830*) is available in the setup.

The sample can be accessed optically from the side via a focusing objective (*Nikon*, focal length $f = 17$ mm, super long working distance, numerical aperture 0.4). In a specially designed orthogonal excitation-detection geometry the photons are collected from top of the sample via another microscope objective ($f = 17$ mm objective). This 90° configuration is especially useful for laser stray-light suppression under resonant QD excitation, where the scattered laser light and the quantum dot s-shell emission have exactly the same frequency and are therefore not spectrally separable. Figure 3.1(b-c) illustrate the orthogonal excitation-detection geometry of a QD embedded in a micropillar together with a webcam image of the side-excitation of such a micropillar sample.

Spatial positioning of the excitation-laser can be achieved by controllable movement of the side-excitation assembly along (z -direction in Fig. 3.1) and vertical to the sample edge (y -direction) by a three axis stepper motor (*Nanomax 300*, *Thorlabs*) that additionally allows to alter the focus (x -direction) with an incremental stepsize of ~ 60 nm. The cryostat together with the objective for side-excitation can be horizontally moved with respect to the top-collection objective by two stepper motors (xz -plane) (*Physik Instrumente*, minimal stepwidth ~ 50 nm). The top focus objective can be positioned by a piezoelectric actuator (y -direction).

In addition to the orthogonal geometry for stray-light suppression explained above a pinhole with $15\ \mu\text{m}$ or $50\ \mu\text{m}$ -diameter is installed in the detection path to limit the photon collection to a small sample spot area of $3\ \mu\text{m}$ or $10\ \mu\text{m}$, respectively. Due to the Glan Thompson polarizer inserted after the objective of the side-incoupling with an extinction ratio of 10^{-6} the excitation laser has a well defined polarization state. Therefore polarization suppression via a $\lambda/2$ retarder plate in combination with a polarizing beam splitter is employed as an effective technique for laser stray-light suppression in the detection path. How-

ever, one has to keep in mind that this also suppresses the QD emission component with similar polarization as the excitation laser.

The luminescence collected from the sample is detected by one of two *Acton Research* spectrometers integrated in the setup. They both have two available gratings (1200 and 18001/mm) and a focal length of 500 mm and 750 mm respectively, therefore providing a maximal resolution of $\Delta E \sim 35 \mu\text{eV}$ at 900 nm. The nitrogen/peltier-cooled CCD cameras attached to the spectrometers serve as sensitive detectors with the ability to record the emission spectra (*vertical binning* mode) or spatial/spectral intensity distribution (*imaging* mode) of the collected emission.

3.2 Hanbury Brown & Twiss-interferometer for photon statistics measurements

To gain insight into the temporal correlation of photons emitted by a single QD, e.g. to prove that it is a true single-photon source, it is instructive to measure the second-order correlation function $g^{(2)}(\tau)$ via a *Hanbury Brown & Twiss*-type interferometer.

Fig. 3.2 displays the basic functionality of a *Hanbury Brown & Twiss*-interferometer (HBT) [43, 44] for auto-correlation measurements. The experimental apparatus consists of a 50 : 50 non-polarizing beam splitter with each of the two orthogonal output ports connected to an avalanche photo diode (APD: *Perkin Elmer AQR-14*). Due to a high signal-to-noise ratio with ~ 100 cts/s dark counts and a typical signal strength of more than 3000 cts/s, the APDs allow sensitive photon detection. The complete setup provides a time resolution of approximately 450 ps (FWHM). For auto-correlation measurements the emission line of interest is pre-filtered by a spectrometer and then sent to the 50 : 50 beam splitter. The depiction of photon coincidence events in terms of a histogram takes place in a two-step process. For the detection of one photon on APD *start* and subsequent detection of another on APD *stop* the time-to-amplitude converter (TAC, *Ortec model 566*) creates a TTL-shaped output pulse corresponding to a defined delay time $\tau = t_{\text{stop}} - t_{\text{start}}$. The multi-channel analyzer (MCA, *Ortec model 927*) stores the different coincidence events in separate channels according to the TTL-shaped output pulse. Additionally the employment of an electronic delay (*Ortec model 425A*) in the *stop* circuit (displayed

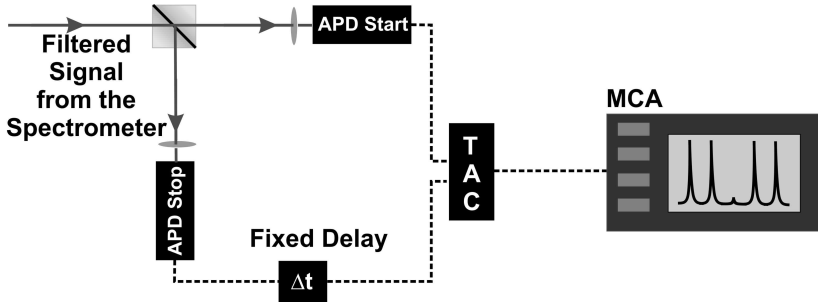


Figure 3.2: Schematic of a Hanbury Brown & Twiss-interferometer for auto-correlation $g^{(2)}(\tau)$ measurements. The photons are pre-filtered by a spectrometer and sent to a 50 : 50 non-polarizing beam splitter. The reflected and transmitted signal is detected via two avalanche photo diodes (APDs) acting as start and stop of the coincidence measurement. The output histogram is electronically accumulated by a combination of time-to-amplitude converter (TAC) and multi-channel analyser (MCA).

as Δt in Fig. 3.2) also allows the measurement of negative coincidence delays $\tau < 0$.

For photon cross-correlations between two distinctly different emission lines the basic principle of the measurement stays the same, only the light is first sent to the 50 : 50 beam splitter and afterwards spectrally filtered by the two spectrometers of the setup. Each spectrometer filters one of the two desired emission frequencies before subsequent APD detection takes place.

To analyse the experimentally derived temporal distribution of coincidence events $n(\tau)$ the histogram needs to be normalized with regard to the expectation value of a completely uncorrelated light source (e.g. Poissonian light), revealing $g^{(2)}(\tau) = 1$. For measurements under cw excitation the Poissonian level n_p^{cw} equals the average counts for large time delays $\tau \gg \tau_{corr}$. For normalization the histogram needs to be divided by n_p^{cw} . Pulsed correlation measurement with the *Coherent Mira 900* laser reveal peaks with a time delay corresponding to the inverse pulse repetition frequency of the laser (13.12 ns). The Poissonian level for the peak areas equals the average area for peaks with large time delays $\tau \gg \tau_{corr}$, therefore all peaks need to be normalized with respect to this average peak area value. Moreover the well known temporal separation between adjacent peaks can be employed for time-conversion of

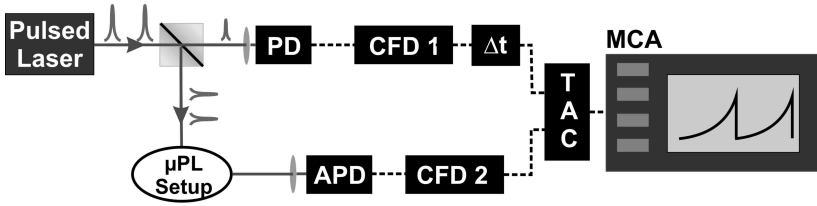


Figure 3.3: The pulsed laser beam is partitioned by a beam splitter (4 : 96). The 4%-fraction is sent to a photodiode (PD) providing the stop signal for the TAC. QD excitation and emission detection (96%-laser fraction) is carried out with the μ -PL setup described in chapter 3.1. After spectral selection the filtered luminescence is sent to an APD triggering the start of the time-correlation measurement. For the suppression of temporal fluctuations a constant fraction discriminator (CFD) is joint up in circuit between the APD or rather the PD and the TAC. The final histogram processing takes place similarly as described in chapter 3.2.

the histogram x-axis.

3.3 Time-correlated single photon counting for radiative decay time measurements

The radiative recombination timescale of electron-hole pairs is a characteristic quantity that describes the emission dynamics of a QD. Time-resolved photoluminescence is carried out by the experimental technique of time-correlated single photon counting (TCSPC), the corresponding setup is depicted in Fig. 3.3.

TCSPC measurements are carried out under pulsed non-resonant or quasi-resonant QD excitation with the Ti:Sapphire *Coherent Mira 900* laser. The basic principle is the temporal correlation of the desired QD luminescence from the μ -PL with the time trigger provided by the laser pulses directly via an internal photodiode (PD). The QD emission is detected with a fast APD with a temporal resolution of ~ 40 ps (*ID-Quantique id 100-20*, darkcounts ~ 30 cts/s) and serves as the *start* of the correlation in order to allow most effective counting. Therefore the laser trigger provides the *stop* of the measurement.

To minimize temporal fluctuation, a constant fraction discriminator is

joint in circuit between APD or rather PD and TAC. The histogram is created similarly as explained in chapter 3.2 with TAC and MCA. For the time-conversion of the histogram x-axis it is instructive to set the delay Δt to a value so that two peaks are visible in the histogram. The delay time between two neighboring peaks is given by 13.12 ns, i.e. the inverse of the laser pulsing frequency of 76.2 MHz.

3.4 *Michelson* interferometer for coherence time measurements

One important property characterizing the light emission from a QD is the coherence time. It is reflected by the spectral width of the emission line and normally determined by first order auto-correlation measurements $g^{(1)}(\tau)$, defined as

$$g^{(1)}(\tau) = \frac{\langle E^*(t)E(t+\tau) \rangle}{\langle E^*(t)E(t) \rangle} \quad . \quad (3.1)$$

The first-order coherence is linked to the spectrum of the emission line by the *Wiener-Khintchine theorem*

$$F(\omega) = \frac{1}{2\pi} \int_{-\infty}^{\infty} g^{(1)}(\tau) \exp(i\omega\tau) d\tau \quad . \quad (3.2)$$

Therefore $g^{(1)}(\tau)$ measurements are carried out by Fourier spectroscopy performed with a *Michelson* interferometer, schematically illustrated in Fig. 3.4(a). Collimated light from the sample is sent to a non-polarizing 50 : 50 beam splitter, with retroreflectors or planar mirrors at the end of each interferometer arm. The back reflected light is then brought to interference at the beam splitter and sent to a grating spectrometer for spectral filtering with subsequent intensity detection via an APD, as described in chapter 3.1. When moving one retroreflector mounted on a computer-controlled high-precision linear stage (*Physik Instrumente M-511.HD*) with a minimum unidirectional motion resolution of 20 nm, thus changing the path length of one interferometer arm, while keeping the path length of the other fixed, the conditions for constructive and destructive interference change periodically. Figure 3.4(b) shows the resulting interference fringes of the detected intensity on the APD from such a laser interference measurement.

From the recorded data the visibility can be extracted by determining the minimum and maximum value of the recorded sinusoidally varying

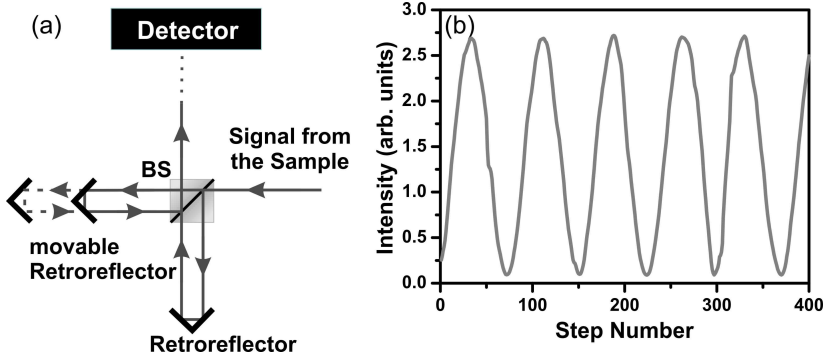


Figure 3.4: (a) Illustration of the functionality of a Michelson interferometer for Fourier spectroscopy. Collimated light entering the Michelson interferometer is sent to a 50 : 50 non-polarizing beam splitter (BS), from which it is transmitted/reflected to the two orthogonal interferometer arms with retroreflectors at the end of each. One retroreflector is mounted on a computer-controlled movable linear stage, which is employed to alter the delay between the two paths. Due to the systematic runtime delay variation, the intensity at the detector reveals a periodically varying interference pattern from which the visibility can be extracted. (b) Experimental data of a laser-visibility measurement.

intensity I_{min}/I_{max} . For the ideal case of a balanced 50 : 50 beam splitter the calculated visibility V equals the value of the first order correlation function [25]

$$V = \frac{I_{max} - I_{min}}{I_{max} + I_{min}} = |g^{(1)}(\tau)| \quad . \quad (3.3)$$

The degree of coherence can be classified as follows

$$\begin{aligned} |g^{(1)}(\tau)| &= 1 \quad \forall \tau && \text{fully coherent light} \\ 0 < |g^{(1)}(\tau)| &\leq 1 \quad \forall \tau && \text{partially coherent light} \quad . \end{aligned} \quad (3.4)$$

To determine the coherence time of the photons from a QD, the interference contrast of the emission has to be measured for different delay positions to reconstruct $g^{(1)}(\tau)$. Due to a limited coherence, the interference contrast is expected to decrease with increasing path delay between the two interferometer arms. Finally the visibility needs

to be corrected to account for imperfections in the Michelson alignment. Therefore the laser-visibility, which is ideally expected to be $g^{(1)}(\tau) = 1$, for all accessible delay positions (much smaller than the coherence length of the laser), is measured for the cw ring laser. The visibility correction for a distinct delay position is then easily achieved by dividing the extracted visibility of the QD emission by that of the laser.

3.5 Scanning *Fabry-Pérot* interferometer for high-resolution μ -PL

Strictly resonant emitter state preparation above saturation of the QD reveals the characteristic Mollow triplet structure in the spectral domain, being the hallmark of dressed state emission. Due to the Mollow triplet center-to-sideband splitting typically in the range $< 50 \mu\text{eV}$, standard μ -PL with a maximal spectral resolution of $35 \mu\text{eV}$ is not suitable to fully resolve the Mollow triplet. Therefore the μ -PL setup introduced in chapter 3.1 is complemented by a scanning *Fabry-Pérot* interferometer (FPI) for high-resolution micro-photoluminescence (HRPL) investigations.

As depicted in Fig. 3.5, the spectrally pre-filtered light is collimated and sent to the scanning FPI (*EXFO TL-15*) composed of two plane mirrors with parallel orientation and a spacer ring in between. Due to the cavity length of $d = 10 \text{ mm}$ the free-spectral range of the FPI is found to be $\Delta\nu_{FSR} = \frac{c}{2nd} = 15 \text{ GHz} \hat{=} \Delta E_{FSR} = 62.04 \mu\text{eV}$, with $c = \text{speed of light}$ and $n = 1$ (refractive index of air). The maximal spectral resolution of the *Fabry-Pérot* setup after proper alignment is found to be $\Delta E \approx 0.6 \mu\text{eV}$ (145 MHz). For the FPI alignment the transmitted signal of the narrow band cw Ti:Sapphire laser (nominally $\sim 500 \text{ kHz}$) is systematically maximized by changing the orientation of the interferometer cavity end-mirror. Additionally the four degrees of freedom of the gimbal-mounted interferometer itself can be used for improving the adjustment.

An output histogram of the signal as shown in Fig. 3.5 (right panel) is created by periodically scanning the mirrors of the FPI with piezo-actuators controlled by the periodic voltage ramps ranging from $0 - 1000 \text{ V}$ of a *Burleigh RG-93 Ramp Generator*. The linear change in the mirror distance systematically alters the frequency that interferes

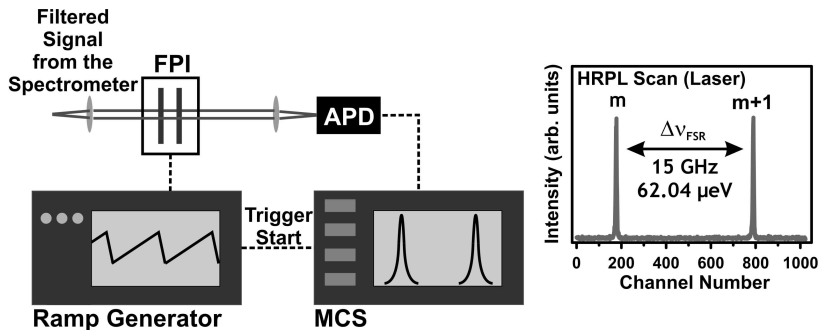


Figure 3.5: Left-panel: Spectrally pre-filtered light is collimated and sent through the Fabry-Pérot interferometer (FPI). Via synchronization with a voltage ramp that alters the FPI mirror distance periodically, the transmitted signal is detected via an APD and fed to a multi-channel scaler that accumulates the output histogram over typically 500 – 1000 scan loops. The FPI setup provides a spectral resolution of $\Delta E = 0.6 \mu\text{eV}$. Right panel: HRPL test measurement with a narrowband Ti:Sapphire ring laser. The free spectral range (FSR) between the two neighboring interference orders ($\Delta E_{FSR} = 62.04 \mu\text{eV}$) can be used to convert the channel numbers of the histogram into the desired relative energy axis.

constructively in transmission. The signal is detected via an APD and fed to a multi-channel scaler (MCA: *Stanford Research SR-430 MCS*) which creates the output histogram, synchronized with the logic start trigger voltage ramp. The MCA channels can be converted to frequency scale by the channel peak-to-peak distance of two neighboring interference orders that equal the FSR of the FPI.

Chapter 4

Emission properties of resonantly excited QDs

One of the first theoreticians who predicted a power-dependent three-peak structure for the spectral distribution of a resonantly excited atom was Newstein in 1968 [45]. Nevertheless this well-known spectral feature is usually referred to as *Mollow triplet* after *B. R. Mollow* who published a first complete theoretical description about the *Power spectrum of light scattered by two-level systems* in 1969 [35]. In this semiclassical approach the intensity ratio between the coherent and incoherent part of the resonance fluorescence (RF) emission is compared, the latter one revealing the well-known Mollow triplet in the emission spectrum. Shortly after the first full quantum-electrodynamical description was presented by Stroud *et al.* [46]. What was fundamentally new was the introduction of *dressed states* as combined energy eigenstates of the interacting atom-photon system. Several publications refined the quantum mechanical description in the dressed state picture, e.g. Cohen Tannoudji *et al.* [47]. When comparing the semiclassical description and the quantum mechanical model, it has been shown [48] that they are in full agreement about the basic features of resonance fluorescence. Shortly after the first theoretical descriptions about the resonance fluorescence emission of a TLS, several studies investigated the regime above saturation of a resonantly driven TLS on atoms, experimentally. One of the pioneering works by Wu *et al.* showed power- and detuning-dependent Mollow triplet series of the resonance fluorescence of atomic sodium. Moreover Kimble *et al.* [49] reported about photon

anti-bunching of strongly driven sodium atoms.

From the pioneering observations of resonance fluorescence emission from atoms it took quite some time until the first studies of resonance fluorescence on solid state emitters appeared in literature. In 2008 Wrigge *et al.* presented measurement results of the Mollow fluorescence triplet from a dye molecule. Almost simultaneously the first experimental proofs of RF from QDs were presented. The next section will give an overview of the development of RF investigations of the QD emission and the current state of research.

4.1 Resonance fluorescence on QDs

The main challenge in observing QD resonance fluorescence is to separate the energetically degenerate laser stray-light from the true QD emission. Due to this, the first signatures of dressed state formation under excitation above saturation have been reported via indirect measurements. In a pioneering work Xu *et al.* [50] verified the dressed state formation via resonantly exciting one exciton fine-structure component while probing the other. The absorption spectra clearly exhibit Autler-Townes splitting, and for increasing excitation power the linear dependence of the extracted Rabi frequency with the square root of excitation power. Shortly after this study, several other publications [51, 52] reported on spectral signatures of dressed excitonic states via the absorption or transmission of a probe field of the exciton-biexciton system. The distinct advantage of this experimental technique is the difference of the pump and probe laser energy.

The first direct investigation of resonance fluorescence emission has been presented by Muller *et al.* [53]. Via a special technique of orthogonal QD excitation and emission detection it was made possible to strongly suppress the laser stray-light and directly measure the first-order correlation function of the RF signal. The oscillations in the Michelson interferometric measurement in the time domain reveal the dressed state emission in terms of the Mollow triplet in the spectral domain. Shortly after a series of publications followed, reporting on the direct observation of the Mollow triplet as the hallmark of RF [54–56]. In these complementary studies Flagg *et al.* [54] observed Rabi oscillations in second-order photon correlation measurements, whereas Ates *et al.* [55] verified two-photon indistinguishability of the resonance fluorescence emission close to saturation. The main focus of the work of

Vamivakas *et al.* [56] is on the control of spin-tagged Mollow triplet sidebands of a negatively charged trion via a combination of the Zeeman effect and the dynamic Stark effect. In addition to this, Ulhaq *et al.* [57] have verified photon anti-bunching of the individual Mollow triplet sidebands and cascaded photon emission between the Mollow sidebands.

All these investigations are performed in the regime of strong emitter excitation and it was only recently that the resonance fluorescence regime below emission saturation was accessed experimentally. In two independent experimental studies Matthiesen *et al.* [58] and Nguyen *et al.* [59] verified the emission characteristics of the resonance fluorescence emission in the so-called *Heitler* regime. Interesting characteristics of this regime are the long coherence properties liberated from the QD transition in terms of the decay rate and predominantly tailored by the excitation laser coherence properties. In contrast to the long coherence linked to an ultra-narrow linewidth, the photon-statistics is not ruled by the excitation laser (Poissonian statistics). The emission in the Heitler regime is theoretically expected to reveal anti-bunching in terms of $g^{(2)}(0) = 0$.

4.2 Resonance fluorescence: A quantum mechanical description

A semiclassical description of resonance fluorescence was presented in chapter 2.3.4. In this section a fully quantum mechanical treatment of a resonantly driven TLS in the framework of *dressed states* will be introduced. This is particularly important to explain the non-classical features of resonance fluorescence, e.g. the photon correlations on the Mollow triplet components.

In the following the QD is treated as a two-level system with ground and excited state denoted as $|g\rangle$ and $|e\rangle$. The excitation laser is represented by coherent light states, which are a superposition of photon number Fock states $|n\rangle$ (for details see chapter 2.2.4). The uncoupled TLS and photon number states are illustrated in Fig. 4.1. They can be expressed as combined uncoupled states $|x, n\rangle$, where x denotes the TLS state, while n represents the Fock state with the corresponding photon number. Via the AC Stark interaction of the TLS with the intense excitation laser (excitation conditions above saturation $\Omega_0^2 \gg$

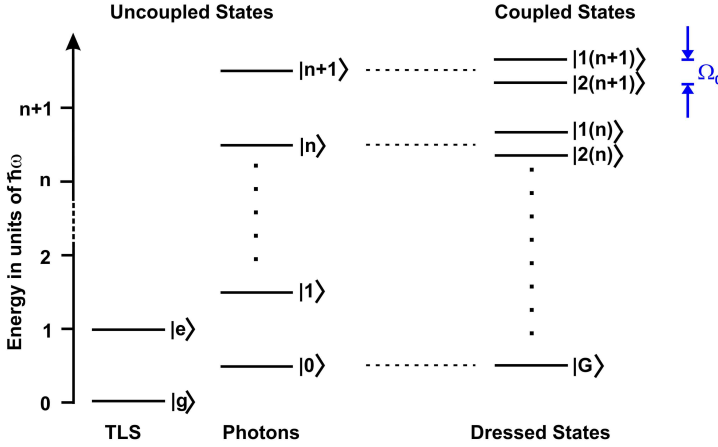


Figure 4.1: The uncoupled states are the TLS ground $|g\rangle$ and excited state $|e\rangle$ and the excitation laser photon Fock states $|n\rangle$. In the depiction the laser is energetically in resonance with the TLS. The two sub-systems get coupled due to AC Stark interaction under excitation above saturation. The new eigenstates of the Hamiltonian are the dressed states $|1(n)\rangle$ and $|2(n)\rangle$ that are a linear combination of the uncoupled states according to Eqs. 4.1, 4.2. Each state is defined by the number of quanta n in the sub-manifold. The energetic separation between the pairs of states equals the Rabi frequency Ω_0 .

$(T_1 T_2)^{-1}$) the combined uncoupled states are no good eigenstates of the system anymore. The new eigenstates are denoted as $|1(n)\rangle$ and $|2(n)\rangle$ and usually called *dressed states*. These coupled states between the two sub-systems are a superposition of the $|x, n\rangle$ -states. For a total number of n photons in the system they are [60]

$$|1(n)\rangle = c|g, n\rangle - s|e, n-1\rangle \quad (4.1)$$

$$|2(n)\rangle = s|g, n\rangle + c|e, n-1\rangle \quad (4.2)$$

The complex amplitudes c and s are given as

$$c = \sqrt{\frac{\Omega + \Delta}{2\Omega}}, \quad s = \sqrt{\frac{\Omega - \Delta}{2\Omega}} \quad (4.3)$$

What is worth mentioning is that laser-detunings $\Delta = E_{Laser} - E_{QD}$

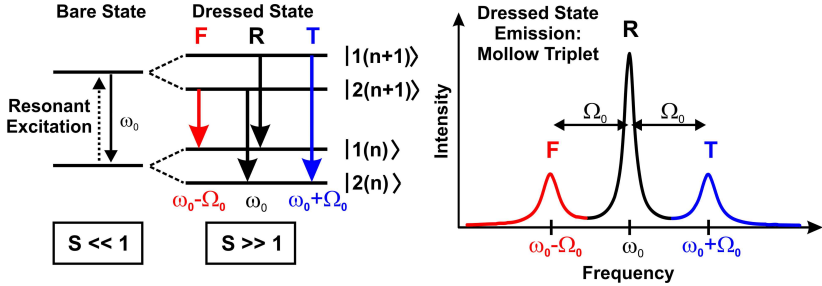


Figure 4.2: Left panel: Resonant excitation above saturation $S \gg 1$ leads to the formation of dressed states. The four optically allowed transitions are indicated by arrows. Right panel: In the spectral domain, the dressed state emission reveals the characteristic Mollow triplet. Due to the energetic separation of Ω_0 between the dressed state pairs, the Mollow triplet center-to-sideband splitting equals the Rabi frequency Ω_0 (adapted from [28]).

from the bare TLS resonance lead to an increase in the effective Rabi frequency Ω , assuming that $\Omega_0 = \text{constant}$. The definition of this generalized Rabi frequency Ω reads:

$$\Omega = \sqrt{\Omega_0^2 + \Delta^2} \quad . \quad (4.4)$$

For strictly resonant excitation conditions $\Delta = 0 \rightarrow \Omega = \Omega_0$ the two coefficients become $s = c = \frac{1}{\sqrt{2}}$.

Due to the equal energetic separation of the dressed states for all manifolds unlike the Jaynes-Cummings ladder (see chapter 2.4.1), the physical properties of a strongly driven TLS can be explained via considering a reduced part of only two neighboring manifolds of the hole ladder structure as depicted in Fig. 4.2. The four optically allowed transitions are indicated in the left panel of Fig. 4.2 via arrows. In the spectral domain these transitions are reflected by the characteristic Mollow triplet, visualized in the right panel of the graph. The transitions from $|1(n+1)\rangle \rightarrow |1(n)\rangle$ and $|2(n+1)\rangle \rightarrow |2(n)\rangle$ give rise to the emission at the TLS resonance referred to as Rayleigh line (R). The two sidebands arise from the transitions $|1(n+1)\rangle \rightarrow |2(n)\rangle$ and $|2(n+1)\rangle \rightarrow |1(n)\rangle$. For consistency with the historical nomenclature in literature (e.g. [60]), the lower energetic sideband is referred to as Fluorescence line (F) because it is nearest to the TLS resonance for $\Delta > 0$. The high-energetic sideband can be understood to arise from a three-

photon excitation as illustrated in Ref. [61] and is therefore termed three-photon line (T). Due to the fact that there are two possible transitions for a R photon to be emitted, compared to one possibility how an F or T photon can be emitted, the central peak has twice the area of the individual sidebands. Shifting the laser frequency from the TLS resonance $\Delta \neq 0$ results in a shift of the central Rayleigh line with the laser according to

$$E_R(\Delta) = \hbar\omega_0 + \Delta \quad . \quad (4.5)$$

The off-resonant excitation is accompanied by an increased center-to-sideband splitting in terms of the effective Rabi frequency Ω . For $\Delta \neq 0$ the Mollow sidebands are spectrally located at

$$E_{T,F}(\Delta) = \hbar\omega_0 + \Delta \pm \sqrt{\Omega_0^2 + \Delta^2} \quad . \quad (4.6)$$

4.3 Planar sample structure

For the experimental investigations presented within this chapter and also the study about indistinguishable photons from the Mollow sidebands (chapter 5) as well as the phonon-assisted incoherent excitation of a QD (chapter 6), a planar sample structure has been employed for the measurements. This planar sample is grown by metal organic vapor epitaxy (MOVPE), details about this technique can for example be found in Ref. [62]. The self-assembled In(Ga)As/GaAs QDs are embedded in a GaAs λ -cavity sandwiched between 29 periods of bottom and 4 periods of top distributed Bragg reflectors (DBRs) composed of $\lambda/4$ -thick AlAs/GaAs layers (see also chapter 7.2). As illustrated in Fig. 4.3, the DBR structure is employed mainly due to its waveguiding effect on the excitation laser. In combination with the orthogonal excitation-detection technique the sample structure is particularly suitable for resonant excitation, since it allows to spatially separate the laser light from the QD luminescence.

4.4 Resonant spectroscopy of single QDs

For the investigation of the resonance fluorescence of a single QD, the experimental difficulty is to separate the parasitic laser stray-light from

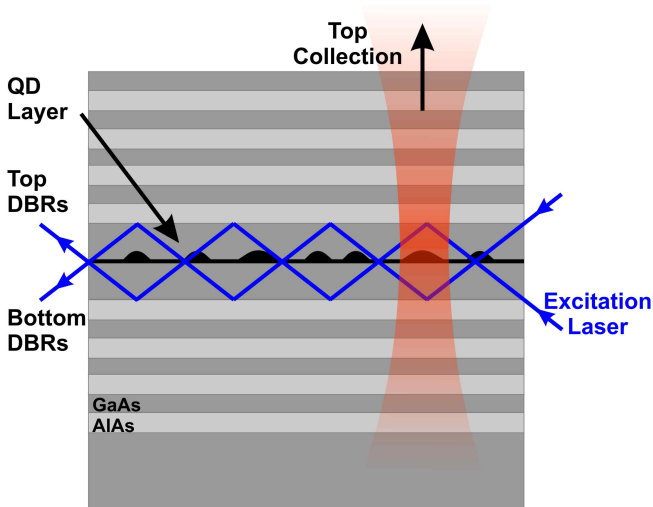


Figure 4.3: Schematic depiction of the planar sample structure. In(Ga)As/GaAs QDs are embedded in a GaAs λ -thick cavity sandwiched between 29(4) pairs of bottom (top) DBRs. For the side excitation the sample structure provides a waveguiding effect, as schematically indicated in blue. Together with the perpendicular excitation-detection geometry, the sample structure allows very good laser stray-light suppression and therefore investigations of the resonance fluorescence of single QDs.

the true resonance fluorescence signal. Compared to non-resonant excitation schemes the obstacle is the degeneracy of QD s-shell emission and the excitation laser energy. For typical laser-detunings Δ of a fine laser scan over the resonance (see e.g. Fig. 4.4), the combined signal of both the laser stray-light and the QD luminescence appears as one single line and cannot be spectrally resolved and separated with the spectrometer. As explained in section 3.1 three different techniques are employed to minimize the laser stray-light of resonantly excited QDs in a planar sample structure. These are an orthogonal excitation-detection geometry (introduced by A. Muller *et al.* [53]) in combination with spatial and polarization-based filtering in the detection path of the photoluminescence setup.

To achieve strictly resonant excitation of a QD in the experiment, the

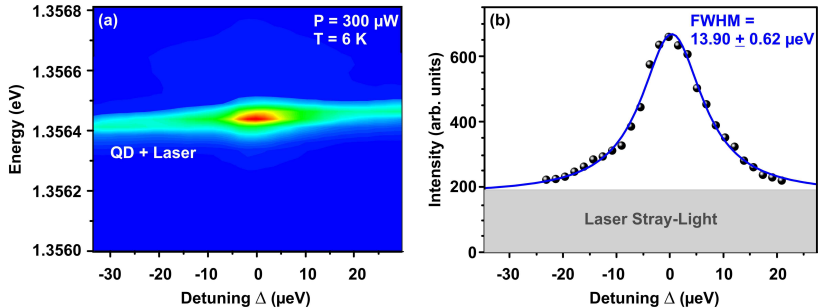


Figure 4.4: (a) Resonance scan over the QD s-shell resonance in steps of $\sim 2 \mu\text{eV}$ depicted in an intensity color plot. The collected combined QD luminescence and laser stray-light signal reveals the onset of resonance fluorescence around $\Delta = 0$. All the spectra were taken at the same excitation power. (b) Combined integrated QD + laser intensity versus detuning Δ , extracted from the spectra of the resonance scan. The solid line is a Lorentzian fit from which a linewidth of $\text{FWHM} = 13.90 \pm 0.62 \mu\text{eV}$ is extracted. The vertical offset indicated in grey originates from the constant laser stray-light background contributing to the collected signal.

QD is first excited via a non-resonant excitation scheme to derive the approximate s-shell emission energy. The s-shell energy extracted from the spectra is limited by the resolution of the spectrometer. Therefore it is necessary to record a so-called resonance scan over the extracted QD s-shell to exactly determine the resonance energy. Figure 4.4(a) shows a color intensity plot of such a laser scan where the cw ring laser, which has a narrow linewidth of $\sim 2 \text{ neV}$ and is thus much smaller than the exciton linewidth in the range of $10 - 20 \mu\text{eV}$, is scanned with energetic steps of $\sim 2 \mu\text{eV}$ over the QD resonance. For laser-detunings that are larger than the emission linewidth of the QD, the collected light is only parasitic laser stray-light. Around $\Delta = 0$ the onset of resonance fluorescence is clearly reflected in the increase of the combined QD and laser stray-light signal. The spectra of the resonance scan have all been taken under the same excitation power of the laser ($\sim \pm 5\%$ variation). Figure 4.4(b) shows the integrated intensity of the composite laser and QD signal extracted from the resonance scan spectra. The vertically shifted Lorentzian profile reflects the QD absorption profile, whereas the constant background is due to the laser stray-light.

If the effective potential of the QD has a symmetry lower than D_{2D} , the excitonic emission of the QD has a fine-structure splitting, typically in the range of $\Delta_{FSS} = 10 \mu\text{eV}$ (see chapter 2.1.3). This can also be traced in the fine laser scan over the QD resonance as has been shown by Ates *et al.* [63]. The scan in Fig. 4.4 does not reveal any exciton fine-structure, which can be due to two reasons. First the QD can be aligned in a way that the linearly polarized laser excites only one exciton fine-structure component. Secondly, the polarizer for laser stray-light suppression in the detection beam path is set to an angle that fully suppresses one of the exciton fine-structure emission components.

4.5 Power- and detuning-dependence of resonance fluorescence

This section focuses on the introduction of basic experimental results of a resonantly excited TLS in dependence on excitation power and laser-detuning. Compared to the theoretical treatment of the QD as a bare TLS, the experimental results reveal first hints of the interaction of the QD with the surrounding solid state medium, which will be explained in a refined version of RF under consideration of QD-phonon interaction in chapter 4.7.

As a typical example, the left panel of Fig. 4.5 shows the evolution of the Mollow triplet under strictly resonant emitter state preparation $\Delta = 0$ with excitation power. The excitation strength is increased from bottom to top. The arrows mark the Mollow triplet sidebands that correspond to the Rayleigh line at $\delta = 0$. Because of the *Fabry-Pérot technique* in HRPL, all spectral features appear periodically with an offset equal to the interferometer FSR. As theoretically expected, the F and T sidebands are found to have equal Rabi splittings Ω_0 from the Rayleigh line and identical peak areas. The central Rayleigh line has contributions from the incoherent and coherent emission part of RF and it also contains parasitic laser-stray light. The incoherent part of the resonance fluorescence emission is expected to reveal a ratio of 2 : 1 for the central peak area to the individual sideband areas. For the Mollow triplet, which is depicted in green in Fig. 4.5 the ratio is found to be 2.5 : 1. The larger central Rayleigh. peak area can be attributed to two reasons. First, the resonance fluorescence contains a coherent emission part in addition to the incoherent Mollow

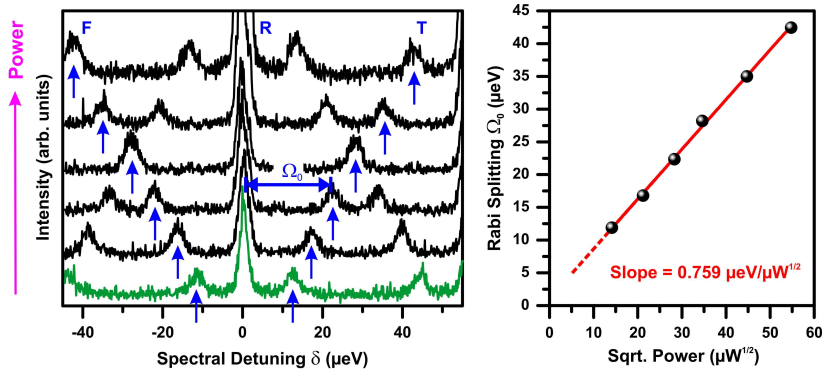


Figure 4.5: Left panel: Power-dependent Mollow triplet series under resonant excitation $\Delta = 0$. The blue arrows indicate the Mollow triplet sidebands that belong to the Rayleigh line at $\delta = 0$, the other peaks belong to an adjacent order of the scanning Fabry-Pérot interferometer. With increasing excitation power, the Rabi frequency Ω_0 that is manifested in the Mollow triplet center-to-sideband splitting increases. Right panel: Ω_0 versus \sqrt{P} reveals the expected linear behavior.

triplet emission, which is theoretically expected to be a δ -peak at the Rayleigh line energy. Depending on the exact value of the saturation parameter $S = \Omega^2/(\Gamma_2\Gamma_1)$ the ratio of the coherent to incoherent part can be calculated. Figure 2.13 depicts these two resonance fluorescence contributions in dependence on S . The incoherent part decreases with increasing saturation parameter, its value is also critically dependent on the pure dephasing T_{pure} that the system undergoes. The Rabi splitting of the green Mollow triplet in Fig. 4.5 is found to be $\Omega_0 = 11.9 \mu\text{eV}$. To get a rough estimation of the percentaged contribution of the coherent emission part reasonable values for T_1 and T_2 of a QD in a planar MOVPE grown sample structure are assumed. With $T_1 = 800 \text{ ps}$ and $T_2 = 800 \text{ ps}$ the saturation parameter is $S \approx 5$. In this case the ratio of the incoherent to coherent emission part is approximately 9 : 1, thus the contribution of the coherent part to the central peak area $A_{central} = 2.5$ is $A_{coherent} \approx 0.45$. The remaining contribution is due to stray-light of the excitation laser, that was not filtered out completely by the employed laser-suppression techniques. From the estimation it can be concluded, that the laser stray-light suppression

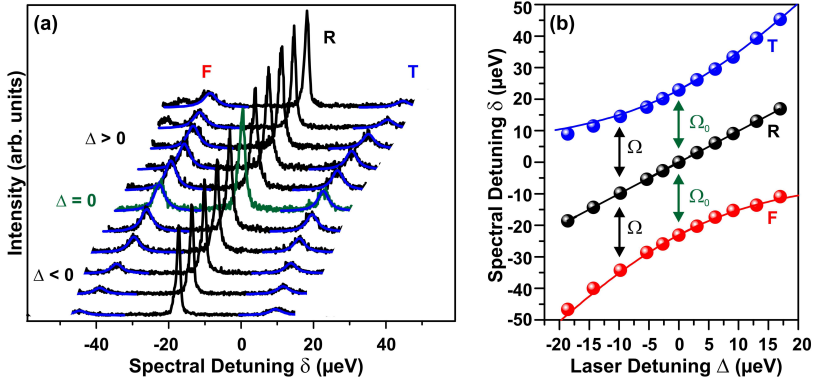


Figure 4.6: (a) HRPL of the QD resonance fluorescence under systematic variation of the laser-excitation detuning Δ , taken at a fixed power of $P = 500 \mu\text{W}$. δ denotes the spectral emission detuning from the bare emitter resonance. Green center trace: Mollow triplet under strictly resonant excitation $\Delta = 0$. (b) Spectral evolution of the Mollow sidebands with laser-detuning Δ , extracted from (a).

is very good and the predominant part of the collected light is true resonance fluorescence of the QD emission. In the right panel of Fig. 4.5 the extracted Rabi frequency Ω_0 is plotted versus the square root of excitation power \sqrt{P} . As theoretically expected from the definition of the Rabi frequency (see Eq. 2.50) $\Omega_0 \propto \sqrt{P}$, a straight line nicely fits the data extracted from the HRPL spectra, thus revealing consistency with theoretical expectations. The slope of the line depends on the specific system under investigation and the experimental conditions. It is worth mentioning that the power P was measured outside the cryostat and can only be regarded in terms of a relative excitation intensity. In contrast, the experimentally observed Rabi frequency includes the electric field at the TLS location inside the semiconductor sample.

Figure 4.6(a) shows a series of laser-detuning-dependent Mollow triplet spectra taken at a constant excitation strength of $P = 500 \mu\text{W}$. The laser-detuning between the driving field and the bare emitter resonance $\hbar\omega_0$ modifies the dressed emission, according to Eqs. 4.5, 4.6.

The extracted spectral positions for the red and blue Mollow sidebands and the central Rayleigh line are depicted in Fig. 4.6(b). The fit corre-

sponding to Eqs. 4.5, 4.6 perfectly reproduces the experimental data. So far the power- and detuning-dependent observations have been in agreement with theoretical predictions of a resonantly excited TLS. A closer look at the detuning-dependent Mollow triplet series reveals distinct broadening of the Mollow sidebands with increasing Δ , accompanied by a change in the relative sideband intensities. This results from the fact that even when the QD exciton is treated as a TLS, the interaction of the surrounding solid state medium especially with the phonon bath has to be incorporated. In the following sections phonon interaction in the specific case of excitation-induced dephasing will be introduced and a theoretical approach in terms of a polaron master equation will be presented, which includes the phonon interaction in a refined theoretical description.

4.6 Excitation-induced dephasing

State-of-the-art experimental investigations on the resonance fluorescence emission of a single QD by Ulrich *et al.* [64] have revealed a systematic Mollow triplet sideband broadening with increasing excitation strength found to be proportional to the square of the Rabi frequency Ω . These studies in the spectral domain have been in good agreement with earlier experiments from Ramsay *et al.* [65, 66]. Their investigations have revealed a non-monotonic damping of Rabi rotations via pulsed photocurrent spectroscopy under increasing pump strength. The experimentally observed behavior cannot be explained by assuming a constant pure dephasing independent of Ω as the only pure dephasing mechanism that the TLS undergoes. As has been shown in these publications, the data has been convincingly modelled with a power-dependent dephasing rate of $\Gamma_{EID} = K\Omega^2$ being proportional to the square of the Rabi frequency Ω . For a theoretical description of this effect the solid state surrounding medium of the QD has been identified as the principle source of the observations explained above in terms of exciton interaction with longitudinal acoustic phonons via deformation potential coupling [67–71]. The effect is usually termed as *excitation-induced dephasing* (EID) and can be understood qualitatively from a general resonance argument. The dephasing is dominated by the phonons that are most strongly coupled to the QD carriers which correspond to those that have a wavelength comparable to the QD size. The frequency that corresponds to these maximally coupled phonons is

termed *cut-off frequency* ω_c . These modes are most effectively driven when the carrier dynamics, which implies the Rabi frequency, is resonant with them, too. As the Rabi frequency is increased towards ω_c , the carrier-phonon coupling increases as well, leading to a larger dephasing in terms of damped Rabi oscillations in combination with broadened Mollow sidebands. The dephasing rate decreases again when the carrier dynamics and therefore the Rabi frequency is increased further. This resonant nature of the carrier-phonon coupling behavior leads to a subsequent disappearance and reappearance of Rabi rotations as the driving field is systematically increased.

According to Ref. [70] the spectral density for the phonon states reads:

$$\begin{aligned} J(\omega) &= \omega^3 \frac{(D_e - D_h)^2}{4\pi^2 \lambda u^5} \exp\left(-\frac{\omega^2 d^2}{2u^2}\right) \\ &= \alpha_p \omega^3 \exp\left(-\frac{\omega^2}{2\omega_c^2}\right) . \end{aligned} \quad (4.7)$$

For the calculation a spherical harmonic confinement potential of the QD and the assumption of equal electron and hole ground-state localization length have been made. D_e and D_h are the bulk electron and hole deformation potential constants, respectively. u denotes the speed of sound in the material, d is the dot dimension and λ the sample density. In addition the derivation is based on the assumption of a linear dispersion in terms of $\omega_q = uq$. For typical parameters for In(Ga)As/GaAs QDs (see Appendix A), Fig. 4.7 displays the normalized phonon density of states for three different QD sizes $d = 5, 10, 15$ nm. The spectral density increases towards the cut-off frequency $\omega \sim \omega_c = u/d$, and is found to be higher in energy for smaller dots. Thus for increasing driving strength Ω , the density of the resonant phonons increases towards the cut-off frequency, leading to larger dephasing in the system. For very high excitation strength, the phonon density decreases again and therefore the phonon-induced dephasing is also reduced.

From an experimental point of view, the reachable Rabi frequencies under resonant cw excitation $\Omega \ll 100 \mu\text{eV}$ are far below the cut-off frequencies $\omega_c \gg 1 \text{ meV}$. Therefore it is only possible to observe the increased dephasing in terms of Mollow sideband broadening, but not the sideband narrowing regime.

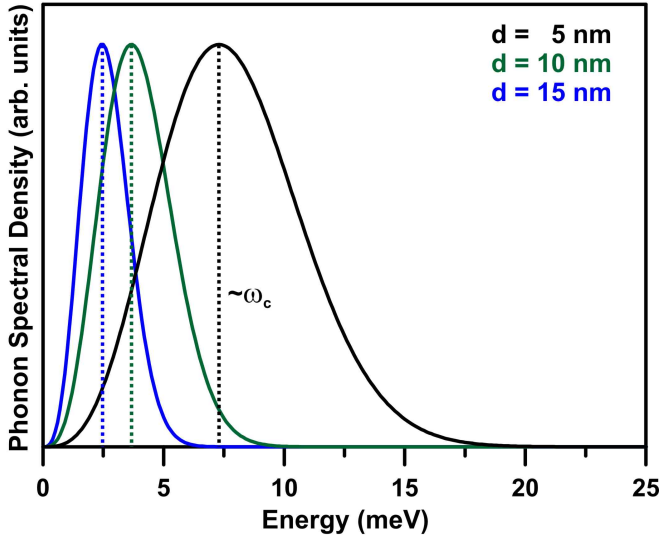


Figure 4.7: Normalized phonon density of states for three different dot diameters d according to Eq. 4.7. For smaller dots the cut-off frequency ω_c indicating the energy maximum of the phonon density function shifts to higher energies.

4.7 Polaron master equation for a resonantly excited TLS with phonon interaction

In chapter 2.3 the interaction of a bare TLS and a monochromatic laser field was introduced. For a thorough description of the excitonic emission spectra of a QD, the exciton-phonon interaction has to be incorporated into the theoretical model. From a theoretical point of view, there are various different approaches how to obtain an equation of motion for the QD dynamics from the system Hamiltonian. One way is to apply the numerically exact path integral method [72, 73], another option is to use a fourth-order correlation expansion [74, 75] or employ a master equation approach of weak coupling [70], variational [76] or polaron type [71, 77].

The joint experimental-theoretical investigations of the detuning-de-

pendence of a coherently excited QD [78] presented in chapter 4.8, the research about the Mollow quintuplets of a coherently excited QD [79] (see chapter 4.9), and the work about phonon-assisted incoherent excitation of a QD [80] (see chapter 6) have been performed in close cooperation with the group of *Prof. Stephen Hughes* (*Queen's University*, Kingston, Ontario, Canada). The experimental data have been modelled with a polaron master equation-based theory, which has been developed by *Prof. Stephen Hughes* and co-workers, as described in detail in Refs. [71, 77–80]. In this section, a brief introduction into the system Hamiltonian will be given together with the discussion of several important aspects of the model. For a comprehensive description, which is not the aim of this section, the reading of the listed above references is suggested.

Theoretically the QD is modelled as an effective TLS driven by a coherent cw pump field. The phonon bath is represented by a continuum of harmonic oscillators of frequency ω_q with phonon annihilation and creation operators b_q, b_q^\dagger . λ_q is the coupling strength of the electron-phonon interaction due to deformation potential coupling with LA phonons. The system Hamiltonian is the starting point for the theoretical analysis. After transformation to the frame rotating with respect to the laser pump frequency ω_L , the Hamiltonian reads

$$H = -\hbar\Delta\sigma^+\sigma^- + \hbar\eta_x(\sigma^+ + \sigma^-) \quad (4.8)$$

$$+ \sigma^+\sigma^- \sum_q \hbar\lambda_q(b_q + b_q^\dagger) + \sum_q \hbar\omega_q b_q^\dagger b_q \quad ,$$

with $\sigma^{+/-}$ being the Pauli operators of the exciton and $\eta_x = 2\Omega$ the exciton pump rate of the coherent cw laser field. In the following Ω_r denotes the renormalized Rabi frequency due to exciton-phonon interaction. For negligible phonon interaction Ω_r equals Ω .

The first part of the Hamiltonian expresses the exciton energy, the second one the dipole interaction of the TLS with the driving field (see chapter 2.3.2). The third summand accounts for the electron-phonon interaction, whereas the last term is the total phonon energy of the system. Via the transformation

$$H' = e^S H e^{-S} \quad \text{with} \quad (4.9)$$

$$S = \sigma^+ \sigma^- \sum_q \frac{\lambda_q}{\omega_q} (b_q^\dagger - b_q) \quad , \quad (4.10)$$

the Hamiltonian is transformed into the polaron frame. The Hamiltonian can be divided into three summands, a system part H'_S , a reservoir part H'_R , and an interaction part H'_I , according to

$$H'_S = \hbar(-\Delta - \Delta_P) \sigma^+ \sigma^- + \langle B \rangle X_g \quad (4.11)$$

$$H'_R = \sum_q \hbar \omega_q b_q^\dagger b_q \quad (4.12)$$

$$H'_I = X_g \xi_g + X_u \xi_u \quad . \quad (4.13)$$

The following abbreviations are used above: $\xi_g = 1/2(B_+ + B_- - 2\langle B \rangle)$, $\xi_u = 1/(2i)(B_+ - B_-)$, $X_g = \hbar \eta_x (\sigma^- + \sigma^+)$, and $X_u = i \hbar \eta_x (\sigma^+ - \sigma^-)$.

B_\pm are the coherent displacement operators of the phonon modes

$$B_\pm = \exp \left(\pm \sum_q \frac{\lambda_q}{\omega_q} (b_q - b_q^\dagger) \right) \quad , \quad (4.14)$$

after thermally averaging the operator reads

$$\langle B \rangle = \exp \left(-\frac{1}{2} \int_0^\infty d\omega \frac{J(\omega)}{\omega^2} \coth(\hbar\omega/(2k_B T)) \right) \quad . \quad (4.15)$$

The polaron frequency shift is given by

$$\Delta_P = \int_0^\infty d\omega \frac{J(\omega)}{\omega} \quad , \quad (4.16)$$

it accounts for the renormalization of the QD exciton resonance frequency due to coupling to the phonon modes; however, it is assumed that the polaron shift is implicitly included in the exciton energy ω_x . The phonon-induced renormalization also affects the Rabi frequency and the radiative decay rate. The former can be visualized as the slowing down of the Rabi rotation under resonant excitation due to phonon-coupling. Due to the interaction, the oscillation accumulates a

phase difference with respect to the excitation, which leads to a reduction in the Rabi frequency. Secondly, due to the phonon interaction, the radiative decay rate is also renormalized and therefore lowered, resulting in a larger decay time [77]. The renormalized Rabi frequency Ω_r can be significantly smaller than Ω for suitably large electron-phonon coupling, even at low temperatures. For In(Ga)As/GaAs material parameters given in Appendix.A and at low phonon bath temperature of $T = 6$ K, $\langle B \rangle \approx 0.75$ and this value decreases with increasing bath temperature.

In addition to the electron-phonon interaction, it is necessary to include pure dephasing γ' and radiative decay γ into the model to obtain a complete description of the system dynamics. This is done in a phenomenological manner via Lindblad operators of the form $\hat{L}[O] = 2O\rho O^\dagger - O^\dagger O\rho - \rho O^\dagger O$. It is then possible to derive the Markovian time-convolutionless master equation, and based on several restricting assumptions an effective phonon master equation, which leads to the same results as the full master equation for the regime of interest as discussed in detail in Ref. [78]. The effective master equation reads:

$$\begin{aligned} \frac{\partial \rho}{\partial t} = & \frac{1}{i\hbar} [H'_S, \rho(t)] + \frac{\gamma}{2} \hat{L}[\sigma^-] + \frac{\gamma'}{2} \hat{L}[\sigma^+ \sigma^-] + \frac{\Gamma_{ph}^{\sigma^+}}{2} \hat{L}[\sigma^+] \\ & + \frac{\Gamma_{ph}^{\sigma^-}}{2} \hat{L}[\sigma^-] - \Gamma_{ph}^{cd} (\sigma^+ \rho \sigma^+ + \sigma^- \rho \sigma^-) \quad . \end{aligned} \quad (4.17)$$

The pump-driven scattering processes are obtained from

$$\Gamma_{ph}^{\sigma^+/\sigma^-} = \frac{\Omega_r^2}{2} \text{Re} \left[\int_0^\infty d\tau e^{\pm i\Delta\tau} (e^{\phi(\tau)} - 1) \right] \quad (4.18)$$

$$\Gamma_{ph}^{cd} = \frac{\Omega_r^2}{2} \text{Re} \left[\int_0^\infty d\tau \cos(\Delta\tau) (1 - e^{-\phi(\tau)}) \right] \quad , \quad (4.19)$$

with the phonon correlation function

$$\phi(t) = \int_0^\infty d\omega \frac{J(\omega)}{\omega^2} [\coth(\hbar\omega)/(2k_B T) \cos(\omega t) - i \sin(\omega t)] \quad . \quad (4.20)$$

It is worthwhile having a closer look at the different physical origins of the dephasing that the system undergoes.

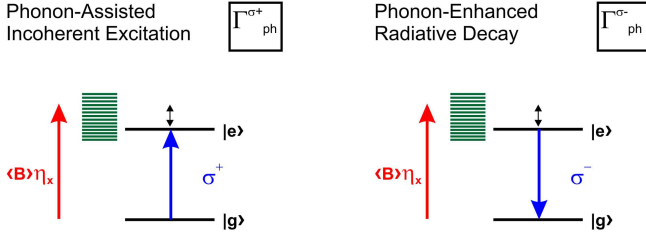


Figure 4.8: Illustration of the physical meanings of $\Gamma_{ph}^{\sigma+/-}$. Left: $\Gamma_{ph}^{\sigma+}$ results in phonon-assisted incoherent excitation of a TLS for laser excitation-detuning from the bare TLS resonance. The energetic difference between laser energy and TLS resonance is compensated by the absorption or emission of a phonon with corresponding energy. The phonon vibration modes are indicated by green horizontal lines. Right: $\Gamma_{ph}^{\sigma-}$ is the phonon-assisted rate corresponding to the opposite process termed phonon-enhanced radiative decay.

- $\Gamma_{ph}^{\sigma+}$ is the rate of phonon-assisted incoherent excitation as illustrated in Fig. 4.8. When the laser excitation is slightly detuned from the TLS resonance, the difference energy is mediated via phonon absorption or emission. A detailed study of this effect is presented in chapter 6.
- $\Gamma_{ph}^{\sigma-}$ corresponds to the opposite process of $\Gamma_{ph}^{\sigma+}$, termed phonon-enhanced radiative decay, illustrated in Fig. 4.8.
- The magnitude of the combined phonon scattering rates $\gamma_{ph} = \Gamma_{ph}^{\sigma+} + \Gamma_{ph}^{\sigma-}$ is proportional to Ω_r^2 . γ_{ph} affects the spectral width of the Mollow triplet components according to Eq. 4.22 and is therefore identified as the origin of *excitation-induced dephasing*.
- Γ_{ph}^{cd} is the cross-dephasing rate that only affects the off-diagonal components of the Bloch equations (see Ref. [78]). Therefore it only affects the polarization but not the population of the system. According to Eq. 4.18, it is dependent on the excitation strength and the phonon correlation function. Concerning the spectral width of the Mollow triplet components, the cross-dephasing term acts to squeeze the sidebands while broadening the center line.

From the calculations in the limit of high-fields and on-resonance excitation ($\Delta = 0$), the system reveals the familiar Mollow triplet [81]

$$S_{Mollow}(\omega) \approx \left[\frac{\gamma_{center}}{\frac{\gamma_{center}^2}{4} + (\omega - \omega_0)^2} + \frac{1}{2} \frac{\gamma_{side}}{\frac{\gamma_{side}^2}{4} + (\omega - \omega_0 - \Omega_r)^2} + \frac{1}{2} \frac{\gamma_{side}}{\frac{\gamma_{side}^2}{4} + (\omega - \omega_0 + \Omega_r)^2} \right], \quad (4.21)$$

with the following abbreviations for the Mollow sideband width γ_{side} and central linewidth γ_{center} :

$$\gamma_{center} = \gamma + \gamma' + \gamma_{ph}(\Omega_r) + \gamma_{cd}(\Omega_r) \quad (4.22)$$

$$\gamma_{side} = \frac{3}{2}(\gamma + \gamma_{ph}(\Omega_r)) + \frac{1}{2}\gamma' - \gamma_{cd}(\Omega_r) \quad (4.23)$$

It is perfectly obvious that the Mollow sidebands and the central line have a different linewidth. All three lines are broadened by γ_{ph} . The central line is additionally broadened by γ_{cd} , whereas the sidebands are squeezed due to the cross-dephasing rate. In the ideal case of a Fourier transform-limited system (only intrinsic radiative decay $\gamma \neq 0$ and $\gamma' = \gamma_{ph} = \gamma_{cd} = 0$) the sidebands have a width of $\gamma_{side}^{FTL} = \frac{3}{2}\gamma$, whereas the central linewidth is $\gamma_{center}^{FTL} = \gamma$ (given in angular frequencies), hence the coherence of the sidebands and the central line differs.

4.8 Detuning-dependent Mollow triplet: Regimes of sideband broadening and narrowing

The effect of Mollow triplet sideband narrowing dependent on the laser-excitation detuning from the bare emitter resonance was previously reported by Ulrich *et al.* on a QD embedded in a micropillar structure [64]. Nevertheless, in this publication the explanation of the phenomenon had to be left open for further in-depth theoretical analysis. Motivated by these findings, McCutcheon *et al.* [82] have shown theoretically that increased excitation-detuning from the excitonic resonance

can lead to an increased narrowing of the Mollow triplet sidebands (see Fig. 2 of their publication). In this section, which is based on the publication of Ref. [78], the change of the Mollow sideband width in terms of sideband broadening or narrowing will be discussed and the theoretical predictions will be compared to a detailed analysis of a detuning-dependent Mollow triplet series. The calculations are based on the polaron master equation approach introduced in chapter 4.7.

In order to distinguish the different regimes of sideband narrowing and broadening the ratio r , defined as

$$r = \frac{\gamma_{pol} + \gamma_{cd}}{\gamma_{pop}} = \frac{1}{2} \left[1 + \frac{\gamma' + 2\gamma_{cd}}{\gamma + \gamma_{ph}} \right] , \quad (4.24)$$

is introduced, with the following abbreviations for polarization and population decay

$$\gamma_{pol} = \frac{1}{2} (\Gamma_{ph}^{\sigma^+} + \Gamma_{ph}^{\sigma^-} + \gamma + \gamma') \quad (4.25)$$

$$\gamma_{pop} = \Gamma_{ph}^{\sigma^+} + \Gamma_{ph}^{\sigma^-} + \gamma \quad , \quad (4.26)$$

and

$$\gamma_{ph} = \Gamma_{ph}^{\sigma^+} + \Gamma_{ph}^{\sigma^-} \quad (4.27)$$

$$\gamma_{cd} \equiv \Gamma_{ph}^{cd} \quad . \quad (4.28)$$

As illustrated in Fig. 4.9, a systematic increase of the excitation-detuning Δ can either result in spectral sideband broadening or narrowing, depending upon the value of r , which is defined in a way that the cross-over between the two different regimes occurs at $r \approx 1$. For $r < 1$, spectral sideband narrowing is predicted theoretically, this is the case if $\gamma' + 2\gamma_{cd} < \gamma + \gamma_{ph}$. For typical experimental conditions γ_{cd} and γ_{ph} are much smaller than γ' and γ , therefore the approximate condition for sideband narrowing becomes $\gamma' < \gamma$, thus it can be observed for systems with small pure dephasing rate compared to the radiative decay rate. The opposite trend of sideband broadening occurs for $r > 1$ and therefore for systems with large pure dephasing fulfilling $\gamma' > \gamma$. Interestingly enough, the reverse trend is observed for the center resonance. When the sidebands broaden (narrow) the center line narrows (broadens) with increasing Δ . For strictly resonant

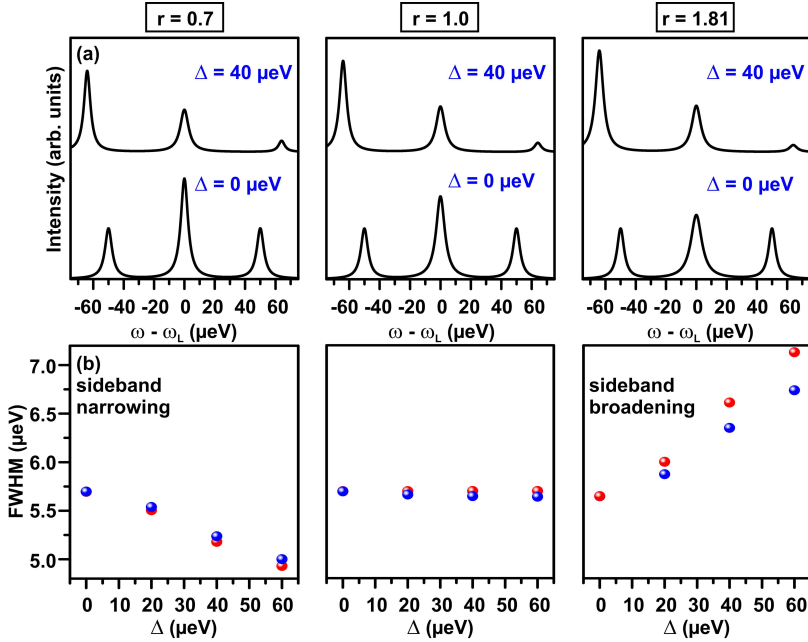


Figure 4.9: (a) Analytically computed spectrum as a function of detuning for three different values of r . Positive and negative detunings $|\Delta|$ simply reveal a mirror image of each other. For the calculation, the following parameters are used: $\Omega_r = 50 \mu\text{eV}$, $\gamma_{cd} \approx 0.6 \mu\text{eV}$ and $\gamma_{ph} \approx 1.6 \mu\text{eV}$. γ and γ' are adjusted to maintain the same on-resonance FWHM value of the sidebands of $5.6 \mu\text{eV}$. For $r = 0.7, 1.0, 1.81$, $\gamma'(\gamma)$ are $0.4(2.4), 2.2(1.8)$ and $5.1(0.8) \mu\text{eV}$, respectively. (b) Extracted FWHM of the lower (red dots) and higher (blue dots) energy sideband as a function of detuning Δ . The trend of either increasing or decreasing sideband linewidth as a function of increasing laser-detuning Δ , depending upon the value of r , can clearly be observed. r is defined in a way that $r \approx 1$ denotes the cross-over between sideband broadening and narrowing. In addition to the change of the sidebands' width the red and blue sidebands reveal different areas for $\Delta \neq 0$ for all values of r .

excitation $\Delta = 0$, the Mollow sidebands have equal width and area. In contrast, off-resonant driving $\Delta \neq 0$ leads to a Mollow triplet where the two sidebands have different areas. For $\Delta \neq 0$ the Mollow triplet is only symmetric for the hypothetical case where all phonon terms are neglected and $\gamma' = 0$ (i.e. no pure dephasing).

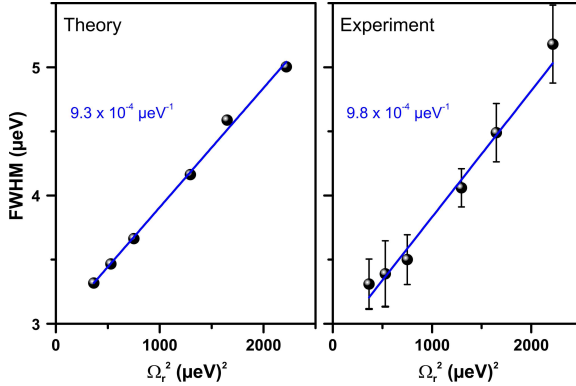


Figure 4.10: Determination of the pure dephasing rate γ' and electron-phonon coupling strength α_p . The graphs show the expected linear increase of the FWHM of the Mollow sidebands versus Ω_r^2 as extracted from a power-dependent Mollow series (not shown) under strictly resonant excitation ($\Delta = 0$) due to excitation-induced dephasing. A comparison between (a) the theoretical predictions (slope: $9.3 \times 10^{-4} (\mu\text{eV})^{-1}$) and (b) the experimental data (slope: $9.8 \times 10^{-4} (\mu\text{eV})^{-1}$) reveals best consistency for a dephasing rate of $\gamma' = 4.08\gamma = 3.43 \mu\text{eV}$ and $\alpha_p/(2\pi)^2 = 0.15 \pm 0.01 \text{ ps}^2$ ($T = 6.0 \pm 0.5 \text{ K}$, $\gamma = 0.84 \pm 0.04 \mu\text{eV}$ ($784 \pm 10 \text{ ps}$)). γ_{cd} and γ_{ph} scale with Ω_r^2 . Evaluated at $\Omega_r = 22.7 \mu\text{eV}$, they have the following values: $\gamma_{cd} = 0.13 \pm 0.01 \mu\text{eV}$ and $\gamma_{ph} = 0.34 \pm 0.02 \mu\text{eV}$.

In the following, an experimentally measured detuning-dependent Mollow triplet series for the conditions $r > 1$ will be compared to the theoretical descriptions. Before modelling the data, the characteristic values for the theoretical calculations were derived via independent experiments. The sample temperature was measured to be $T = 6.0 \pm 0.5 \text{ K}$. Due to the planar sample structure with no Purcell-like enhancement, all QDs have a similar decay rate γ , which is extracted from time-correlated photon counting measurements. Typical decay times are found to be $750 - 850 \text{ ps}$, yielding $\gamma \approx (0.77 - 0.88 \mu\text{eV})$. The renormalized Rabi frequency of $\Omega_r = 22.7 \mu\text{eV}$ is derived from the Mollow center-to-sideband splitting of a excitation power-dependent Mollow triplet series at $\Delta = 0$. The cut-off frequency proportional to the inverse dot size is set to $\omega_c = 1 \text{ meV}$. To carefully identify the pure dephasing rate γ' and the electron-phonon coupling strength α_p , the

spectra of a power-dependent Mollow triplet series of the QD at zero-laser-detuning $\Delta = 0$ were modelled with γ' and α_p as the only free parameters. The extracted FWHM of the Mollow sidebands in dependence on Ω_r^2 can be reproduced adequately with a pure dephasing rate of $\gamma' = 4.08\gamma = 3.43 \mu\text{eV}$, equivalent to a pure dephasing time of 192 ps and $\alpha_p/(2\pi)^2 = 0.15 \pm 0.01 \text{ ps}^2$. A direct comparison between the extracted FWHM of the experimental data and the theoretical model is shown in Fig. 4.10. The theoretically expected linear increase in the FWHM with Ω_r^2 due to EID (left panel) shows very good agreement with the experimentally extracted slope of the linear fit (right panel). The extracted value for the electron-phonon coupling constant α_p is higher than the values used in Ref. [80,83]. However, no accepted numbers exist in literature to date. α_p quantifies the strength of the exciton phonon-coupling linked to the dimensionless Huang-Rhys parameter via the relation $S_{HR} = \alpha_p/(2\pi)^2 c_l^2/l_{e/h}^2$ (c_l being the speed of sound and $l_{e/h}$ the electron/hole confinement length) [83]. For the experimental conditions above the calculated Huang-Rhys parameter is found to be $S_{HR} = 0.085$. Experimentally the Huang-Rhys factor is often derived directly from the ratio of phonon replica compared to the ZPL in photoluminescence measurements. For In(Ga)As/GaAs QDs the experimentally derived values cover a large range $S_{HR} = 0.01 - 0.5$ [84, 85]. As has been shown, S_{HR} varies from sample to sample and is dependent on the size, shape, and possible inhomogeneity of the strain distribution in the QD and therefore the excitonic wave function of the confined carriers. In addition, S_{HR} is known to be enhanced in zero-dimension QDs compared to bulk material [86]. Here the usually employed adiabatic approximation, assuming that the confinement energies exceed characteristic phonon energies so that phonon coupling between different electronic states can be neglected, might not be valid anymore. Non-adiabatic effects and defects surrounding the QD have to be considered for the calculation of a phonon-coupling strength that is in agreement with experimental results.

According to the calculations in Ref. [78], the phonon scattering rates $\gamma_{ph} = 0.34 \mu\text{eV}$ and cross-dephasing $\gamma_{cd} = 0.13 \mu\text{eV}$ can be derived and are found to be constant in the detuning range accessible in the experiments.

With all parameters at hand, the experimentally measured detuning-dependent Mollow triplet series is compared with the theoretical expectations in terms of sideband broadening and the change in the relative sideband areas $A_{F/T} = I_{F/T}/(I_F + I_T)$, with I denoting the integrated

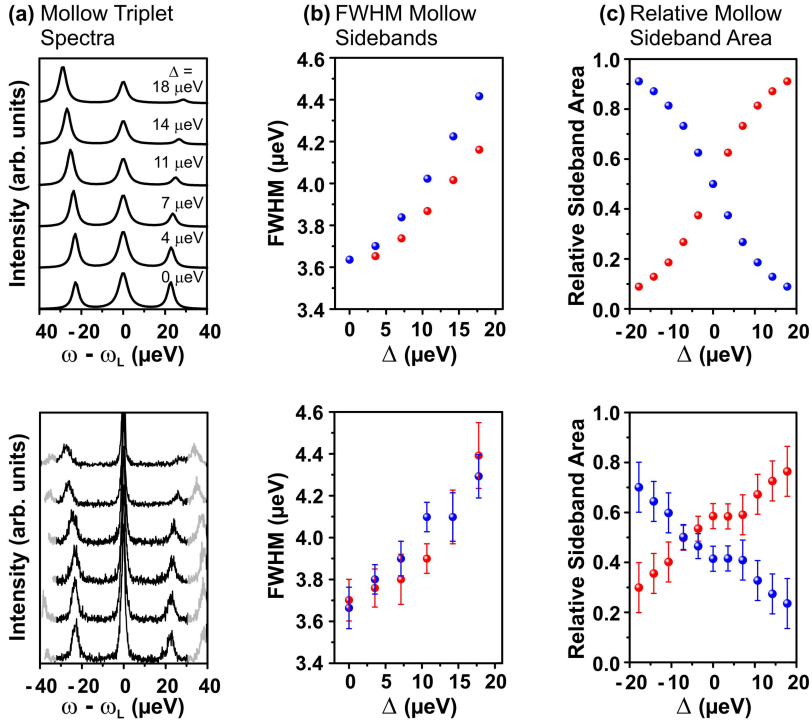


Figure 4.11: Detuning-dependent Mollow triplet series at $P = 500 \mu\text{eV}$, showing theoretical predictions (upper panel) versus experimental results (lower panel) for a system with $r = 2.01$. (a) Mollow triplet spectra for increasing detunings, Δ , the spectra are plotted with respect to the energetic laser position set to zero. (b) FWHM of the blue and red Mollow sideband reveal distinct sideband broadening with increasing laser-detuning. (c) Change of the relative Mollow sideband area with Δ . In all three cases the theoretically expected trend is in accordance with experimental findings.

peak areas of the F and T sideband, respectively. Figure 4.11(a) shows a direct comparison of the Mollow triplet spectra for increasing detuning $\Delta > 0$, from which the FWHM and relative intensities are extracted. The discrepancy between the expected and measured central Mollow line intensity results from the fact that the theoretical calculations include only the incoherent part of the resonance fluorescence, whereas

in the experiment the central R-line has additional contributions of the coherent emission part and scattered laser stray-light that cannot be experimentally separated. It is therefore only possible to compare the theoretical expectation for the Mollow sidebands with the experiments, but not the central Rayleigh peak. As calculated via the different dephasing rates, the system under investigation reveals $r = 2.01$ and therefore an increase in the sidebands' width is expected according to the theoretical model. As a matter of fact, Fig. 4.11(b) reveals a systematic increase with increasing detuning Δ . In addition, the relative sideband areas $A_{F/T}$ dependent on Δ are plotted in Fig. 4.11(c). As becomes visible from the Mollow spectra for positive detunings, the red sideband gains in intensity whereas the blue sideband area decreases and vice versa. The crossing between relative intensities is expected to occur at $\Delta = 0$. Interestingly enough, the detailed analysis of all detuning-dependent Mollow triplet series performed on different QD revealed a crossing at moderate negative laser-detuning values. A detailed interpretation of the physics behind this effect has to be left open to further in-depth analysis.

Due to the high value of pure dephasing γ' in the MOVPE grown sample, which causes $r > 1$, the effect of spectral sideband narrowing could not be observed experimentally on QDs in the planar sample structure. Nevertheless, the regime of distinct sideband narrowing has been accessed experimentally by Ulrich *et al.* [64] (see Fig. 3(d) of the publication) on a QD embedded in a micropillar cavity structure. Due to the small pure dephasing in the sample grown by molecular beam epitaxy, the regime of $r < 1$ can be reached. A direct comparison of the results with the theoretical model requires the inclusion of QED-cavity coupling into the polaron master equation approach. It is worth mentioning that previous numerical studies by Prof. Stephen Hughes [81] were performed in this regime. The experimentally observed very strong narrowing with increasing laser-detuning could not be obtained quantitatively, suggesting that further work is required to explain the significant narrowing effects that can be observed in the experiment.

4.9 Mollow quintuplets

As described in chapter 2.1.3 the excitonic QD state is subject to electron-hole spin exchange interaction. For QDs with anisotropic con-

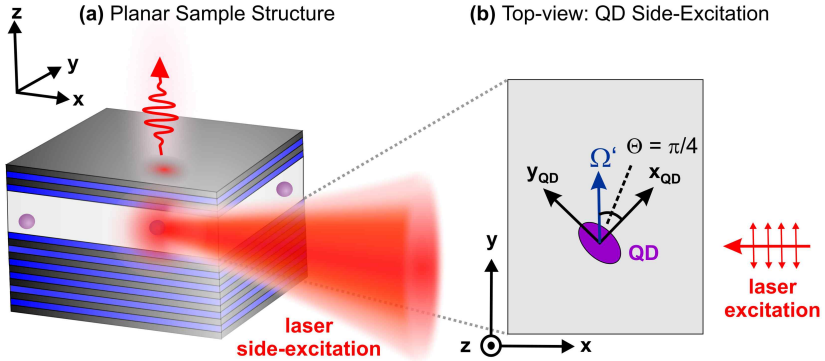


Figure 4.12: Schematic depiction of a QD embedded in a weakly coupled planar cavity under cw laser-excitation with a field vector that is linearly polarized within the $x - y$ plane and tilted by an angle Θ (e.g. $\Theta = (\pi/4)$) relative to x_{QD} . Both fine-structure components with their electric dipole oriented along x_{QD} and y_{QD} (internal coordinate system of the QD, as indicated in the graph) can be excited simultaneously with the laser. The linear laser polarization is indicated by double arrows.

finement (symmetry lower than D_{2D}) the corresponding emission reveals a so-called fine-structure splitting, typically in the range of $\sim 10 \mu\text{eV}$ [63]. Depending on the QD orientation and therefore the orientation of the dipole moments of the two fine-structure components with respect to the excitation laser, it is possible to resonantly excite both components at the same time. The two different exciton configurations for the electron-hole pair can be considered as two individual excitons. Therefore both should display the typical Mollow triplet in the spectral domain under resonant excitation above saturation. Hence, intuitively the combined spectrum should theoretically reveal a six-peak structure, the combination of two Mollow triplets, one for each exciton. For the investigations of the Mollow quintuplets from coherently excited QDs [79], the theoretical expectations based on the polaron master equation approach (see chapter 4.7) will be presented first. Then the theoretically expected behavior will be compared to experimentally derived Mollow triplet HRPL spectra.

To better illustrate the system, Fig. 4.12 shows a schematic of the excitation geometry and a QD with random orientation with respect to the sample edge. The theoretical calculations are again based on a polaron master equation approach as described in chapter 4.7. The Hamiltonian is modified to account for the two fine-structure components of the exciton; they are treated as two independent excitons coupled to a common phonon bath. Neglecting any QD zero-phonon line decay mechanism and working in the rotating frame with respect to the pump laser frequency ω_L , the Hamiltonian reads

$$H = - \sum_j \hbar \Delta_j \sigma_j^+ \sigma_j^- + \sum_j (\hbar \Omega_j^0 / 2) (\sigma_j^+ + \sigma_j^-) \quad (4.29)$$

$$+ \sum_{j, \mathbf{q}} \hbar \lambda_{j, \mathbf{q}} \sigma_j^+ \sigma_j^- (b_{\mathbf{q}}^\dagger + b_{\mathbf{q}}) + \sum_{\mathbf{q}} \hbar \omega_{\mathbf{q}} b_{\mathbf{q}}^\dagger b_{\mathbf{q}} \quad . \quad (4.30)$$

In accordance with chapter 4.7, the following notations are used: $\Delta_j \equiv \omega_L - \omega_{xj}$ are the laser exciton detunings (where the index $j = 1, 2$ indicates the correspondence to the two different excitons), σ_j^+ , σ_j^- are the Pauli operators of the j th exciton, $\lambda_{j, \mathbf{q}}$ are the exciton-phonon coupling strength, and Ω_j^0 are the effective Rabi frequencies.

In the most general case, the two exciton fine-structure components will have different dipole moments, leading to different maximum renormalized effective Rabi frequencies $\Omega_j = \langle B \rangle \Omega_j^0$. According to the illustration in Fig. 4.12(b), the pump polarization angle Θ with respect to the dipole orientation needs to be considered. Therefore the two renormalized effective Rabi frequencies are $\Omega'_1 = \Omega_1 \cos(\Theta)$ and $\Omega'_2 = \Omega_2 \sin(\Theta)$. For the theoretical calculations illustrated in Fig. 4.13, equal Rabi frequencies were assumed for the sake of clarity $\Omega_{1,2} = \langle B \rangle \Omega_{1,2}^0 \equiv \Omega'$, though in general these will differ. The red traces in Fig. 4.13 show the theoretically calculated emission spectra without exciton-phonon coupling, whereas the blue traces show the results with phonon scattering. As directly reflected from the Rabi center-to-sideband splitting in all the spectra, the interaction with phonons leads to a renormalization of the Rabi frequency in terms of a reduction due to $\langle B \rangle < 1$. The different peak width and areas are due to the slightly detuned excitation with respect to the exciton resonance. These characteristic features are explained in detail in chapter 4.8. The main parameters for the calculations are given in the figure caption. The left panel of Fig. 4.13 shows the theoretical expectations for the incoherent part of the resonance fluorescence emission for a fixed Rabi frequency and

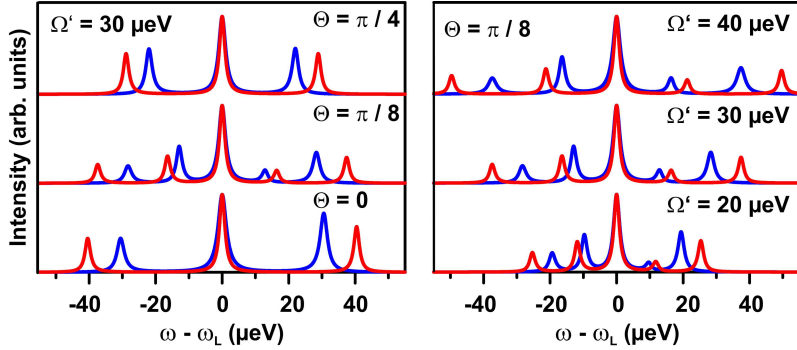


Figure 4.13: Theoretical calculations of the incoherent resonance fluorescence spectrum. The red trace shows the spectrum without phonon scattering whereas the blue trace depicts the spectrum with exciton-phonon interaction. The maximum Rabi frequencies Ω' are assumed to be equal for both excitons, and therefore $\Omega'_1 = \Omega' \cos(\Theta)$ and $\Omega'_2 = \Omega' \sin(\Theta)$. As is clearly visible, phonon scattering leads to a renormalization and therefore a reduction of the Rabi frequency. Left panel: Spectra for three different excitation angles Θ for fixed $\Omega' = 30 \mu\text{eV}$. Right panel: Ω' is increased (from bottom to top) under the assumption of a fixed $\Theta = \pi/8$, leading to an increasing Mollow center-to-sideband splitting. For the calculation the following parameters are used: A phonon bath temperature of $T = 6 \text{ K}$, a radiative and pure dephasing decay rate of $\gamma_{1,2} = \gamma'_{1,2} = 1 \mu\text{eV}$, a fine-structure splitting of $\Delta_{FSS} = -12 \mu\text{eV}$ with the two detunings $\Delta_1 = -\Delta_2 = -6 \mu\text{eV}$ from the bare resonance of the two excitons. In addition, standard parameters for $\text{In}(\text{Ga})\text{As}/\text{GaAs}$ QDs are employed (see Appendix A). $\alpha_{1,2}$ is a scaling parameter that adjusts the strength of the excitonic emission through cavity decay. It is proportional to the exciton dipole moments and may differ depending upon the amount of asymmetry in the QD, here $\alpha_{1,2} = 1$.

different angles between laser-excitation and dipole orientation Θ . For $\Theta = 0$, only one exciton component (x_{QD}) is excited and the spectrum shows the expected Mollow triplet for a resonantly excited QD under strong excitation conditions. As Θ increases, the other orthogonal exciton component (y_{QD}) is gradually excited, as can be clearly seen at $\Theta = \pi/8$, where the Mollow triplet evolves into a Mollow quintuplet. At $\Theta = \pi/4$, the quintuplet merges into a triplet again if the two excitons share symmetric parameters. In this case the effective renormalized Rabi frequencies are equal $\Omega'_{1,2} = \Omega' \cos(\pi/4) = \Omega' \sin(\pi/4)$ and both

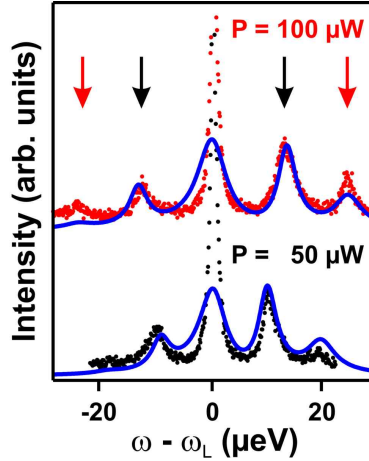


Figure 4.14: Experimental data for a resonantly excited In(Ga)As/GaAs QD and the corresponding theoretical simulations for a phonon bath temperature of $T = 6$ K. Black lower and red upper trace: Experimental HRPL spectra for pump powers of $50 \mu\text{W}$ and $100 \mu\text{W}$, respectively. Blue: Theoretical fits to the data using the following parameters: $\gamma_1 = 0.55 \mu\text{eV}$ ($\hat{=} 1197$ ps), $\gamma_2 = 0.85 \mu\text{eV}$ ($\hat{=} 774$ ps), $\gamma'_1 = 5.93 \mu\text{eV}$ ($\hat{=} 111$ ps), $\gamma'_2 = 7.13 \mu\text{eV}$ ($\hat{=} 92$ ps), $\Delta_{FSS} = 10 \mu\text{eV}$, $\alpha_1 = 1$ and $\alpha_2 = 0.4$. The Rabi frequencies are $\Omega'_1 = 13.66/\sqrt{2} \mu\text{eV}$, $\Omega'_2 = 21.96/\sqrt{2} \mu\text{eV}$ (black lower trace) and $\Omega_1 = 13.66 \mu\text{eV}$, $\Omega_2 = 21.96 \mu\text{eV}$ (red upper trace).

individual Mollow triplets coincide. In the right panel of Fig. 4.13 the spectra at $\Theta = \pi/8$ for various Rabi fields are depicted. As expected, the Rabi center-to-sideband splitting increases with increasing pump strength (bottom to top). Theoretically, one might expect six peaks for the incoherent spectrum in the general case. However, both central Rayleigh peaks are situated at the laser pump frequency and therefore merge to one peak, so there are actually five peaks resolvable.

Figure 4.14 shows the experimental results (black lower and red upper trace) in combination with the theoretical simulations (blue traces). Due to the fact that the experimental central peak includes both coherent and incoherent contributions from the resonance fluorescence signal and additional parasitic laser stray-light, the theoretical expectations can only be compared for the Mollow sidebands, but not with the central Rayleigh line. The black data points belong to an excitation

strength of $P = 50 \mu\text{W}$ whereas the red points correspond to twice the excitation power $P = 100 \mu\text{W}$. The black inner arrows and red outer arrows indicate the inner and outer sidebands of the quintuplet. It should be mentioned that no additional characterization measurements exist for the QD on which the HRPL data has been taken. Therefore the values necessary to model the data are set to reasonable values in accordance with Refs. [78,80,87], where the investigations were performed on QDs of the same planar sample structure. The aim of the comparison between experiment and theory is therefore to prove the validity of the theoretical model and the observation of the effect of Mollow quintuplet emission in a qualitative manner. For the reasonable parameters given in the figure caption, the experimental results obtain very good agreement with the theoretical expectations. It is worth mentioning that the spectral features of Mollow quintuplets were observed on many In(Ga)As/GaAs QDs in the planar sample under investigation.

In the theoretical model the two fine-structure components of the exciton are treated as two independent excitons. The comparison of the experimentally derived Mollow quintuplet emission spectra with the theoretical investigations has been found to be in very good agreement, thus validating the theoretical approach. Nevertheless it is worth having a closer look at the outcome of the cross-correlation of for example the two higher energetic Mollow quintuplet sidebands originating from the two different fine-structure components of the resonantly excited exciton. For the auto-correlation of the Mollow triplet sidebands single-photon emission with $g^{(2)}(0) = 0$ is expected, as discussed in chapter 5.1. For the cross-correlation between two independent antibunched emission lines the auto-correlation should display $g^{(2)}(0) = 0.5$. In fact, the two fine-structure components are not independent. Resonant excitation of a QD leads to the creation of exclusively one electron-hole pair corresponding to one fine-structure component. The creation of a second electron-hole pair would lead to the formation of a biexciton and not to the population of the second fine-structure component. Thus both exciton fine-structure components cannot be excited simultaneously. Due to this reason the cross-correlation among the Mollow sidebands of different exciton spin configurations should display antibunching in terms of $g^{(2)}(0) = 0$.

Chapter 5

Indistinguishable photons from the Mollow sidebands

The experimental verification of two-photon indistinguishability is based on a simple beam splitter experiment, as depicted in Fig. 5.1. Classically, two photons entering a beam splitter from opposite sides have four different possibilities to exit the BS, either through different ports or through the same output port. Figure 5.1 left panel shows the the joint probability of photon-detection at the two outputs. Ideally, $g^{(2)}(0)$ can be as low as 0.5. If the two photons that enter the BS are indistinguishable, meaning they have identical wave packets, the simultaneous coincidence detections will be zero, under the prerequisite of perfect photon wave packet overlap at the BS. The coalescence of photons at the same output port reflects the bosonic nature of photons. The described above experiment is termed *Hong-Ou-Mandel* (HOM) experiment after Hong Ou and Mandel, who were the first to report on two-photon interference from photons created by parametric down conversion in a seminal work in 1987 [88].

It is worth mentioning that the outcome of the HOM experiment is exactly contrary for the interference of indistinguishable fermions instead of bosons. In this case both fermions repel one another and exit the BS through different output ports. Bocquillon *et al.* [89] have recently verified this behavior for indistinguishable single electrons created by independent synchronized sources.

The pioneering indistinguishability measurements of consecutively emit-

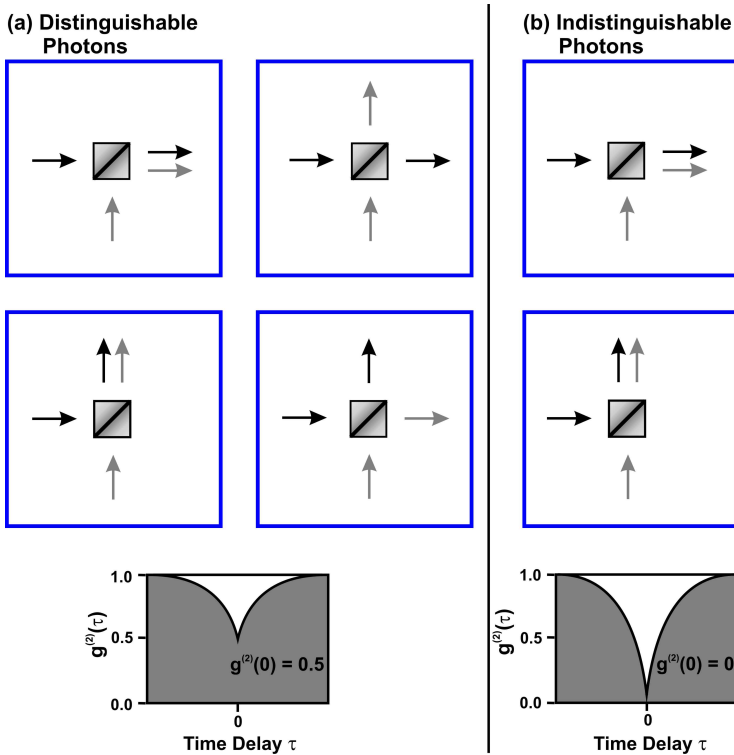


Figure 5.1: Schematic depiction of the different possibilities of two photons that enter a BS simultaneously from opposite sides. (a) Distinguishable photons have four different possibilities to exit the BS either through the same or via different output ports. A typical photon-correlation measurement of such a two-photon interference experiment under cw excitation is depicted at the bottom of panel (a), with the characteristic zero-delay dip of $g^{(2)}(0) = 0.5$. (b) The interference of indistinguishable photons with perfect spatial overlap at the BS causes them to always exit through the same output port. Here the two-photon coalescence at zero delay cancels completely, reflected by $g^{(2)}(0) = 0$.

ted photons from a QD have been reported by Santori *et al.* [90]. In this study the QDs were quasi-resonantly excited with a pulsed laser, revealing a visibility contrast up to 81%. Shortly after, many other groups published their results of the investigations on indistinguishable

photons from QDs [91]. A particular focus of the studies has been placed on the indistinguishability of electrically excited QDs [92–94], site-controlled grown QDs [95] and the specific influence of the *Purcell* effect of a surrounding photonic crystal [96] or micropillar cavity [97–99] on the indistinguishability of consecutively emitted photons. These experiments have all been performed under non-resonant emitter state preparation, where the degree of indistinguishability has so far been limited to 82% [98]. In the non-resonant excitation scheme the carriers have to relax via phonon-mediation to the QD ground state before radiative recombination can take place, thus inducing additional dephasing and a timing jitter that limits the two-photon visibility. In order to circumvent these indistinguishability-limiting processes, a direct creation of electron-hole pairs in the QD s-shell has a beneficial influence. As a matter of fact, three publications have reported high two-photon interference visibilities $\geq 90\%$ for the indistinguishability of photons under resonant QD excitation. In the Heitler regime (excitation below emitter saturation), Matthiesen *et al.* [100] have demonstrated two-photon indistinguishability under pulsed excitation with a visibility that reaches 100% within the experimental uncertainty. This regime offers the distinct advantage of phase coherence of the QD emission with the excitation laser, which might allow to build a network of multiple QDs all phase-locked to one master laser. One major drawback is the limited generation efficiency ($\sim 5 - 10\%$) under excitation below saturation. In a different study, Ates *et al.* [55] have verified indistinguishable photons with a post-selected visibility of 90% under resonant cw excitation at 80% saturation of a QD in a micropillar cavity. Recently, He *et al.* [101] have measured triggered two-photon interference with a visibility contrast of 97% at saturation, employing π pulses that invert the TLS system.

From an application point of view, the generation of indistinguishable photons from remote QDs is appreciable. The emission wavelength of self-assembled grown QDs is in general not degenerate and depends on the effective potential of the carrier confinement, thus on the QD size, material composition and strain. Therefore, the major challenge for the creation of indistinguishable photons from different QDs is to tune the QD s-shell emission of two separate QDs into resonance exactly. Up to the present day, two groups have verified two-photon interference from remote QDs. Flagg *et al.* [102] employed strain tuning, to controllably

tune the emission of one QD into resonance with a spatially separated other dot. The *Hong-Ou-Mandel* type two-photon interference experiment under pulsed emitter state preparation reveals a visibility of 18% (47 % post-selected). It is worth noting that the limited indistinguishability is claimed to be mainly due to dephasing in the system and not to the different wave packets of the two-photons because of the different coherence and lifetimes. In another study, Patel *et al.* [103] have shown indistinguishability of separate QDs under electrical excitation of one and cw optical excitation of the other QD. To tune the individual s-shells into resonance they applied an electric field. The raw measurement data reveals 33% visibility.

Besides the generation of indistinguishable photons from remote QDs, the verification of two-photon indistinguishability of the photons of a QD with photons generated by different physical processes has been studied. Bennett *et al.* [104] interfered photons from the spontaneous QD emission with the stimulated photon emission from a tunable laser. Polyakov *et al.* [105] measured two-photon interference of photons from a QD with photons from parametric down conversion (PDC). Whereas the coherence of the photon emission from the QD is limited due to the interaction of the exciton with the solid-state surrounding medium, PDC offers the advantage of a decoherence-free process. For the pulsed experiment, the photons from the spectrally broad PDC process are pre-filtered via a *Fabry-Pérot* interferometer. The degree of indistinguishability is found to be 16%, limited by the coherence of the QD. For typical In(Ga)As/GaAs QDs the s-shell emission is usually around ~ 900 nm, but frequency conversion can be employed to up or down-convert the original QD emission wavelength. Ates *et al.* [106] have shown that frequency conversion with a high signal-to-background ratio does not lead to a degradation in purity of the photon wave packet in terms of single-photon emission and two-photon interference.

Solid-state single-photon emitters offer the distinct advantage of easier integrability when compared to e.g. atoms. Besides QDs, there are of course other solid-state single-photon emitter systems able to emit highly indistinguishable photons. Several out of the many publications of current research shall be mentioned in the following. For example the two-photon interference of the emission of single [107] and remote [108] molecules under cw excitation were tested successfully. The latter investigation also reveals quantum beats for energetic detuning between

the two emitter emission energies as already observed for atoms by Legero *et al.* [109]. Sanaka *et al.* [110] verified quantum interference of photons generated by the radiative decay of excitons that are bound to spatially separate isolated fluorine donor impurities.

In this chapter a comprehensive study of the emission of indistinguishable photons from the Mollow triplet sidebands is presented. As already mentioned above, resonant excitation has a beneficial influence to achieve high two-photon interference visibilities. To date the reported verification of indistinguishability on the QDs' emission under resonant excitation has been limited to excitation powers at or below saturation. The regime above saturation has not been accessed experimentally via *Hong-Ou-Mandel* type two-photon interference experiments so far. Since background-free single-photon emission is a crucial requirement for the experimental verification of photon indistinguishability the expected photon statistics for the different Mollow triplet components will be presented first in the following.

5.1 Mollow triplet photon statistics

In a pioneering work of 1980, Aspect *et al.* [61] provided the first experimental demonstration of photon correlation bunching between the Mollow triplet sidebands on a strontium atomic beam. Shortly after the expected photon correlations on and among the individual Mollow triplet components were described theoretically by Dalibard *et al.* [111]. A comprehensive presentation of the intensity correlations between the components of the resonance fluorescence triplet in a dressed TLS picture together with supporting experiments on natural barium was published by Schrama *et al.* [60]. This work was based on an earlier publication by Arnoldus *et al.* [112] and complemented by Refs. [113, 114]. In this section, the brief presentation about photon correlations will be restricted to the auto-correlations on the individual Mollow triplet components. The nomenclature is in accordance with Ref. [60] and the dressed state representation in chapter 4.2.

In the experiment the Mollow triplet components are individually selected with a filter having a spectral bandwidth that is larger than the Mollow triplet emission channels, to assure no deformation of the selected lines. In addition the filter is much smaller than the Rabi fre-

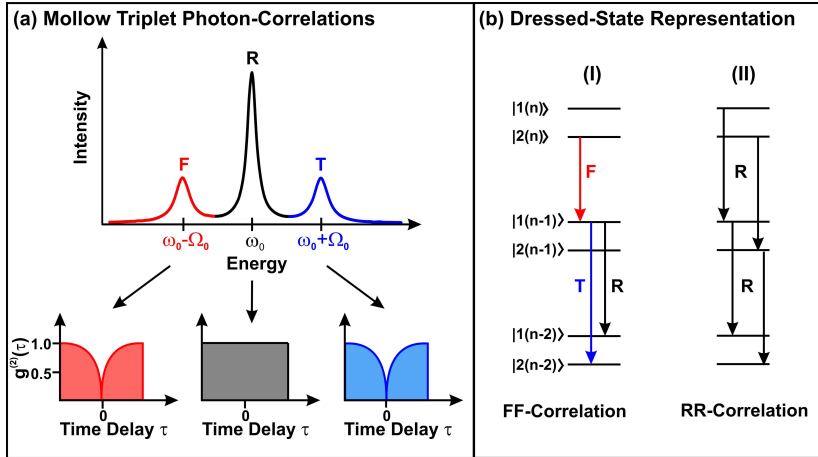


Figure 5.2: (a) Illustration of the photon correlations on the individual Mollow triplet components. For the auto-correlations $g_{FF/TT}^{(2)}(\tau)$ on the F and T sideband, perfect anti-bunching is expected, whereas the photon statistics on the central Rayleigh lines displays Poissonian statistics $g_{RR}^{(2)}(\tau) = 1$. (b) Dressed state representation to illustrate the expected results for the auto-correlations depicted in (a). (I) $g_{FF}^{(2)}(\tau)$: After the emission of an F photon the system ends up in dressed state $|2\rangle$. Therefore it can emit either a T or an R photon, but never a subsequent F photon. This leads to anti-bunching in the second-order photon correlation of the Mollow triplet sideband. A similar scenario applies to the explanation of the anti-bunching of the blue Mollow sideband. (II) $g_{RR}^{(2)}(\tau)$: Rayleigh photon emission can start either from state $|1\rangle$ or state $|2\rangle$, respectively. After the emission of an R photon the system ends up in the same state of the adjacent manifold therefore the population of the system is not changed, which results in Poissonian statistics for the central Rayleigh line.

quency, to grant that only one single Mollow component is selected. Figure 5.2(a) illustrates the theoretically expected outcome of auto-correlation measurements on the individual Mollow triplet components. For the second-order photon correlation on the F or T sideband, anti-bunching is theoretically predicted, according to

$$g_{TT}^{(2)}(\tau) = g_{FF}^{(2)}(\tau) = 1 - e^{-\gamma(c^4 + s^4)\tau} \quad , \quad (5.1)$$

where γ denotes the spontaneous decay rate of the TLS. Thus the anti-

bunching timescale under resonant excitation is given by the modified emission rate $\gamma_{mod} = \gamma(c^4 + s^4)$.

The anti-bunching behavior can be explained by the aid of the dressed state picture illustrated in Fig. 5.2(bI). Considering the auto-correlation on the F sideband, after the first emission of an F photon the system ends up in dressed state $|2\rangle$ and therefore has no population from which a second F photon emission is possible. As is indicated schematically the F photon will be followed by a possible emission of a T or R photon. Therefore there will never be two subsequent F photons, resulting in the theoretically expected anti-bunching behavior. An analogue explanation is valid for the T Mollow sideband (not shown). The first experimental evidence of single-photon emission from the Mollow triplet sidebands of a resonantly excited QD was presented by Ulhaq *et al.* [57].

In contrast to the sidebands, the correlation function of the central Rayleigh line is found to be independent of time, revealing

$$g_{RR}^{(2)}(\tau) = 1 \quad . \quad (5.2)$$

The Poissonian statistics reflects, that the emission of a Rayleigh photon does not modify the density matrix in terms of $|1\rangle$ and $|2\rangle$ and that the emission rate of Rayleigh photons is independent of the dressed state populations. Figure 5.2(bII) illustrates that if the dressed state initially is in state $|1(n+1)\rangle$ for example, it ends up in state $|1(n)\rangle$ of the neighboring manifold, which means that the electronic configuration is not changed and a subsequent emission of another R photon is possible.

5.2 Experimental techniques

For the indistinguishability measurements on the Mollow triplet sidebands sophisticated experimental techniques are employed besides the commonly used experimental methods, which are described in chapter 3. For the verification of indistinguishable photons a *Hong-Ou-Mandel* setup is required, which will be introduced in the next section. In addition a double Michelson setup will be presented in chapter 5.2.2, which was used to spectrally pre-filter the individual Mollow triplet components.

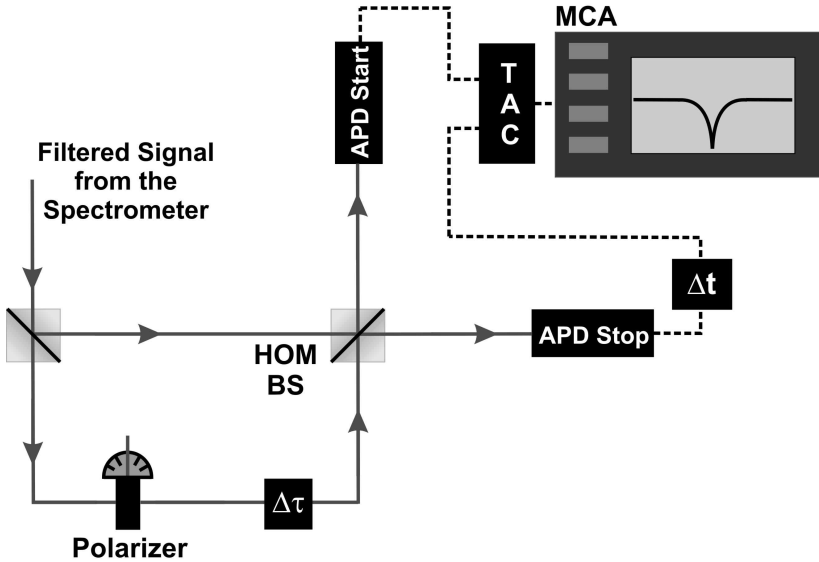


Figure 5.3: Schematic depiction of the fiber-based *Hong-Ou-Mandel* setup employed for two-photon interference measurements. Spectrally pre-filtered light is divided by a non-polarizing 50 : 50 beam splitter and sent to an unbalanced *Mach-Zehnder* interferometer, imposing a fixed delay of $\Delta\tau$ between the two arms. The photons are then interfered at a second beam splitter (*HOM-BS*), where the *Hong-Ou-Mandel* type two-photon interference measurement takes place. To set the polarization of the interfering photons mutually parallel or perpendicular, a polarizer is incorporated in one interferometer arm. For the coincidence detection two APDs are employed with subsequent histogramming via TAC and MCA.

5.2.1 *Hong-Ou-Mandel*-setup for two-photon interference measurements

The aim of this section is to introduce the *Hong-Ou-Mandel* setup for the indistinguishability measurements. The crucial requirement is to experimentally assure, that photons enter the *Hong-Ou-Mandel* beam splitter simultaneously from opposite sides.

The heart of the fiber-based *Hong-Ou-Mandel* (*HOM*) setup illustrated in Fig. 5.3 is an asymmetric *Mach-Zehnder* interferometer. The spec-

trally pre-filtered photons are coupled into a single-mode polarization-maintaining fiber and split by a non-polarizing 50 : 50 beam splitter. The two fiber-arms between the beam splitters have different length imposing a fixed photon runtime delay of $\Delta\tau = 13$ ns. This delay is chosen much greater than the coherence length of the individual photons, ensuring that only fourth-order interference effects occur at the second beam splitter, where the *Hong-Ou-Mandel* type two-photon indistinguishability experiment takes place. The bosonic photon-interference is crucially dependent on the spatial overlap of the two photon streams entering the second beam splitter from opposite directions. This overlap has been independently derived to be $V = 0.98 \pm 0.02$. Further setup characterizations have revealed $T = R = 0.5 \pm 0.02$ for the transmission T and reflection R of the two beam splitters.

For the studies of the indistinguishability of photons under continuous wave excitation, the *Hong-Ou-Mandel* experiment has to be performed for mutually perpendicular and parallel polarized photons, to extract the interference contrast V_{HOM} from the experimental data according to Eq. 5.12. Therefore a polarizer ($\lambda/2$ wave-retarder plate) is integrated into the long optical fiber arm to set the photon polarization mutually parallel or perpendicular, thus making them indistinguishable or distinguishable, respectively. The coincidence detection via APDs and further analysis is carried out similarly as described in chapter 3.2 via TAC and MCA.

5.2.2 Double Michelson interferometer filtering technique

The auto-correlation and especially the two-photon interference measurements presented in this chapter crucially rely on the spectral purity of the signal. In addition, a high enough countrate > 2000 cts/s is required to achieve any reasonable photon statistics measurement. Due to the small energetic separation of the Mollow triplet components (typically in the range of $20 - 60 \mu\text{eV}$), the conventional method of spectral filtering with the 750 mm focal length spectrometer is not suitable for filtering just one Mollow triplet component. For the experimental conditions, the 1200 lines/mm grating had to be employed to achieve a high enough correlation countrate on the Mollow sidebands, offering a resolution of $\Delta E \sim 55 \mu\text{eV}$. Under these conditions, it is not possible to separate one Mollow line from the other two with the spectrometer. It is worth mentioning that it was not possible to use the 1800 lines/mm

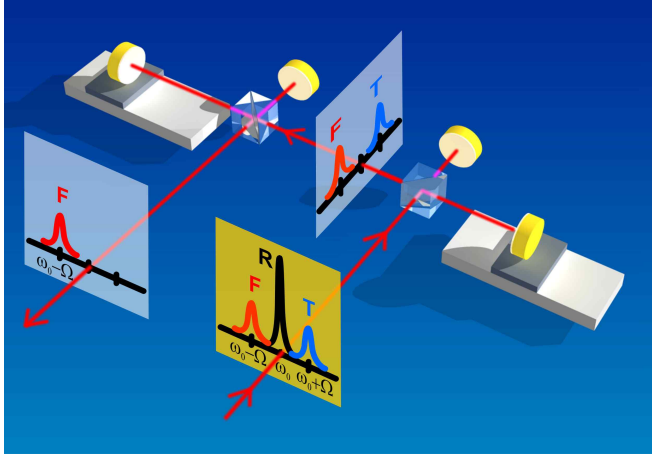


Figure 5.4: Schematic depiction of the double Michelson interferometer used to selectively filter one individual Mollow triplet component from the other two. The input signal consists of the full Mollow triplet. The delay between the arms of the first interferometer is set to a position according to Eq. 5.6, where the central Mollow triplet line interferes destructively, whereas the two sidebands exit the interferometer via constructive interference. The two sidebands are sent to a second Michelson interferometer. Here one sideband is suppressed via destructive interference, whereas the other one interferes constructively at the output of the Michelson interferometer.

grating with a better resolution, because of the low countrate, verified in test measurements. The same is true for the scanning *Fabry-Pérot* interferometer, where the resolution is $\Delta E \approx 0.6 \mu\text{eV}$, but the signal is impaired by very low transmission efficiency.

For the correlations on the Mollow triplet sidebands a specially designed double Michelson interferometer is therefore adapted in the setup as a pre-filtering technique introduced by Aichele *et al.* [115]. Via this method the exciton and biexciton emissions from a single QD were previously separated [115]. In another recent study [57] the Mollow triplet sidebands were spectrally filtered from the central Rayleigh line via the same method.

The idea of the filtering technique in principle is based on selective constructive interference of one Mollow triplet component at the output

port of the double Michelson interferometer (depicted in Fig. 5.4) in combination with destructive interference of the other two Mollow lines via a two-step filtering process.

The output probability of the Michelson interferometer for photons with wavelength λ is a sinusoidal function oscillating between 1 and 0 [115]

$$I_{1,2} = 0.5 \pm 0.5 \cos(2\pi\Delta s/\lambda) \quad , \quad (5.3)$$

where Δs denotes the path length difference between the two interferometer arms. The minimum path difference S at which two spectral components with wavelength separation $\Delta\lambda$ show opposite phases in their interference pattern can easily be calculated according to Ref. [115]. The path delay for destructive interference for a wavelength λ reads

$$S = (n + \frac{1}{2})\lambda \quad n = 0, 1, 2, 3 \dots \quad , \quad (5.4)$$

and for the same delay the wavelength $\lambda + \Delta\lambda$ needs to interfere constructively according to

$$S = n(\lambda + \Delta\lambda) \quad n = 0, 1, 2, 3 \dots \quad . \quad (5.5)$$

The path difference S that fulfills both conditions simultaneously found by inserting Eq. 5.5 in Eq. 5.4 is

$$S = \pm \frac{1}{2} \frac{\lambda(\lambda + \Delta\lambda)}{\Delta\lambda} \quad . \quad (5.6)$$

For the experiment one has to consider that the light passes the interferometer arm twice, therefore the delay has to be set to $S/2$. The output probability for the three Mollow triplet components is depicted in Fig. 5.5(a) and (b). In the first filtering step the Rayleigh line interferes destructively at S whereas the Mollow sidebands both interfere constructively. As obvious from the graph, the same situation is valid for the neighboring interference cycles. In the second filtering step the output from the first Michelson at S is sent to a second Michelson interferometer. The filtering procedure is similar. A precondition of the applicability of this method is that the path difference between the two interferometer arms S is well below the coherence length l_{coh} of the photons, which is readily fulfilled for the experimental conditions of the correlation measurements. The minimum coherence length is

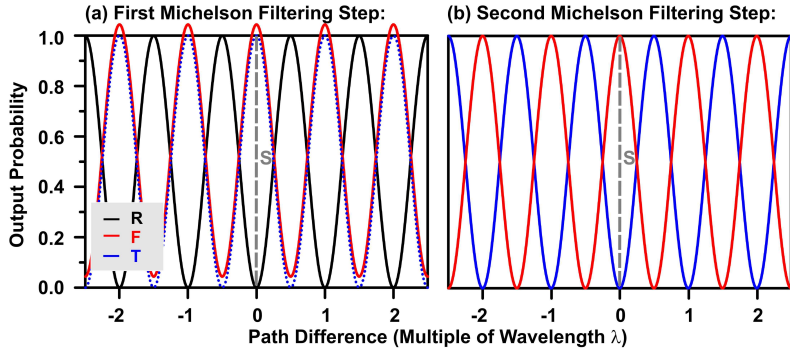


Figure 5.5: Basic concept of the double Michelson filtering technique. (a) First Michelson interferometer: Output probability of the different Mollow triplet components through one interferometer arm versus path difference with respect to S (calculated according to Eq. 5.6). S represents the delay position for which the R photons interfere destructively, whereas both the sidebands pass the interferometer via constructive interference. Indicated in black, red (vertically shifted for clarity), blue: central R line, F and T Mollow sideband output probability. (b) The output signal from the first interferometer (two constructively interfering Mollow sidebands) is sent to the second Michelson interferometer. Here the filtering takes place in a similar manner. At S one sideband is suppressed via destructive interference, while the other one passes the double Michelson due to constructive interference.

$l_{coh} \approx 71$ mm, corresponding to a coherence time of 237 ps (see chapter 5.3.1), whereas the maximum path difference $S \approx 14$ mm, corresponding to a Rabi splitting of $45.5 \mu\text{eV}$, is significantly below the coherence length.

To grant the functionality of the Michelson filtering technique, a very good beam overlap after the two Michelson interferometers in terms of a high laser visibility has to be assured. Therefore the alignment was checked with a laser, where the visibility in the experimentally accessible delay range is expected to reach 100%, due to its long coherence length. A corresponding measurement and the resulting visibility versus linear stage position for both interferometers is shown in Fig. 5.6. For the correlation measurements the linear stages are positioned in the yellow-shaded regions, here the visibility is found to exceed 99%. In addition to the visibility check, the double Michelson interferometer has been tested to ensure the functionality of the described above

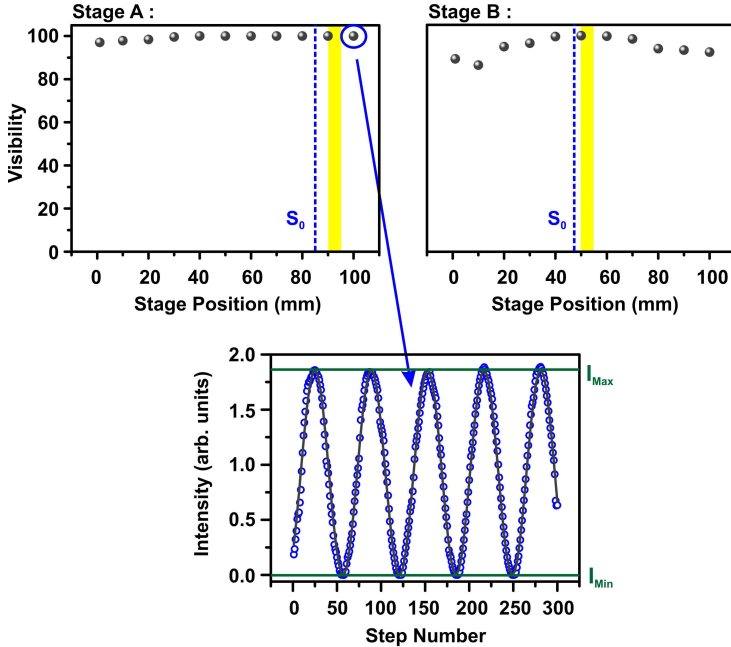


Figure 5.6: Laser alignment test of the two Michelson interferometers. Upper panel: The laser visibility has been measured for different stage positions of both linear stages of the Michelson interferometers. S_0 denotes the zero path delay position for the two Michelson interferometer arms, respectively. The yellow-shaded regions display the range where the linear stage is positioned for the calculated delay position S in the experiments. In the region of interest the visibility is almost ideal, exceeding 99%, and therefore granting very good beam overlap. Lower panel: Laser visibility measurement with sinusoidal fit to the data for extracting $I_{max/min}$ for the visibility calculation according to Eq. 3.3.

technique. The corresponding HRPL spectra after the first and second filtering steps are depicted in Fig. 5.7.

The technique of the Michelson interferometric filtering relies on a high degree of stability of the path difference between the two interferometer arms. For the wavelength of the QD emission ~ 905 nm, constructive and destructive interference have a path difference of only ~ 230 nm. Thus, even slight drifts in the stage position lead to a non-vanishing

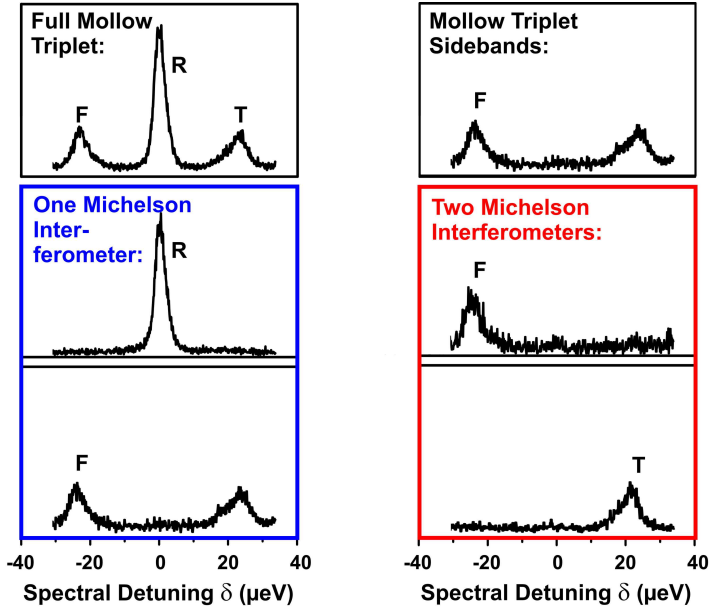


Figure 5.7: Performance check of the double Michelson interferometer. Via high-resolution spectroscopy the functionality of the double Michelson interferometer has been tested. Left panel: The full Mollow triplet is sent to the first Michelson interferometer. The path delay between the two arms is set to the position where either the R line or the two Mollow sidebands interfere constructively. Right panel: The two Mollow sidebands are sent to the second Michelson interferometer. The path delay is chosen in a way to selectively suppress the T or the F sideband, while the other one passes the double Michelson setup via constructive interference.

contribution of the undesired other two Mollow triplet components as visible in Fig. 5.8. Stability tests have revealed that a few minutes after maximizing for instance on the T Mollow triplet line, the other components start to contribute to the Michelson interferometer output signal, thus indicating a drift from the original linear stage positions. Due to the high sensitivity of the double Michelson interferometer, the correct stage positioning was verified and realigned every 5 minutes during the measurement if necessary, to guarantee for the spectral selection of only one Mollow component for the correlation measurements.

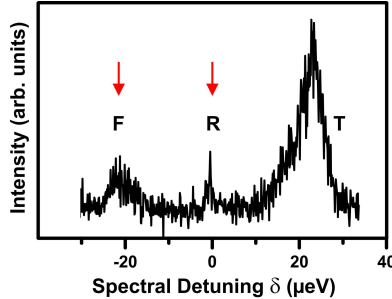


Figure 5.8: Stability test of the double Michelson interferometer. The path delays were adjusted so that originally the *T* Mollow sideband interferes constructively, while the *R* and *F* lines are suppressed. High-resolution spectroscopy reveals a drift in the path delay and therefore distinct contribution of the *R* and *F* line to the detected signal on a timescale of, typically, a few minutes.

5.3 Experimental results

For the two-photon interference measurements on the Mollow triplet sidebands a suitable QD embedded in a planar sample structure (as described in chapter 4.3) was chosen that revealed a background-free Mollow triplet dressed state emission in combination with an adequate countrate on the Mollow sidebands necessary for correlation measurements. Pre-characterization measurements were performed to independently derive the coherence time T_2 and $g^{(2)}(0)$ for the Mollow sidebands. These parameters are used for modelling the *Hong-Ou-Mandel* correlation data. It is worth mentioning that the evaluations presented in the following are based on a TLS affected by two dephasing mechanisms, radiative decay and pure dephasing. The phonon interactions of the exciton are only accounted for by a phenomenological pure dephasing time. This is in contrast to the polaron master equation approach presented in chapter 4.7, where the exciton-phonon interaction is explicitly introduced in the system Hamiltonian additional to further pure dephasing effects. Nevertheless, the aim of the experimental investigations is to prove the emission of indistinguishable photons in general. The employed theoretical description can of course be refined in terms of exciton interactions with the solid-state surrounding medium, e.g. in the framework of the polaron master equation approach.

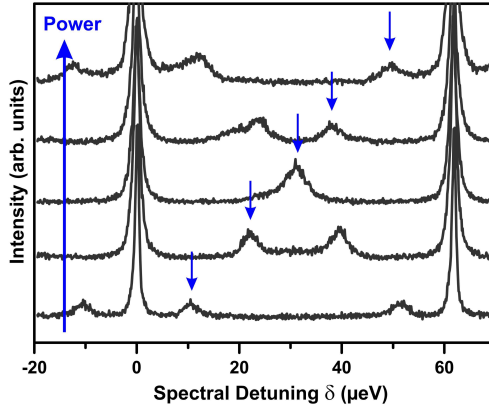


Figure 5.9: Power-dependent Mollow triplet series of the QD under investigation. The FWHM and the coherence of the Mollow triplet sidebands are extracted from Lorentzian fits to the sidebands. The results are shown in Fig. 5.10.

5.3.1 Mollow triplet sideband coherence

From a power-dependent Mollow triplet series of the QD depicted in Fig. 5.9 the coherence time of the Mollow sidebands was extracted. Because of the *Fabry-Pérot*-based technique in HRPL, all spectral features appear periodically with an offset equal to the free spectral range of the interferometer ($\Delta E_{FSR} = 62.04 \mu\text{eV}$). With increasing excitation power, the evolution of two symmetrically spaced sidebands is clearly visible (blue arrows) around the central Rayleigh line.

To extract the coherence time T_2 from the Mollow sidebands, a Lorentzian was fitted. The FWHM of the Mollow sidebands versus the squared Rabi frequency Ω is plotted in Fig. 5.10(a). The expected linear increase due to *excitation-induced dephasing* is clearly observable. The FWHM of the sidebands is linked to the coherence time T_2 according to

$$\Delta E_{FWHM} = \frac{h}{\pi T_2} . \quad (5.7)$$

The coherence time is calculated from the spectral width of the Mollow sidebands, the results are depicted in Fig. 5.10(b). The data can be fitted with a straight line and allows to derive the coherence times

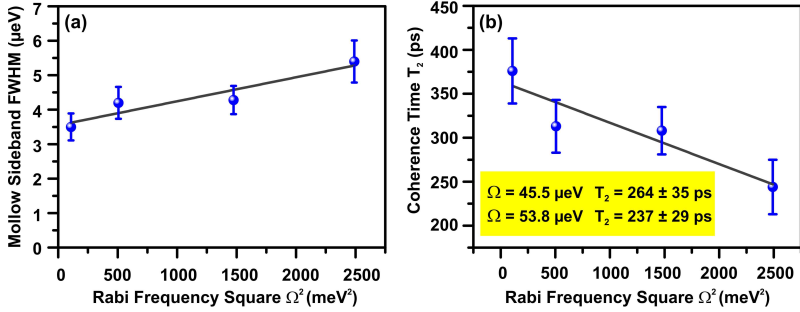


Figure 5.10: (a) Lorentzian FWHM of the Mollow sidebands versus square of Rabi frequency. The linear increase of the FWHM with Ω^2 is due to excitation-induced dephasing. (b) From the sidebands' width the coherence time T_2 is calculated according to Eq. 5.7. The coherence times T_2 corresponding to the experimental Rabi splittings of the correlation measurements were calculated via the linear fit to the data. The values are given in the inset box.

for the Rabi splittings that are employed for the correlation measurements. From the fit the following coherence times are extracted: For $\Omega = 45.5 \mu\text{eV}$ the coherence is $T_2 = 264 \pm 35 \text{ ps}$ and for $\Omega = 53.8 \mu\text{eV}$, $T_2 = 237 \pm 29 \text{ ps}$, respectively.

For an ideal bare two-level system only affected by radiative decay, but no pure dephasing, the Mollow triplet emission is *Fourier transform-limited*. As described in chapter 2.3.4, the Mollow sidebands at the *Fourier-transform limit* have a spectral width of $\Delta\omega = 3/2 \cdot \gamma$. Assuming the experimentally measured decay time of $\tau_{dec} = 1008 \text{ ps}$ (for details see chapter 5.3.4), a linewidth of $\Delta E = 0.98 \mu\text{eV}$ for the Mollow triplet sidebands at the *Fourier-transform limit* is expected, linked to a coherence time of $T_2 = 1343 \text{ ps}$. Obviously, the emission of the QD under investigation is not *Fourier-transform limited* for the chosen Rabi splittings of the correlation measurements. This is due to *excitation-induced dephasing* and additional interaction of the exciton with the solid-state surrounding medium, e.g. carrier-carrier scattering.

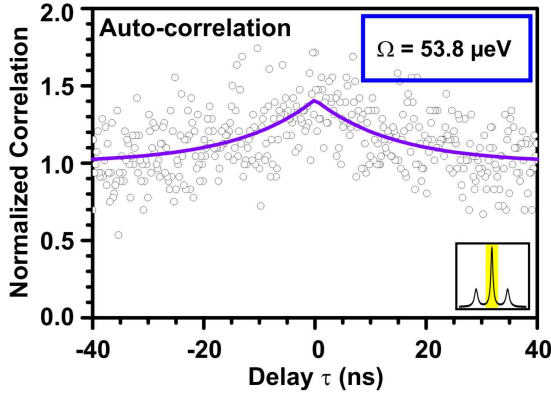


Figure 5.11: Auto-correlation on the central Rayleigh line for a Rabi splitting of $53.8 \mu\text{eV}$. Theoretically, Poissonian statistics in terms of $g^{(2)}(\tau) = 1$ can be expected. Experimentally, the Poissonian statistics is found to be superimposed with a long-timescale bunching. The bi-directional exponential fit to the data reveals a bunching timescale of $\tau_{\text{bunch}} = 14.3 \text{ ns}$.

5.3.2 Auto-correlations

For the *Hong-Ou-Mandel* type two-photon interference on a beam splitter, single-photon emission is a crucial experimental requirement. One pre-characterization measurement has therefore been the auto-correlation on the individual Mollow sidebands as well as on the central Rayleigh line. For the first set of correlations a Rabi splitting of $\Omega = 53.8 \mu\text{eV}$ was chosen. Spectral filtering of the individual Mollow components was performed with the double Michelson interferometer filtering technique.

Figure 5.11 shows the auto-correlation on the *R* line. For the photon-correlation, theory predicts Poissonian statistics in terms of $g^{(2)}(\tau) = 1$. As is clearly visible, the Poissonian statistics is superimposed by a long-time bunching, as commonly observed due to so-called *blinking* of the excitonic state between two or more neighboring competing states.

The blinking effect can be assigned to the switching of the QD exciton from one configuration to another. For example the QD carriers can undergo a spin flip mediated by phonon interaction or carrier exchange interaction. Via this process the exciton can switch from a

bright to a dark spin state, which is non-radiative in nature. This results in a bunching effect with a certain power-dependent blinking timescale [116]. The phenomenon of blinking can also be explained by different charge configurations of the excitonic complexes. The emission of one of these configurations is energetically outside the detection window of the correlation measurement, which also results in blinking of the detected signal. This effect was investigated under quasi-resonant excitation [117], where τ_{bunch} was found to be in the *ns* range. In addition, the blinking effect was observed even under strictly resonant excitation [118, 119]. Here a non-resonant laser leads to the neutralization of residual charges inside the QD before a neutral exciton can be excited. The neutralization is limited by the recapture of a hole, thus leading to a resonance fluorescence intermittency and therefore a blinking in the signal. In this experiment, ultraslow capture timescales in the range of μs are found. For the QD under investigation the blinking due to different charge configurations is unlikely since the excitation is strictly resonant and an optical gating effect similar to the work of Nguyen *et al.* [118, 119] has not been observed. The blinking is therefore most likely due to switching between the dark and bright spin state configuration of the exciton.

The bunched auto-correlation data has been fitted with a bi-directional exponential fit

$$g^{(2)}(\tau) = 1 + a \cdot \exp(-|\tau|/\tau_{bunch}) \quad , \quad (5.8)$$

revealing a bunching timescale of $\tau_{bunch} = 14.3$ ns. This bunching is found to be power-dependent and to superimpose all photon correlation measurements.

Figure 5.12 displays the auto-correlation on the *F* Mollow sideband. The anti-bunching is superimposed by the long-timescale bunching already observed on the auto-correlation of the Rayleigh photons. The data is fitted by the following function [120]

$$g^{(2)}(\tau) = 1 - b \cdot \exp(-|\tau|/\tau_r) + a \cdot \exp(-|\tau|/\tau_{bunch}) \quad , \quad (5.9)$$

which accounts for the bunching as well as the anti-bunching of the correlation data. The fit reveals $g^{(2)}(0)_{conv} = 0.36 \pm 0.03$ (blue solid line). Deconvolution with the Gaussian instrumental response function

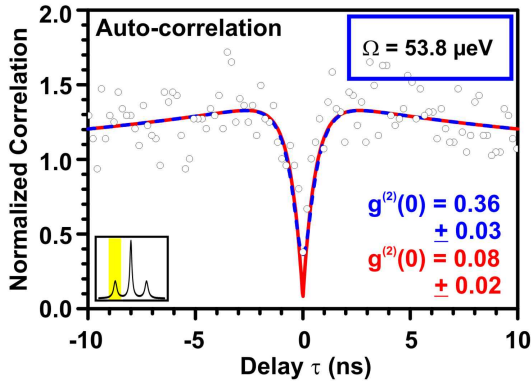


Figure 5.12: Auto-correlation on the red Mollow sideband for a Rabi splitting of $53.8 \mu\text{eV}$. The observed and theoretically expected anti-bunching is superimposed by the long-timescale bunching. The fit to the raw data (blue dashed line) reveals a $g^{(2)}(0) = 0.36 \pm 0.03$ and a decay time constant of $\tau_r = 570$ ps. Deconvolution with the instrumental response of 400 ps (red solid line) leads to $g^{(2)}(0) = 0.08 \pm 0.02$.

with a FWHM of 400 ps displays $g^{(2)}(0)_{\text{deconv}} = 0.08 \pm 0.02$. The correlation data unambiguously demonstrates single-photon emission with a fitted decay time constant of $\tau_r = 570$ ps. The finite background in the auto-correlation can be attributed to a small drift of the Michelson interferometers during the correlation measurement, allowing the spectrally close Mollow central peak to contribute to the detected signal as non-vanishing uncorrelated background.

5.3.3 Indistinguishability of the Mollow triplet sideband emission

The very good background-suppression in the auto-correlation on the Mollow sideband is a promising starting point for indistinguishability measurements, which crucially rely on single-photon emission. The experimentally employed *Hong-Ou-Mandel* setup for these two-photon interference experiments is presented in chapter 5.2.1. The delay of the fiber-coupled asymmetric *Mach-Zehnder* interferometer is fixed and has been independently measured to be $\Delta\tau = 13$ ns [33]. To extract the degree of indistinguishability the two-photon interference experiment

was performed for mutually perpendicular (distinguishable) and parallel (indistinguishable) photon polarizations between the two interferometer arms. The data has been modelled according to Ref. [103] with the following functions:

$$g_{\perp}^{(2)}(\tau) = 4(T_I^2 + R_I^2)R_{II}T_{II}g^{(2)}(\tau) + 4R_I T_I [T_{II}^2 g^{(2)}(\tau - \Delta\tau) + R_{II}^2 g^{(2)}(\tau + \Delta\tau)] \quad (5.10)$$

$$g_{\parallel}^{(2)}(\tau) = 4(T_I^2 + R_I^2)R_{II}T_{II}g^{(2)}(\tau) + 4R_I T_I [T_{II}^2 g^{(2)}(\tau - \Delta\tau) + R_{II}^2 g^{(2)}(\tau + \Delta\tau)] [1 - V \exp(-2|\tau|/T_2)] \quad (5.11)$$

T and R denote the reflectivities and transmittivities of the two BS of the asymmetric *Mach-Zehnder* interferometer and V is a function that depends on the overlap of the wave functions at the HOM-BS.

Before the experimental data is presented, it is worth having a closer look at the fit functions of the two-photon correlations. The behavior of $g_{\perp}^{(2)}(\tau)$ and $g_{\parallel}^{(2)}(\tau)$ is depicted in Fig. 5.13. Figure 5.13(I) shows the expected photon correlations for a system at the *Fourier-transform limit*, whereas Fig. 5.13(II) depicts a system with the approximate values of the experimental conditions of the measurements presented below. Balanced beam splitters with $R = T = 0.5$, perfect overlap of the photons at the HOM-BS in terms of $V = 1$ and background-free single-photon emission (without bunching) have been assumed for the sample calculation. In the perpendicular case the first summand leads to $g_{\perp}^{(2)}(0) = 0.5$ and simply reflects the single-photon emission of the emitter in the two-photon interference measurement. The neighboring side dips at $\Delta\tau$ with $g_{\perp}^{(2)}(\pm\Delta\tau) = 0.75$ indicate the single-photon emission in the case where subsequent photons take the same arm of the asymmetric *Mach-Zehnder* interferometer. In addition equal side dips reflect a balanced 50 : 50 BS. The widths of the dips are governed by T_1 , here $T_1 = 600$ ps has been used for the calculations in both cases, therefore the perpendicular two-photon correlations in (I) and (II) are identical. For the parallel configuration the fitting function differs from the perpendicular one by the last factor in Eq. 5.11. For a vanishing photon overlap at the HOM-BS $V = 0$ the photons do not interfere and $g_{\perp}^{(2)}(\tau) = g_{\parallel}^{(2)}(\tau)$. For the case of ideal photon overlap in terms of $V = 1 \rightarrow g_{\parallel}^{(2)}(0) = 0$, reflecting the coalescence of simultaneously

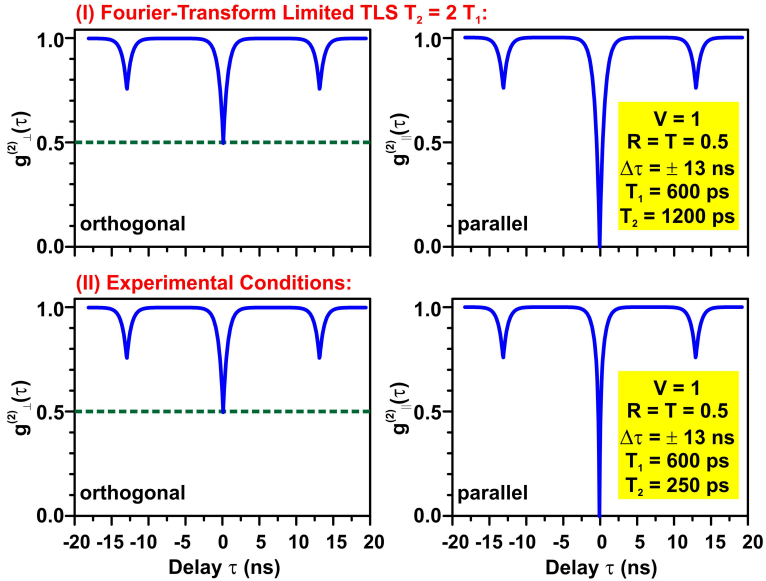


Figure 5.13: Theoretical expectations for the two-photon interference correlations according to Eqs. 5.10, 5.11. It is assumed that the system is not affected by blinking, therefore the correlations exhibit no superimposed bunching behavior. (I) System at the Fourier-transform limit $T_2 = 2T_1$. (II) System close to the conditions of the experiments. (left panel) Distinguishable (perpendicularly polarized) two-photon interference $g_{\perp}^{(2)}(\tau)$: The dip at zero delay $g_{\perp}^{(2)}(0) = 0.5$ reflects that single perfectly anti-bunched photons enter the HOM-BS from opposite sides. The side dips with $g_{\perp}^{(2)}(\pm\Delta\tau) = 0.75$ reflect the delay of the asymmetric Mach-Zehnder interferometer and arise from single-photons that take the same interferometer arm. The widths of the dips are governed by T_1 and are therefore equal for (I) and (II). (right panel) Two-photon interference for indistinguishable (parallelly polarized) photons $g_{\parallel}^{(2)}(\tau)$: The difference to the perpendicular case is the vanishing photon-correlation at zero delay $g_{\parallel}^{(2)}(0) = 0$, reflecting the bosonic nature of photons that coalesce at the same output of the BS. The width of the central dip is governed by T_1 and T_2 , therefore it is broader for the Fourier-transform limited system compared to the narrower dip in (II) due to the smaller coherence time of $T_2 = 250$ ps close to the experimental conditions.

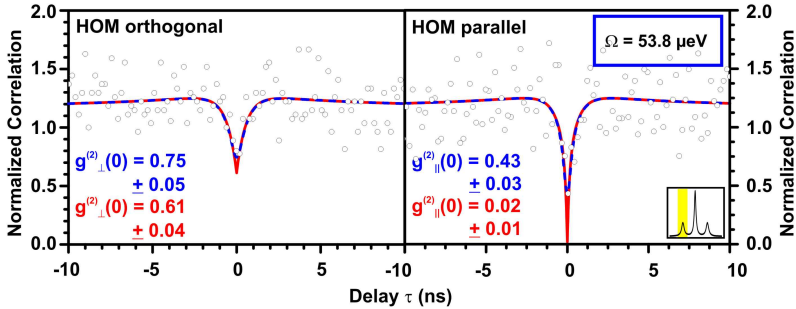


Figure 5.14: Data set for two-photon interference correlation on the red Mollow sideband at $\Omega = 53.8 \mu\text{eV}$. The raw measurement data clearly reveals the classical behavior of two-photon interference of perpendicularly polarized photons at the BS with $g_{\perp}^{(2)}(0) > 0.5$ and the non-classical behavior in the parallel case $g_{\parallel}^{(2)}(0) < 0.5$. Equations 5.10, 5.11 fit the data perfectly in full accordance with the values derived from the pre-characterizations ($\tau_r = 570 \text{ ps}$, $\tau_{\text{bunch}} = 14.3 \text{ ns}$, $T_2 = 237 \text{ ps}$). Via Eq. 5.12 the post-selected visibility is calculated to be $V_{\text{HOM}}^{\text{conv}} = 0.43 \pm 0.07$, with a deconvoluted value of $V_{\text{HOM}}^{\text{deconv}} = 0.97 \pm 0.02$.

entering photons at one output of the BS. The width of the *Hong-Ou-Mandel* dip is ruled by T_1 and the coherence time, assumed to be (I) $T_2 = 1200 \text{ ps}$ and (II) 250 ps , hence it is narrower for the experimental conditions compared to the *Fourier-transform limited* system.

For this analysis of the experimental data the reflectivities R and transmittivities T of the beam splitters were independently measured as $R = T = 0.5 \pm 0.02$ and the wave packet overlap at the *Hong-Ou-Mandel* beam splitter was determined to be $V = 0.98 \pm 0.02$. Figure 5.14 displays the data set for the two-photon interference correlations for a Rabi splitting of $\Omega = 53.8 \mu\text{eV}$. This corresponds to the experimental conditions of the pre-characterization auto-correlation measurements presented above. From the raw measurement data the non-classical behavior of indistinguishable photons (parallel polarization) is already visible, at zero delay $g_{\parallel}^{(2)}(0) = 0.43$, distinctly below the classical limit of 0.5. The width of the *Hong-Ou-Mandel* dip is governed by the coherence time of the emission, which is in the same range as the instrumental response of the setup. Due to this, the *Hong-Ou-Mandel* dip is narrow and cannot be fully resolved in the raw measurement

data. The side dips at $\tau = \Delta\tau = \pm 13$ ns are not shown in the correlation data because they are not perfectly resolved in the raw data sets. Due to the tricky experimental conditions, which necessitated a regular repositioning of the Michelson linear states in combination with a moderate countrate on the detectors, it was possible to gather approximately ~ 30 cts/channel at the Poisson level. Therefore the data is not as smooth as the *Hong-Ou-Mandel* data achieved by Ates *et al.* [63], that has been measured with the same experimental setup, in this study the side dips are resolved. The fits to the experimental data are found to be in full accordance with the pre-characterizations presented above: $\tau_{bunch} = 14.3$ ns, $\tau_r = 570$ ps and the extracted coherence time $T_2 = 237$ ps derived from the HRPL power series. Via the parallel and perpendicular measurements the two-photon visibility is calculated according to [103]

$$V_{HOM}(\tau) = \frac{g_{\perp}^{(2)}(\tau) - g_{\parallel}^{(2)}(\tau)}{g_{\perp}^{(2)}(\tau)}. \quad (5.12)$$

A very high post-selected two-photon visibility (at $\tau = 0$) of $V_{HOM} = 0.97 \pm 0.02$ (convoluted $V_{HOM} = 0.43 \pm 0.07$) was extracted from the deconvoluted fits to the two-photon interference data.

Indistinguishable photon emission was also verified for the blue Mollow sideband under the same experimental conditions ($\Omega = 53.8 \mu\text{eV}$). The auto- and two-photon interference correlation measurements are depicted in Fig. 5.15. From the auto-correlation on the blue Mollow sideband a decay time of $\tau_r = 570$ ps is extracted. From the $g^{(2)}(\tau)$ -measurement on the central Rayleigh line at $\Omega = 53.8 \mu\text{eV}$ a bunching time constant of $\tau_{bunch} = 14.3$ ns is derived and the coherence time is $T_2 = 237$ ps. The fitting of the two-photon interference correlations reveals full consistency with the pre-characterization measurements and the experimental results on the red Mollow sideband at the same Rabi splitting. The post-selected *Hong-Ou-Mandel* visibility is calculated to be $V_{HOM} = 0.92 \pm 0.02$ (convoluted $V_{HOM} = 0.39 \pm 0.08$).

To prove that indistinguishable photon emission from the Mollow sidebands is a general feature of the dressed state emission independent of a specific Rabi splitting, the auto- and two-photon interference correlation measurements were performed on the red Mollow sideband for a different Rabi splitting of $\Omega = 45.5 \mu\text{eV}$. The corresponding data set

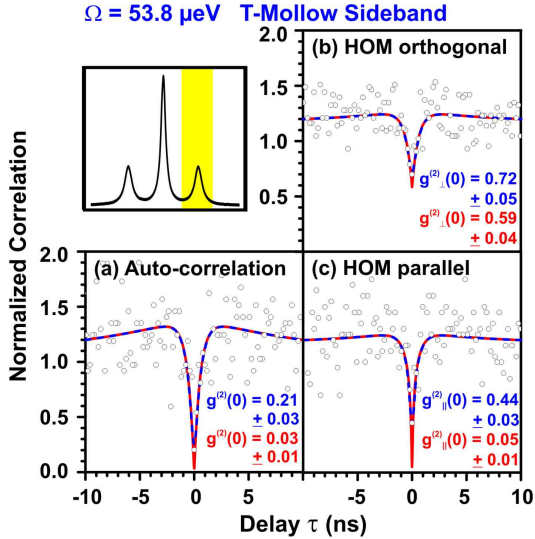


Figure 5.15: Auto- and two-photon interference correlations for the blue Mollow sideband at $\Omega = 53.8 \mu\text{eV}$. (a) The pre-characterization auto-correlation reveals $\tau_r = 570$ ps, the bunching timescale is $\tau_{\text{bunch}} = 14.3$ ns (see auto-correlation on R chapter 5.3.2). The Hong-Ou-Mandel data set can be reproduced perfectly when employing the values from the pre-characterizations ($T_2 = 237$ ps). The extracted deconvoluted post-selected visibility is $V_{\text{HOM}}^{\text{deconv}} = 0.92 \pm 0.02$ ($V_{\text{HOM}}^{\text{conv}} = 0.39 \pm 0.08$).

is depicted in Fig. 5.16. The auto-correlation on the central Rayleigh line again reveals bunching on top of the Poissonian statistics, showing a timescale of $\tau_{\text{bunch}} = 9.51$ ns. The auto-correlation on the sideband reveals a decay time of $\tau_r = 540$ ps. Together with a coherence time of $T_2 = 300$ ps, close to the experimentally extracted value from the power-dependent Mollow triplet series of $T_2 = 264 \pm 35$ ps, these values reveal a good fit to the two-photon interference correlations. It is worth mentioning that $g^{(2)}(0)$ for the parallel two-photon correlation measurement is assumed to be slightly better than for the fits in Fig. 5.16 (b) and (c). Due to the fact that the anti-bunching value is very sensitive to the positioning and the stability of the two Michelson interferometers, the better $g^{(2)}(0)$ -value for the parallel two-photon interference measurement can be related to a more stable positioning of the Michelson

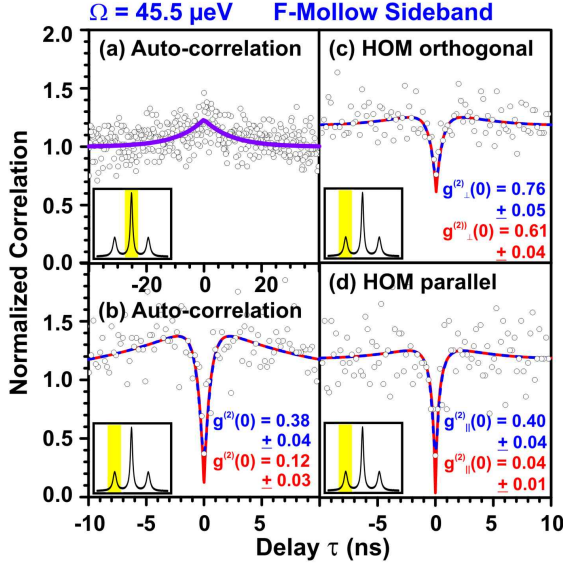


Figure 5.16: Auto- and two-photon interference correlation for the red Mollow sideband at $\Omega = 45.5 \mu\text{eV}$. (a) The auto-correlation of the central Rayleigh line reveals bunching on top of the Poissonian statistic with an extracted value of $\tau_{\text{bunch}} = 9.51 \text{ ns}$. (b) The auto-correlation on the sideband is anti-bunched with a decay timescale of $\tau_r = 540 \text{ ps}$. (c-d) Hong-Ou-Mandel correlation measurements: For data modelling τ_r , τ_{bunch} and $T_2 = 300 \text{ ps}$, close to the value of $T_2 = 264 \text{ ps}$ extracted from the power-dependent Mollow triplet series, are used. The post-selected visibility is found to be $V_{\text{HOM}}^{\text{deconv}} = 0.93 \pm 0.01$ ($V_{\text{HOM}}^{\text{conv}} = 0.47 \pm 0.08$).

interferometers during the measurement time (less background from the Mollow central line). Considering the setup response, the following values are extracted from the fits: $g_{\perp}^{(2)}(0)_{\text{deconv}} = 0.61 \pm 0.04$ and $g_{\parallel}^{(2)}(0)_{\text{deconv}} = 0.04 \pm 0.01$. Therefore, a close to ideal post-selected visibility of $V_{\text{HOM}} = 0.93 \pm 0.01$ (convoluted $V_{\text{HOM}} = 0.47 \pm 0.08$) for the indistinguishability of the red Mollow sideband can be concluded.

Under cw excitation the value of the post-selected two-photon interference visibility at $\tau = 0$ is ruled by the instrumental response time of the setup $\delta\tau$ and given by the ratio $T_2/(2\delta\tau)$. The visibility extracted

from the raw measurement data is limited by the fact that the Mollow sideband emission has a rather short coherence time. In the ideal case of infinitely fast detectors (deconvolution), the post-selected visibility should always reach $V_{HOM} = 1$. The experimentally measured visibility values are found to be ≤ 0.97 , the deviations from the ideal value can mainly be assigned to the imperfect auto-correlation anti-bunching values of the selected emission channels in terms of $g^{(2)}(0) \neq 0$. This can be attributed to slight drifts from the ideal position of the Michelson interferometers during the course of the measurement. Due to this, the neighboring central Rayleigh line emission contributes to the correlated signal and lowers the degree of single-photon emission.

The post-selected visibility is more a theoretical value since it only considers the simultaneous photons arrival at $\tau = 0$, but even single-photon wave packets have a certain time duration. From an application point of view, triggered indistinguishable photons are desirable. In contrast to cw excitation, the suppressed central peak in the pulsed two-photon correlation reveals insight into pure dephasing of the system since the maximum visibility in the pulsed experiment is ruled by $T_2/(2T_1)$ and reaches one for *Fourier-transform limited* photons.

5.3.4 Decay timescale of the emission

As discussed above, the results of the pre-characterization measurements are found to be in excellent agreement with the values used for fitting the *Hong-Ou-Mandel* type two-photon correlations. In spite of this, it should not be withheld that the extracted value of the decay time τ_r derived from fitting the Mollow sideband auto-correlations and the experimentally derived τ_{dec} extracted from TCPC measurements reveal distinctly different values.

As theoretically described by Schama *et al.* [60], the emission time modifies under resonant excitation according to

$$\tau_{mod} = \frac{\tau_{rad}}{c^4 + s^4} . \quad (5.13)$$

The coefficients c and s are defined in Eq. 4.3. For the experimental conditions of resonant excitation ($\Delta = 0$), they are found to be $c = s = \frac{1}{\sqrt{2}}$.

For the independent derivation of τ_{mod} , time-resolved photoluminescence investigations under pulsed quasi-resonant emitter-state preparation have been performed. The experimental data of the TCSPC

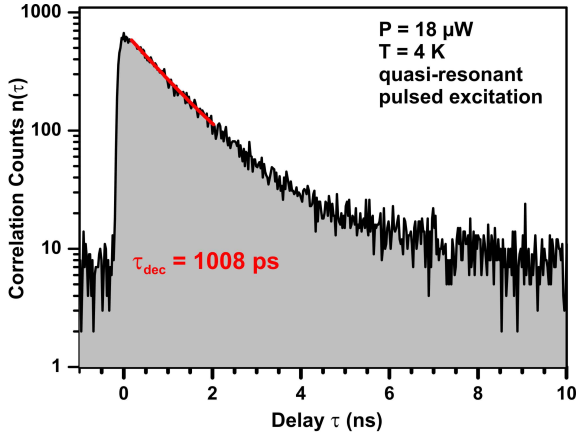


Figure 5.17: TCSPC raw measurement data. The first decade is fitted by a mono-exponential function revealing a decay time of $\tau_{dec} = 1008 \pm 67$ ps. The experiment was performed under pulsed d-shell excitation at $P = 18 \mu\text{W}$ and a sample temperature of $T = 4$ K.

measurement is shown in Fig. 5.17. Via a mono-exponential fit to the first decade of the data a decay time of $\tau_{dec} = 1008$ ps is extracted. Therefore the modified decay time of the system is calculated to be $\tau_{mod} = 2016$ ps. The corresponding time constant from fitting the auto-correlations on the Mollow sidebands consistent with the two-photon interference correlations τ_r is found to be distinctly smaller: $\tau_r = 540 - 570$ ps. It should be emphasized that a similar discrepancy between the experimentally extracted τ_r to the theoretically calculated τ_{mod} was already observed previously by Ata Ulhaq and co-authors [28, 57].

The deviation might be attributed to the different experimental conditions of the cw resonant excitation for the correlation measurements and the pulsed quasi-resonant emitter-state preparation for the TCSPC measurement. The quasi-resonant excitation into higher energetic shells of the QD is accompanied by relaxation of the carriers into the QD s-shell before radiative recombination can take place. Thus the experimentally accessible time constant of decay characterizes the time between laser excitation and radiative electron-hole pair recombination, including the relaxation processes. But it is worth mentioning that the

relaxation timescale is usually in the range of a few tenth of ps and can therefore not explain fully the much larger time difference of more than 1000 ps between τ_r and τ_{dec} .

As already discussed above, the evaluation of the indistinguishability measurements only includes dephasing effects of the exciton and the solid-state medium in terms of a phenomenological pure dephasing time. The polaron master equation-based theory (described in chapter 4.7) explicitly includes exciton-phonon coupling in terms of deformation potential coupling with LA phonons. The phonon interaction also leads to a renormalization of the radiative decay rate according to $\gamma_{renorm} = \langle B \rangle^2 \gamma$. Since the thermally averaged bath displacement operator is found to be smaller than 1 for non-zero temperatures $\langle B \rangle < 1$, the decay rate should be smaller under exciton-phonon interaction. Thus the radiative lifetime should be expected to be longer. When comparing τ_r with τ_{dec} , the experimental results presented in this chapter reveal the opposite behavior, to what the polaron master theory would suggest. For these reasons a plausible explanation of the effect is not possible so far and a profound theoretical analysis has to be left to further in-depth analysis.

Chapter 6

Phonon-assisted incoherent excitation

6.1 Dephasing in semiconductor QDs

In the optical Bloch equations of a TLS interacting with a monochromatic laser field introduced in chapter 2.3.3, two different damping terms have been added via the Lindblad formalism. These are pure dephasing with a time constant of T_{pure} and T_1 being the lifetime of the excited state. They are found to be connected via the relation

$$\frac{1}{T_2} = \frac{1}{2T_1} + \frac{1}{T_{pure}} \quad , \quad (6.1)$$

where T_2 denotes the coherence time of the system. Due to the fact that the decay of an exciton is an intrinsic property, the coherence can maximally reach the so-called *Fourier transform-limit*, yielding $T_2/(2T_1) = 1$. This is the case when all pure dephasing effects are fully suppressed, thus $T_{pure} \rightarrow \infty$. The decay of the exciton leads to a loss of phase due to population change in the QD, whereas the pure dephasing accounts for all processes that change the phase but not the population of the QD. Pure dephasing can be due to carrier-phonon and also carrier-carrier scattering of the exciton in the QD because of its' interaction with the solid-state surrounding medium.

The optical Bloch equations of a TLS and the dephasing relation of

Eq. 6.1 are a good starting point to describe the dephasing in a QD. The phenomenologically introduced pure dephasing can be refined under consideration of the specific physical mechanism that leads to the dephasing of the exciton, for example in terms of exciton-phonon interaction due to the solid-state surrounding medium. The interaction of excitons with phonons in *III – V* semiconductor QDs has been an intensively discussed topic in literature since the early 1990s and several aspects are still under discussion. In the following, the different dephasing mechanisms and the resulting spectral properties of QDs will be discussed.

6.1.1 Radiative dephasing

The decay of an electron-hole pair in a QD provides a fundamental limitation of the coherence of the emitted photon. The maximally achievable emission coherence at the *Fourier transform-limit* is found to be $T_2/(2T_1) = 1$. The decay time is measured via TCSPC, the corresponding experimental setup is presented in chapter 3.3. A typical data set from a time-resolved photoluminescence measurement is shown in Fig. 6.1(a) together with a mono-exponential fit to the first decade of the correlation data to extract the decay time of the system. As is visible from the raw data, the decay behavior is more complicated and the mono-exponential function does not fit the data in the full delay time range. There are various reasons for the non-mono-exponential behavior. Uncorrelated background in the correlation measurement leads to a certain *y*-offset. The addition of a constant to a mono-exponential decay function results in a non-linear dependence in the logarithmic plot. Another reason for the deviation from a mono-exponential is the asymmetric response function of the *ID-Quantique* APDs used for the TCSPC measurements, depicted in Fig. 6.1(b). For a correct reproduction of the experimental data the function that accounts for the physical behavior of the decaying system has to be convoluted with the instrumental response of the setup. These two factors lead to a non-exponential appearance of the TCSPC raw data, even for a mono-exponentially decaying TLS. For an exciton in a QD it can also be the case that the decay deviates from a simple mono-exponential due to physical reasons. Two different theoretical approaches that explain the non-mono-exponential behavior of the time-resolved data are worth mentioning. Wiersig *et al.* [122] reported about non-exponential and also excitation intensity-dependent decay of the QD emission. This is

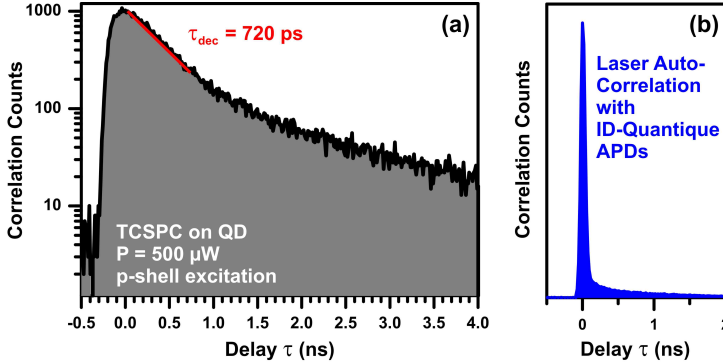


Figure 6.1: (a) TCSPC measurement of a single QD under pulsed p-shell excitation at $T = 6\text{ K}$ and $P = 500\ \mu\text{W}$. The solid line is a mono-exponential fit to the experimental data, yielding a decay time of $\tau_{dec} = 720\text{ ps}$, which is a typical value of an $\text{In}(\text{Ga})\text{As}/\text{GaAs}$ QD in a planar sample without Purcell enhancement. (b) Auto-correlation of the pulsed laser with the ID-Quantique APDs used for TCSPC correlations. The data has been taken by S. Bounouar [121].

attributed to scattering processes that can redistribute electrons and holes independently. In addition, dephasing and screening effects can reduce the electron-hole correlations due to Coulomb interaction, resulting in a non-mono-exponential decay. Another explanation for a bi-exponential decay of the transient in time-resolved photoluminescence is the competing between bright and dark excitonic states. The solution of the rate equation of a three-level system results in the bi-exponential decay of the QD emission as described by Johansen *et al.* [123]. The spin-flip process is phonon-mediated by a phonon with energy that matches the exchange energy between bright and dark state; typical spin-flip times are found to be in the ns range. Experimentally, the QD is excited under quasi-resonant (p-shell) pulsed excitation for TCSPC measurements. In this case the extracted τ_{dec} -value additionally includes the carrier relaxation between p- and s-shell which is in the range of $10 - 20\text{ ps}$. To derive the decay time from the raw measurement data, the first decade is fitted with a mono-exponential function under the assumption that there is no non-radiative carrier recombination, or that the spin flip from dark to bright state is on a much longer

timescale. In addition, the carrier relaxation from higher energetic levels is within much shorter timescales compared to the radiative decay time and therefore negligible, i.e. $T_1 \approx \tau_{\text{dec}}$.

6.1.1.1 Phonon bottleneck effect

Experimentally, it has been observed that electron-hole pairs that are quasi-resonantly generated in a QD can relax down to the lowest energetic QD state from where they radiatively recombine. This relaxation process does not alter the coherence of the QD s-shell emission but it induces a time jitter to the photon emission event. This can be a limitation of the indistinguishability derived from two-photon interference experiments where the simultaneous arrival of photons on a beam splitter is a crucial experimental requirement.

Due to the discrete nature of the QD states the conservation of energy in the relaxation process is hardly fulfilled for LO phonons. This is also supported by calculations via Fermi's golden rule which predict that the relaxation of carriers between electronic levels is prohibited, resulting in the so-called *phonon bottleneck* effect [124]. The experimental observations of the phonon bottleneck, i. e. the reduced exciton relaxation rate from the inefficient phonon emission at low temperatures, have been controversial. A large number of experimental photoluminescence investigations under quasi-resonant QD state preparation have negated the existence of the phonon bottleneck, and fast relaxation processes are experimentally observed.

There are several different explanations of the fast carrier-relaxation process inside a QD. An overview about the different proposed mechanisms is given in Ref. [20] and references therein. For example, intradot relaxation within a continuum of states (cross-over between $2D$ continuous wetting layer and $0D$ discrete QD states) via the emission of localized phonons was proposed by Toda *et al.* [125].

The strength of the LO phonon-exciton coupling depends on the dipole moment of the electron-hole pair and therefore the spatial separation of the wave functions in the QD. When electrons and optical phonons enter the strong coupling regime, the new eigenstates of the interacting exciton-phonon system are the excitonic polarons [126]. In the polaron frame the optical phonon absorption or emission by an exciton is not a valid image anymore. Instead, what allows relaxation between ener-

getic QD states is the instability of the phonon part of the polaron wave function. In analogy to the exciton-photon interaction in a strongly coupled cavity this can be visualized by a phonon exchange which results in damped Rabi oscillation between excited and ground state of the QD. The Rabi frequency is given by the polaron coupling strength. Due to the short lifetime of the LO phonons the oscillations are quickly damped, which basically leads to the relaxation from a higher energetic (p-shell) to the QD ground state within a typical timescale of ~ 10 ps. This kind of relaxation is efficient for a wide range of energy detunings between LO phonons and the electronic level splitting inside QDs [20].

6.1.2 Pure dephasing

6.1.2.1 Independent boson model

The framework used to describe dephasing effects due to the interaction between an excited two-level system (exciton) with acoustic as well as optical phonons is the exactly solvable *independent boson model* (IBM) [127]. The IBM is based on the adiabatic approximation, which assumes that the confinement energies exceed the energy of the phonons, therefore the energy mixing of different electronic states by phonon coupling can be neglected. The corresponding Hamiltonian includes linear coupling between the exciton and phonons. After transformation in the frame rotation with respect to the laser ω_L it reads [77]:

$$H = \hbar\omega_0\sigma^+\sigma^- + \sigma^+\sigma^- \sum_{\mathbf{q},j} \hbar\lambda_{\mathbf{q},j}(b_{\mathbf{q},j} + b_{\mathbf{q},j}^\dagger) + \sum_{\mathbf{q},j} \hbar\omega_{\mathbf{q},j}b_{\mathbf{q},j}^\dagger b_{\mathbf{q},j} \quad , \quad (6.2)$$

with $\sigma^{+/-}$ being the Pauli operators of the exciton. The index j denotes the different acoustic and optical phonon branches, whereas $\hbar\omega_{\mathbf{q},j}$ is the phonon energy including the energy dispersion of the individual phonon branches. $b_{\mathbf{q},j}$ and $b_{\mathbf{q},j}^\dagger$ are the bosonic phonon field operators, $\hbar\omega_0$ the exciton energy and $\lambda_{\mathbf{q},j}$ the exciton-phonon coupling constant. In the IBM the carrier-phonon interaction does not lead to a change in the QD exciton occupation because the Hamiltonian commutes with the occupation operator $\sigma^+\sigma^-$. Due to the fact that the IBM does not provide an energy relaxation mechanism, the recombination of the electron-hole pair has to be included phenomenological via the Lindblad formalism described in chapter 2.3.3. Because of the dephasing arising from the

calculation of the IBM Hamiltonian of Eq. 6.2, it is only possible to describe the pure dephasing of the system that is not accompanied by a population change. Under the assumption that the surrounding barrier and QD material do not differ significantly in their lattice properties, the phonon modes of the corresponding three-dimensional bulk modes of the barrier material can be used for the calculations [75]. This is also supported by the investigations by Stork *et al.*, where optical phonon replica of electrically excited QDs are observed only at the energy of the GaAs bulk material energetically detuned by 36.6 meV from the exciton s-shell, but not at an energetic detuning of 30.3 meV, which would correspond to the phonons of the InAs QD material.

A convenient variation of the IBM is the polaron transformation, which is described in chapter 4.7. Metaphorically speaking, due to its charge the electron creates a polarization cloud in a polar lattice, which moves around with the electron and changes its dynamic properties. Thus, electron-phonon interaction leads to a new quasi-particle, the electron and its polarization cloud, called *polaron*, due to the polar electron-phonon coupling that causes the interaction. A theoretical model based on a polaron master equation approach is used for modelling the experimental data of phonon-assisted incoherent excitation described in this chapter as well as the study of the investigations of the detuning-dependent Mollow triplet emission properties in chapter 4.8 and also the study of Mollow quintuplets (see chapter 4.9).

Based on the calculations of the IBM with linear coupling to acoustic phonons, the ZPL is a δ -peak and does not show any broadening with temperature, in contrast to what is usually observed in the experiment, e.g. Ref. [128]. To date the physical understanding of the broadening of the ZPL has not been clarified yet. There are several possible mechanism that can lead to temperature-dependent and temperature-independent ZPL broadening. As mentioned above, the IBM does not account for the decay of the exciton. Inclusion of the finite lifetime of the exciton leads to a broadening of the ZPL. The extension of the IBM in terms of quadratic coupling to acoustic phonons in addition to the linear coupling leads to a broadening of the ZPL with increasing temperature [129]. The ZPL can also be broadened by exciton-carrier interaction as described in section 6.1.2.3 below.

6.1.2.2 Exciton-phonon coupling mechanisms

There are several coupling mechanisms of the exciton either to optical phonons (LO) or the acoustic phonons (LA, TA), which can be attributed to distinctly different physical origins. In the following, the different coupling mechanisms will be introduced together with the resulting spectral properties of the QD absorption. The discussion is based on the publication by Krummheuer *et al.* [75].

For all types of coupling mechanisms the coupling matrix elements can be factorized in a coupling constant that accounts for the specific coupling mechanism and a contribution that can be calculated from the wave function of the electron and hole in the QD potential according to

$$F_{\mathbf{q}}^{e,h} = \int d^3r |\psi^{e,h}(\mathbf{r})|^2 \exp(i\mathbf{q}\mathbf{r}) \quad . \quad (6.3)$$

$F_{\mathbf{q}}^{e,h}$ is termed form factor and is the Fourier transformation of the probability density function that characterizes which values in k-space the carrier wave function square covers. Due to a resonance argument the exciton-phonon interaction only occurs between carriers and phonons with the same momentum. The effective form factor that includes the difference between electron and hole form factor is depicted in Fig. 6.2 (left panel). In smaller (larger) dots the wave function is restricted to a smaller (larger) area in real space leading to a larger (smaller) distribution in k-space.

Polar optical coupling to LO phonons

The LO phonon-exciton coupling in polar semiconductors arises from the polarization of the lattice due to different charge distributions of the electron and hole in the QD. The coupling is sensitive to the specific wave functions of the carriers, in the special case of identical electron-hole wave functions LO phonon features would not be observable. In contrast, the dipole moment and therefore the coupling strength can be enhanced by the Stark effect, shape asymmetries, and compositional nonuniformities that reduce the electron-hole wave function overlap.

As mentioned above, the coupling is described by a product of effective form factor and specific coupling mechanism. Fig. 6.2 (left panel) de-

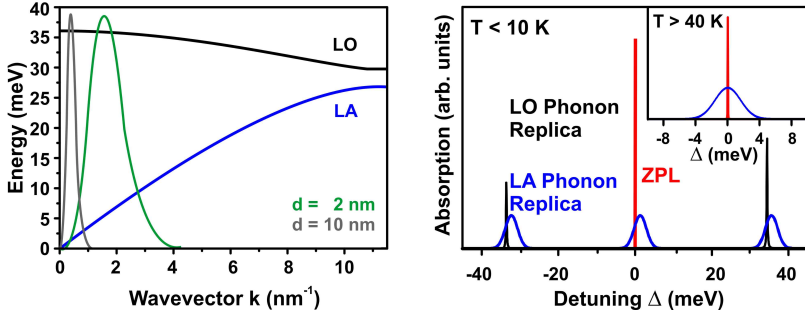


Figure 6.2: Left panel: Schematic depiction of the dispersion relation for LO and LA phonons together with the normalized effective form factors that describe the coupling of the exciton confined in QDs with two different diameters $d = 2, 10$ nm, respectively (adapted from Ref. [75]). Right panel: Schematic QD absorption spectrum with respect to detuning from the s -shell resonance for low temperatures ($T < 10$ K) under consideration of exciton-phonon coupling. At $\Delta = 0$ the unbroadened ZPL is visible surrounded by asymmetric acoustic phonon sidewings. At a detuning of $\Delta = 36.6$ meV corresponding to the LO phonon energy in bulk GaAs broadened LO phonon replica are visible, surrounded by acoustic phonon sidebands. Inset: At higher temperatures the acoustic phonon sidebands become symmetric due to the increasing probability of phonon absorption (adapted from Ref. [28]).

picts the normalized effective form factor together with the dispersion relation of LO as well as LA phonons. For larger dots with diameter $d > 10$ nm the LO phonon energy is almost constant for the wave vector range covered by the effective form factor. In the absorption spectrum a δ -peak like unbroadened ZPL and sharp peaks at the LO phonon energy detuning $\Delta = 36.6$ meV are expected. For smaller dots the dispersion of LO phonons comes into play, leading to a broadening of the LO phonon features with decreasing QD size. The spectrum changes from purely discrete to a system with continuum parts in the spectrum. Figure 6.2 (right panel) illustrates the spectral position and shape of the phonon features; the relative weights of the various lines depend on temperature and the effective coupling constant.

Up to the present day many experimental studies have reported about LO phonon features in QD spectra. To name but a few, Lemaître *et al.* [130] observed first- and second-order LO phonon sidebands in PLE

absorption, whereas Duf aker *et al.* [131] observed LO phonon replica up to second-order in PL emission.

Deformation potential coupling to LA phonons

Acoustic phonons are characterized by a continuous dispersion spectrum starting at zero frequency as depicted in Fig. 6.2(a). Therefore the acoustic phonon sidebands are continuous and approach the ZPL. The pronounced temperature dependence is also visible in Fig. 6.2(b). At low T the acoustic phonon sidebands are asymmetric due to unequal probabilities of phonon absorption and emission. The inset shows that the phonon replica become more symmetric at elevated temperatures $T > 40$ K.

For In(Ga)As/GaAs QDs deformation potential coupling is the physical origin of coupling between the exciton and longitudinal acoustic (LA) phonons. The local homogeneous compression or dilation $\Delta(\mathbf{r})$ caused by acoustic phonons can be described as a local relative volume change according to [132]

$$\Delta(\mathbf{r}) = \left. \frac{\Delta V}{V} \right|_{\mathbf{r}} . \quad (6.4)$$

It is experienced by a carrier as a local change in the lattice constant which shifts the single particle energy. The interaction Hamiltonian which accounts for deformation potential coupling can be written as [132]

$$H_{el-ph} = - \sum_j D \Delta(\mathbf{r}_j) , \quad (6.5)$$

where D denotes the deformation potential constant. These deformation potential constants, which are different for electrons and holes, describe how an energetic level shifts with increasing pressure (accompanied by a volume change) on the solid [127]. Until the present day there have been no solid numbers for the deformation potential constants in literature [133]. Several theoretical calculations receive a good reproduction of experimental data with the values of $D_e = -14.6$ eV and $D_h = -4.8$ eV [75].

One of the first observations of electron-acoustic phonon coupling was reported by Besombes *et al.* [134], where acoustic phonon sidebands

were observed in the PL emission spectra around the ZPL. In another study Favero *et al.* [135] found that the relevant parameter for the observation of acoustic phonon sidebands is the linewidth of the central ZPL.

Piezoelectric coupling to LA and TA phonons

The third electron-phonon coupling mechanism is the piezoelectric coupling. The piezoelectric effect describes the situation where homogeneous static strain causes a polarization. This can be extended to dynamical strain fields connected with acoustic-phonons, which give rise to piezoelectric electron-phonon coupling with LA as well as TA phonons.

The relevant tensor that describes the piezoelectric coupling only has nonvanishing elements for crystals without inversion symmetry [132]. Therefore piezoelectric coupling between exciton and acoustic phonons can be neglected for In(Ga)As/GaAs QDs due to the inversion symmetry of the zinc blende type crystal structure. For this material system, the piezoelectric coupling has been found to be less than 1% [75] compared to deformation potential coupling. The relevant exciton-acoustic phonon interaction mechanism of In(Ga)As/GaAs QDs is deformation potential coupling.

6.1.2.3 Pure dephasing due to the fluctuating charge environment

Due to the fact that the QD is embedded in a solid-state host matrix, charges can be trapped in the vicinity of the QD by impurities or defects. These charges can randomly hop in and out the traps, leading to a fluctuating charge environment of the QD. This induces micro-electric fields that shift the QD emission line due to the quantum-confined Stark effect. This effect of Coulomb interaction of the bound carriers inside the QD with surrounding charges is usually termed *spectral diffusion*. In the In(Ga)As/GaAs QD type studied in this thesis, spectral diffusion effects shift the QD emission energy slightly, thus leading to a time-integrated single-emission line in micro-photoluminescence investigations which is larger than the *Fourier transform-limit*, determined by the statistical distribution of the small energetic shifts of the QD emission. The introduced spectral jitter can range from tens of μeV to

several meV [136], depending on the conditions of emitter-state preparation.

Resonant emitter-state preparation can decrease the QD emission linewidth at low sample temperatures compared to quasi-resonant or non-resonant excitation schemes, where more carriers are created in the vicinity of the QD. A possibility to measure the timescale of spectral diffusion was presented by Sallen *et al.* [137]. Auto-correlation measurements on the spectral half of the emission line reveal the spectral diffusion timescale as a superimposed bunching on top of the anti-bunching due to the single-photon emitter nature of the QD. The technique offers a time-resolution limited only by the system response time.

Depending on the distinct values of the modulation amplitude that randomizes the emission energy over a spectral range of Σ within a characteristic timescale of the modulation τ_c , spectral diffusion can lead to a broadening of the emission line as well as to the opposite effect referred to as motional-narrowing. Considering the ratio $(\Sigma\tau_c)/\hbar$, the two regimes can be distinguished from each other. In the regime of slow modulation $(\Sigma\tau_c)/\hbar \gg 1$, the first-order correlation function exhibits a gaussian decay, leading to a gaussian emission in the spectral domain as well. In the regime of fast modulation $(\Sigma\tau_c)/\hbar \ll 1$, the visibility decays exponentially, resulting in a Lorentzian emission lineshape. In the limit of fast modulation the fluctuations of the environment are smoothed out and the lineshape is therefore motionally narrowed. Berthelot *et al.* [138] experimentally observed the cross-over between the exponential to gaussian decay in Michelson interferometric visibility measurements with increasing excitation power and temperature. This result is counter-intuitive, at first glance one would expect the opposite behavior due to more motion in the carrier environment with higher excitation power. The asymmetry of the capture and escape mechanisms is the fundamental reason why motional-narrowing strikingly occurs with decreasing excitation power, as explained in detail in Ref. [138].

Figure 6.3 depicts two data sets of first-order coherence time measurements under different excitation conditions of two different QDs. Under an excitation power of $P = 250 \mu W$ a mono-exponential decay of the visibility can be observed as shown in Fig. 6.3(a), indicating that the system is operating in the fast modulation regime, where the emis-

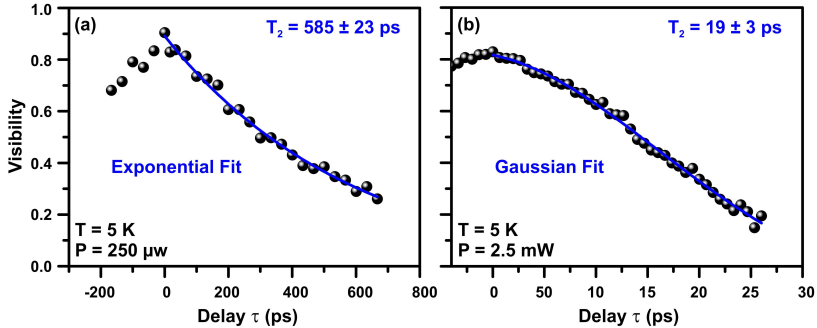


Figure 6.3: First-order correlation function measured via a Michelson interferometric visibility measurement. For the experimental conditions in (a) $P = 250 \mu\text{W}$ the visibility decay versus delay time can be reproduced with an exponential fit to the data. In contrast, the higher excitation power in (b) $P = 2.5 \text{ mW}$ leads to a Gaussian decay of the QD emission visibility.

sion has Lorentzian lineshape. In contrast, Fig. 6.3(b) shows a gaussian decay of the visibility with a distinctly shorter coherence time of $T_2 = 19 \text{ ps}$ for a QD excited at an excitation power of $P = 2.5 \text{ mW}$, thus revealing a *Gaussian* lineshape of the QD emission characteristic for a system in the slow modulation regime. In agreement with the observations of Berthelot *et al.*, at a low temperature the system is in the fast modulation regime at low powers, whereas slow modulation occurs at higher excitation powers.

6.2 Experimental results

The investigations on the effect of phonon-assisted incoherent excitation (PAIE) have all been measured on the planar sample structure described in chapter 4.3. First experimental indications of PAIE are shown in Fig. 6.4(a). The experimental conditions reveal that the laser excitation is energetically blue-detuned from the emitter by $\Delta = \hbar(\omega_L - \omega_{\text{QD}}) = 596 \mu\text{eV}$. Interestingly enough, even though the laser is non-resonant, considerable emitter intensity can be observed in the $\mu\text{-PL}$ spectrum. Due to a typical energetic s- to p-shell separation of $\sim 25 \text{ meV}$ it can be ruled out that the laser excites electron-hole pairs into higher energetic QD shells. Figure 6.4(b) shows the corresponding

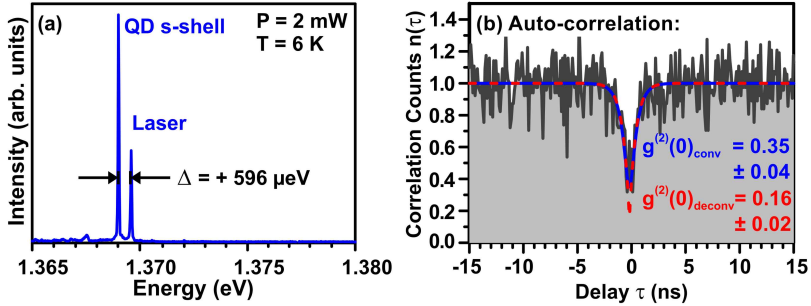


Figure 6.4: Demonstration of photon-assisted incoherent excitation of a single QD. (a) μ -PL emission spectrum of a QD non-resonantly excited via a cw laser. Even though the laser is detuned by $\Delta = 596 \mu\text{eV}$ from the QD s-shell, the QD reveals significant emission intensity. (b) Corresponding auto-correlation measurement on the QD s-shell proving almost background-free single-photon emission with a deconvoluted anti-bunching value of $g^{(2)}(\tau)_{\text{deconv}} = 0.16 \pm 0.02$ (convoluted: $g^{(2)}(\tau)_{\text{conv}} = 0.35 \pm 0.04$).

auto-correlation measurement of the QD emission. The single-photon emission nature can be proven unambiguously via a $g^{(2)}(0)_{\text{conv}}$ -value of 0.35 ± 0.04 . Deconvolution with respect to the setup time resolution of 450 ps yields $g^{(2)}(0)_{\text{deconv}} = 0.16 \pm 0.02$.

To gain more insight into the effect of the phonon-induced incoherent excitation, the cw laser was scanned over the QD resonance in steps of $\sim 15 \mu\text{eV}$. Under constant excitation power, a μ -PL spectrum was taken at each step. The gathered spectra are depicted in Fig. 6.5(a). This near resonance scan reveals appreciable QD emission over a long range of frequencies even detuned from the s-shell resonance. The persistent continuous presence of the QD signal for a relatively large range of laser energies rules out excitation of the QD via the quantized energy eigenstates of the dot itself. Instead, this is a first indication that the excitation of the QD over a continuum of frequencies might be attributed to the presence of the phonon bath. Via phonon coupling the QD is effectively excited by either emitting ($\Delta > 0$) or absorbing ($\Delta < 0$) phonons which compensate for the energy difference between the excitation source and the exciton s-shell energy. Figure 6.5(b), which shows a zoom into the region $\Delta \approx 0$, displays the fine frequency (resonance) scan over the QD s-shell with a step size of $\sim 2 \mu\text{eV}$. The

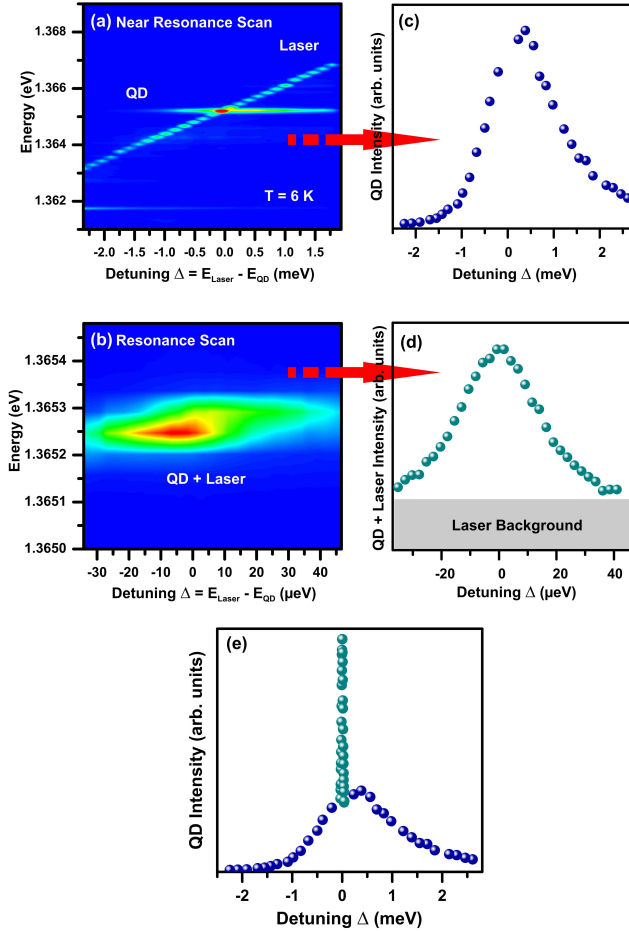


Figure 6.5: (a) Near resonance scan: The excitation laser energy was varied systematically in steps of $\sim 15 \mu\text{eV}$ to scan over the QD s-shell with a constant power of $P = 500 \mu\text{W}$. As is evident from the color plot, emission from the QD can be traced continuously. (b) Resonance scan: Detailed scan over the QD s-shell in steps of $\sim 2 \mu\text{eV}$ revealing the onset of resonance fluorescence around $\Delta = 0$. (c-d) QD and combined QD+laser stray-light emission intensity extracted from (a) and (b), respectively. (e) QD intensity profile: Combination of (c) and (d).

increase of the signal towards $\Delta = 0$ reflects the clear onset of resonance fluorescence which overtakes the laser stray-light intensity in the composite fluorescence and laser signal. To evaluate the PAIE effect quantitatively, the QD emission intensity versus detuning is extracted from the scans in Fig. 6.5(a-b). The near resonance scan reveals QD emission in the meV detuning range, where the excitation is mediated by LA phonons. The extracted intensity is asymmetric with respect to zero detuning, this can be explained by the fact that at low sample temperatures phonon-mediated excitation is more likely for the case of a higher energetic laser, since the excitation leads to phonon emission whereas the opposite scenario requires phonon absorption. Figure 6.5(d) depicts the combined QD and laser stray-light intensity extracted from the resonance scan spectra. On top of the nearly constant laser background the resonance fluorescence profile in terms of the ZPL is visible. Combining the evaluation of Fig. 6.5(c) and (d) results in the QD intensity profile depicted in 6.5(e). The aim of the PAIE investigations is to theoretically explain and model these intensity profiles. In the following, the theory in terms of the polaron master equation will be introduced, the influence of different theoretical parameters on the intensity profiles will be investigated, and the theoretical model will be compared to experimentally derived data sets.

6.2.1 Theory

The effect of phonon-assisted incoherent excitation is theoretically modelled with the polaron master equation introduced in chapter 4.7. The explicit expression for the steady-state exciton population reads

$$\bar{N}_x = \frac{1}{2} \left[1 + \frac{\Gamma_{\text{ph}}^{\sigma^+} - \Gamma_{\text{ph}}^{\sigma^-} - \gamma}{\Gamma_{\text{ph}}^{\sigma^+} + \Gamma_{\text{ph}}^{\sigma^-} + \gamma + \frac{4\eta_x^2(B)^2\gamma_{\text{pol}}}{\gamma_{\text{pol}}^2 + \Delta^2}} \right]. \quad (6.6)$$

For the planar system of interest, the QD intensity from the vertical decay channel of the sample is simply $I_{QD} \propto \bar{N}_x$. What is important is that, Eq. 6.6 includes the detuning and pump dependence of the phonon-induced scattering rates. For the PAIE effect the $\Gamma_{\text{ph}}^{\sigma^+}$ rate plays a major role, since this process describes the phonon-assisted incoherent excitation responsible for the phonon side wings which are predicted theoretically and observed experimentally. The PAIE process is illustrated in Fig. 4.8. It is worth mentioning that for the PAIE-calculations the cross-dephasing rate γ_{cd} has been neglected, due to its

negligible influence on the observations of phonon-assisted incoherent excitation.

Before the experimental results are compared to the theoretical predictions, it is very instructive to have a closer look at the influence of the different parameters ω_c , T , α_p , η_x , γ and γ' on the resulting QD intensity profile. The calculated intensity profiles are depicted in Fig. 6.6. One parameter is varied as indicated in the graph, whereas the other parameters are kept fixed according to $\omega_c = 0.5 \text{ meV}$, $T = 6 \text{ K}$, $\alpha_p = 6 \times 0.06\pi^2 ps^2$, $\gamma = 0.8 \mu\text{eV}$ (823 ps), $\gamma' = 0.8 \mu\text{eV}$ (823 ps), $\eta_x = 12 \mu\text{eV}$. In the following, the physical meaning of the parameters and their influence on the QD intensity profile will be discussed in detail.

(a) Cut-off frequency

The cut-off frequency ω_c is proportional to the inverse QD size [70], therefore it is higher for dots with smaller height. The effective form factor for different dot sizes that characterizes the exciton-phonon coupling strength is depicted in Fig. 6.2. For smaller dots (higher cut-off frequency) the effective form factor covers a larger range in k -space, thus phonons with higher k -vectors couple to the exciton as compared to larger dots (with lower cut-off frequency). Due to this, the phonon side wings show a strong dependence on ω_c . With increasing cut-off frequency the phonon replica cover a larger range of energies. In addition, the maximum of the phonon side wings shifts to higher detuning Δ values. Both effects result from the effective form factor dependence on the QD size and therefore the cut-off frequency.

(b) Temperature

With increasing temperature T the phonon side wings on the higher and lower detuning side of the ZPL become more symmetric. The average thermal occupation number of the phonon mode \mathbf{k} at a temperature T is described by the Bose-Einstein statistic, according to

$$n_{\mathbf{k}} = \frac{1}{(\exp(\hbar\omega_{\mathbf{k}}/k_B T)) - 1} \quad . \quad (6.7)$$

At low T $n_{\mathbf{k}}$ is small, therefore the probability of phonon absorption $\Delta < 0$ is less likely than phonon emission $\Delta > 0$, leading to asymmetric

phonon side wings. With increasing temperature these features become more symmetric due to the increasing phonon occupation, according to Eq. 6.7. In addition, the phonon features become more intense with increasing temperature.

(c) Coupling Constant

The coupling constant α_p is a material parameter that includes the deformation potential constants of electrons and holes. It defines the strength of exciton-phonon coupling. Due to this, the phonon side wings are more intense for a larger coupling constant. In the graph (...) denotes $(0.06\pi^2 ps^2)$.

(d) Pump rate

The pump rate η_x is linked to the Rabi frequency via the definition $\eta_x = 2\Omega$. With increasing pump strength the effect of phonon-assisted excitation becomes more effective, therefore the phonon side wings gain in intensity.

(e) Radiative decay

Compared to the parameters discussed above, γ as well as γ' have a very small influence on the phonon side wings. Increasing the radiative decay rate γ leads to a broadening of the ZPL of the QD intensity profile. Larger γ means a shorter T_1 -time of the system, hence the coherence time decreases as well, reflected by the broader ZPL.

(f) Pure dephasing

Pure dephasing γ' accounts for dephasing effects besides linear exciton-phonon coupling which is explicitly included in the polaron master equation approach. An increase in γ' broadens the ZPL, due to the decrease in the emission coherence. Overall, the pure dephasing rate has only a minor effect on the QD intensity profile, as visible in the graph.

For modelling the experimental data, three of the parameters discussed above are derived independently. The temperature T of the sample is measured. The pump strength η_x is linked to the Rabi frequency

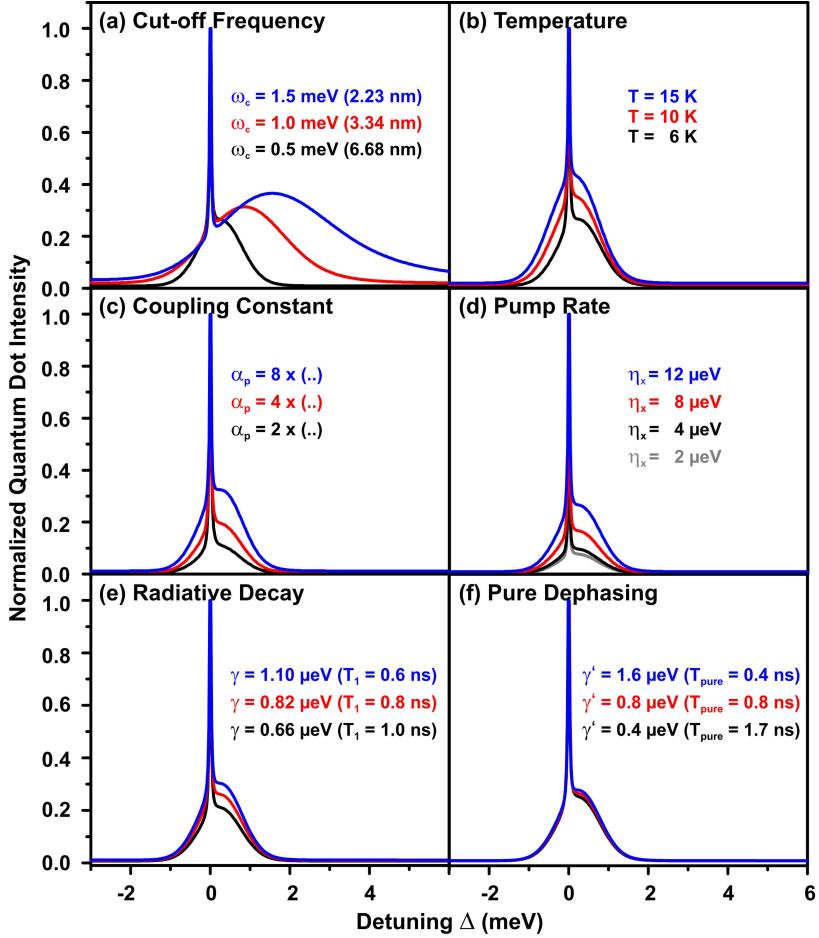


Figure 6.6: Theoretical investigations of the influence of the relevant parameters on the intensity profile of the QD emission. While keeping the other parameters fixed ($\omega_c = 0.5$ meV, $T = 6$ K, $\gamma = 0.8$ μeV (823 ps), $\gamma' = 0.8$ μeV (823 ps), $\eta_x = 12$ μeV , $\alpha_p = 6 \times (0.06\pi^2 ps^2)$), the (a) phonon bath cut-off frequency ω_c , (b) temperature T , (c) coupling constant α_p , the (d) pump rate η_x , the (e) radiative decay rate γ and the (f) pure dephasing rate γ' were systematically increased as indicated in the graphs.

of the system, it can therefore be extracted from the Mollow triplet center-to-sideband splitting extracted from HRPL measurement data under resonant QD excitation. The decay rate γ can be derived from time-resolved photoluminescence measurements (TCSPC). The other three parameters ω_c , α_p and γ' are used as fit parameters in the data modelling.

6.2.2 Experiment versus Theory

To compare the theoretical predictions of Eq. 6.6 to experimental results, combined near resonance and resonance μ -PL scans have been evaluated in terms of normalized QD intensity versus detuning. For the investigation two scans on the same QD were taken, but at a different sample temperature T and excitation strength η_x , respectively. The results of these scans are displayed in Figs. 6.7(a) and (b) as black data points. The raw experimental data reveals strong resonance fluorescence emission of the QD near $\Delta \approx 0$ in terms of the ZPL. Moreover, a less intense, but distinctly broad QD phonon-assisted emission with a corresponding detuning range between $\Delta \approx -1.5$ meV and $+2$ meV can be traced clearly. The data was modelled with a fit derived from the polaron master equation theory as described above, indicated by red solid lines. To unambiguously identify the physical process resulting in the phonon side wings, the theoretical calculation with $\Gamma_{\text{ph}}^{\sigma^+}$ turned off is depicted as a dashed blue line in the graph. For $\Gamma_{\text{ph}}^{\sigma^+} = 0$ only the ZPL can be reproduced, but no phonon side wings are expected theoretically. This confirms that the laser-driven incoherent excitation process is the dominant phonon-scattering process.

For a quantitative modelling of the data the sample temperature T , pump rate η_x , and radiative decay γ were derived experimentally by independent measurements and are therefore fairly accurate values within their experimental margin of error. η_x can be accessed experimentally by measuring the Rabi frequency of the system. The corresponding on resonance HRPL spectrum is depicted in the inset of Fig. 6.7(a). The center-to-sideband Rabi-splitting Ω is found to be $(16.7 \pm 0.7 \mu\text{eV})$, giving $\eta_x = \frac{2\Omega}{2\pi} = (5.32 \pm 0.23 \mu\text{eV})$. The decay time for most of the QDs in the sample is found to be rather similar due to no preferential radiative enhancement of selective QDs by Purcell-like effects. Independent time-correlated photon counting measurements have revealed a typical radiative decay time of $(750 - 850 \text{ ps})$, which gives $\gamma \approx (0.77 - 0.88 \mu\text{eV})$.

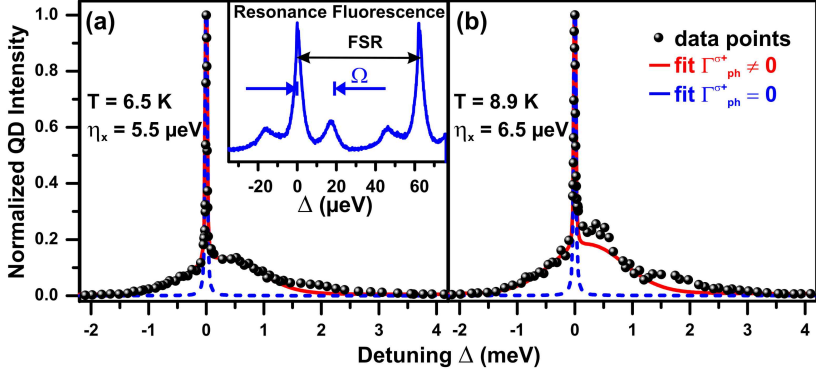


Figure 6.7: Intensity profiles: Integrated QD intensity derived from a combined near resonance and resonance scan (similar to those depicted in Fig. 6.5) plotted as a function of laser-QD detuning. The scans were performed at different temperatures and different excitation strengths (Rabi frequencies). Black filled circles: Experimentally derived data points. Red solid line: Theoretical fits to the data including $\Gamma_{ph}^{\sigma^+} + \Gamma_{ph}^{\sigma^-}$. The following values are used to reproduce both data sets: $\omega_c = 0.6 \text{ meV}$, $\alpha_p = 6 \times 0.06 \times \pi^2 ps^2$, $\gamma = 0.82 \text{ } \mu\text{eV}$ (803 ps) and $\gamma' = 0.6 \text{ } \mu\text{eV}$ (1097 ps). The thermally averaged bath displacement operator is calculated to be $\langle B \rangle = 0.91$ for the conditions in (a) and $\langle B \rangle = 0.87$ for (b). Inset: HRPL spectrum with the characteristic resonance fluorescence spectrum in the spectral domain, revealing a Rabi frequency (center-to-sideband splitting) of $\Omega = 16.7 \pm 0.7 \text{ } \mu\text{eV}$. The blue dashed line shows the theoretical expectations for the $\Gamma_{ph}^{\sigma^+}$ process turned off. Under these conditions the theory can reproduce only the ZPL, but no phonon side wings, giving clear evidence that the phonon-assisted incoherent excitation process is the origin of the LA phonon replica.

The coupling constant describing the interaction between the exciton and the LA phonons via deformation potential $\alpha_p = 6 \times 0.06 \pi^2 ps^2$, the pure dephasing rate $\gamma' = 0.6 \text{ } \mu\text{eV}$ (1097 ps), and the cut-off frequency $\omega_c = 0.6 \text{ meV}$ are then derived via fitting. The values are not affected by temperature or excitation strength, therefore they are the same for the two different intensity scans in Fig. 6.7.

The theoretical fits show very good agreement with the experimentally derived data points. It should be mentioned that in most of our measurements the experimentally extracted phonon side wing intensity shows a dip at a certain detuning, whereas the fit is smooth and

monotonically decreasing with increasing detuning Δ , similar to the situation in Fig. 6.7(b) (dip at ~ 1 meV). A recent publication by Nysteen *et al.* [139] suggests a theoretical explanation of this quenching of phonon-induced processes at certain detunings via electron-hole asymmetries. The red line in Fig. 1(a) in their publication shows the QD population that reveals a similar behavior as the experimental data in Fig. 6.7(b). For their study they used different wave functions for electrons and holes, because due to the different effective masses of the carriers the confinement in the QD potential and the eigenenergies are different. At a certain detuning (corresponding to a certain phonon energy) it is therefore possible that the different deformation potential constants for electrons and holes can be compensated by the different wave functions, leading to a suppressed coupling of certain phonon-modes. In the polaron master equation-based theory, which is used to model the data in Fig. 6.7, the same wave functions for electrons and holes are assumed. In this case the suppressed phonon interaction would appear at infinite detuning. The spectral position of the dips that correspond to suppressed phonon coupling is dependent on the QD material composition and also on the exact QD potential.

6.2.3 Emission coherence

Photon-visibility measurements have been performed via Michelson interferometry to determine the coherence properties of photons emitted under both resonant and off-resonant excitation conditions. Figure 6.8(a) shows the sinusoidally-varying visibility of the QD emission under strictly resonant excitation which indicates the presence of the Mollow triplet in the spectral regime. The data was fitted by the following function

$$\begin{aligned}
 g^{(1)}(\tau) &= \frac{1}{2} \exp(-\gamma_{center}\tau) \exp(i\omega\tau) \\
 &+ \frac{1}{4} \exp(-\gamma_{side}\tau) \exp(i(\omega - \Omega)\tau) \\
 &+ \frac{1}{4} \exp(-\gamma_{side}\tau) \exp(i(\omega + \Omega)\tau) \quad , \quad (6.8)
 \end{aligned}$$

which is the Fourier transform of the spectral Mollow triplet (see Eq. 4.21), according to the *Wiener Khintchine theorem*. The following denotations are used: $\gamma_{center} = 2\gamma_{pol}$ and $\gamma_{side} = \gamma_{pol} + \gamma_{pop}$, as defined

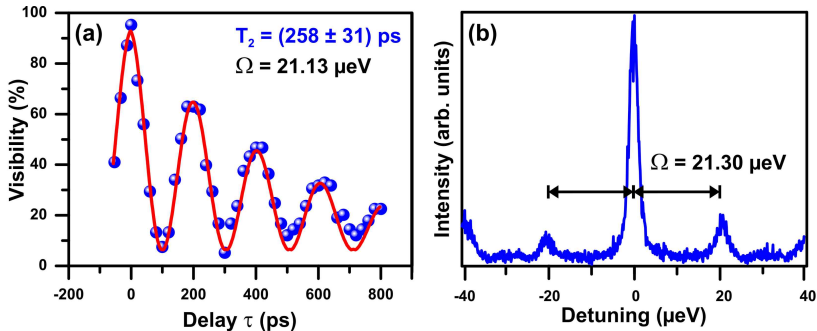


Figure 6.8: (a) Visibility of a Michelson interferometric coherence time measurement of the QD emission under resonant excitation ($\Delta = 0$). The oscillations in the visibility-delay time plot indicate the different Mollow triplet frequency components in the spectral domain. The oscillation period reveals a Rabi frequency of $\Omega = 21.1 \mu\text{eV}$. From the overall exponential decay of the visibility, a coherence time of $T_2 = 258 \text{ ps}$ is extracted. (b) Corresponding HRPL measurement. The Rabi frequency $\Omega = 21.3 \mu\text{eV}$ extracted from the Mollow triplet center-to-sideband splitting is in excellent agreement with Ω extracted from the visibility-oscillations.

in Eqs. 4.25 and 4.26.

Via the decay of the visibility-oscillations, a coherence time of $T_2 = 258 \pm 31 \text{ ps}$ is extracted. The oscillations period of the visibility of $\tau_{osc} = 196 \text{ ps}$ reflects the Rabi frequency $\Omega = 21.1 \mu\text{eV}$ of the resonantly excited QD. This value can be compared to the renormalized Rabi frequency extracted from the HRPL data depicted in Fig. 6.8(b). The Mollow triplet center-to-sideband splitting of $\Omega = 21.3 \mu\text{eV}$ is found to be in excellent agreement with the value derived from the visibility oscillations. It is worth mentioning that even under strictly resonant excitation the emission is not *Fourier transform-limited*, which may be attributed to spectral diffusion effects.

As a comparison, the emission coherence was also measured under the non-resonant excitation conditions of phonon-assisted excitation. Figure 6.9 depicts Michelson interferometric visibility measurements for three different detuning conditions Δ . The data is fitted with a *Gaussian* function and reveals a coherence time of (a) $T_2 = 17 \text{ ps}$ at

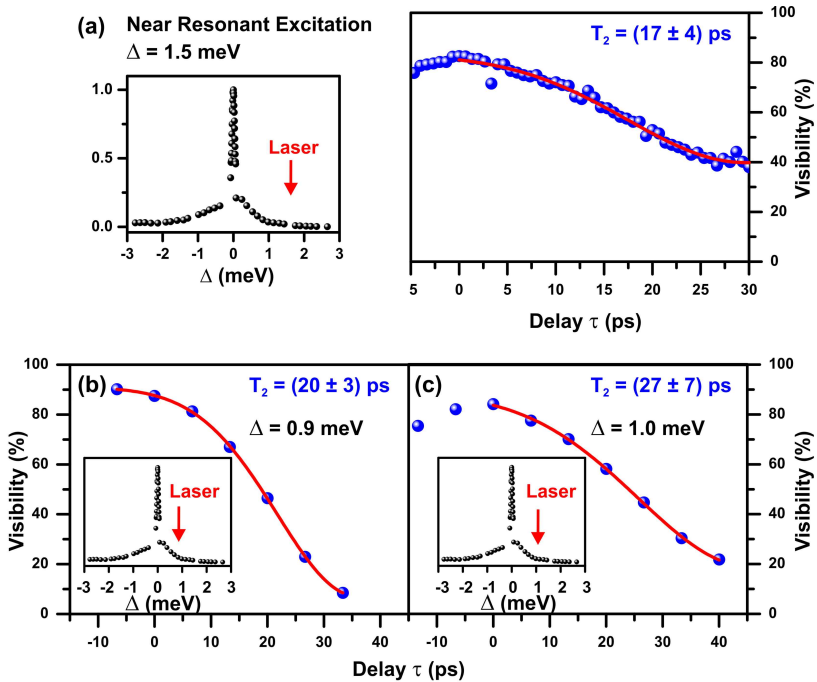


Figure 6.9: The QD visibility under phonon-assisted incoherent QD excitation reveals short T_2 -times of 17 ± 4 ps for $\Delta = 1.5$ meV, 20 ± 3 ps for $\Delta = 0.9$ meV, and 27 ± 7 ps for $\Delta = 1.0$ meV. In comparison to the longer resonance coherence of 258 ± 31 ps, the distinctly shorter coherence times can be attributed to the phonon-assisted incoherent excitation process. Solid lines are the corresponding Gaussian fits to the experimental data.

$\Delta = 1.5$ meV, (b) $T_2 = 20$ ps at $\Delta = 0.9$ meV, and (c) $T_2 = 27$ ps at $\Delta = 1.0$ meV. The coherence is found independent of the specific excitation-QD s-shell emission detuning. It is rather limited compared to the value under resonant excitation. This might be attributed to the phonon-assisted excitation mechanism that induces additional dephasing compared to the resonant emitter-state preparation, resulting in an emission coherence approximately 10-times higher.

6.3 Discussion

It is worth mentioning that QD excitation via phonon-coupling is observed to be efficient and approximately 20% of the QD intensity is achieved with respect to strictly resonant excitation with the distinct advantage that the laser stray-light can easily be separated from the QD emission.

Besides the described above off-resonant pumping, which leads to QD s-shell emission, the opposite effect of resonant QD excitation and detuned phonon-assisted QD emission should also be observed experimentally. It should not be withheld that in the experiment it was not possible to trace phonon side wings under resonant s-shell excitation. This might be attributed to the very weak intensity of the phonon features compared to the intense ZPL dominating the spectrum. Nevertheless, this effect was monitored recently by Matthiesen *et al.* [100], the corresponding spectrum is shown in the inset of Fig. S6(b) of the supplementary material of their publication.

One of the advantages of carrier-phonon interaction for QD state preparation was pointed out by Glässl *et al.* [140]. In their publication they show that the exciton and biexciton state of a QD can be prepared with high fidelity on a picosecond timescale when a strong but slightly off-resonant laser pulse is applied to the system. The exciton-phonon interaction leads to a relaxation of the system towards the dressed states and was found to be very robust in terms of pulse intensity and detuning, provided that the pulse is strong enough. In fact, the performance of the presented protocol is shown to be better the stronger the carrier-phonon interaction is. One drawback of this kind of emitter state preparation might be the low emission coherence, which has been found to be limited under cw phonon-assisted excitation, as discussed in chapter 6.2.3. It is worth mentioning that very recent experimental investigations by M. Müller and co-workers [141] revealed similar coherence times for a system that is excited via resonant two-photon absorption compared to the scenario where the excitation is slightly detuned from the two-photon resonance and mediated via phonons. These investigations point towards the fact that the phonon-mediation apparently does not destroy the coherence of the emitted photons. The difference compared to the *cw* coherence time investigations presented above is the *pulsed* excitation of the system. A possible explanation might be

based on the fact that under cw excitation phonons are continuously present in the system and their interaction with the electron-hole pair leads to a limited coherence of the emission. Under the pulsed excitation conditions, with pulse length of a few tenth of ps [141], phonons are only present for short periods of time, compared to the electron-hole pair recombination time usually in the range of ~ 800 ps. This might be the reason why phonons do not affect the emission coherence under pulsed off-resonant excitation. These contrary observations are indeed interesting, but a profound explanation cannot be given at the current stage of research. Detailed experimental investigations will be needed in the regime of cw as well as pulsed excitation to further consolidate the experimental results and to find a convincing theoretical description.

Chapter 7

Non-resonant quantum dot-cavity coupling

Effects of emitter-mode coupling are usually described in the Jaynes-Cummings picture that considers the interaction of a TLS with the photon mode of the surrounding cavity. When the detuning between the emitter and cavity resonance is increased by a few linewidths out of resonance, the mode intensity is expected to decrease considerably. This behavior has been consistently observed for atoms coupled to optical microcavities [142]. In contrast recent investigations in solid state cavity QED have traced unexpectedly intense mode emission even for large spectral detunings between emitter and cavity. This effect is usually referred to as non-resonant coupling (NRC).

Initial reports about NRC date from Hennessy *et al.* [143] and Press *et al.* [144]. In these pioneering studies of 2007 NRC has been explored under strong-emitter mode coupling via photon cross-correlation measurements. The experimentally detected anti-correlation between emitter and mode emission indicates, that the mode is non-resonantly fed by the single quantum emitter. On the basis of these studies great achievements have been made to investigate the emission characteristics of non-resonantly coupled QD-mode systems in the strong, as well as in the weak coupling regime.

The experimental work of Suffczyński *et al.* [145] reveals insight into the emission dynamics of the non-resonantly coupled mode. Systematic time-resolved experiments show that the cavity emission is governed by the dynamics of the spectrally closest QD state. In the case of two

similarly detuned dots, the emission at the mode energy is driven by the spectrally widest QD state.

The effect of NRC is also of special interest when considering resonant QD excitation. Whereas the emission from the quantum emitter is superimposed by laser stray-light from the excitation laser, the mode can be employed for a background-free monitoring of distinct emitter characteristics. Therefore several studies focus on exploring NRC under resonant excitation conditions [146, 147], e.g. Ates *et al.* [63] have been able to monitor the exciton fine-structure splitting via the off-resonant cavity mode. Additionally, Ulhaq *et al.* [148] present the effect of linewidth broadening and emission saturation with increasing excitation power via monitoring the off-resonant cavity emission.

Besides the common procedure of exciting the QD and observing the non-resonantly coupled mode signal, the opposite scenario of pumping the cavity can lead to a clear and selective excitation of a QD, spatially located close to the electric field maximum of the cavity mode [149].

Recently it has been shown that selective excitation of one QD can lead to the emission of another spectrally detuned dot mediated by an off-resonant cavity [150, 151]. Additionally NRC has been verified on site-controlled QDs [152], as well as on a QD coupled to an external cavity [153]. What is interesting in terms of applications is also the work by Strauf *et al.* [154] where lasing has been achieved from QDs non-resonantly coupled to a photonic crystal cavity.

7.1 Theoretical descriptions of NRC

In the past years many groups have presented different theoretical models to provide a fundamental explanation of NRC [83, 155–157]. Basically the effect of NRC can be classified into two different regimes, i.e. small detuning between the QD exciton and the coupled cavity mode ($\Delta = E_{QD} - E_{mode}$) with $\Delta < 3$ meV and large emitter-mode detuning $\Delta > 5$ meV. The theoretical explanations for the physical origin of NRC is inherently different for these two regimes, as will be discussed in the following.

7.1.1 NRC for large emitter-mode detunings

Based on their experimental findings of NRC for large detunings beyond $\Delta \sim \pm 10$ nm ($\Delta \sim \pm 15$ meV) under wetting layer excitation of

the QD, two studies of the Finley group [158, 159] attribute the physical origin of NRC to multi-exciton or charged exciton effects. They propose so-called *photon-induced shake-up processes*, in which charged exciton decay takes place into a continuum of final states, where the holes are distributed between the dot and the wetting layer continuum. The transitions that are energetically in resonance with the cavity mode can effectively feed photons into the mode and contribute to the observed mode emission. A more refined version of this theory has been presented by Winger *et al.* [160]. Their theoretical calculations are based on multi-excitonic eigenstates with up to 18 electron and 32 hole states including spin. Due to the variety of initial and final states the possible transitions merge to a quasi-continuum that gives rise to background emission that feeds the mode. Subsequent experimental studies of Laucht *et al.* [161] reveal a superlinear power dependence of the mode emission, indicating that the emission stems from multi-excitons. This strongly supports the theoretical explanation by Winger *et al.*, which is additionally substantiated by the investigation of the temporal evolution of the photoluminescence of the system.

7.1.2 NRC for small emitter-mode detunings

NRC for small emitter-mode detunings was initially explained by pure dephasing effects. Neasby *et al.* [162] have introduced a quantum mechanical description where pure dephasing is modelled via different output reservoirs coupled to the cavity or the QD respectively. With their theoretical approach they are able to reproduce the intensity-shifting effect of NRC from the emitter to the cavity frequency. Additionally, they present a very instructive mechanical analog within their publication to illustrate how pure dephasing events cause NRC.

In accordance with Neasby *et al.*, Auffèves *et al.* [163] also attribute the NRC effect to pure dephasing. In their publication they have highlighted the usability of NRC for wavelength-stabilized single-photon sources robust against spectral diffusion.

Other theoretical approaches model the energy transfer from the QD to the detuned mode via mediation of acoustic phonons. Hohenester *et al.* [164] introduces the phonon-assisted scattering between QD and cavity mode within the framework of the independent boson Hamiltonian. The energetic difference between the excitonic s-shell emission energy and the detuned cavity is compensated by the emission or absorption of a phonon with corresponding energy. The calculations predict a

strong asymmetry in the phonon-assisted scattering rate for positive and negative exciton-cavity detunings, explainable due to the unequal probabilities of phonon emission and absorption at low temperatures. This asymmetry is also manifested in the decay times of the emitter for different detunings. These theoretical predictions are compared with experimental results and are found to be in good agreement, thus validating the theoretical model further.

Kaer *et al.* [165] employ a non-Markovian model taking into account memory effects of the phonon bath. Similar to Hohenester, they find a phonon-induced asymmetry when detuning the cavity from the QD resonance. Additionally they discuss the phonon-induced lowering of the effective coupling strength g , which was found to change the criterion for strong and weak coupling.

Roy *et al.* [71] have modelled NRC under resonant excitation. The polaron-based master equation approach includes the interaction with an acoustic phonon bath up to all orders. Their study puts special emphasis on the emission characteristics of the Mollow triplet dependent on the emitter-cavity detuning.

NRC for resonant s-shell excitation of the QD has also been theoretically described by Majumdar *et al.* [166]. In their work they show that a pure dephasing model is not able to theoretically explain NRC under resonant excitation. The cavity emission is attributed to so-called cavity-enhanced phonon processes. Their results demonstrate that these phonon-mediated processes effectively extend the detuning range in which off-resonant QD-cavity coupling may occur beyond what is given by pure dephasing processes.

Furthermore Kaer *et al.* [167, 168] have investigated the influence of non-Markovian phonon-induced processes for a coupled QD-cavity system on the indistinguishability of photons emitted by the QD and the cavity respectively.

Summarizing the current understanding of the NRC phenomenon for the regime of small emitter-mode detunings under consideration of the above-mentioned publications, it can be concluded that non-resonant coupling is a combined effect originating from pure dephasing and electron-phonon coupling. Pure dephasing includes electron-phonon as well as carrier-carrier scattering, whereas the contribution of electron-phonon coupling is a direct mediation of the energetic discrepancy between exciton and cavity-mode energy via phonon absorption or emission.

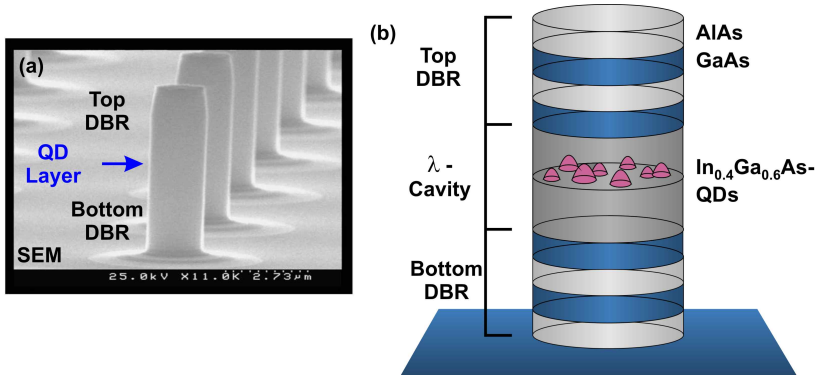


Figure 7.1: (a) Scanning electron microscope image (SEM) of a micropillar sample (by courtesy of University of Würzburg). (b) Schematic depiction of a cylindrical micropillar cavity. Self-assembled $\text{In}_{0.4}\text{Ga}_{0.6}\text{As}$ -QDs are embedded at the center of a GaAs- λ -cavity sandwiched between top (29-pair) and bottom (26-pair) distributed Bragg reflectors (DBRs) composed of $\lambda/4$ -thick periods of alternating AlAs/GaAs.

7.2 Micropillar sample structure

For the investigations of non-resonant emitter-mode coupling, micropillar cavities as depicted in Fig. 7.1 are employed. The sample was grown by molecular-beam epitaxy (MBE) on a (001)-oriented undoped GaAs substrate [169, 170]. It was fabricated by the *Technische Physik, Universität Würzburg* by the group of Prof. Alfred Forchel.

Initially, a planar sample structure is grown, in which the vertical mode confinement is achieved by distributed Bragg reflectors (DBRs) consisting of quarterwavelength-thick layers of GaAs and AlAs as high reflectivity mirrors on either side of a GaAs one λ -thick-cavity (29-pair of top and 26-pair of bottom DBRs). The self-assembled $\text{In}_{0.4}\text{Ga}_{0.6}\text{As}$ -QDs are grown in *Stranski-Krastanow* growth mode [171]. Here the deposition of InAs on the GaAs substrate primarily leads to the formation of the so-called two-dimensional *wetting layer*, compressed uniformly due to the higher lattice constant of InAs compared to GaAs. Further deposition of InAs increases the in-plane strain, which is finally relaxed by the formation of small islands called self-assembled QDs. For three-dimensional carrier confinement the QDs are overgrown by

another layer of the GaAs substrate. This layer of self-assembled QDs with a lateral dot density of approximately $6 \cdot 10^{-9} \text{cm}^{-2}$ is located in the middle of the λ -cavity. The approximately lens-shaped dots have typical diameters ranging between 20 – 35 nm and a height of 3 – 4 nm. Due to the intermixing of InAs with the GaAs substrate at elevated growth temperatures, the QDs also contain Ga atoms. For the sample under investigation the Ga content is approximately 60% [172].

In order to fabricate arrays of high-quality micropillar cavities from the planar sample structure, an optimized technique of electron-beam lithography and reactive ion etching in an inductively coupled Ar/Cl_2 plasma has been employed. Via this method circular pillars with cross-section diameters ranging from $1.5 \mu\text{m}$ up to $4 \mu\text{m}$ are produced. Due to the optimized etching process a very smooth pillar surface with few structural defects is achieved, resulting in a small amount of optical losses due to photon scattering at surface irregularities, while providing strong and uniform optical confinement. Therefore the micropillars have high quality factors exceeding $Q > 10000$ on average. The sample is finally cleaved parallel to the pillar rows for optimal pillar accessibility under the use of the side-excitation technique described in chapter 3.1.

The electrical field confinement in the pillar causes the formation of certain eigenmodes within the cavity. A detailed analytic derivation of the eigenvalue equation has been carried out by *Wolfgang-Michael Schulz* [62]. In Fig. 7.2 the theoretically calculated mode emission energies are compared to the corresponding experimentally measured μ -PL spectrum of a pillar with a nominal diameter of $1.75 \mu\text{m}$. The spectrum has been taken at high excitation powers under electron-hole pair creation above the bandgap, therefore it reveals only the distinct mode energies, whereas the QD intensities are small due to the saturation of the emitters. The theoretically calculated energetic positions of HE- and EH-hybrid modes are in very good agreement with the experimentally measured fundamental mode (FM) and higher-order mode energies. The slight discrepancies can be attributed to the idealized assumption of a cylindrical resonator. Deviations from the circular pillar shape lead to a splitting of degenerate eigenmodes as shown by *Ates et al.* [174]. Additionally, the calculation does not include the relative intensities of the modes, which might explain the missing EH_{11} mode in the spectrum of Fig. 7.2(a).

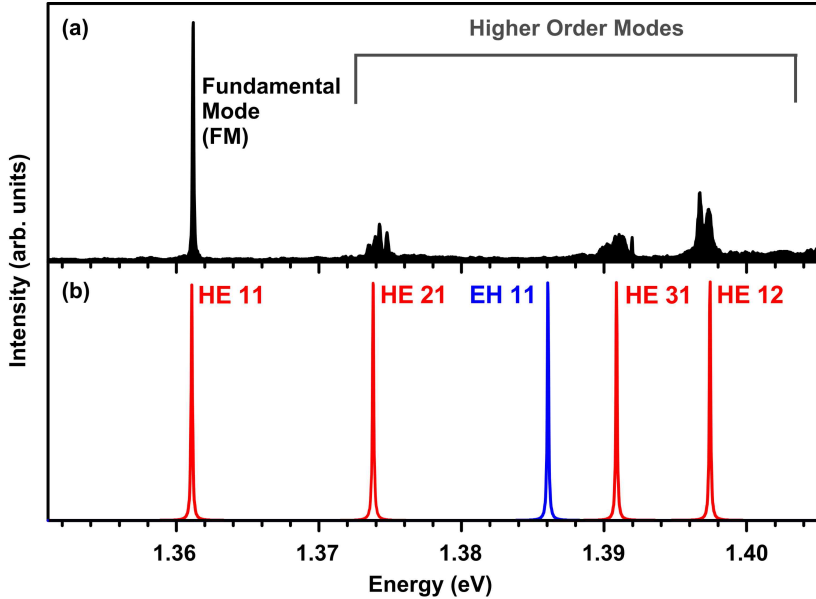


Figure 7.2: (a) High-power μ -PL spectrum of a pillar with a nominal diameter of $1.75 \mu\text{m}$ under carrier excitation above the bandgap. The spectrum reveals the distinct mode emission energies. Due to saturation at high excitation powers the QD intensities are small compared to those of the modes and therefore not visible in the spectrum. (b) Theoretically calculated micropillar eigenenergies for a pillar diameter of $1.74 \mu\text{m}$ and a refractive index of $n_{\text{GaAs}} = 3.45$ and $n_{\text{AlAs}} = 1$ respectively [62, 173].

7.3 NRC under quasi-resonant QD excitation

All results of the study of non-resonant emitter-mode coupling presented in this chapter are measured on a QD-cavity system with a pillar diameter of $3.5 \mu\text{m}$. The focus of the investigations is to study the coupling between a single QD and the fundamental mode (HE_{1,1} mode referred to as FM) as well as the spectrally closest first excited mode (denoted as M2), with respect to the emission characteristics of the system.

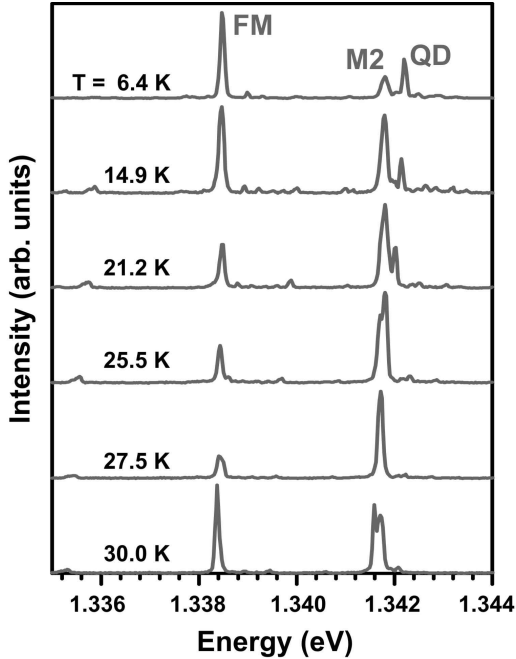


Figure 7.3: Series of temperature-dependent micropillar emission spectra taken under pulsed p-shell excitation of the QD ($P = 80 \mu\text{W}$). The system under investigation consists of a QD, the spectrally close first excited mode (labeled as M2), and the fundamental mode (FM) of the pillar cavity. The quality factors of the two modes are found to be $Q_{FM} \simeq 15000$ and $Q_{M2} \simeq 8000$ respectively.

7.3.1 Temperature-dependent μ -PL

A temperature-dependent μ -PL series depicted in Fig. 7.3 has been taken under pulsed p-shell excitation of the QD (excitation $\sim 24 \text{ meV}$ above the QD s-shell) for initial characterization of the system. At low temperatures of $T \sim 6 \text{ K}$, photons originating from the excitonic s-shell emission have an energy of 1.3422 eV , blue detuned from both the FM (1.3384 eV) and M2 (1.3418 eV) emission channels. With increasing sample temperature T the QD as well as the FM and M2 emission shifts to lower energies, due to the temperature dependencies of the bandgap $E_{gap}(T)$ and the refractive indices $n(T)$ of the material. A change of

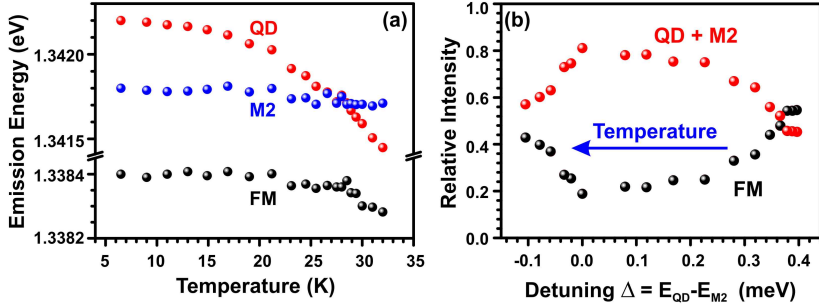


Figure 7.4: (a) Emission energy of QD, M2 and FM versus temperature T extracted from Fig. 7.3 respectively. The crossing of QD and M2 emission as a typical sign of weak-coupling is visible at $T = 27.5$ K. (b) Relative FM intensity and combined QD + M2 intensity as a function of detuning Δ , revealing strong emission-intensity anti-correlation.

the bandgap is accompanied by a change in the QD s-shell emission energy which exceeds the change of mode energies with temperature ruled by $\Delta n(T)$, according to

$$\Delta E_{QD}(T) \approx \Delta E_{gap}(T) \gg \Delta E_{mode}(\Delta n(T)) \quad . \quad (7.1)$$

This difference in temperature shift leads to the fact that the originally higher energetic QD can be tuned through the mode resonance to its lower energetic side by systematically increasing the sample temperature. A crossing between the QD and M2 is observed at $T = 27.5$ K, as a typical feature of a cavity-emitter system operating in the weak coupling regime. Due to the fact that at low T the FM is far-detuned from the excitonic s-shell emission ($\Delta E_{QD-FM} \approx 3.8$ meV), a crossing between QD and FM emission energies could not be achieved experimentally. The emission energies of QD, FM and M2 are depicted in Fig. 7.4(a), revealing the different shift-strength of mode and QD s-shell emission as well as the crossing between QD and M2.

Based on the μ -PL-measurement data, the integrated relative intensities of the QD and M2 signals have been analyzed according to

$$I_{QD+M2}^{rel} = \frac{\int (I_{QD} + I_{M2}) dE}{\int (I_{QD} + I_{M2} + I_{FM}) dE} \quad (7.2)$$

in comparison to the relative FM intensity

$$I_{FM}^{rel} = \frac{\int I_{FM} dE}{\int (I_{QD} + I_{M2} + I_{FM}) dE} \quad (7.3)$$

as a function of the detuning $\Delta(T) = E_{QD} - E_{M2}$. The results are depicted in Fig. 7.4(b). The data reveals a clear increase of the relative QD + M2 emission signal around resonance $\Delta \rightarrow 0$ at the expense of the relative FM intensity. This indicates predominant non-resonant QD emission coupling to the spectrally nearest mode M2 and points to a pronounced anti-correlation between the single QD and two distinct modes of the surrounding microcavity under study.

7.3.2 Correlation measurements

To gain deeper insight into the emission-correlations of the system that are already indicated by the anti-correlation in the combined QD + M2 versus FM relative intensities, correlation measurements have been performed on all possible combinations of the three emission channels of the spectrum. The experiments have been carried out under pulsed QD p-shell excitation at $T = 6.4$ K. The corresponding histograms are depicted in Fig. 7.5(a)-(e). Figure 7.5(a) shows the auto-correlations of the QD s-shell emission, in which almost background-free single-photon emission with a Poisson-normalized value of $g_{QD}^{(2)}(0) = 0.10 \pm 0.01$ was verified. In addition to the QD the auto-correlations on FM and M2 also reveal a suppressed central peak with $g_{FM}^{(2)}(0) = 0.56 \pm 0.03$ and $g_{M2}^{(2)}(0) = 0.64 \pm 0.03$, respectively. This reflects an anti-correlation in the time domain of the individual mode emissions, but it also indicates time-uncorrelated background contribution within the mode signals. The anti-correlation can be attributed to the pre-dominant non-resonant feeding of the modes by the QD under investigation. The non-vanishing zero-delay time peak can be explained by the spectrally broad laser pulse under quasi-resonant excitation of the QD p-shell. In addition to the p-shell of this QD, the laser with a spectral width of $\geq 650 \mu\text{eV}$ has spectral overlap with higher energetic shells of other QDs in the pillar. This becomes obvious in the μ -PL spectra in Fig. 7.3, where besides the three emission channels under investigation different other tiny emission lines can be seen. These additionally excited QDs can also couple non-resonantly to the two modes, leading to uncorrelated background with respect to the QD under study.

Even though the auto-correlations already indicate the coupling between the emitter-modes system, these measurements are not suffi-

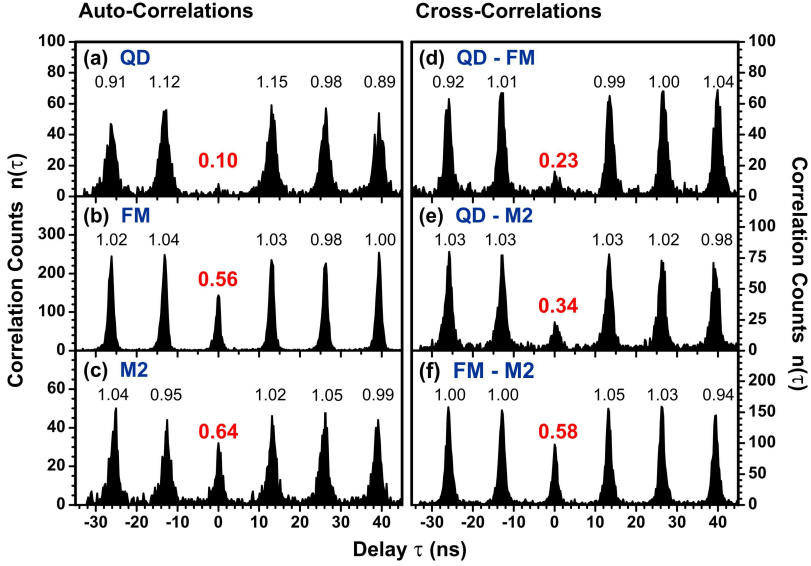


Figure 7.5: Photon-correlation measurements of the coupled QD, M2 and FM system under pulsed QD p-shell excitation (experimental conditions $T = 6.4$ K, $P = 110$ μ W). (a) Auto-correlation of the QD signal revealing almost background-free single-photon emission. [(b) and (c)] Auto-correlations of the individual M2 and FM decay channels, demonstrating sub-Poissonian statistics indicative of dominant coupling to a single-photon emitter. [(d) and (e)] Cross-correlations between QD-FM and QD-M2, proving dominant feeding of each distinct mode via non-resonant coupling to the single QD. (f) Cross-correlation of FM-M2, showing pronounced anti-correlation between both signals.

cient to prove the coupling of the system. Therefore in a second step cross-correlation measurements have been performed between all three emission channels, to prove that the suppressed zero-delay peak ($\tau = 0$) in the FM and M2 auto-correlations originates from the fact that mainly photons from the detuned QD under investigation contribute to these signals. The experimentally obtained results of the cross-correlation central peak value are $g^{(2)}(0)_{QD-FM} = 0.23 \pm 0.02$, $g^{(2)}(0)_{QD-M2} = 0.34 \pm 0.02$ and $g^{(2)}(0)_{FM-M2} = 0.58 \pm 0.03$, clearly demonstrating that the system of single QD and two distinct cavity modes is highly correlated. For the correlations between the QD and

the two individual mode emissions the anti-bunching of the central peaks clearly proves that the QD predominantly feeds both the modes via non-resonant coupling. Moreover, an anti-correlation between FM and M2 has also been experimentally verified (see Fig. 7.5(f)), revealing that the photons emitted by the two modes are anti-correlated as well. In other words, coupling of the driving single-photon source (QD) to either mode (M2 or FM) appears exclusively, i.e. transfer of energy to M2 or FM will not appear at the same cycle of QD excitation. This is verified by the suppressed coincidence rate in Fig. 7.5(f). As expected, it is found that all cross-correlation $g^{(2)}(0)$ -values are in between the corresponding auto-correlations zero-peak values of the contributing decay channels.

7.3.3 Decay time and coherence time measurements

To investigate the emission dynamics of the system, TCSPC measurements under pulsed p-shell excitation have been performed to derive the decay time τ_{dec} of all three emission channels of the system. The results are shown in Figs. 7.6(a)-(c). As expected for systems operating in the weak emitter-mode coupling regime, the decay time of the QD emission decreases towards QD-M2 resonance $\Delta \rightarrow 0$. The Purcell enhancement factor of the QD-M2 system has been calculated from the ratio $\tau_{dec}^{\Delta \gg 0} / \tau_{dec}^{\Delta=0}$ and found to be $F_{PE} = 7.1 \pm 1.4$. For the photon emission of M2, predominantly originating from the non-resonantly coupled QD, an almost identical change in the radiative decay time τ_{dec}^{M2} with a pronounced decrease towards zero detuning Δ has been extracted from the TCSPC measurement data. Figure 7.6(b) shows the raw TCSPC measurement data for all three emission channels at $\Delta = 79 \mu\text{eV}$ ($T = 25.5 \text{ K}$). The first order of magnitude of the transient decay was fitted with a mono-exponential function, which reveals the decay time τ_{dec} of the photon emission. For these experimental conditions nearly identical decay times of $\tau_{dec}^{QD} = 242.5 \pm 45 \text{ ps}$ for the QD and $\tau_{dec}^{M2} = 226.3 \pm 45 \text{ ps}$ for the M2 emission have been derived. As visible from Fig. 7.6(a) the trend of emission dynamics is found to be maintained throughout the non-resonant coupling into M2. It is worth mentioning that the TCSPC raw measurement data displayed in Fig. 7.6(b) cannot be fitted with a mono-exponential function in the full delay time range. The deviation from a single mono-exponential decay in time resolved μ -PL can be attributed to different origins, a detailed discussion about the possible reasons of the non-exponential

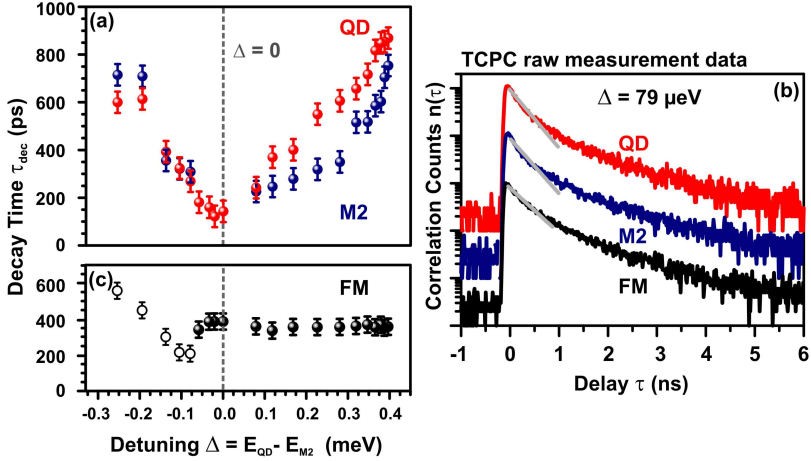


Figure 7.6: (a) Radiative decay time τ_{dec} of QD and M2 under pulsed p-shell excitation ($P = 70 \mu\text{W}$) as a function of spectral detuning Δ , revealing almost identical behavior of both emission channels. (b) Corresponding TCSPC transient data for $\Delta = 79 \mu\text{eV}$ with mono-exponential fits, to extract τ_{dec} . (c) Radiative decay time of the FM emission, revealing an almost constant τ_{dec} unperturbed by the detuning Δ .

decay behavior is given in chapter 6.1.1.

When comparing the QD and FM emission, they are found to be distinctly detuned, so no Purcell induced decay time decrease is expected for the non-resonantly coupled FM photon emission. From Fig. 7.6(b) the FM emission at $\Delta = 79 \mu\text{eV}$ shows a decay time of $\tau_{dec}^{FM} = 359 \pm 47$ ps. Indeed the dynamics of the FM effectively remains the same for all detunings shown here, with $\tau_{dec}^{FM} \sim 350$ ps. This value is smaller as the expected radiative decay time of the QD emission with no Purcell enhancement of the emitter, i.e. $\tau_{dec} \sim 800$ ps. The shorter decay time can be attributed to contributions from other additionally excited QDs in the pillar, due to the fact that the emission dynamics of the non-resonantly coupled mode follows the spectrally closest QD [145]. The extracted lifetimes of the FM for higher temperatures, i.e. detunings $\Delta < -0.1$ meV, are found to deviate slightly from the expected nearly constant τ_{dec}^{FM} value because of the contribution of an extra QD tuning into the mode at these temperatures. The correspond-

ing data points are depicted as open circles in Fig. 7.6(c). This second QD also feeds the FM and influences its emission dynamics due to its spectral vicinity [145].

To conclude the detailed studies on the emission characteristics of the coupled QD and multi-mode system, a Michelson interferometer was used to perform $g^{(1)}(\tau)$ -type coherence time measurements on all three emission lines. For a damped two-level system including radiative decay and pure dephasing as described in chapter 2.3.3 the coherence time T_2 is linked to the radiative lifetime T_1 and the pure dephasing time T_{pure} according to the following equation:

$$\frac{1}{T_2} = \frac{1}{2T_1} + \frac{1}{T_{pure}} \quad . \quad (7.4)$$

Here T_1 denotes the spontaneous emission lifetime of an exciton in the s-shell which is only slightly different from τ_{dec}^{QD} derived via TCSPC measurements. Under the assumption that there is only radiative recombination of the carriers in the QD the decay time can be extracted from a mono-exponential function to the first decade of the measurement data. For quasi-resonant excitation conditions the value of τ_{dec}^{QD} additionally includes the carrier relaxation between p- and s-shell which is in the range of 10 – 20 ps, and can be safely neglected in the following discussion, i.e. $T_1 \approx \tau_{dec}$.

The evaluated coherence time results are depicted in Figs. 7.7(a) and (b). For the QD we observe the theoretically expected behavior that can be explained with the aid of Eq. 7.4. At low temperatures, approaching resonance $\Delta \rightarrow 0$ from positive values, the coherence time decreases as a consequence of the Purcell-induced decay time reduction experimentally observed in TCSPC measurements. It is well worth noting that T_2 of the QD emission does not increase again for negative detunings, unlike the decay time T_1 . The low coherence time is due to the increased influence of pure dephasing processes like phonon-scattering, which become dominant at higher temperatures. In contrast to the QD emission, the coherence time of both M2 and FM are essentially not affected by tuning the QD into M2 can be seen in Figs. 7.7(a) and (b). This observation can be explained by two reasons. First of all the mode emission is mediated by non-resonant coupling of the QD to the modes. This coupling effect accounts for some extra dephasing mechanism that the photons undergo while being transferred into either mode. Therefore, the pure dephasing rate (T_{pure}^{-1}) in Eq. 7.4 for non-

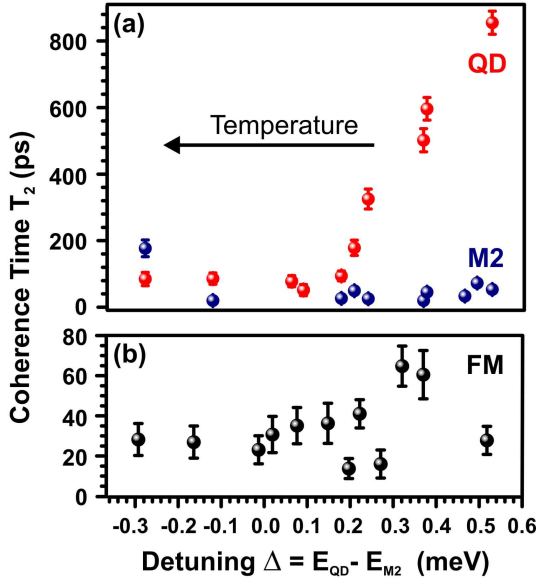


Figure 7.7: [(a) and (b)] Results of QD, M2 and FM coherence time T_2 measurements. The T_2 of the QD reveals significant variations with detuning (and therefore also temperature), in contrast to the two coupled modes. For M2 and FM, T_2 is found to be constant and rather limited due to additional dephasing inherent to non-resonant coupling.

resonantly coupled modes becomes rather high, compared to the pure dephasing of the QD s-shell emission. This leads to a shortening of the mode coherence times compared to the one of the QD. Another reason for the low and almost constant mode coherences is the quality of the cavity modes. Due to the Q -factor each mode allows a certain spectral bandwidth in which the QD can non-resonantly couple. Therefore the coherence of the mode emissions is also determined by the quality of the individual modes. For the coherence times of the two modes depicted in Fig. 7.7 the following average values are found $T_2^{FM} = 34$ ps and $T_2^{M2} = 54$ ps. These T_2 -times are in the same range than the coherence times extracted from the linewidth of the two modes. Namely they are found to be $\tau_{coh}^{FM} = 45$ ps and $\tau_{coh}^{M2} = 26$ ps. Due to this reason it can

be concluded that the mode emission coherence can be enhanced by employing cavities with higher Q -factors. The experimentally derived low coherence of the mode emissions gives an important indication of the limitation of non-resonantly coupled sources. The low coherence of the mode emission will for example affect the indistinguishability of consecutively emitted photons, whereas a high two-photon interference visibility is required for many application in quantum information technology.

7.4 NRC under resonant QD excitation

In addition to the investigations under pulsed p-shell excitation presented above, μ -PL measurements under resonant s-shell excitation with a narrow band cw laser pumping the QD have been carried out. Excitation power-dependent spectra were taken while keeping the laser strictly at the resonance frequency of the s-shell of the QD exciton. The results are depicted in a color plot (logarithmic scale) in Fig. 7.8. It can easily be observed that the spectrally-detuned M2 and FM signals appear sequentially with gradually increasing excitation power P . For excitation powers below $P \sim 2 \mu\text{W}$, only M2 emission is observable, whereas at intermediate levels ($P \sim 8 \mu\text{W}$) we find a M2 : FM intensity ratio of $\sim 52 : 1$ and $\sim 41 : 1$ at $P = 40 \mu\text{W}$ due to the increasing FM emission strength. The emission of the detuned mode signals is again a sign of NRC between the excited QD and the coupled cavity modes. It should be emphasized that the non-resonantly coupled FM is detuned by 3.7 meV from the resonantly excited QD. This is in between the value of the two different regimes of small and large emitter-mode detuning where the non-resonant coupling can be attributed to distinctly different physical origins as presented in chapter 7.1. It is therefore worth to shortly discuss the possible origins for the observed intensity of the non-resonantly coupled FM.

Due to the strictly resonant emitter state preparation, the theories presented above for NRC in the regime of large detunings can be excluded as possible explanations for the observed non-resonant coupling of the QD to the FM. Instead, these theories are based on off-resonant wetting layer excitation therefore including a quasi-continuum of possible transitions in the theoretical description [160]. Here we observe the NRC effect even in the absence of excited states.

The theories on NRC in the regime of small detunings attribute the

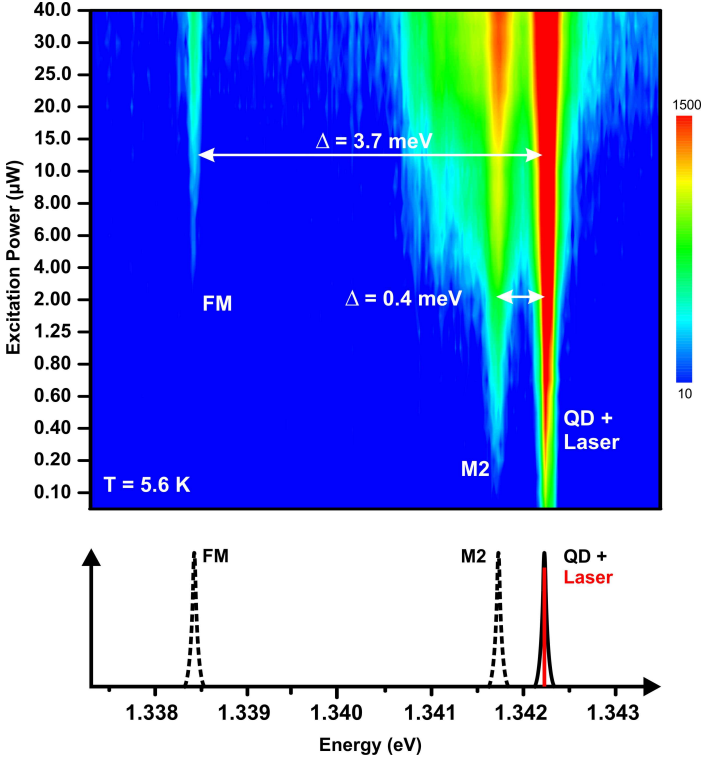


Figure 7.8: Excitation power series of coupling between the single QD and the multimode system under strictly resonant QD s -shell excitation. As illustrated in the lower panel, QD and laser are in resonance and the two signals cannot be spectrally distinguished. The data clearly reveals the power dependence of non-resonant coupling of the excited quantum emitter to two distinctly detuned cavity modes with spacings up to ~ 3.7 meV.

coupling to phonon-mediation in combination with pure dephasing. As it has already been mentioned in Ref. [157], phonon-assisted cavity feeding can play a dominant role for dot-cavity systems with detunings in the order of a few millielectron volts. Additionally, the coupling range of the acoustic phonons and also the corresponding coupling strength depend on the size of the QD [75]. For the current experimental situation of low sample temperatures but with the mode on the lower energetic side of the QD emission, the suggested explanation is non-

resonant QD-FM coupling via acoustic phonon emission. These high energetic phonons are at the tail end of the phonon density of states, therefore much higher excitation-powers are needed to trace NRC for the FM compared to the spectrally close M2.

The results on non-resonant emitter-mode coupling presented in this chapter have been published by Weiler *et al.* [175].

Chapter 8

Conclusion and Outlook

Conclusion

The investigations in this thesis focus on two main aspects. One is the detailed investigation of the emission properties of the Mollow triplet under resonant emitter state preparation above saturation. The other is the profound examination of dephasing effects in semiconductor quantum dots. Resonant emitter excitation in combination with suppression of dephasing effects caused by the interaction of the exciton with the solid state surrounding medium is beneficial for the creation of close to *Fourier transform-limited* highly indistinguishable photons.

Different laser stray-light suppression techniques have paved the way for a detailed and systematic analysis of the resonance fluorescence emission above emitter saturation with a high signal-to-noise ratio. The detuning-dependent Mollow triplet emission was studied with special focus on the dephasing due to longitudinal acoustic phonons interacting with the electron-hole pair inside the QD. The study clearly revealed the distinct differences of a solid state QD emitter structure in contrast to a bare two-level system without phonon- and/or carrier-assisted dephasing. The joint experimental theoretical study revealed Mollow triplet sideband broadening with increasing laser-detuning away from the QD s-shell resonance; thus the coherence of the Mollow sidebands decreases with increasing detuning, as concluded from the *Wiener-Khintchine theorem*. From a theoretical point of view, Mollow triplet sideband narrowing can be achieved for samples where the excitons in QDs un-

dergo much smaller dephasing compared to the planar MOVPE-grown sample, which was employed for the study presented in this thesis. In order to use the Mollow triplet sideband photons for possible applications, a narrow linewidth is beneficial for the generation of photons with long coherence times. A route to achieve Mollow triplet sideband narrowing is to use MBE-grown sample structures and/or QDs embedded in microcavities. In these structures *Purcell* enhancement can be employed to reduce the lifetime of the electron-hole pair in the QD, hence pure dephasing effects such as phonon scattering can be reduced due to a shorter possible interaction time with the exciton [64].

With the aid of a sophisticated filtering technique based on a double Michelson interferometer it was possible to measure the two-photon interference of the Mollow triplet sideband emission. Under the conditions of strictly resonant continuous wave excitation the *Hong-Ou-Mandel* type interference experiments revealed a close to ideal post-selected interference contrast with photon indistinguishabilities up to 97%. The data was found to be in excellent agreement with emission pre-characterization values derived from systematic independent measurements. These investigations revealed almost background-free single-photon emission from the Mollow sidebands with a deconvoluted second-order auto-correlation value as low as $g^{(2)}(0) = 0.03$ and a Mollow sideband emission coherence of $T_2 \sim 250$ ps. The emission of the sidebands was found to be not *Fourier transform-limited*, due to excitation-induced dephasing. A possible route to increase the sideband coherence is to reduce the Rabi splitting via applying lower excitation power. In a previous study the cascaded photon emission between the Mollow triplet sidebands had already been verified [57]. The combination of both characteristic features, cascaded photon emission among and indistinguishable photon emission of the individual Mollow sidebands, makes them a very attractive source for possible applications in quantum information processing.

For the verification of indistinguishable photons from the Mollow triplet sidebands, a background-free Mollow triplet was a crucial requirement. It has frequently been experimentally observed that the resonance fluorescence emission deviates from the Mollow triplet and reveals a typical Mollow quintuplet structure. In a combined experimental/theoretical study it has been shown that this observation has a profound physical cause and is not due to coincidental excitation of two nearby QDs with

degenerate s-shell energies. Instead, the effect of Mollow quintuplet emission can be explained theoretically by the excitation of an exciton in one of the two spectrally close fine-structure components of the QD exciton. The combined integrated spectrum results in the Mollow quintuplet structure. For experimental investigations the background-free Mollow *triplet* emission of one exciton fine-structure component is desirable. This can be achieved by either employing a suitable QD, with one exciton fine-structure aligned parallel to the polarization of the excitation laser. In this case the other fine-structure component is perpendicular to the laser polarization and will not be excited. Another option to achieve this geometry is to tilt the sample or the excitation laser with respect to the QD. An alternative approach is to suppress the Mollow triplet of one exciton fine-structure via polarization filtering in the detection path, if the experimental technique of polarization suppression is not already used for laser stray-light suppression.

The dephasing in solid state QDs has been studied in terms of deformation potential coupling of longitudinal acoustic phonons to excitons. The analysis unequivocally proved that phonon-assisted incoherent excitation is the mechanism that leads to the creation of an electron-hole pair by an energetically off-resonant laser via phonon mediation. The influence of the different parameters on the quantum dot intensity profile has been verified systematically. Whereas pure dephasing and radiative decay influence the QD intensity profile only slightly, the increase in the coupling strength, temperature, cut-off frequency and excitation strength increase the QD emission intensity under phonon-assisted incoherent excitation. The emission coherence has been found to be $T_2 \sim 20$ ps under these non-resonant excitation conditions and therefore one order of magnitude lower compared to the coherence under strictly resonant excitation of $T_2 = 258$ ps. This knowledge is particularly important for the emission coherence under pulsed resonant excitation conditions. Due to the fact that these laser pulses are spectrally broader compared to the width of the laser under continuous wave excitation, the excitation leads to direct resonant electron-hole pair creation as well as phonon-assisted off-resonant excitation. Therefore the emission coherence under pulsed resonant excitation might be lower compared to cw resonant excitation conditions. In addition, phonon-assisted incoherent excitation can be employed to gain insight into the QD size as well as the exciton-phonon coupling strength α_p . Via the theoretical modelling of the experimentally derived intensity plots the

diameter height of the QD under investigation has been found to be $d = 5.6 \text{ nm}$ ($\omega_c = 0.6 \text{ meV}$) and the exciton-phonon coupling strength $\alpha_p = 6 \times (0.06\pi^2 ps^2)$. Phonon-assisted incoherent excitation offers the advantage of off-resonant excitation with the distinct benefit, that no laser stray-light suppression is necessary. Experimentally it has been found that the QD emission intensity reaches up to 20% compared to strictly resonant excitation.

The second study of dephasing properties of semiconductor QDs was carried out on a QD embedded in a micropillar sample structure. In the study the emission properties of a non-resonantly coupled system of a single QD coupled to two distinct modes of the surrounding cavity were analyzed systematically under electron-hole pair creation into the QD p-shell. Whereas both mode emissions reveal the expected decay time dynamics due to *Purcell* enhancement, the coherence times of the non-resonantly coupled mode emissions reveal $T_2 \sim 40 \text{ ps}$ and are therefore limited compared to the maximum QD emission coherence of $T_2 \sim 820 \text{ ps}$. In addition to the investigations under quasi-resonant excitation, a power-dependent micro-photoluminescence series revealed non-resonant coupling under strictly resonant excitation conditions. The observation of non-resonant coupling even for large emitter-mode detunings up to $\Delta = 3.7 \text{ meV}$ under resonant excitation reveals insight into the origin of non-resonant coupling. It rules out possible explanations via so-called *photon shake-up mechanism*, which are based on a multitude of involved QD states, and points towards acoustic phonon-mediation as the origin of non-resonant emitter mode coupling.

The studies presented in this thesis were published in various journals, the references and the corresponding chapters are given below.

- Chapter 4 is based on the publications: Detuning-dependent Mollow triplet of a coherently-driven single quantum dot [78] and Mollow quintuplets from coherently excited quantum dots [79].
- Chapter 5 is based on the publication: Postselected indistinguishable single-photon emission from the Mollow triplet sidebands of a resonantly excited quantum dot [87].
- Chapter 6 is based on the publication: Phonon-assisted incoherent excitation of a quantum dot and its emission properties [80].

- Chapter 7 is based on the publication: Emission characteristics of a highly correlated system of a quantum dot coupled to two distinct micropillar cavity modes [175].

Outlook

Up to now, investigations of the spectral Mollow triplet have been performed under cw resonant excitation. From an application point of view, triggered photon generation is desirable, and this demand makes profound studies of the Mollow triplet emission properties under pulsed excitation indispensable. First experimental studies of pulsed resonant excitation were performed in the *Heitler* regime below emitter saturation [100], but the regime above emitter saturation has not been investigated experimentally so far. For pulsed resonant excitation, spectrally narrow laser pulses have to be created. This can, for example, be realized with an electro-optic modulator where the laser output signal can be controlled by an applied bias voltage.

In a theoretical publication Moelbjerg *et al.* [176] calculated the Mollow triplet dressed state emission under strong optically pulsed excitation. Due to the fact that the Rabi frequency of the system changes within the laser pulse, which leads to interference effects, triggered excitation results in several - more than the usual two - Mollow side peaks. Because of excitation-induced dephasing in the system these side peaks might overlap and thus smear out the spectral feature to one broad line. A detailed experimental study of the *Mollow triplet* under pulsed excitation would be of interest from a fundamental point of view to compare the experimental findings with theoretical expectations. The spectra would also reveal insight into whether the pulsed dressed state emission above saturation is suitable for the generation of triggered indistinguishable photons.

Besides the experimental realization of pulsed resonant excitation another interesting objective is to investigate the properties of resonantly excited QDs embedded in micropillar cavities.

Microcavities offer the distinct advantage that the emission dynamics can be influenced controllably by utilization of the *Purcell* effect. One achievement would, for example, be to reduce the excitonic lifetime inside the QD and therefore also the possible interaction time for phonons as well as carrier-dephasing processes. Via this method the coherence and the indistinguishability of consecutively emitted photons can be enhanced controllably.

For the detection of the QD resonance fluorescence a sufficient signal-to-noise ratio is crucial. Before further investigations can be carried out, the challenging goal of laser stray-light suppression on micropillar samples has to be tackled. Due to the different sample geometry the very effective techniques used for stray-light suppression on planar sample structures are not capable to sufficiently suppress the laser stray-light when micropillar samples are employed. The main reason is the fact that the laser light, which is scattered at the pillar surface, mostly loses its defined polarization. By comparison, the excitation laser light scattered at the smooth surface of the planar sample is found to be highly polarized. Due to this reason the polarization suppression technique is not very effective for micropillar samples and an alternative technique will have to be adopted. To improve the stray-light suppression and thus to make possible a reliable detection of the resonance fluorescence signal, the pillar sample design has been improved. The principle idea is to have an aluminum shadow mask on top of the pillars as can be seen in Fig. 8.1. Under orthogonal excitation-detection geometry, the laser stray-light scattered in the direction of the top-collection is effectively reduced by the shielding effect of the aluminum mask. The sample structure shown below is currently being investigated and continuous improvements are made to reduce the laser stray-light in order to achieve a high signal-to-noise ratio of the resonance fluorescence emission. This will pave the way for resonance fluorescence investigations on QDs in micropillar structures.

For a QD in a micropillar sample another interesting feature that is worth investigating is phonon-mediated population inversion, which was predicted theoretically by Hughes and Carmichael [177, 178]. The effect of phonon-assisted incoherent excitation can lead to population inversion at large driving strength under off-resonant higher energetic laser excitation. This population inversion can be enhanced further if the QD is embedded in a high-quality microcavity structure with the cavity mode located on the higher energetic side of the excitonic s-shell emission. In cavity samples the population inversion cannot only be reached for scenario of exciton excitation described above, but also in the case of cavity pumping, which is accompanied by the annihilation of a cavity photon that leads to the excitation of an electron-hole pair inside the QD, which is basically the reverse process of cavity feeding. Experimentally, the verification of population inversion in the system can be done via first- and second-order auto-correlation measurements

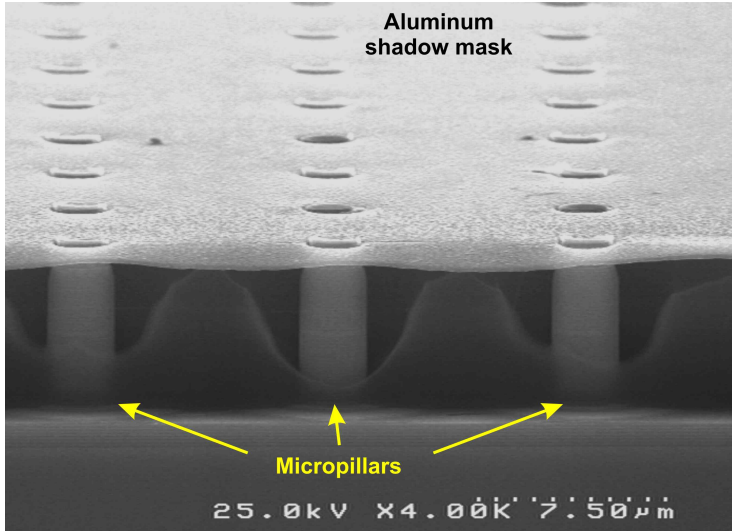


Figure 8.1: Scanning electron microscope image (SEM) of a micropillar sample (by courtesy of University of Würzburg). The micropillars are covered with an aluminum shadow mask for effective laser stray-light suppression under resonant QD excitation.

under increasing excitation strength. At low excitation strength the excitonic emission reveals anti-bunching, due to the fact that the QD is a single-photon source. Under high excitation powers the population inversion leads to stimulated emission and therefore lasing. This is manifested in *Poissonian* statistics of the second-order auto-correlation and additionally accompanied by an increase in the coherence length compared to the regime of spontaneous electron-hole pair recombination.

Hybrid semiconductor-atomic interfaces are a trendsetting approach that could make the storage of the QD emission feasible. In a pioneering study Akopian *et al.* [179] have been able to slow down single-photons from an GaAs QD in atomic Rubidium vapor. For wavelength between the two hyperfine transitions of the D_2 line the atomic vapor shows weak absorption but a steep slope in the dispersion curve, which leads to a slow group velocity. In the publication the photon storage

time was found to be ~ 15 times its temporal width. In addition, it has been shown that the photon polarization is preserved during the propagation through the cell, which is important for quantum memories, if the quantum information is stored in the photons' polarization degrees of freedom.

The study by Akopian and coworkers was performed under non-resonant QD excitation. Another interesting approach would be to investigate the QD-atom interaction under resonant electron-hole pair creation in the regime above and/or below saturation. First experimental tests have been carried out with the Mollow triplet resonance fluorescence emission of In(Ga)As/GaAs QDs sent through atomic caesium vapor. In contrast to the central Rayleigh line, which might contain energetically degenerate laser stray-light, the Mollow triplet sidebands are ideally background-free. The energetic sideband position can be altered systematically by the detuning-dependence of the Mollow triplet sidebands in terms of the effective Rabi frequency. Via this technique a transmission dip could be verified while tuning one Mollow sideband through an atomic resonance. This is a promising starting point for in-depth studies of the possibility to slow down the resonance fluorescence emission, with the distinct advantage of optimized emission coherence.

Kapitel 9

Zusammenfassung

Ziel dieser Zusammenfassung ist es, einen Überblick über die Struktur der vorliegenden Arbeit und den Inhalt der einzelnen Kapitel in deutscher Sprache zu geben.

In **Kapitel 2** werden die theoretischen Grundlagen eingeführt, die für das Verständnis der vorliegenden Arbeit unerlässlich sind. Zuerst wird auf die Eigenschaften niederdimensionaler Halbleiterstrukturen eingegangen. Speziell werden hier die möglichen Energieniveaus für Elektronen und Löcher in null-dimensionalen Quantenpunkt-Strukturen (QP) diskutiert. Dabei können Elektronen-Lochpaare sogenannte Exzitonen in QPen ausbilden, die aufgrund der Coulomb-Wechselwirkung korreliert sind. Unter Berücksichtigung der Spin-Spin-Wechselwirkung zwischen Elektronen und Löchern kann es unter der Voraussetzung eines nicht rotationssymmetrischen QP-Potentials zu einer Feinstrukturaufspaltung zwischen den beiden optisch erlaubten Exziton-Übergängen geben; dieser Sachverhalt wird in Kapitel 2.1.3 dargelegt.

Eine wichtige Kenngröße bei der Charakterisierung der von QPen emittierten Photonen stellt die Ermittlung der Photonenstatistik dar. Die zeitliche Korrelation der Photonen hängt von der Art des Lichtfeldes ab. Die verschiedenen Eigenschaften thermischen Lichts, kohärenter Lichtzustände und von Fock-Zuständen werden in Kapitel 2.2 eingeführt. Bei thermischem Licht treten die Photonen in Bündeln auf, was sich im *Bunching* der Photonenstatistik widerspiegelt, wohingegen bei kohärentem Licht die Photonen zeitlich unkorreliert sind. Fock-Zustände hingegen weisen eine zeitliche Antikorrelation der Photonen auf, die

sich als *Antibunching* in Autokorrelationsmessungen manifestiert.

Zur Beschreibung des mit einem monochromatischen Lichtfeld angeregten Zwei-Niveau-Systems wird der Dichtematrixformalismus eingeführt und der Hamiltonian für das System aufgestellt. Mit seiner Hilfe lassen sich die in Kapitel 2.3 vorgestellten optischen Blochgleichungen unter spezieller Berücksichtigung von Dephasierungstermen gewinnen. Die Emission eines derartigen resonant angeregten Zwei-Niveau-Systems wird als Resonanzfluoreszenz (RF) bezeichnet. In Kapitel 2.3.4 werden die grundlegenden Eigenschaften der RF im Regime unter und oberhalb der Emittersättigung im Bezug auf die spektrale Gestalt der Emission und die Korrelationsfunktion erster und zweiter Ordnung diskutiert.

Das Verhalten eines Zwei-Niveau-Systems in einem umgebenden Resonator wird im Rahmen der Quantenelektrodynamik im Resonator beschrieben. Prinzipiell kann das System sich im Regime starker oder schwacher Kopplung befinden, abhängig vom Verhältnis der charakteristischen Raten des Systems. Für die Untersuchung der nicht-resonanten Kopplung in dieser Arbeit ist speziell das Regime der schwachen Kopplung mit dem hierfür charakteristischen *Purcell-Effekt* relevant, mit Hilfe dessen es möglich ist, die Dynamik des Systems gezielt zu verändern.

Die für die Gewinnung der Messdaten verwendeten experimentellen Techniken werden in **Kapitel 3** kurz eingeführt. Die Basis für alle weitergehenden Messverfahren stellt die in Kapitel 3.1 erläuterte Mikrophotolumineszenz bei kryogenen Temperaturen dar. Von Interesse sind hierbei im Speziellen die Methoden zur effektiven Streulichtunterdrückung (orthogonale Geometrie zwischen Anregung und Detektion, Lochblende und Polarisationsunterdrückung), die es ermöglichen, unter resonanter Quantenpunktanregung das energetisch entartete Laserstreulicht von der QP-Resonanzfluoreszenz zu separieren.

Eine grundlegende Charakterisierungsmethode der QP-Emission ist die Verifizierung der Photonenstatistik. Diese Messung gibt Aufschluss über die zeitliche Korrelation der Photonenemission. Als Autokorrelationen werden hierbei die Korrelationen der Photonen einer einzelnen Emissionslinie bezeichnet, während so genannte Kreuzkorrelationen Informationen über die Emissionskorrelation von Photonen aus verschiedenen Emissionssignalen geben. Die Photonenkorrelationsmessungen werden mit einem *Hanbury Brown & Twiss*-Versuchsaufbau durchgeführt; dieser wird in Kapitel 3.2 erläutert.

Eine weitere zentrale Charakterisierung stellt die Messung der Zerfalls-

zeit eines Elektronen-Lochpaares im QP dar. Die Messtechnik wird als zeitlich korreliertes Einzelphotonenzählen (engl. *time-correlated single photon counting*, kurz TCSPC) bezeichnet; nähere Details werden in Kapitel 3.3 beschrieben.

Eine weitere wichtige Kenngröße der QP-Emission stellt die Kohärenzzeit der emittierten Photonen dar. Diese ist über das *Wiener-Khintchine-Theorem* mit der spektralen Gestalt der Emissionslinie verbunden und kann mit Hilfe der Michelson interferometrischen *Fourier-Spektroskopie* ermittelt werden. In Kapitel 3.4 werden die Messmethode und die Auswertung der experimentell gewonnenen Daten zur Ermittlung der Kohärenzzeit genau erläutert.

Für Photolumineszenzmessungen mit hoher spektraler Auflösung $\Delta E \approx 0.6 \mu\text{eV}$, wie es beispielsweise für die Auflösung der energetisch dicht benachbarten Mollow-Triplett-Linien unter resonanter Anregung vonnöten ist, wird ein *Fabry-Pérot-Interferometer* verwendet, dessen Funktionsweise in Kapitel 3.5 erklärt wird.

Mehrere Untersuchungen in der vorliegenden Arbeit befassen sich mit den Emissionseigenschaften des Mollow-Tripletts, der spektralen Emission unter resonanter QP-Anregung oberhalb der Sättigung. Einführend werden in **Kapitel 4** die grundlegenden Eigenschaften der RF eines Zwei-Niveau-Systems und speziell der QP-RF unter besonderer Berücksichtigung der Festkörperwechselwirkung vorgestellt. In einem einleitenden Literaturüberblick werden die vorliegenden Arbeiten in den Kontext bereits vorhandener Publikationen gestellt. Zudem ist für die Erklärung einiger Eigenschaften der RF eine rein quantenmechanische RF-Beschreibung vonnöten; diese wird in Kapitel 4.2 eingeführt.

Die experimentellen Untersuchungen der RF im vorliegenden Kapitel sowie die Messungen der Ununterscheidbarkeit an den Mollow-Triplett-Seitenbanden und die Experimente zur Phononen-medierte QP-Anregung wurden jeweils an QPen in einer planaren Probenstruktur durchgeführt; diese wird in Kapitel 4.3 vorgestellt.

Für die resonante Anregung von QPen ist die genaue spektrale Ermittlung der QP-s-Schale notwendig; das hierfür angewandte experimentelle Vorgehen wird in Kapitel 4.4 anhand eines Beispiels erläutert. Nachfolgend werden in Kapitel 4.5 die theoretischen Erwartungen für eine RF-Leistungsserie unter strikt resonanter Anregung sowie eine Mollow-Triplett-Verstimmungsserie unter konstanter Anregungsleistung mit experimentellen Ergebnissen verglichen. Schon an dieser Stelle wird deutlich, dass die RF von QPen Abweichungen vom Verhalten eines reinen

Zwei-Niveau-System zeigt und erste Hinweise auf die Wechselwirkung des resonant angeregten Elektronen-Lochpaares mit dem umgebenden Festkörper aufweist.

Ein wichtiges Phänomen, das aus dieser Exziton-Festkörper-Wechselwirkung resultiert, ist die so genannte anregungsinduzierte Dephasierung (engl. *excitation-induced dephasing*, kurz EID); sie wird in Kapitel 4.6 erläutert. EID spiegelt sich in der Verbreiterung der Mollow-Triplett-Seitenbanden bzw. der Dämpfung von Rabi-Rotationen mit steigender Anregungsleistung wider.

Ein theoretisches Modell, das speziell die Wechselwirkung eines Exzitons im QP mit akustischen Phononen in Form von Deformationspotential-Kopplung berücksichtigt, ist die polaronische Master-Gleichung (engl. *polaron master equation*). Die theoretische Modellierung der experimentellen Daten in diesem Kapitel sowie den Untersuchungen in Kapitel 5 und 6 wurde mit einer solchen Theorie, die von *Prof. Stephen Hughes* und seinen Mitarbeitern aufgestellt wurde, durchgeführt. In Kapitel 4.7 wird ein kurzer Überblick über den Formalismus der *polaron master equation* gegeben, zusätzlich wird die physikalische Bedeutung der wichtigsten Kenngrößen erklärt.

Die kombinierte experimentelle und theoretische Untersuchung in Kapitel 4.8 befasst sich mit der Betrachtung der spektralen Breiten und relativen Flächen der Mollow-Triplett-Seitenbanden unter Verstimmung der Laseranregung von der exakten Resonanz der QP-s-Schale. Abhängig vom Verhältnis der Rate purer Dephasierung zur Elektronen-Lochpaar-Rekombinationsrate kann es aus theoretischer Sicht sowohl zu einer Verschmälerung als auch zu einer Verbreiterung der Mollow-Triplett-Seitenbanden mit zunehmender Laserverstimmung kommen. Aufgrund der hohen Dephasierung im System konnte experimentell nur der Fall der Seitenbandenverbreiterung beobachtet werden, diese geht mit einer Reduktion der Kohärenzzeit einher. Der Vergleich der experimentell gewonnenen Daten mit den theoretischen Vorhersagen auf der Basis unabhängiger Messungen zur Ermittlung der Modellierungsparameter liefert eine sehr gute Übereinstimmung. Aus theoretischer Sicht kann eine Verschmälerung der Seitenbanden mit zunehmender Laserverstimmung erreicht werden, wenn statt der in dieser Arbeit verwendeten mittels MOVPE-Wachstum hergestellten Probe eine vergleichbare MBE-Probe verwendet würde, in der Effekte purer Dephasierung deutlich geringer sind. Des Weiteren ist es möglich QPe in Mikrokavitäten zu verwenden, hier kann der *Purcell* Effekt ausgenutzt werden, um die Lebensdauer des Elektronen-Loch Paares zu reduzie-

ren und somit Wechselwirkungen mit dem umgebenden Festkörper auf einen geringeren möglichen Zeitraum zu begrenzen.

Die zweite kombiniert experimentelle und theoretische Untersuchung in Kapitel 4.9 befasst sich mit so genannten Mollow-Quintupletts. Aufgrund der möglichen Feinstrukturaufspaltung des exzitonischen QP-Zustandes kann der anregende Laser prinzipiell in beiden Feinstrukturkomponenten ein Exziton anregen. Die resonante Anregung jeder einzelnen Exziton-Feinstrukturkomponente oberhalb der Sättigung führt spektral zur Emission eines Mollow-Tripletts, die kombinierte integrale Emission beider Feinstrukturkomponenten weist spektral ein Mollow-Quintuplett auf. Die theoretische Vorhersage der auf die beschriebene Weise zustandekommenden Mollow-Quintupletts wird in diesem Kapitel mit Hilfe von experimentellen Messdaten bestätigt. Für viele experimentelle Untersuchungen ist eine möglichst untergrundfreie Mollow *Triplet* Emission notwendig. Um sicherzustellen nur eine Feinstrukturkomponente des Exzitons anzuregen bestehen mehrere Möglichkeiten: Zum einen kann die Geometrie zwischen QP und der Polarisation des anregenden Lasers so gewählt werden, dass eine Feinstrukturkomponente parallel und die andere orthogonal zur Laserpolarisation orientiert ist. In diesem Fall können nur in einer Komponente Elektronen-Loch Paare erzeugt werden. Zum anderen besteht die Möglichkeit mittels Polarisationsunterdrückung im Detektionsstrahlengang eines der beiden Mollow Tripletts zu unterdrücken.

Ziel der in **Kapitel 5** vorgestellten Untersuchungen ist die Verifizierung ununterscheidbarer Photonen von der Emission der Mollow-Triplett-Seitenbanden unter resonanter Laser-Dauerstrichanregung. Für Ununterscheidbarkeitsmessungen ist experimentell die möglichst untergrundfreie Einzelphotonenemission der Emissionsquelle vonnöten. Das theoretisch zu erwartende Resultat der Photonenstatistikmessungen an den einzelnen Mollow-Triplett-Emissionslinien wird in Kapitel 5.1 dargestellt.

Der Versuchsaufbau zur Messung der Ununterscheidbarkeit von Photonen wird in Kapitel 5.2.1 beschrieben. Er ist nach *Hong, Ou* und *Mandel*, den Autoren der ersten Publikation über ununterscheidbare Photonen aus dem Jahre 1987 benannt. Für die untergrundfreie spektrale Selektion der einzelnen Komponenten des Mollow-Tripletts wird ein Doppel-Michelson-Interferometer eingesetzt; dies wird im Detail in Kapitel 5.2.2 erläutert. Sein Funktionsprinzip basiert auf der gezielten Unterdrückung zweier Mollow-Triplett-Linien mittels destruktiver

Interferenz, während die dritte Komponente konstruktiv interferiert. Um die Parameter für die Modellierung der Ununterscheidbarkeitsmessungen mit experimentell unabhängig gewonnenen Werten vergleichen zu können, sind die systematischen Voruntersuchungen zur Ermittlung dieser Parameter den eigentlichen Ununterscheidbarkeitsmessungen vorangestellt. Hier wird im Speziellen die Gewinnung der Mollow-Triplett-Seitenbandenkohärenz mittels einer leistungsabhängigen Mollow-Triplett-Serie erläutert. Die Emission der Seitenbanden unter den gewählten Messbedingungen beträgt $T_2 \sim 250$ ps und ist somit erwartungsgemäß aufgrund des EID-Effekts nicht *Fourier transform limited*. Zudem werden die Autokorrelationsmessungen an den einzelnen Mollow-Triplett-Linien in Kapitel 5.3.2 gezeigt. Die Zentrallinie offenbart die erwartete *Poisson*-Statistik, während das gemessene *Antibunching* auf den Mollow Triplett Seitenbanden mit Minimalwerten bis zu $g^{(2)}(0) = 0.03$ die hochgradig untergrundfreie Einzelphotonemission nachweist, und somit die Stabilität des Doppel-Michelson-Interferometers im Messzeitraum bestätigt. Mit den in Kapitel 5.3.3 gezeigten Messdaten zur Ununterscheidbarkeit auf der roten sowie der blauen Mollow-Triplett-Seitenbande lässt sich die Emission hochgradig ununterscheidbarer Photonen von den Mollow-Triplett-Seitenbanden auch bei verschiedenen Rabi-Aufspaltungen nachweisen. Die Daten weisen einen post-selektierten Interferenzkontrast von bis zu 97% auf. Darüber hinaus stimmen die Werte der theoretischen Modellierung sehr gut mit denen der unabhängigen Vorcharakterisierungen überein. Einzig der experimentell gemessene und mittels Fit gewonnene Wert für die Zerfallszeit des Elektronen-Lochpaares weist Diskrepanzen auf; mögliche Ursachen für diesen Sachverhalt werden in Kapitel 5.3.4 genau erörtert.

In **Kapitel 6** wird die Studie zur sogenannten Phononen-mediierten Anregung eines QPes (engl. *phonon-assisted incoherent excitation*, kurz PAIE) vorgestellt. Die Wechselwirkung des QPes mit dem umgebenden Festkörper beeinflusst die Dephasierung des Systems. In der hier präsentierten Untersuchung wird speziell die longitudinal akustische (LA) Exziton-Phononen-Kopplung untersucht.

Einführend werden die strahlende Rekombination sowie verschiedene Mechanismen, die zur reinen Dephasierung führen, erläutert. Theoretischer Ausgangspunkt der Beschreibung purer Dephasierung, basierend auf linearer Phononen-Exziton-Wechselwirkung, ist das unabhängige Bosonen-Modell. Neben der speziell für diese Arbeit relevanten Kopp-

lung von LA-Phononen mit Exzitonen über das Deformationspotential gibt es prinzipiell noch die piezoelektrische Kopplung an transversal und longitudinal akustische Phononen und die Kopplung von Exzitonen an longitudinal optische Phononen.

Ein weiterer Dephasierungseffekt, der als so genannte spektrale Diffusion bezeichnet wird, ist die Wechselwirkung des Exzitons im QP mit dem elektrischen Feld der Ladungsträger in der unmittelbaren Umgebung des QPes; dieser Effekt wird in Kapitel 6.1.2.3 erläutert.

Der sowohl experimentell als auch theoretisch untersuchte Effekt der Phononen-medierten Anregung, die es erlaubt, den QP nahe, aber nicht resonant der QP-s-Schale über Phononenkopplung anzuregen, wird anhand erster experimenteller Befunde in Kapitel 6.2 eingeführt. Die Extrahierung der Quantenpunktmissionsintensität unter gezielter Verstimmung des anregenden Lasers ergibt den sogenannten QP-Intensitäts-Graphen. Dieser weist neben der Null-Phononen-Linie Seitenbanden auf, die durch die Kopplung akustischer Phononen mit dem Exziton stammen. Die theoretische Modellierung erfolgt mit Hilfe der *polaron master equation*. Der Einfluss der einzelnen Parameter auf den QP-Intensitäts-Graphen wird in Kapitel 6.2.1 diskutiert. Die experimentell gewonnenen Messdaten werden dann mit den theoretischen Erwartungen verglichen. Hierbei zeigt sich eine sehr gute Übereinstimmung. Die Modellierung gewährt zudem Einblicke in die Exziton-Phonon-Kopplung darüber hinaus kann die Größe des QPes ermittelt werden. Für den im Experiment gewählten QP beträgt die Kopplungsstärke $\alpha_p = 6 \times (0.06\pi^2 ps^2)$ und der QP-Höhe $d = 5.6 \text{ nm}$ ($\omega_c = 0.6 \text{ meV}$). Für viele Anwendungen ist eine hohe Kohärenzzeit der Photonenemission vonnöten, aus diesem Grund wird in Kapitel 6.2.3 die Emissionskohärenz unter resonanter Anregung mit der unter PAIE verglichen. Die Kohärenzzeit unter resonanter Anregung ist mit $T_2 = 258 \text{ ps}$ im Vergleich zur ermittelten Kohärenzzeit unter PAIE, die unabhängig von der genauen Verstimmung ungefähr 20 ps beträgt, zehnmal höher. Dieses Wissen ist speziell für die Emissionskohärenz unter gepulst resonanter Anregung wichtig. Im Vergleich zum Laser unter Dauerstrichanregung sind die Laserpulse spektral breiter. Aus diesem Grund werden Elektronen-Loch-Paare sowohl direkt in die QP-s-Schale angeregt, als auch über die PAIE-Anregung erzeugt. Die Kohärenz der Emission unter gepulst resonanter Anregung könnte daher geringer sein, als die unter vergleichbarer Dauerstrichanregung. Bezogen auf die QP-Emissionsintensität unter resonanter Anregung, können mittels PAIE Intensitäten von bis zu 20% erreicht werden, die Anregung bieten den

entscheidenden Vorteil, dass keine Laserstreulichtunterdrückung vorgenommen werden muss.

Kapitel 7 befasst sich mit der Untersuchung der Emissionseigenschaften eines Systems nicht-resonant gekoppelter Moden (Fundamentalmode FM sowie einer Mode höherer Ordnung, die als M2 bezeichnet wird) mit einem QP. In Kapitel 7.1 findet sich ein detaillierter Literaturüberblick über die theoretischen und experimentellen Studien zur nicht-resonanten Kopplung (engl. *non-resonant coupling*, kurz: NRC), zudem wird die physikalische Ursache für die NRC im Regime kleiner sowie großer Emitter-Moden-Verstimmungen diskutiert.

Für die experimentelle Untersuchung wurde die Kopplung eines QPes an die Moden des umgebenden Mikroresonators untersucht. In Kapitel 7.2 wird die Probenstruktur sowie das theoretisch errechnete Modenspektrum für einen derartigen Mikroresonator vorgestellt.

Ausgangspunkt der experimentellen Untersuchungen ist eine temperaturabhängige Mikrophotolumineszenz-Serie unter quasi-resonanter QP-Anregung. Das Kreuzen von QP und der energetisch benachbarten Mode M2 mit steigender Temperatur weist auf ein System schwacher Kopplung mit einem ermittelten *Purcell*-Überhöhungsfaktor von $F_{PE} = 7.1$ hin. Anhand der Auto- und Kreuzkorrelationsmessungen an und zwischen allen drei Emissionskanälen kann nachgewiesen werden, dass der QP nicht-resonant an beide Moden koppelt und diese füttert.

Die TCSPC-basierten Messungen zur Rekombinationszeit in Kapitel 7.3.3 spiegeln den *Purcell*-Effect der schwachen Emitter-Moden-Kopplung wider. Während die energetisch stark verschobene FM keine Änderung in der Zerfallszeit aufweist, unterliegen sowohl QP als auch M2 einer *Purcell*-bedingten Lebensdauerverkürzung nahe der Resonanz. Die Kohärenzzeit der beiden Modenemissionen ist mit $T_2 \sim 40$ ps kurz und unabhängig von der Emitter-Moden-Verstimmung, während der QP bei tiefen Temperaturen außerhalb der Modenresonanz eine deutlich längere Photonenkohärenz von $T_2 \sim 820$ ps aufweist.

Die nicht-resonante Kopplung des QPes konnte auch unter resonanter QP-Anregung verifiziert werden. Mit steigender Anregungsleistung ist zuerst ein Koppeln der energetisch dicht benachbarten Mode M2 ($\Delta = 0.4$ meV) und bei höheren Leistungen auch der energetisch stärker verstimmten Mode FM ($\Delta = 3.7$ meV) zu beobachten. Diese Verifikation nicht-resonanter Kopplung unter resonanter Anregung schließt als mögliche Ursache Erklärungsansätze die auf eine Vielzahl von QP-Zuständen basieren aus und deutet auf die Mediation akustischer Pho-

nonen als die Quelle nicht-resonanter Kopplung hin.

Appendix A

Material parameters

Tabelle A.1: Parameters of In(Ga)As/GaAs material system, taken from Krummheuer *et al.* [75].

Quantity	Symbol	Value
Electron rest mass	m_0	$9.109 \times 10^{-31} \text{ kg}$
Effective electron mass	m_e	$0.067 m_0$
Effective hole mass (in plane)	$m_h^{x,y}$	$0.112 m_0$
Effective hole mass (vertical)	m_h^z	$0.377 m_0$
LO phonon energy	$\hbar\omega_{LO}$	36.6 meV
Density	λ	5.37 g/cm^3
Longitudinal sound velocity	v_L	5110 m/s
Transverse sound velocity	v_T	3340 m/s
Deformation potential for electrons	D_e	-14.6 eV
Deformation potential for holes	D_h	-4.8 eV

Bibliography

- [1] N. Gisin and R. Thew, “Quantum communication,” *Nature Photon.*, vol. 1, pp. 165–171, 2007.
- [2] C. H. Bennett and G. Brassard, “Quantum cryptography: public key distribution and coin tossing,” *Proc. IEEE Int. Conf. on Computers, Systems and Signal Processing, Bangalore (India)*, vol. 11, p. 175, 1984.
- [3] T. Heindel, C. A. Kessler, M. Rau, C. Schneider, F. Furst, M. Hagarth, W.-M. Schulz, M. Eichfelder, R. Robach, S. Nauerth, M. Lermer, H. Weier, M. Jetter, M. Kamp, S. Reitzenstein, S. Hffling, P. Michler, H. Weinfurter, and A. Forchel, “Quantum key distribution using quantum dot single-photon emitting diodes in the red and near infrared spectral range,” *New J. Phys.*, vol. 14, p. 083001, 2012.
- [4] S. Nauerth, F. Moll, M. Rau, C. Fuchs, J. Horwath, S. Frick, and H. Weinfurter, “Ait-to-ground quantum communication,” *Nature Photon.*, vol. 7, pp. 382–386, 2013.
- [5] J.-Y. Wang, B. Yang, S.-K. Liao, L. Zhang, Q. Shen, X.-F. Hu, J.-C. Wu, S.-J. Yang, H. Jiang, Y.-L. Tang, B. Zhong, H. Liang, W.-Y. Liu, Y.-H. Hu, Y.-M. Huang, B. Qi, J.-G. Ren, G.-S. Pan, J. Yin, J.-J. Jia, Y.-A. Chen, K. Chen, C.-Z. Peng, and J.-W. Pan, “Direct and full-scale experimental verifications towards ground-satellite quantum key distribution,” *Nature Photon.*, vol. 7, pp. 387–393, 2013.
- [6] P. Michler, A. Kiraz, C. Becher, W. V. Schoenfeld, P. M. Petroff, L. Zhang, E. Hu, and A. Imamoglu, “A Quantum Dot Single-Photon Turnstile Device,” *Science*, vol. 290, pp. 2282–2285, 2000.

- [7] P. Michler, A. Imamoglu, M. D. Mason, P. J. Carson, G. F. Strouse, and S. K. Buratto, “Quantum correlation among photons from a single quantum dot at room temperature,” *Nature*, vol. 406, pp. 968–970, 2000.
- [8] A. Politi, M. J. Cryan, J. G. Rarity, S. Yu, and J. L. O’Brien, “Silica-on-Silicon Waveguide Quantum Circuits,” *Science*, vol. 320, pp. 646–649, 2008.
- [9] Z.-S. Yuan, Y.-A. Chen, B. Zhao, S. Chen, J. Schmiedmayer, and J.-W. Pan, “Experimental demonstration of a BDCZ quantum repeater node,” *Nature*, vol. 454, pp. 1098–1101, 2008.
- [10] D. Bouwmeester, J.-W. Pan, K. Mattle, M. Eibl, H. Weinfurter, and A. Zeilinger, “Experimental quantum teleportation,” *Nature*, vol. 390, pp. 575–579, 1997.
- [11] R. M. Stevenson, R. J. Young, P. Atkinson, K. Cooper, D. A. Ritchie, and A. J. Shields, “A semiconductor source of triggered entangled photon pairs,” *Nature*, vol. 439, pp. 179–182, 2006.
- [12] R. Hafenbrak, S. M. Ulrich, P. Michler, L. Wang, A. Rastelli, and O. G. Schmidt, “Triggered polarization-entangled photon pairs from a single quantum dot up to 30 K,” *New J. Phys.*, vol. 9, p. 315, 2007.
- [13] A. Dousse, J. Suffczynski, A. Beveratos, O. Krebs, A. Lemaître, I. Sagnes, J. Bloch, P. Voisin, and P. Senellart, “Ultrabright source of entangled photon pairs,” *Nature*, vol. 466, pp. 217–220, 2010.
- [14] M. Müller, S. Bounouar, K. D. Jöns, and P. Michler, “On-demand generation of indistinguishable polarization-entangled photon pairs,” *arXiv*, vol. 1308.4256[quant-ph], 2013.
- [15] O. Madelung, U. Rössler, and M. Schulz, *Group IV Elements, IV-IV and III-V Compounds. Part b - Electronic, Transport, Optical and Other Properties*. Springer, 2002.
- [16] A. Babiński, J. Borysiuk, S. Kret, M. Czyż, A. Golnik, S. Raymond, and Z. R. Wasilewski, “Natural quantum dots in the InAs/GaAs wetting layer,” *Appl. Phys. Lett.*, vol. 92, p. 171104, 2008.

- [17] J. Kampmeier, M. Rashad, U. Woggon, M. Ruth, C. Meier, D. Schikora, K. Lischka, and A. Pawlis, “Enhanced photoluminescence of colloidal nanocrystals embedded in epitaxially grown semiconductor microstructures,” *Phys. Rev. B*, vol. 85, p. 155405, 2012.
- [18] S. Bednarek, B. Szafran, K. Lis, and J. Adamowski, “Modeling of electronic properties of electrostatic quantum dots,” *Phys. Rev. B*, vol. 68, p. 155333, 2003.
- [19] J. Weis, R. J. Haug, K. von Klitzing, and K. Ploog, “Competing channels in single-electron tunneling through a quantum dot,” *Phys. Rev. Lett.*, vol. 71, pp. 4019–4022, 1993.
- [20] P. Michler, ed., *Single Quantum Dots: Fundamentals, Applications and New Concepts*. Springer, 2003.
- [21] J. Kettler, “*Optical Spectroscopy on Single Charge Tunable In-GaAs/GaAs Quantum Dots*,” Master’s thesis, University of Stuttgart, 2010.
- [22] D. Gammon, E. S. Snow, B. V. Shanabrook, D. S. Katzer, and D. Park, “Fine Structure Splitting in the Optical Spectra of Single GaAs Quantum Dots,” *Phys. Rev. Lett.*, vol. 76, pp. 3005–3008, 1996.
- [23] V. D. Kulakovskii, G. Bacher, R. Weigand, T. Kummell, A. Forchel, E. Borovitskaya, K. Leonardi, and D. Hommel, “Fine Structure of Biexciton Emission in Symmetric and Asymmetric CdSe/ZnSe Single Quantum Dots,” *Phys. Rev. Lett.*, vol. 82, pp. 1780–1783, 1999.
- [24] S. M. Ulrich, *Non-Classical and Stimulated Photon Emission Processes from Self-Assembled Semiconductor Quantum Dots*. PhD thesis, University of Stuttgart, 2007.
- [25] R. Loudon, *The Quantum Theory of Light*. Oxford University Press, 2000.
- [26] L. Allen and J. H. Eberly, *Optical Resonance and Two-Level Atoms*. Dover Publications, Inc., New York, 1975.
- [27] M. Fox, *Quantum Optics: An Introduction*. Oxford University Press, 2006.

- [28] A. Ulhaq, *Photon Statistics and Dephasing of the Resonance Fluorescence from Single Quantum Dots*. PhD thesis, University of Stuttgart, 2012.
- [29] G. Lindblad, “On the generators of quantum dynamical semi-groups,” *Communications in Mathematical Physics*, vol. 48, pp. 119–130, 1976.
- [30] P. Meystre and M. Sargent, *Elements of Quantum Optics*. Springer, 2007.
- [31] A. Muller, *Resonance Fluorescence and Cavity Quantum Electrodynamics with Quantum Dots*. PhD thesis, University of Texas, 2007.
- [32] G. Wrigge, *Coherent and Incoherent Light Scattering in the Resonance Fluorescence of a Single Molecule*. PhD thesis, ETH Zürich, 2008.
- [33] S. Ates, *Resonance Fluorescence and Stimulated Light Emission from Coupled Semiconductor Quantum Dot-Cavity Systems*. PhD thesis, University of Stuttgart, 2011.
- [34] M. O. Scully and M. S. Zubairy, *Quantum Optics*. Cambridge University Press, 1997.
- [35] B. R. Mollow, “Power Spectrum of Light Scattered by Two-Level Systems,” *Phys. Rev.*, vol. 188, pp. 1969–1975, 1969.
- [36] K. J. Vahala, “Optical microcavities,” *Nature*, vol. 424, pp. 839–846, 2003.
- [37] E. Jaynes and F. W. Cummings, “Comparison of quantum and semiclassical radiation theories with application to the beam maser,” *Proceedings of the IEEE*, vol. 51, pp. 89–109, 1963.
- [38] P. Michler, ed., *Single Semiconductor Quantum Dots*. Springer, 2009.
- [39] L. C. Andreani, G. Panzarini, and J.-M. Gérard, “Strong-coupling regime for quantum boxes in pillar microcavities: Theory,” *Phys. Rev. B*, vol. 60, pp. 13276–13279, 1999.

- [40] T. Yoshi, A. Scherer, J. Hendrickson, G. Khitrova, H. M. Gibbs, G. Rupper, C. Ell, O. B. Shchekin, and D. G. Deppe, “Vacuum Rabi splitting with a single quantum dot in a photonic crystal nanocavity,” *Nature*, vol. 432, pp. 200–203, 2004.
- [41] E. M. Purcell, H. C. Torrey, and R. V. Pound, “Resonance Absorption by Nuclear Magnetic Moments in a Solid,” *Phys. Rev.*, vol. 69, pp. 37–38, 1946.
- [42] B. Gayral and J.-M. Gérard, “Comment on “Single-Mode Spontaneous Emission from a Single Quantum Dot in a Three-Dimensional Microcavity”,” *Phys. Rev. Lett.*, vol. 90, p. 229701, 2003.
- [43] R. H. Brown and R. Q. Twiss, “Correlation between Photons in two Coherent Beams of Light,” *Nature*, vol. 177, pp. 27–29, 1956.
- [44] R. H. Brown and R. Q. Twiss, “The Question of Correlation between Photons in Coherent Light Rays,” *Nature*, vol. 178, pp. 1447–1448, 1956.
- [45] M. C. Newstein, “Spontaneous Emission in the Presence of a Prescribed Classical Field,” *Phys. Rev.*, vol. 167, pp. 89–96, 1968.
- [46] C. R. Stroud, “Quantum-Electrodynamic Treatment of Spontaneous Emission in the Presence of an Applied Field,” *Phys. Rev. A*, vol. 3, pp. 1044–1052, 1971.
- [47] C. Cohen-Tannoudji and S. Reynaud, “Dressed-atom description of resonance fluorescence and absorption spectra of a multi-level atom in an intense laser beam,” *J. Phys. B: At. Mol. Phys.*, vol. 10, pp. 345–363, 1977.
- [48] B. R. Mollow, “Pure-state analysis of resonant light scattering: Radiative damping, saturation, and multiphoton effects,” *Phys. Rev. A*, vol. 12, pp. 1919–1943, 1975.
- [49] H. J. Kimble, M. Dagenais, and L. Mandel, “Photon Antibunching in Resonance Fluorescence,” *Phys. Rev. Lett.*, vol. 39, pp. 691–695, Sep 1977.
- [50] X. Xu, B. Sun, P. R. Berman, D. G. Steel, A. S. Bracker, D. Gammon, and L. J. Sham, “Coherent Optical Spectroscopy of a Strongly Driven Quantum Dot,” *Science*, vol. 317, pp. 929–932, 2007.

- [51] G. Jundt, L. Robledo, A. Högele, S. Fält, and A. Imamoglu, “Observation of Dressed Excitonic States in a Single Quantum Dot,” *Phys. Rev. Lett.*, vol. 100, p. 177401, 2008.
- [52] B. D. Gerardot, D. Brunner, P. A. Dalgarno, K. Karrai, A. Boodoloto, P. M. Petroff, and R. J. Warburton, “Dressed excitonic states and quantum interference in a three-level quantum dot ladder system,” *New J. Phys.*, vol. 11, p. 013028, 2009.
- [53] A. Muller, E. B. Flagg, P. Bianucci, X. Y. Wang, D. G. Deppe, W. Ma, J. Zhang, G. J. Salamo, M. Xiao, and C. K. Shih, “Resonance Fluorescence from a Coherently Driven Semiconductor Quantum Dot in a Cavity,” *Phys. Rev. Lett.*, vol. 99, p. 187402, 2007.
- [54] E. B. Flagg, A. Muller, J. W. Robertson, S. Founta, D. G. Deppe, M. Xiao, W. Ma, G. J. Salamo, and C. K. Shih, “Resonantly driven coherent oscillations in a solid-state quantum emitter,” *Nature Phys.*, vol. 5, pp. 203–207, 2009.
- [55] S. Ates, S. M. Ulrich, S. Reitzenstein, A. Löffler, A. Forchel, and P. Michler, “Post-Selected Indistinguishable Photons from the Resonance Fluorescence of a Single Quantum Dot in a Microcavity,” *Phys. Rev. Lett.*, vol. 103, p. 167402, 2009.
- [56] A. N. Vamivakas, Y. Zhao, C.-Y. Lu, and M. Atatüre, “Spin-resolved quantum-dot resonance fluorescence,” *Nature Phys.*, vol. 5, pp. 925–925, 2009.
- [57] A. Ulhaq, S. Weiler, S. M. Ulrich, R. Roßbach, M. Jetter, and P. Michler, “Cascaded single-photon emission from the Mollow triplet sidebands of a quantum dot,” *Nature Phot.*, vol. 6, pp. 238–242, 2012.
- [58] C. Matthiesen, A. N. Vamivakas, and M. Atatüre, “Subnatural Linewidth Single Photons from a Quantum Dot,” *Phys. Rev. Lett.*, vol. 108, p. 093602, 2012.
- [59] H. S. Nguyen, G. Sallen, C. Voisin, P. Roussignol, C. Diederichs, and G. Cassabois, “Ultra-coherent single photon source,” *Appl. Phys. Lett.*, vol. 99, p. 261904, 2011.

- [60] C. A. Schrama, G. Nienhuis, H. A. Dijkerman, C. Steijsiger, and H. G. M. Heideman, “Intensity correlations between the components of the resonance fluorescence triplet,” *Phys. Rev. A*, vol. 45, pp. 8045–8055, 1992.
- [61] A. Aspect, G. Roger, S. Reynaud, J. Dalibard, and C. Cohen-Tannoudji, “Time Correlations between the Two Sidebands of the Resonance Fluorescence Triplet,” *Phys. Rev. Lett.*, vol. 45, pp. 617–620, 1980.
- [62] W.-M. Schulz, *InP/AlGaInP Quantenpunkte - Design, Epitaxie und Charakterisierung von Halbleiter-Quantenpunkt-Bauelementen für Laser und Einzelphotonenquellen*. PhD thesis, University of Stuttgart, 2011.
- [63] S. Ates, S. M. Ulrich, A. Ulhaq, S. Reitzenstein, A. Löffler, S. Höfling, A. Forchel, and P. Michler, “Non-resonant dot–cavity coupling and its potential for resonant single-quantum-dot spectroscopy,” *Nature Phot.*, vol. 3, pp. 724–728, 2009.
- [64] S. M. Ulrich, S. Ates, S. Reitzenstein, A. Löffler, A. Forchel, and P. Michler, “Dephasing of Triplet-Sideband Optical Emission of a Resonantly Driven *InAs/GaAs* Quantum Dot inside a Microcavity,” *Phys. Rev. Lett.*, vol. 106, p. 247402, 2011.
- [65] A. J. Ramsay, A. V. Gopal, E. M. Gauger, A. Nazir, B. W. Lovett, A. M. Fox, and M. S. Skolnick, “Damping of Exciton Rabi Rotations by Acoustic Phonons in Optically Excited *InGaAs/GaAs* Quantum Dots,” *Phys. Rev. Lett.*, vol. 104, p. 017402, 2010.
- [66] A. J. Ramsay, T. M. Godden, S. J. Boyle, E. M. Gauger, A. Nazir, B. W. Lovett, A. M. Fox, and M. S. Skolnick, “Phonon-Induced Rabi-Frequency Renormalization of Optically Driven Single *InGaAs/GaAs* Quantum Dots,” *Phys. Rev. Lett.*, vol. 105, p. 177402, 2010.
- [67] J. Förstner, C. Weber, J. Danckwerts, and A. Knorr, “Phonon-Assisted Damping of Rabi Oscillations in Semiconductor Quantum Dots,” *Phys. Rev. Lett.*, vol. 91, p. 127401, 2003.
- [68] P. Machnikowski and L. Jacak, “Resonant nature of phonon-induced damping of Rabi oscillations in quantum dots,” *Phys. Rev. B*, vol. 69, p. 193302, 2004.

- [69] A. Vagov, M. D. Croitoru, V. M. Axt, T. Kuhn, and F. M. Peeters, “Nonmonotonic Field Dependence of Damping and Reappearance of Rabi Oscillations in Quantum Dots,” *Phys. Rev. Lett.*, vol. 98, p. 227403, 2007.
- [70] A. Nazir, “Photon statistics from a resonantly driven quantum dot,” *Phys. Rev. B*, vol. 78, p. 153309, 2008.
- [71] C. Roy and S. Hughes, “Phonon-Dressed Mollow Triplet in the Regime of Cavity Quantum Electrodynamics: Excitation-Induced Dephasing and Nonperturbative Cavity Feeding Effects,” *Phys. Rev. Lett.*, vol. 106, p. 247403, 2011.
- [72] M. Thorwart, J. Eckel, and E. R. Mucciolo, “Non-Markovian dynamics of double quantum dot charge qubits due to acoustic phonons,” *Phys. Rev. B*, vol. 72, p. 235320, 2005.
- [73] M. Glässl, M. D. Croitoru, A. Vagov, V. M. Axt, and T. Kuhn, “Influence of the pulse shape and the dot size on the decay and reappearance of Rabi rotations in laser driven quantum dots,” *Phys. Rev. B*, vol. 84, p. 125304, 2011.
- [74] F. Rossi and T. Kuhn, “Theory of ultrafast phenomena in photoexcited semiconductors,” *Rev. Mod. Phys.*, vol. 74, pp. 895–950, 2002.
- [75] B. Krummheuer, V. M. Axt, and T. Kuhn, “Theory of pure dephasing and the resulting absorption line shape in semiconductor quantum dots,” *Phys. Rev. B*, vol. 65, p. 195313, 2002.
- [76] D. P. S. McCutcheon, N. S. Dattani, E. M. Gauger, B. W. Lovett, and A. Nazir, “A general approach to quantum dynamics using a variational master equation: Application to phonon-damped Rabi rotations in quantum dots,” *Phys. Rev. B*, vol. 84, p. 081305, 2011.
- [77] C. Roy and S. Hughes, “Influence of Electron–Acoustic-Phonon Scattering on Intensity Power Broadening in a Coherently Driven Quantum-Dot–Cavity System,” *Phys. Rev. X*, vol. 1, p. 021009, 2011.
- [78] A. Ulhaq, S. Weiler, C. Roy, S. M. Ulrich, M. Jetter, S. Hughes, and P. Michler, “Detuning-dependent Mollow triplet of a

- coherently-driven single quantum dot,” *Opt. Express*, vol. 21, pp. 4382–4395, 2013.
- [79] R.-C. Ge, S. Weiler, A. Ulhaq, S. M. Ulrich, M. Jetter, P. Michler, and S. Hughes, “Mollow quintuplets from coherently excited quantum dots,” *Opt. Lett.*, vol. 38, pp. 1691–1693, 2013.
- [80] S. Weiler, A. Ulhaq, S. M. Ulrich, D. Richter, M. Jetter, P. Michler, C. Roy, and S. Hughes, “Phonon-assisted incoherent excitation of a quantum dot and its emission properties,” *Phys. Rev. B*, vol. 86, p. 241304, 2012.
- [81] S. Hughes, “private communication.”.
- [82] D. P. S. McCutcheon and A. Nazir, “Model of the Optical Emission of a Driven Semiconductor Quantum Dot: Phonon-Enhanced Coherent Scattering and Off-Resonant Sideband Narrowing,” *Phys. Rev. Lett.*, vol. 110, p. 217401, 2013.
- [83] S. Hughes, P. Yao, F. Milde, A. Knorr, D. Dalacu, K. Mnaymneh, V. Sazonova, P. J. Poole, G. C. Aers, J. Lapointe, R. Cheriton, and R. L. Williams, “Influence of electron-acoustic phonon scattering on off-resonant cavity feeding within a strongly coupled quantum-dot cavity system,” *Phys. Rev. B*, vol. 83, p. 165313, 2011.
- [84] R. Heitz, I. Mukhametzhanov, O. Stier, A. Madhukar, and D. Bimberg, “Enhanced Polar Exciton-LO-Phonon Interaction in Quantum Dots,” *Phys. Rev. Lett.*, vol. 83, pp. 4654–4657, 1999.
- [85] M. Bissiri, G. Baldassarri Höger von Högersthal, A. S. Bhatti, M. Capizzi, A. Frova, P. Frigeri, and S. Franchi, “Optical evidence of polaron interaction in InAs/GaAs quantum dots,” *Phys. Rev. B*, vol. 62, pp. 4642–4646, 2000.
- [86] M. A. Odnoblyudov, I. N. Yassievich, and K. A. Chao, “Polaron Effects in Quantum Dots,” *Phys. Rev. Lett.*, vol. 83, pp. 4884–4887, 1999.
- [87] S. Weiler, D. Stojanovic, S. M. Ulrich, M. Jetter, and P. Michler, “Postselected indistinguishable single-photon emission from the Mollow triplet sidebands of a resonantly excited quantum dot,” *Phys. Rev. B*, vol. 87, p. 241302, 2013.

- [88] C. K. Hong, Z. Y. Ou, and L. Mandel, "Measurement of sub-picosecond time intervals between two photons by interference," *Phys. Rev. Lett.*, vol. 59, pp. 2044–2046, 1987.
- [89] E. Bocquillon, V. Freulon, J.-M. Berroir, P. Degiovanni, B. Plaçais, A. Cavanna, Y. Jin, and G. Fève, "Coherence and Indistinguishability of Single Electrons Emitted by Independent Sources," *Science*, vol. 339, pp. 1054–1057, 2013.
- [90] C. Santori, D. Fattal, J. Vučković, G. S. Solomon, and Y. Yamamoto, "Indistinguishable photons from a single-photon device," *Nature*, vol. 419, pp. 594–597, 2002.
- [91] A. J. Bennett, D. C. Unitt, A. J. Shields, P. Atkinson, and D. A. Ritchie, "Influence of exciton dynamics on the interference of two photons from a microcavity single-photon source," *Opt. Express*, vol. 13, pp. 7772–7778, 2005.
- [92] R. B. Patel, A. J. Bennett, K. Cooper, P. Atkinson, C. A. Nicoll, D. A. Ritchie, and A. J. Shields, "Postselective Two-Photon Interference from a Continuous Nonclassical Stream of Photons Emitted by a Quantum Dot," *Phys. Rev. Lett.*, vol. 100, p. 207405, 2008.
- [93] R. B. Patel, A. J. Bennett, K. Cooper, P. Atkinson, C. A. Nicoll, D. A. Ritchie, and A. J. Shields, "Quantum interference of electrically generated single photons from a quantum dot," *Nanotechnology*, vol. 21, p. 274011, 2010.
- [94] A. J. Bennett, R. B. Patel, A. J. Shields, K. Cooper, P. Atkinson, C. A. Nicoll, and D. A. Ritchie, "Indistinguishable photons from a diode," *Appl. Phys. Lett.*, vol. 92, p. 193503, 2008.
- [95] K. D. Jöns, P. Atkinson, M. Müller, M. Heldmaier, S. M. Ulrich, O. G. Schmidt, and P. Michler, "Triggered Indistinguishable Single Photons with Narrow Line Widths from Site-Controlled Quantum Dots," *Nano Lett.*, vol. 13, pp. 126–130, 2012.
- [96] S. Laurent, S. Varoutsis, L. Le Gratiet, A. Lemaître, I. Sagnes, F. Raineri, A. Levenson, I. Robert-Philip, and I. Abram, "Indistinguishable single photons from a single-quantum dot in a two-dimensional photonic crystal cavity," *Appl. Phys. Lett.*, vol. 87, p. 163107, 2005.

- [97] S. Varoutsis, S. Laurent, P. Kramper, A. Lemaître, I. Sagnes, I. Robert-Philip, and I. Abram, “Restoration of photon indistinguishability in the emission of a semiconductor quantum dot,” *Phys. Rev. B*, vol. 72, p. 041303, 2005.
- [98] S. Weiler, A. Ulhaq, S. M. Ulrich, S. Reitzenstein, A. Löffler, A. Forchel, and P. Michler, “Highly indistinguishable photons from a quantum dot in a microcavity,” *Phys. Status Solidi (b)*, vol. 248, pp. 867–871, 2011.
- [99] D. Fattal, C. Santori, J. Vučković, G. S. Solomon, and Y. Yamamoto, “Indistinguishable single photons from a quantum dot,” *Phys. Status Solidi (b)*, vol. 238, pp. 305–308, 2003.
- [100] C. Matthiesen, M. Geller, C. H. H. Schulte, C. Le Gall, J. Hansom, Z. Li, M. Hugues, E. Clarke, and M. Atatüre, “Phase-locked indistinguishable photons with synthesized waveforms from a solid-state source,” *Nature Commun.*, vol. 4, p. 1600, 2013.
- [101] Y.-M. He, Y. He, Y.-J. Wei, D. Wu, M. Atatüre, C. Schneider, S. Höfling, M. Kamp, C.-Y. Lu, and J.-W. Pan, “On-demand semiconductor single-photon source with near-unity indistinguishability,” *Nat. Nanotechnol.*, vol. 8, p. 213, 2013.
- [102] E. B. Flagg, A. Muller, S. V. Polyakov, A. Ling, A. Migdall, and G. S. Solomon, “Interference of Single Photons from Two Separate Semiconductor Quantum Dots,” *Phys. Rev. Lett.*, vol. 104, p. 137401, 2010.
- [103] R. B. Patel, A. J. Bennett, I. Farrer, C. A. Nicoll, D. A. Ritchie, and A. J. Shields, “Two-photon interference of the emission from electrically tunable remote quantum dots,” *Nature Phot.*, vol. 4, pp. 632–635, 2010.
- [104] A. J. Bennett, R. B. Patel, C. A. Nicoll, D. A. Ritchie, and A. J. Shields, “Interference of dissimilar photon sources,” *Nature Phys.*, vol. 5, pp. 715–717, 2009.
- [105] S. V. Polyakov, A. Muller, E. B. Flagg, A. Ling, N. Borjemscaia, E. Van Keuren, A. Migdall, and G. S. Solomon, “Coalescence of Single Photons Emitted by Disparate Single-Photon Sources: The Example of InAs Quantum Dots and Parametric Down-Conversion Sources,” *Phys. Rev. Lett.*, vol. 107, p. 157402, 2011.

- [106] S. Ates, I. Agha, A. Gulinatti, I. Rech, M. T. Rakher, A. Badolato, and K. Srinivasan, “Two-Photon Interference Using Background-Free Quantum Frequency Conversion of Single Photons Emitted by an InAs Quantum Dot,” *Phys. Rev. Lett.*, vol. 109, p. 147405, 2012.
- [107] A. Kiraz, M. Ehrl, T. Hellerer, O. E. Müstecaplıođlu, C. Bräuchle, and A. Zumbusch, “Indistinguishable Photons from a Single Molecule,” *Phys. Rev. Lett.*, vol. 94, p. 223602, 2005.
- [108] R. Lettow, Y. L. A. Rezus, A. Renn, G. Zumofen, E. Ikonen, S. Götzinger, and V. Sandoghdar, “Quantum Interference of Tunably Indistinguishable Photons from Remote Organic Molecules,” *Phys. Rev. Lett.*, vol. 104, p. 123605, 2010.
- [109] T. Legero, T. Wilk, M. Hennrich, G. Rempe, and A. Kuhn, “Quantum Beat of Two Single Photons,” *Phys. Rev. Lett.*, vol. 93, p. 070503, 2004.
- [110] K. Sanaka, A. Pawlis, T. D. Ladd, K. Lischka, and Y. Yamamoto, “Indistinguishable Photons from Independent Semiconductor Nanostructures,” *Phys. Rev. Lett.*, vol. 103, p. 053601, 2009.
- [111] J. Dalibard and S. Reynaud, “Correlation signals in resonance fluorescence: interpretation via photon scattering amplitudes,” *J. Physique*, vol. 44, pp. 1337–1343, 1983.
- [112] H. F. Arnoldus and G. Nienhuis, “Photon correlations between the lines in the spectrum of resonance fluorescence,” *J. Phys. B: At. Mol. Phys.*, vol. 17, pp. 963–977, 1984.
- [113] C. A. Schrama, G. Nienhuis, H. A. Dijkerman, C. Steijsiger, and H. G. M. Heideman, “Destructive interference between opposite time orders of photon emission,” *Phys. Rev. Lett.*, vol. 67, pp. 2443–2445, 1991.
- [114] G. Nienhuis, “Spectral correlations in resonance fluorescence,” *Phys. Rev. A*, vol. 47, pp. 510–518, 1993.
- [115] T. Aichele, G. Reinaudi, and O. Benson, “Separating cascaded photons from a single quantum dot: Demonstration of multiplexed quantum cryptography,” *Phys. Rev. B*, vol. 70, p. 235329, 2004.

- [116] C. Santori, M. Pelton, G. Solomon, Y. Dale, and Y. Yamamoto, “Triggered Single Photons from a Quantum Dot,” *Phys. Rev. Lett.*, vol. 86, pp. 1502–1505, 2001.
- [117] B. Piętka, J. Suffczyński, M. Goryca, T. Kazimierczuk, A. Golnik, P. Kossacki, A. Wyszomolek, J. A. Gaj, R. Stepniowski, and M. Potemski, “Photon correlation studies of charge variation in a single GaAlAs quantum dot,” *Phys. Rev. B*, vol. 87, p. 035310, 2013.
- [118] H. S. Nguyen, G. Sallen, C. Voisin, P. Roussignol, C. Diederichs, and G. Cassabois, “Optically Gated Resonant Emission of Single Quantum Dots,” *Phys. Rev. Lett.*, vol. 108, p. 057401, 2012.
- [119] H. S. Nguyen, G. Sallen, M. Abbarchi, R. Ferreira, C. Voisin, P. Roussignol, G. Cassabois, and C. Diederichs, “Photoneutralization and slow capture of carriers in quantum dots probed by resonant excitation spectroscopy,” *Phys. Rev. B*, vol. 87, p. 115305, 2013.
- [120] F. Jelezko and J. Wrachtrup, “Single defect centres in diamond: A review,” *Phys. Status Solidi (a)*, vol. 203, pp. 3207–3225, 2006.
- [121] S. Bounouar, “private communication.”
- [122] J. Wiersig, C. Gies, N. Baer, and F. Jahnke, “Intrinsic Non-Exponential Decay of Time-Resolved Photoluminescence from Semiconductor Quantum Dots,” *Advances in Solid State Physics*, vol. 48, p. 91, 2009.
- [123] J. Johansen, B. Julsgaard, S. Stobbe, J. M. Hvam, and P. Lodahl, “Probing long-lived dark excitons in self-assembled quantum dots,” *Phys. Rev. B*, vol. 81, p. 081304, 2010.
- [124] U. Bockelmann, “Exciton relaxation and radiative recombination in semiconductor quantum dots,” *Phys. Rev. B*, vol. 48, pp. 17637–17640, 1993.
- [125] Y. Toda, O. Moriwaki, M. Nishioka, and Y. Arakawa, “Efficient Carrier Relaxation Mechanism in InGaAs/GaAs Self-Assembled Quantum Dots Based on the Existence of Continuum States,” *Phys. Rev. Lett.*, vol. 82, pp. 4114–4117, 1999.

- [126] O. Verzelen, R. Ferreira, and G. Bastard, “Excitonic Polarons in Semiconductor Quantum Dots,” *Phys. Rev. Lett.*, vol. 88, p. 146803, 2002.
- [127] G. D. Mahan, *Many-Particle Physics*. Plenum, New York, 1990.
- [128] P. Borri, W. Langbein, U. Woggon, V. Stavarache, D. Reuter, and A. D. Wieck, “Exciton dephasing via phonon interactions in InAs quantum dots: Dependence on quantum confinement,” *Phys. Rev. B*, vol. 71, p. 115328, 2005.
- [129] E. A. Muljarov and R. Zimmermann, “Dephasing in Quantum Dots: Quadratic Coupling to Acoustic Phonons,” *Phys. Rev. Lett.*, vol. 93, p. 237401, 2004.
- [130] A. Lemaître, A. D. Ashmore, J. J. Finley, D. J. Mowbray, M. S. Skolnick, M. Hopkinson, and T. F. Krauss, “Enhanced phonon-assisted absorption in single InAs/GaAs quantum dots,” *Phys. Rev. B*, vol. 63, p. 161309, 2001.
- [131] D. Dufåker, K. F. Karlsson, L. O. Mereni, V. Dimastrodonato, G. Juska, E. Pelucchi, and P. O. Holtz, “Evidence of nonadiabatic exciton-phonon interaction probed by second-order LO-phonon replicas of single quantum dots,” *Phys. Rev. B*, vol. 87, p. 085317, 2013.
- [132] U. Rössler, *Solid State Theory*. Springer Verlag, 2004.
- [133] M. Glässl, “private communication.”
- [134] L. Besombes, K. Kheng, L. Marsal, and H. Mariette, “Acoustic phonon broadening mechanism in single quantum dot emission,” *Phys. Rev. B*, vol. 63, p. 155307, 2001.
- [135] I. Favero, G. Cassaboïs, R. Ferreira, D. Darson, C. Voisin, J. Tignon, C. Delalande, G. Bastard, P. Roussignol, and J. M. Gérard, “Acoustic phonon sidebands in the emission line of single InAs/GaAs quantum dots,” *Phys. Rev. B*, vol. 68, p. 233301, 2003.
- [136] I. Favero, A. Berthelot, G. Cassaboïs, C. Voisin, C. Delalande, P. Roussignol, R. Ferreira, and J. M. Gérard, “Temperature dependence of the zero-phonon linewidth in quantum dots: An effect of the fluctuating environment,” *Phys. Rev. B*, vol. 75, p. 073308, 2007.

- [137] G. Sallen, A. Tribu, T. Aichele, R. André, L. Besombes, C. Bougerol, M. Richard, S. Tatarenko, K. Kheng, and J.-P. Poizat, “Subnanosecond spectral diffusion measurement using photon correlation,” *Nature Phot.*, vol. 4, pp. 696–699, 2010.
- [138] A. Berthelot, I. Favero, G. Cassabois, C. Vioisin, C. Delalande, P. Roussignol, R. Ferreira, and J. M. Gérard, “Unconventional motional narrowing in the optical spectrum of a semiconductor quantum dot,” *Nature*, vol. 2, pp. 759–764, 2006.
- [139] A. Nysteen, P. Kaer, and J. Mork, “Proposed Quenching of Phonon-Induced Processes in Photoexcited Quantum Dots due to Electron-Hole Asymmetries,” *Phys. Rev. Lett.*, vol. 110, p. 087401, 2013.
- [140] M. Glässl, A. M. Barth, and V. M. Axt, “Proposed Robust and High-Fidelity Preparation of Excitons and Biexcitons in Semiconductor Quantum Dots Making Active Use of Phonons,” *Phys. Rev. Lett.*, vol. 110, p. 147401, 2013.
- [141] M. Müller, “private communication.”
- [142] S. Haroche and J.-M. Raimond, *Exploring the Quantum: Atoms, Cavities and Photons*. Oxford University Press, 2006.
- [143] K. Hennessy, A. Badolato, M. Winger, D. Gerace, M. Atatüre, S. Gulde, S. Fält, E. L. Hu, and A. Imamoglu, “Quantum nature of a strongly coupled single quantum dot–cavity system,” *Nature*, vol. 445, pp. 896–899, 2007.
- [144] D. Press, S. Götzinger, S. Reitzenstein, C. Hofmann, A. Löffler, M. Kamp, A. Forchel, and Y. Yamamoto, “Photon Antibunching from a Single Quantum-Dot-Microcavity System in the Strong Coupling Regime,” *Phys. Rev. Lett.*, vol. 98, p. 117402, 2007.
- [145] J. Suffczyński, A. Dousse, K. Gauthron, A. Lemaître, I. Sagnes, L. Lanco, J. Bloch, P. Voisin, and P. Senellart, “Origin of the Optical Emission within the Cavity Mode of Coupled Quantum Dot-Cavity Systems,” *Phys. Rev. Lett.*, vol. 103, p. 027401, 2009.
- [146] D. Englund, A. Majumdar, A. Faraon, M. Toishi, N. Stoltz, P. Petroff, and J. Vučković, “Resonant Excitation of a Quantum Dot Strongly Coupled to a Photonic Crystal Nanocavity,” *Phys. Rev. Lett.*, vol. 104, p. 073904, 2010.

- [147] A. Majumdar, A. Papageorge, E. D. Kim, M. Bajcsy, E. D. Kim, P. Petroff, and J. Vučković, “Probing of single quantum dot dressed states via an off-resonant cavity,” *Phys. Rev. B*, vol. 84, p. 085310, 2011.
- [148] A. Ulhaq, S. Ates, S. Weiler, S. M. Ulrich, S. Reitzenstein, A. Löffler, S. Höfling, L. Worschech, A. Forchel, and P. Michler, “Linewidth broadening and emission saturation of a resonantly excited quantum dot monitored via an off-resonant cavity mode,” *Phys. Rev. B*, vol. 82, p. 045307, 2010.
- [149] M. Kaniber, A. Neumann, A. Laucht, M. F. Huck, M. Bichler, M.-C. Amann, and J. J. Finley, “Efficient and selective cavity-resonant excitation for single photon generation,” *New J. Phys.*, vol. 11, p. 013031, 2009.
- [150] E. Gallardo, L. J. Martínez, A. K. Nowak, D. Sarkar, H. P. van der Meulen, J. M. Calleja, C. Tejedor, I. Prieto, D. Granados, A. G. Taboada, J. M. García, and P. A. Postigo, “Optical coupling of two distant InAs/GaAs quantum dots by a photonic-crystal microcavity,” *Phys. Rev. B*, vol. 81, p. 193301, 2010.
- [151] A. Majumdar, M. Bajcsy, A. Rundquist, E. Kim, and J. Vučković, “Phonon-mediated coupling between quantum dots through an off-resonant microcavity,” *Phys. Rev. B*, vol. 85, p. 195301, 2012.
- [152] D. Dalacu, K. Mnaymneh, V. Sazonova, P. J. Poole, G. C. Aers, J. Lapointe, R. Cheriton, A. J. SpringThorpe, and R. Williams, “Deterministic emitter-cavity coupling using a single-site controlled quantum dot,” *Phys. Rev. B*, vol. 82, p. 033301, 2010.
- [153] A. Muller, E. B. Flagg, M. Metcalfe, J. Lawall, and G. S. Solomon, “Coupling an epitaxial quantum dot to a fiber-based external-mirror microcavity,” *Appl. Phys. Lett.*, vol. 95, p. 173101, 2009.
- [154] S. Strauf, K. Hennessy, M. T. Rakher, Y.-S. Choi, A. Badolato, L. C. Andreani, E. L. Hu, P. M. Petroff, and D. Bouwmeester, “Self-Tuned Quantum Dot Gain in Photonic Crystal Lasers,” *Phys. Rev. Lett.*, vol. 96, p. 127404, 2006.
- [155] G. Tarel and V. Savona, “Emission spectrum of a quantum dot embedded in a nanocavity,” *Phys. Status Solidi (c)*, vol. 4, pp. 902–905, 2009.

- [156] S. Hughes and P. Yao, “Theory of quantum light emission from a strongly-coupled single quantum dot photonic-crystal cavity system,” *Opt. Express*, vol. 17, no. 5, pp. 3322–3330, 2009.
- [157] U. Hohenester, “Cavity quantum electrodynamics with semiconductor quantum dots: Role of phonon-assisted cavity feeding,” *Phys. Rev. B*, vol. 81, p. 155303, 2010.
- [158] A. Laucht, N. Hauke, A. Neumann, T. Günthner, F. Hofbauer, A. Mohtashami, K. Müller, G. Böhm, M. Bichler, M.-C. Amann, M. Kaniber, and J. J. Finley, “Nonresonant feeding of photonic crystal nanocavity modes by quantum dots,” *J. Appl. Phys.*, vol. 109, p. 102404, 2011.
- [159] M. Kaniber, A. Laucht, A. Neumann, J. M. Villas-Bôas, M. Bichler, M.-C. Amann, and J. J. Finley, “Investigation of the nonresonant dot-cavity coupling in two-dimensional photonic crystal nanocavities,” *Phys. Rev. B*, vol. 77, p. 161303, 2008.
- [160] M. Winger, T. Volz, G. Tarel, S. Portolan, A. Badolato, K. J. Hennessy, E. L. Hu, A. Beveratos, J. Finley, V. Savona, and A. Imamoglu, “Explanation of Photon Correlations in the Far-Off-Resonance Optical Emission from a Quantum-Dot-Cavity System,” *Phys. Rev. Lett.*, vol. 103, p. 207403, 2009.
- [161] A. Laucht, M. Kaniber, A. Mohtashami, N. Hauke, M. Bichler, and J. J. Finley, “Temporal monitoring of nonresonant feeding of semiconductor nanocavity modes by quantum dot multiexciton transitions,” *Phys. Rev. B*, vol. 81, p. 241302, 2010.
- [162] A. Naesby, T. Suhr, P. T. Kristensen, and J. Mørk, “Influence of pure dephasing on emission spectra from single photon sources,” *Phys. Rev. A*, vol. 78, p. 045802, 2008.
- [163] A. Auffèves, J.-M. Gérard, and J.-P. Poizat, “Pure emitter dephasing: A resource for advanced solid-state single-photon sources,” *Phys. Rev. A*, vol. 79, 2009.
- [164] U. Hohenester, A. Laucht, M. Kaniber, N. Hauke, A. Neumann, A. Mohtashami, M. Seliger, M. Bichler, and J. J. Finley, “Phonon-assisted transitions from quantum dot excitons to cavity photons,” *Phys. Rev. B*, vol. 80, p. 201311, 2009.

- [165] P. Kaer, T. R. Nielsen, P. Lodahl, A.-P. Jauho, and J. Mørk, “Non-Markovian Model of Photon-Assisted Dephasing by Electron-Phonon Interactions in a Coupled Quantum-Dot–Cavity System,” *Phys. Rev. Lett.*, vol. 104, p. 157401, 2010.
- [166] A. Majumdar, E. D. Kim, Y. Gong, M. Bajcsy, and J. Vučković, “Phonon mediated off-resonant quantum dot–cavity coupling under resonant excitation of the quantum dot,” *Phys. Rev. B*, vol. 84, p. 085309, 2011.
- [167] P. Kaer, P. Lodahl, A.-P. Jauho, and J. Mørk, “Microscopic theory of indistinguishable single-photon emission from a quantum dot coupled to a cavity: The role of non-Markovian phonon-induced decoherence,” *Phys. Rev. B*, vol. 87, p. 081308, 2013.
- [168] P. Kaer, N. Gregersen, and J. Mørk, “The role of phonon scattering in the indistinguishability of photons emitted from semiconductor QED systems,” *New J. Phys.*, vol. 15, p. 035027, 2013.
- [169] S. Reitzenstein, C. Hofmann, A. Gorbunov, M. Strauß, S. H. Kwon, C. Schneider, A. Löffler, S. Höfling, M. Kamp, and A. Forchel, “AlAs/GaAs micropillar cavities with quality factors exceeding 150.000,” *Appl. Phys. Lett.*, vol. 90, p. 251109, 2007.
- [170] A. Löffler, J. P. Reithmaier, G. Şek, C. Hofmann, S. Reitzenstein, M. Kamp, and A. Forchel, “Semiconductor quantum dot microcavity pillars with high-quality factors and enlarged dot dimensions,” *Appl. Phys. Lett.*, vol. 86, p. 111105, 2005.
- [171] I. N. Stranski and L. Krastanow, “Zur Theorie der orientierten Ausscheidung von Ionenkristallen aufeinander,” *Monatshefte für Chemie/Chemical Monthly*, vol. 71, pp. 351–364, 1937.
- [172] S. Reitzenstein, “private communication.”
- [173] S. Weiler, “*Emissionseigenschaften von resonant gepumpten In-GaAs Quantenpunkten in Mikroresonatoren*,” Master’s thesis, University of Stuttgart, 2010.
- [174] S. Ates, S. M. Ulrich, P. Michler, S. Reitzenstein, A. Löffler, and A. Forchel, “Coherence properties of high- β elliptical semiconductor micropillar lasers,” *Appl. Phys. Lett.*, vol. 90, p. 161111, 2007.

-
- [175] S. Weiler, A. Ulhaq, S. M. Ulrich, S. Reitzenstein, A. Löffler, A. Forchel, and P. Michler, “Emission characteristics of a highly correlated system of a quantum dot coupled to two distinct micropillar cavity modes,” *Phys. Rev. B*, vol. 82, p. 205326, 2010.
- [176] A. Moelbjerg, P. Kaer, M. Lorke, and J. Mørk, “Resonance Fluorescence from Semiconductor Quantum Dots: Beyond the Mollow Triplet,” *Phys. Rev. Lett.*, vol. 108, p. 017401, 2012.
- [177] S. Hughes and H. J. Carmichael, “Phonon-mediated population inversion in a semiconductor quantum-dot cavity system,” *New J. Phys.*, vol. 15, p. 053039, 2013.
- [178] S. Hughes and H. J. Carmichael, “Stationary Inversion of a Two Level System Coupled to an Off-Resonant Cavity with Strong Dissipation,” *Phys. Rev. Lett.*, vol. 107, p. 193601, 2011.
- [179] N. Akopian, L. Wang, A. Rastelli, O. G. Schmidt, and V. Zwiller, “Hybrid semiconductor-atomic interface: slowing down single photons from a quantum dot,” *Nature Photon.*, vol. 5, pp. 230–233, 2011.

Publications

Journal publications

- S. Weiler, D. Stojanovic, S. M. Ulrich, M. Jetter, and P. Michler, *Postselected indistinguishable single-photon emission from the Mollow triplet sidebands of a resonantly excited quantum dot*, Phys. Rev. B **87**, 241302(R) (2013).
- R.-C. Ge, S. Weiler, A. Ulhaq, S. M. Ulrich, M. Jetter, P. Michler, and S. Hughes, *Mollow quintuplets from coherently excited quantum dots*, Opt. Lett. **38**, 1691–1693 (2013).
- A. Ulhaq, S. Weiler, C. Roy, S. M. Ulrich, M. Jetter, S. Hughes, and P. Michler, *Detuning-dependent Mollow triplet of a coherently-driven single quantum dot*, Opt. Express **21**, 4382–4395 (2013).
- S. Weiler, A. Ulhaq, C. Roy, S. Hughes, S. M. Ulrich, D. Richter, M. Jetter, and P. Michler, *Phonon-assisted incoherent excitation of a quantum dot and its emission properties*, Phys. Rev. B **86**, 241304(R) (2012).
- A. Ulhaq, S. Weiler, S. M. Ulrich, R. Roßbach, M. Jetter, and P. Michler, *Cascaded single-photon emission from the Mollow triplet sidebands of a quantum dot*, Nature Phot. **6**, 238–242 (2012).
- S. Weiler, A. Ulhaq, S. M. Ulrich, S. Reitzenstein, A. Löffler, A. Forchel, and P. Michler, *Highly indistinguishable photons from a quantum dot in a microcavity*, Phys. Status Solidi (b) **248**, 867–871 (2011).
- S. Weiler, A. Ulhaq, S. M. Ulrich, S. Reitzenstein, A. Löffler, A. Forchel, and P. Michler, *Emission characteristics of a highly*

correlated system of a quantum dot coupled to two distinct micropillar cavity modes, Phys. Rev. B **82**, 205326 (2010).

- A. Ulhaq, S. Ates, S. Weiler, S. M. Ulrich, S. Reitzenstein, A. Löffler, S. Höfling, L. Worschech, A. Forchel, and P. Michler, *Linewidth broadening and emission saturation of a resonantly excited quantum dot monitored via an off-resonant cavity mode*, Phys. Rev. B **82**, 045307 (2010).

Conference presentations

- S. Weiler, A. Ulhaq, S. M. Ulrich, M. Jetter, and P. Michler, *Emission characteristics of the Mollow triplet sidebands of a resonantly driven quantum dot*, International Workshop on the Optical Properties of Nanostructures (OPON), Bayreuth, Germany (2013).
- A. Ulhaq, S. Weiler, S. M. Ulrich, M. Jetter, and P. Michler, *Cascaded two-photon emission between Mollow triplet sidebands from a resonantly driven quantum dot*, 11th Conference on Nonlinear Optics and Excitation Kinetics in Semiconductors (NOEKS11), Stuttgart, Germany (2012).
- S. Weiler, A. Ulhaq, S. M. Ulrich, D. Richter, M. Jetter, C. Roy, S. Hughes, and P. Michler, *Acoustic phonon-assisted incoherent excitation of a quantum dot and its emission properties*, 11th Conference on Nonlinear Optics and Excitation Kinetics in Semiconductors (NOEKS11), Stuttgart, Germany (2012).
- S. Weiler, A. Ulhaq, S. M. Ulrich, D. Richter, M. Jetter, C. Roy, S. Hughes, and P. Michler, *Acoustic phonon-assisted incoherent excitation of a quantum dot and its emission properties*, 31st International Conference on the Physics of Semiconductors (ICPS 2012), Zürich, Switzerland (2012).
- A. Ulhaq, S. M. Ulrich, S. Weiler, C. Roy, S. Hughes, and P. Michler, *Single- and cascaded two-photon emission from Mollow triplet sidebands of a resonantly driven quantum dot*, 2nd French-German-Korean Workshop on Nanophotonics and Spintronics, Seonunsa, South Korea (2012).

- S. M. Ulrich, A. Ulhaq, S. Weiler, and P. Michler, *Coherence and photon statistics of the Mollow triplet sideband emission of a quantum dot*, DPG Spring Meeting, Berlin, Germany (2012).
- A. Ulhaq, S. Weiler, S. M. Ulrich, D. Richter, W.-M. Schulz, M. Jetter, and P. Michler, *Coherence Properties of Resonance Fluorescence Emission from a Single Quantum Dot in Planar Microcavities*, Optics of Excitons in Confined Systems (OECS12), Paris, France (2011).
- S. Weiler, A. Ulhaq, S. M. Ulrich, S. Reitzenstein, A. Löffler, A. Forchel, and P. Michler, *Emission characteristics of a highly correlated system of a quantum dot coupled to two distinct micropillar cavity modes*, Optics of Excitons in Confined Systems (OECS12), Paris, France (2011).
- S. Weiler, A. Ulhaq, S. M. Ulrich, S. Reitzenstein, A. Löffler, A. Forchel, and P. Michler, *Emission Characteristics of a Highly Correlated System of a Quantum Dot Coupled to Two Distinct Micropillar Cavity Modes*, Fundamental Optical Processes in Semiconductors, Lake Junaluska, North Carolina, USA (2011).
- S. Weiler, A. Ulhaq, S. M. Ulrich, S. Reitzenstein, A. Löffler, A. Forchel, and P. Michler, *Emission characteristics of a highly correlated system of a quantum dot coupled to two distinct micropillar cavity modes*, DPG Spring Meeting, Dresden, Germany (2011).
- A. Ulhaq, S. M. Ulrich, S. Ates, S. Weiler, S. Reitzenstein, A. Löffler, S. Höfling, A. Forchel and P. Michler, *Non-resonant Quantum Dot-Cavity Coupling*, DPG Spring Meeting, Regensburg, Germany (2010).

Lebenslauf

Stefanie Weiler

geboren am 14.01.1985 in Leonberg

1991 – 1995 Schellingschule Leonberg (Grundschule)

1995 – 2004 Johannes-Kepler-Gymnasium Leonberg

Juni 2004 Allgemeine Hochschulreife

10/04 – 02/10 Studium der Physik an der Universität
Stuttgart

02/10 Diplom in Physik
Thema der Diplomarbeit:
Emissionseigenschaften von resonant gepumpten
InGaAs Quantenpunkten in Mikroresonatoren

seit 03/10 Wissenschaftliche Mitarbeiterin mit Gelegenheit
zur Promotion im Fachbereich Physik an
der Universität Stuttgart

Dankssagungen

An dieser Stelle möchte ich mich bei denjenigen bedanken, die direkt zum Gelingen dieser Arbeit beigetragen haben, im Besonderen bei ...

- Herrn Prof. Dr. P. Michler für die Aufnahme am Institut, das große Interesse an meiner Arbeit, die ständige Unterstützung und den großen experimentellen Freiraum.
- Herrn Prof. Dr. T. Pfau für die Übernahme des Mitberichts.
- Herrn Prof. Dr. H. P. Büchler für die Übernahme des Prüfungsvorsitz.
- Der Carl-Zeiss Stiftung für das dreijährige Promotionsstipendium.
- Dr. A. Ulhaq for the extremely good and also very fruitful teamwork during the PHD years and the very nice atmosphere.
- Herrn Dr. S. M. Ulrich für die Einführung in die experimentelle Arbeit im Labor und die große Unterstützung während meiner gesamten Promotion!
- Herrn D. Stojanovic für die zuverlässige Zusammenarbeit bei den Hong-Ou-Mandel Messungen und die extrem gute und angenehme Arbeitsatmosphäre im Labor und im Büro.
- Herrn Dr. M. Jetter und Herrn Dr. W.-M. Schulz für die "gute" planare Probe aus dem Kristalllabor.
- Prof. Dr. S. Hughes for the extremely fruitful cooperation, the quick email responses, the great patience for the explanation of the theoretical concepts, which helped the physical understanding of dephasing in semiconductor quantum dots a lot.

- Herrn Prof. Dr. A. Forchel, Herrn Prof. Dr. S. Reitzenstein, Herrn Dr. M. Kamp, Herrn Dr. S. Höfling, Herrn M. Lermer, Herrn Dr. L. Worschech, Frau M. Emmerling für die zuverlässige und sehr gute Kooperation und die Mikroresonator-Proben aus Würzburg.
- Dr. Rong-Chung Ge and Dr. Chiranjeeb Roy for the very good cooperation during the preparation of several manuscripts.
- Herrn Dr. M. Glässel für die Hilfe beim theoretische Verständnis zum Thema Dephasierung, das Korrekturlesen der entsprechenden Kapitel meiner Arbeit und die große Unterstützung.
- Herrn M. Heldmaier, für die Hilfe bei Problemen im Labor und mit Mathematica.
- Frau U. Schäfer-Zerbst fürs Korrekturlesen meiner Arbeit.

Selbständigkeitserklärung

Hiermit erkläre ich, die vorliegende Arbeit selbständig und ohne fremde Hilfe verfasst bzw. nur die angegebenen Literaturquellen und Hilfsmittel verwendet zu haben.

Ich habe mich anderweitig nicht um einen Doktorgrad beworben und besitze einen entsprechenden Titel nicht.

Ich erkläre die Kenntnisnahme der dem Verfahren zugrundeliegenden Promotionsordnung der Fakultät 8 (Mathematik und Physik) der Universität Stuttgart.

Stuttgart, den December 5, 2013

Stefanie Weiler